A STUDY OF THE GALACTIC CENTRE ENVIRONMENT

A Thesis submitted for the degree of

Doctor of Philosophy

(in Physics)

to the

UNIVERSITY OF PUNE

by

Subhashis Roy

National Centre for Radio Astrophysics
Tata Institute of Fundamental Research
Pune University Campus
Pune - 411 007
India

E-mail : *roy@ncra.tifr.res.in*

JULY 2003

Contents

List of Figures

List of Tables

Acknowledgements

A thesis work spans over several years of time, and such work gets better with encouragement and input from others. This thesis work is observational, and I have used the Giant Metrewave Radio Telescope (GMRT) for a major fraction of the observations presented here. In this respect, I feel to look back in time. I joined here in 1996 and as part of my project work with Pramesh, started using the Giant Metrewave Radio Telescope (GMRT) in 1997. At that time, we could use only 8 antennas at a time with the then existing 8 station correlator. I started studying the Galactic Centre (GC), which being a very complex region, optimising the array configuration with the available antennas used to be quite complex. There also used to be various problems with the antennas, and we were required to understand and sometime act on our own to get the antennas back in work. Later on in 1998, when the 30 station correlator started working, we used to have occasional problem with the correlator, and I used to go and reset it sometime to make it working. This required me to know certain details of the instruments in use. At GMRT site, there used to be various personnel interactions with different academic members of the institute on interferometry and the telescope in general. This helped me to get a much better grasp on these topics than probably what I could have made on my own. I also had developed a knack for trying to attain high dynamic range images with the telescope.

Other than various techniques of interferometry and data analysis and in general on experimental work, I could learn quite a few things on radiation from celestial bodies and the interstellar medium (ISM) while working with Pramesh during the thesis. This

helped me to do this thesis work quite independently, and it is a pleasure to thank him.

I had several discussions with D. J. Saikia on the polarisation properties of the extragalactic sources. I also had discussions on various other chapters of the thesis with him, and I would like to thank him. I discussed with Ravi Subrahmanyan rotation measure of extragalactic sources and their intrinsic contribution, and it is a pleasure to thank him. I had several interesting discussions with Rajaram on general Physics, estimating rotation measure from the polarisation angles and on error analysis. I would like to thank him. I have also discussed the issues related to the magnetic field in galaxies with Kandaswamy Subramaniam, and I would like to thank him.

I used to have quite a few discussions with Govind Swarup on my observations and finally on the progress of the thesis. While discussing with him, I have come to know several interesting field of work in Astrophysics, including scintillation. On several occasions, he had corrected my doubts on working and design of several functional parts of GMRT. I would like to thank him.

Analysing the data acquired from a Radio Interferometer like the GMRT requires quite a good amount of software. In this regard, I would particularly like to thank Sanjay Bhatnagar, whose softwares I have used regularly at the GMRT site. Final analysis of these data sets also require use of standard packages for doing interferometric data analysis like the AIPS and the MIRIAD, and I would like to thank the writers of these softwares. As UNIX (Linux) is quite a standard operating system in educational institutes, observational work also requires a reasonable amount of understanding of the associated softwares. In this regard, some of my seniors have particularly been helpful at the beginning of my thesis. I would particularly like to thank Divya Oberoi, Solai Jeyakumar and Sanjay Bhatnagar in this regard. I also had nice discussions with Rajiv Singh on operating systems and the working of the operating system kernel, and I would like to acknowledge him.

When I was new to this place and at various stages later on, my seniors especially

Divya Oberoi and certain other academic members especially Pradeep had helped to get me accustomed to this place and Pune in general, and I would like to thank them. While I was busy in writing this thesis, my colleagues, especially Dharam Vir Lal and Neeraj Gupta had helped to proof-read certain chapters of the thesis. I would like to thank them. Nimisha G. Kantharia pointed out ways about writing better English, while she proof-read some of the chapters of my thesis, and I would like to thank her.

I would also like to thank Annabhat Joshi, who has particularly helped in dealings with the University.

Finally, I would like to acknowledge my parents and my brother whose moral support have all along been with me.

This thesis uses data from the GMRT, the VLA and the ATCA. I thank the staff of the GMRT that made these observations possible. GMRT is run by the National Centre for Radio Astrophysics of the Tata Institute of Fundamental Research. The National Radio Astronomy Observatory (NRAO) is facility of the National Science Foundation operated under cooperative agreement by Associated Universities, Inc. The Australia Telescope is funded by the Commonwealth of Australia for operation as a National Facility managed by CSIRO.

Declaration

CERTIFIED that the work incorporated in this thesis entitled **“A study of the Galactic Centre Environment"** submitted by **Subhashis Roy** was carried out by the candidate under my supervision. Such material as has been obtained from other sources has been duly acknowledged in the thesis.

Place: Pune — Prof. D. J. Saikia

Date: July 8, 2003 — Thesis Supervisor

Abstract

The central regions of many galaxies emit extremely large amounts of energy ($> 10^{45}$ ergs sec^{-1}). Extensive studies of these central regions have identified many interesting phenomena, which have led us to believe that the central supermassive black hole is the source of energy in many of these galaxies. In the case of our own Galaxy, such studies of the central region have the added advantage of a much higher spatial resolution ($> 10^3$ times) and therefore, it is hoped that detailed studies of this region will lead to a better understanding of the physical processes occurring in this dense region. Such detailed studies also provide inputs to understand processes in the central regions of other similar galaxies.

Though the nucleus of our Galaxy is only mildly active, the central one kiloparsec region, which is referred to as the Galactic Centre (GC) region, harbours a variety of unique and interesting phenomena, not seen elsewhere in the Galaxy. This region shows a concentration of gas, mostly in the form of molecular clouds, which are characterised by densities $\sim 10^4$ molecules cm^{-3}, velocity dispersions $\sim$10 km s^{-1}, temperatures $\sim$70 K and and apparent magnetic fields $\sim$1 milliGauss. Most of these quantities are one to two orders of magnitude larger than that found in the disk of our Galaxy. In addition to the molecular clouds, this region also harbour a 2.6×10^6 $M_\odot$ black hole at the centre of the Galaxy, unique highly polarised non-thermal linear radio filamentary structures, extended non-thermal radiation due to synchrotron emission and regions of ionised hydrogen. The high density in the region, possibly due to a large gradient in the gravitational force, leads to the formation of massive, high luminosity stars with

short life-spans. These stars end their lives in supernova explosions and many of the supernova remnants (SNR) can be seen at radio wavelengths.

This region is largely opaque at optical wavelengths due to very high extinctions caused by the dust and gas, and been studied at radio, infrared and X-ray wavelengths. Though these studies have enabled us to get a broad picture, the complexity of the region has come in the way of our understanding of many of the processes occurring in the region. In this thesis, we have carried out radio studies of the discrete objects and the surrounding Interstellar Medium (ISM) found in the GC region with the Giant Metrewave Radio Telescope (GMRT), Very Large Array (VLA) and the Australia Telescope Compact Array (ATCA).

Our study with the GMRT has resulted in the lowest frequency (620 MHz) detection of radio emission towards the black hole candidate (Sgr A*), which puts new constraints on its emission mechanism. We also investigated the peculiar filamentary structures suspected to be part of candidate supernova remnants (SNRs), and confirmed G3.1-0.6 to be an SNR, and suggested that the large shell-like structure G358.1−0.0 is an old SNR in the region. Some of the peculiar radio sources, like the unique non-thermal filaments (NTFs) have only been observed towards the GC, and it is important to verify that these objects are really located in the GC region and not a foreground or background object. However, out of eight such NTFs, the distances of only two have been constrained. We have carried out atomic hydrogen (HI) absorption line studies towards three more NTFs, which constrains their distances to within a few kilo parsecs of the Galactic Centre. We have investigated the large scale magnetic field prevalent in the ISM of the central $l \times b$ = 12° x 3.6° region of the Galaxy using the ATCA and the VLA. There has been no systematic study of the RM in the inner part of the Galaxy, and our study of the Faraday rotation towards 45 background extragalactic sources indicates that an axisymmetric model of the magnetic field is not valid in the central region of the Galaxy.

In Chapter 1, an introduction to the thesis work has been presented. Based on pre-

vious investigations at radio wavelengths, we present a summary of our understanding of the central region of the Galaxy. The topics which are discussed are: (i) the known physical properties of Sgr-A*, (ii) the central mass distribution, (iii) sources identified from previous radio studies of the region (e.g., SNRs, NTFs, molecular clouds, HII regions and extended synchrotron emission), (iv) distance constraints to the sources seen in the direction of the GC, and (v) the electron density in the GC ISM and the prevalent magnetic field.

Observations of the GC region at 610 MHz with the GMRT are presented in Chapter 2. The GC region has been observed previously in high resolution using the VLA at 330 MHz, 1.4 GHz and 4.8 GHz, and several sources have been identified within the central half a degree region of the Galaxy. At the very centre of the Galaxy is the 2.6 $\times 10^6$ $M_\odot$ black hole candidate, which coincides with a point source in radio-emission known as the Sgr-A*. Along the line of sight to the source is a dense HII region known as the Sgr-A West, east of which is seen the SNR Sgr-A East. Around this region, a $7'$ halo which is thought to be a mixture of thermal and non-thermal emission can also be identified. Assuming the Sgr-A* to be coincident with the black hole, various models have been proposed to explain its emission in different wavebands. At low radio frequencies below 1.0 GHz, this object has not been detected and it has been proposed that the free-free absorption by the HII region Sgr-A West absorbs most of the radiation at frequencies less than 500 MHz. In our observations of the GC with the GMRT at 610 MHz, Sgr-A* was detected. The estimated spectral index of Sgr-A* between 1.4 GHz and 610 MHz is quite flat. However, a comparison of the 610 MHz and 1.4 GHz map of this region indicates that most parts of the Sgr-A West HII region have optical depth ~ 1. Therefore, the flat spectral index of Sgr-A* between 1.4 GHz and 610 MHz, which is similar to its high-frequency spectral index, indicates that Sgr-A* is located in front of the Sgr-A West complex and is not embedded within this complex as was suggested earlier.

In Chapter 3, we describe GMRT 330 MHz observations of the filamentary structures

suspected to be associated with candidate SNRs. Previous observations at 843 MHz by the Molonglo Observatory Synthesis Telescope (MOST) identified 17 new candidate SNRs in this region. From their list, two objects, which appeared to have associated filamentary structures, were observed with the GMRT. It is shown that one of these filamentary structure is actually part of an extended object (G3.1−0.6), which we have confirmed as an SNR. From the observation of the second field, two extended curved objects were identified, which we have suggested to be part of a large shell (G358.1−0.0), with size of $\approx 52' \times 72'$. This is possibly the remains of an old supernova in the region. Three suspected SNRs, G356.3−0.3, G356.6+0.1 and G357.1−0.2 detected in the MOST 843 MHz survey of the GC region appears to be located on this shell like structure. Based on the HI absorption towards the candidate SNR G357.1−0.2, which shows peculiar filamentary structures, we suggested it to be a separate SNR along the same line of sight of the large shell. In this chapter, the radio continuum and HI absorption study of the unusual object known as the 'Tornado nebula' has also been presented. The 'Tornado nebula' is believed to be an SNR, and is the second strongest source in the GC region. The appearance of this source is unique with a compact source near the eastern end, and central filamentary structures reminiscent of the 'Radio-arc' at the GC. Extended emission appears to spread out from the central region like a tail $\approx 7'$ towards north west, which slowly fades out. Due to its similarity with extragalactic head-tail sources, its classification as an SNR have been questioned in the past. Hence, to resolve some of the above ambiguities, new observations have been carried out at 330 MHz. These observations were carried out to study the distribution of spectral index along this object. Further observations have also been carried out with the GMRT in the 1420 MHz band to study the HI absorption profile towards this object. We have compared the existing continuum map at 1.4 GHz with the 330 MHz map, and estimated the spectral index distribution over the source. The mean spectral index between 330 and 1410 MHz is found to be consistent with its estimated value between 1.4 and 5 GHz. Compared

to the central region, the tail of the source does not show any significant steepening of the spectral index, which rules out the possibility of it being an extragalactic head tail source. Also, systematic variation of spectral index at different parts of the object is estimated to be less than 0.2, which is consistent with what is typically observed for SNRs. The HI absorption study of this object confirms the previous tentative detection of weak absorption by the 'Nuclear disk'. This study shows the 'Tornado nebula' is either embedded or located beyond the 'Nuclear disk' feature found within a few hundred parsecs from the GC.

In Chapter 4, we describe our HI absorption study of the non-thermal filaments (NTFs) which are seen only towards the central $\sim 2^{\circ}$ region of our Galaxy. From high-resolution, radio-continuum maps, NTFs appear to be less than $\sim$1 parsec in width, but extend up to 30 parsecs in length. Except one, all the other seven known NTFs are oriented nearly perpendicular to the Galactic plane and they are found to be highly polarised at centimetre wavelengths. Since these NTFs remain straight despite interaction with nearby molecular clouds, it is believed that the molecular clouds and the NTFs are in pressure equilibrium, which indicates a high magnetic field strength (a few milliGauss) inside the NTFs. Magnetic fields of comparable strengths are thought to be present in the central $\sim$ 400 parsecs of the Galaxy. However, except for two NTFs known as the 'Radio-arc' and the 'Snake', distances to other six NTFs are not constrained. In order to estimate their distances, HI absorption study of three NTFs Sgr C, G359.54+0.18 and G359.79+0.17 have been carried out with the GMRT, and details of the study have been presented in this chapter. These three NTFs are located to the south and south west of the Sgr A complex. The Sgr C NTF also appears to have an HII region located close to the NTF. In this chapter, it is shown that the Sgr C NTF and the HII region are located within a few hundred parsecs from the GC. A molecular cloud with a velocity of -100 km s^{-1} appears to be interacting with the central part of the Sgr C NTF. This study indicates that the Sgr C HII region is located further away than the Sgr C NTF and rules out any

possible interaction between them. The NTF G359.54+0.18 shows weak HI absorption at a velocity of -140 km s^{-1}, which is the velocity of a known dense molecular cloud seen towards the filament. This cloud is believed to be located within $\sim$ 200 parsecs from the centre of the Galaxy and this provides a lower limit to the distance. The upper limit to the distance of this NTF is 10.5 kiloparsecs from the sun. The distance to the other NTF G359.79+0.17 is constrained to be between 5.5 and 10.5 kiloparsecs from the sun.

Magnetic fields can play an important role in the central region of a galaxy. However, except the central 200 parsecs region of our Galaxy, the magnetic field in the rest of the inner 5 kiloparsecs region is not observationally constrained. Even the magnetic field within the central 200 parsecs have been determined mainly towards some unique objects like the NTFs. If these NTFs are manifestations of a favourable local environment, the estimated RM towards these objects can provide misleading values of the magnetic field in the GC region. Therefore, observations have been carried out to estimate the line-of-sight magnetic field in the central 2 kiloparsecs region ($-6^\circ \leq l \leq 6^\circ$, $-1.8^\circ \leq b \leq 1.8^\circ$, where l and b are galactic longitude and latitude respectively) by estimating the Faraday Rotation Measure (RM) towards a large number of suspected background extragalactic sources. In Chapter 5, we describe the criteria used for selecting the background sources, which were used as probes to estimate the RM introduced by the GC ISM. Since these sources have not been studied in polarisation earlier, a total of 64 source were observed, out of which 45 were found to be polarised. The maps of the sources and their polarisation fractions are presented in this chapter. Most of the sources has been identified as possible extragalactic sources for the first time.

We have determined polarisation angles from the Stokes Q, U parameters of the polarised sources. Since each source was observed in at least four different frequencies in the 5 and 8 GHz bands, it was possible to use a least square fit to unambiguously estimate the RM from the polarisation angles. The estimated RMs towards the sources

have been presented in Chapter 6. We have estimated depolarisation of the sources between 8 and 5 GHz. Since the scale size of RM fluctuation due to the GC ISM is significantly higher than the resolution, depolarisation indicate Faraday rotation caused by thermal plasma outside of the Galaxy, which introduces additional RM other than the GC ISM. These sources have been rejected while estimating the RM introduced by the GC region. The observed RM towards the sources located within 1.5° from the Galactic plane are quite high with RM $\sim$ 1000 rad m^{-2}. RM estimated towards most of the sources are positive (median value of 467 $\pm$87 rad m^{-2}) and shows no significant variation as a function of galactic longitude. If the magnetic field lines in the GC would be circularly symmetric with respect to the rotation axis of the Galaxy, the observed RM along the Galactic plane would undergo a reversal of sign across l=0°. Our observations, that the RMs do not vary significantly across l=0°, rules out any circularly symmetric model (‘ring model’) of the large scale magnetic field near the central region of the Galaxy. The above result is consistent with a bisymmetric spiral model of the magnetic field in the Galaxy (Simard-Normandin & Kronberg 1980), where the magnetic field do not change sign across ‘l’=0°.and we discuss possible implications of these results.

Publications

(a) Published Papers:

(1) "GMRT observations of four suspected supernova remnants near the Galactic Centre". Roy, S. & Rao, A.P., 2002, Mon. Notices Royal Astron. Soc., 329, 775

(2) "Constraints on distances to Galactic Centre non-thermal filaments from HI absorption", Roy, S., 2003, Astronomy & Astrophysics, 403, 917

(3) “Sgr A* at low radio frequencies: Giant Metrewave Radio Telescope observations”, Roy, S. & Rao, A. P., 2004, Mon. Notices Royal Astron. Soc., 349, L25

(b) Papers submitted for Publication:

(1) “Extragalactic sources towards the central region of the Galaxy”, Roy S., Rao A. P. & Subrahmanyan R., 2004, submitted to MNRAS

(2) “Magnetic field near the Galactic Centre from Rotation Measure observations of Extragalactic sources”, 2004, Roy S., Rao A. P. & Subrahmanyan R., 2004, submitted to MNRAS

(c) Papers in Conference Proceedings

(1) "GMRT Observations of the Galactic Centre region".

Roy, S. & Rao, A.P.

Proceedings of the International Astronomical Union Symposium 199 on *The Universe at low radio frequencies*, 2002, p-274. Eds. A. Pramesh Rao, G. Swarup, Gopal-Krishna.

(2) "Radio Study of the Galactic Centre Environment".

Roy, S.

Invited talk given at the Astronomical Society of India–XXI in February, 2002.

Bulletin of Astronomical Society of India, 2002, 30, 637.

(3) “Observations of the Galactic Centre at 610 MHz with the GMRT”, Roy, S. & Rao, A.P., 2003, Astron. Nachr./AN 324, No. S1, 391.

(4) “Constraints on distances to Galactic Centre non-thermal filaments from HI absorption”, Roy S., 2003, Astron. Nachr./AN 324, No. S1, 229.

(5) “Magnetic field in the Galactic Centre: Rotation Measure (RM) observations of extragalactic sources”, Roy S., Rao A.P. & Subrahmanyan R., 2003, Astron. Nachr./AN 324, No. S1, 41.

Chapter 1

Introduction

1.1 Background

The details with which an astronomical object can be studied is determined by its luminosity and the distance. Due to their high luminosity (10^{45} ergs sec^{-1}), the central regions of galaxies are detected at large distances (millions of parsecs). In a typical radio survey of the sky (e.g., NRAO VLA sky survey (NVSS)), the central regions of a variety of galaxies are detected out to large distances. Since most of their luminosity is confined in a region less than 1 kpc, they usually appear star (point) like due to inadequate angular resolution. High resolution study of these objects in the last few decades have indicated association of a central supermassive black hole with this massive output of energy from the central region of these galaxies. However, the detailed mechanisms involved are quite uncertain, and spatial resolution plays an important role in distinguishing the physical processes taking place. The energy emitted from the central region of our Galaxy is much less than what is observed from the centre of the active galaxies. However, due to its proximity, observing the central region of the Galaxy provides us two major advantages. These are (i) study of faint objects, which cannot be detected in any external galaxy with the presently existing telescopes, and (ii) availability of high spatial resolution. These, in turn help us infer about the physical processes occurring in the central region of similar galaxies.

In this chapter, we first provide a brief overview of the Galactic Centre (GC) region, which is followed by a discussion of the current limitation in our understanding of the region and possible studies than can overcome these deficiencies.

1.2 Overview

The Galactic Centre encompasses a wide variety of phenomena occurring on stellar to galactic scales. With improved observational techniques, research in this area has advanced rapidly in the last three decades. High resolution studies of the central 1 kpc of the Galaxy, commonly referred to as the Galactic Centre (GC) region, have identified a variety of unique objects like the Radio-arc consisting of linear parallel filaments (Yusef-Zadeh et al. 1984) and the $2.6 \times 10^6 M_\odot$ object at the centre (Genzel et al. 1996; Ghez et al. 1998; Reid et al. 1999), probably the best known case of a supermassive black hole at the centre of galaxies. These studies have also established a concentration of gas, mostly in the form of molecular clouds characterised by densities $\sim 10^4$ molecules cm^{-3}, velocity dispersions $\sim$10 km s^{-1}, temperatures $\sim$70 K and apparent magnetic fields $\sim$1 milliGauss in the region. Most of these quantities are one to two orders of magnitude larger than that found in the disk of our Galaxy. In addition to the molecular clouds, non-thermal filaments and the supermassive black hole, this region also harbours extended non-thermal radiation due to synchrotron emission and thermal emission from regions of ionised hydrogen (HII regions). The high density in the GC region, which is possibly due to a large gradient in the gravitational force, leads to the formation of massive, high luminosity stars with short life-spans. These stars end their lives in supernova explosions and many of the supernova remnants (SNRs) can be seen at radio wavelengths. The reviews by Oort (1977); Brown & Liszt (1984); Genzel & Townes (1987); Morris & Serabyn (1996), describes this research. Melia & Falcke (2001) provides the recent advances made in the research on the black hole and the central region (a few pc) of the

Galaxy, while Reid (1993) summarises research on the distance to the Galactic Centre. Since this region is opaque at optical wavelengths, it has mostly been studied in radio, infrared, X-ray and γ-ray. These observations have allowed us to study the discrete objects and the surrounding Interstellar Medium of the region with considerable details. Here, we will concentrate on the radio observations.

1.2.1 Discrete objects in the Radio Continuum images of the GC

Radio emission is due to either thermal (bremsstrahlung) emission as in HII region or non-thermal (mostly synchrotron) emission characterised by power law spectra. Thermal emission from extended sources turnover at low radio frequencies (see section 1.4.1 for details), and this can be used to distinguish from the non-thermal emission, which typically increases at lower frequencies. Earlier studies of the GC at radio wavelengths have been carried out by Little (1974) at 408 MHz, Downes et al. (1978) at 610 MHz and by Mills & Drinkwater (1984) at 843 MHz. However, all these studies had low resolution (∼few arc-min). High resolution (∼arc-sec) multifrequency radio studies of the region have been carried out with the Very Large Array (VLA). A false colour image of the large scale structures seen at 330 MHz in the central 3° region (∼0.5 kpc) of the Galaxy (LaRosa et al. 2000) is shown in Fig. 1.1, which will be discussed below.

1.2.1.1 Sgr A Complex:

As in Fig. 1.1, the most intense emission is seen within the central few arc minute region of the Galaxy, which is called Sgr A complex. The emission at 330 MHz is dominated by non-thermal emission from Sgr A East, which could be a supernova remnant (Pedlar et al. 1989). A 4.8 GHz radio image of this region (Fig. 1.2) shows that Sgr A complex consists of the thermal spiral Sgr A West, the compact source Sgr A* near its centre, the non-thermal source Sgr A East and the 7′ halo surrounding Sgr A East. The compact source Sgr A* coincides with the inferred position of the 2.6×10^6 $M_\odot$ black hole candi-

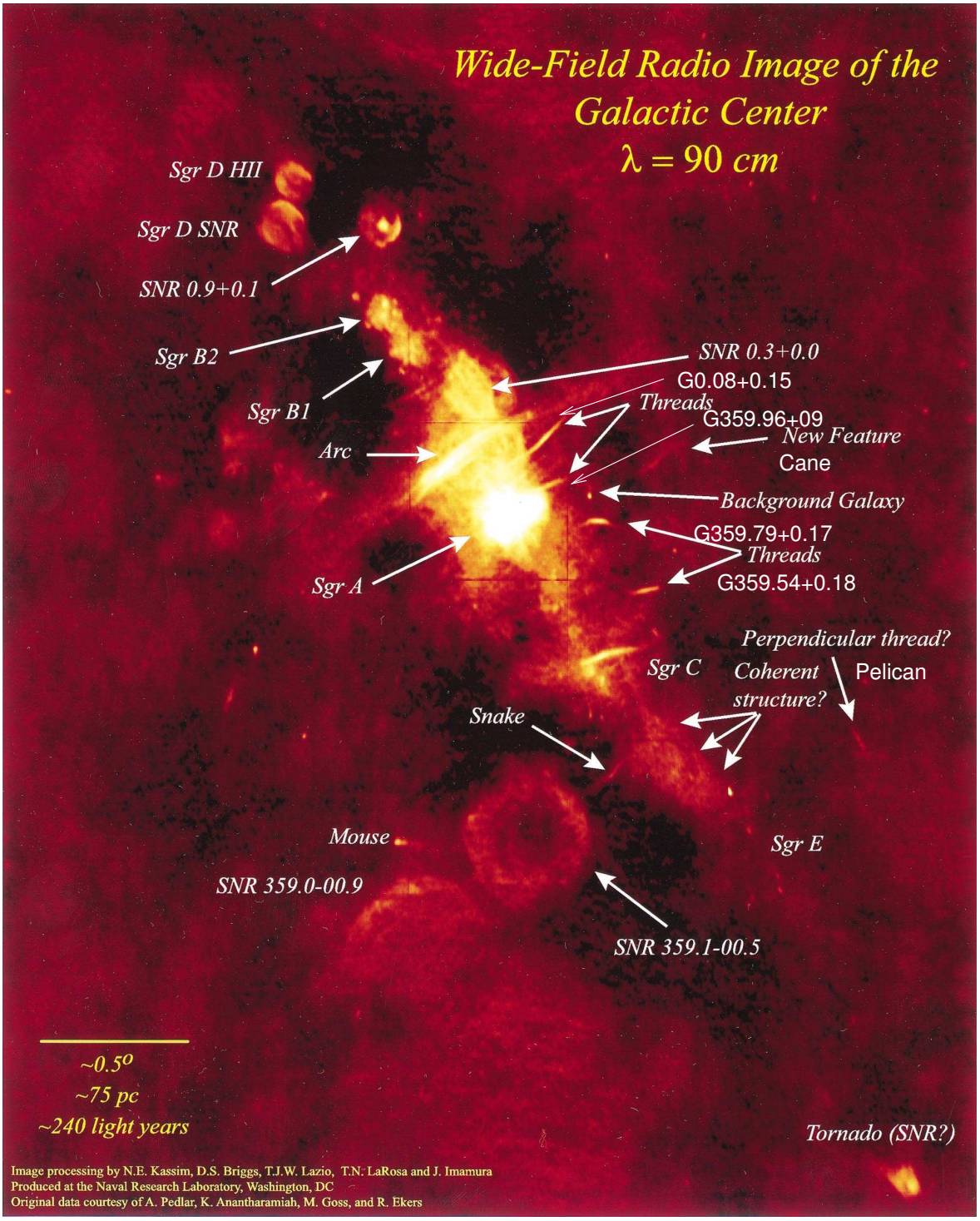

Figure 1.1: 330 MHz false colour image of the GC (LaRosa et al. 2000)

date at the dynamical centre of the Galaxy. Sgr A* has a slightly inverted spectral index (≈ 0.2) in centimetre wavelengths. Previously, this object has not been detected below 1

GHz and it is believed that free-free absorption by Sgr A West causes its non-detection below 1 GHz (Davies et al. 1976). At 330 MHz, Sgr A East is seen in absorption against Sgr A West, indicating that Sgr A East is located behind Sgr A West (Pedlar et al. 1989).

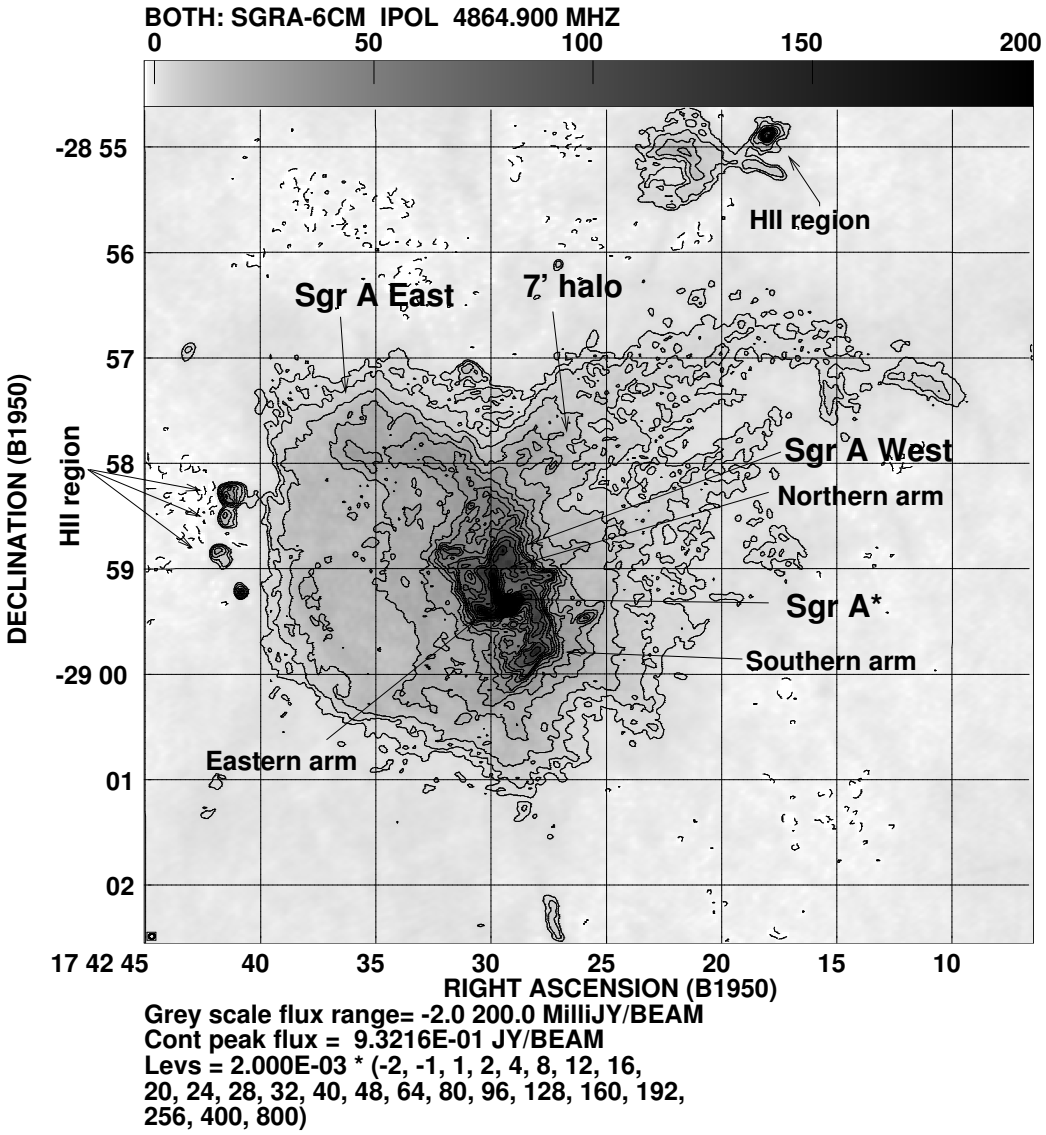

Figure 1.2: 4.8 GHz continuum map of Sgr A complex. The rms noise in the map is 0.5 mJy/beam. The beam size is $3.4'' \times 2.9''$, with beam position angle of –80° (Yusef-Zadeh 1989)

1.2.1.2 Supernova remnants (SNRs)

Six SNRs are seen in the 330 MHz map shown in Fig. 1.1 , which we discuss below, ordered in higher to lower Galactic longitude.

(i) Sgr D SNR: Located at l=1.05°, b=–0.1°, it has a filled-shell morphology and is identified as a shell-type SNR in A Catalogue of Galactic Supernovae Remnants by D. A. Green[1]. In contrast to its 330 MHz image (Fig. 1.1), which shows that this source has a well-defined boundary around the entire circumference, 20 cm observations (Liszt 1992) show a bright northern rim and a very diffuse southern boundary. At 6 cm only the northern rim of this source is detected (Mehringer et al. 1998). The spectral index reported by Green is –0.6 (where $S(\nu) \propto \nu^{\alpha}$; ν is observing frequency, α is the spectral index and $S(\nu)$ is the flux density). However, combining its 330 MHz flux density with those in the literature, LaRosa et al. (2000) estimates a spectral index of –0.4 for this SNR.

(ii) G0.9+0.1: This SNR appears like a composite supernova remnant with two distinct components. Earlier observations of this SNR led Helfand & Becker (1987) to classify it as a composite supernova remnant. It has a flat spectrum core ($\approx 2'$ in diameter) and a steep spectrum shell (diameter $15'$). Mereghetti et al. (1998) have detected X-ray emission from the core with the BeppoSAX satellite. The small angular extent of the X-ray emission, and an estimated age of a few thousand years provides evidence for the core being powered by a young pulsar, giving rise to its flat spectrum core in radio. LaRosa et al. (2000) estimates the spectral index of the core to be 0.12 and of the shell to be –0.77.

(iii) G0.33+0.0: This object was first identified by Larosa & Kassim (1985) in an 80 MHz Clark Lake image of the GC region. Based on multifrequency archival data, Larosa & Kassim (1985) suggested it as a possible SNR (or evidence of Seyfert-like

[1]http://www.mrao.cam.ac.uk/surveys/snrs/

activity), and Kassim & Frail (1995) confirmed it as an SNR. In their 300 MHz image, LaRosa et al. (2000) identifies another shell with lower surface brightness, on which this SNR appears to be superposed. LaRosa et al. (2000) speculate that the lower surface brightness shell is the remnant of another supernova in the region.

(iv) G359.1−0.5: This object has a shell type morphology. Reich & Fuerst (1984) classified it as an SNR on the basis of its nonthermal spectrum (α=−0.37) and polarised emission. Neutral hydrogen (HI) absorption-line observations suggest that this object is located at the Galactic Centre and is possibly associated with the non-thermal filament known as the Snake (Uchida et al. 1992a). This shell is also surrounded by a ring of high velocity molecular gas. The mass of this ring and its energetics imply that the shell may in fact be a superbubble driven by a cluster of roughly 200 O type stars (Uchida et al. 1992a). LaRosa et al. (2000) estimates a spectral index of –0.7 for this object, and is considerably steeper than its high frequency spectrum.

(v) G359.0−0.9: This source appears to be a partial shell with a bright northern rim. Its distance is not known and consequently its location with respect to the GC is ambiguous. LaRosa et al. (2000) estimates its spectral index to be −0.5.

(vi) Tornado nebula (G357.7−0.1): This object has an unusual structure and even its classification as a supernova remnant has been questioned (Becker & Helfand 1985). It shows a similarity to extragalactic head-tail sources (Weiler & Panagia 1980). The 1720 MHz maser line of OH arises from collisionally excited gas behind a C-type shock and is an important diagnostic of the interaction process that may occur between molecular clouds and associated X-ray emitting shell-type supernova remnants (Frail et al. 1994), and detection of OH maser (Brogan et al. 2000) from the region is suggestive of it being an SNR. In spite of its steep spectral index (α=−0.5), its classification as either shell type or filled centre type is still uncertain (Shaver et al. 1985).

1.2.1.3 The non-thermal filaments (NTFs) or threads

The long narrow non-thermal filaments (NTFs) observed in high resolution radio-continuum maps are unique features only seen towards the central $\sim 1^{\circ}$ region of our Galaxy. These structures are less than 1 pc in width and extend up to 30 pc in length. They may occur in isolation (in which case they have been called threads) or in bundles, such as those comprising the linear portion of the prominent Radio Arc (Morris & Serabyn 1996). With the exception of the NTF called the Pelican (Lang et al. 1999a), which is nearly parallel to the Galactic plane, all other NTFs are oriented perpendicular to the Galactic plane to within 20°. Morphologically, the NTFs are strikingly uniform in brightness and curvature and therefore quite different from the meandering, contorted filamentary structures usually observed in supernova remnants and emission-line nebulae. The morphology of the NTFs suggests that they reflect the local magnetic field direction and radio polarisation evidence supports this notion (Morris & Serabyn 1996, and references therein). A clue to the strength of the magnetic field in the NTFs is provided by the near absence of deformation or bending along their lengths. Some of the NTFs which have been sufficiently well studied have been found to be associated with, and are probably interacting with, at least one molecular cloud. However, despite large velocity dispersions within Galactic centre molecular clouds and the likely presence of velocity differences between the molecular cloud and the magnetic field, the magnetic filaments do not show distortions at the interaction sites. By equating the apparent turbulent pressures within clouds (or the ram pressure associated with presumed cloud motion relative to the field) to the magnetic pressure, as a minimum condition on the strength of the magnetic field, Yusef-Zadeh & Morris (1987a) have estimated that the magnetic field strength within the NTFs is $\sim$milliGauss. Nine NTFs are seen in Fig.1.1, and we briefly describe their observed properties below.

(i) Radio arc: Located some $15'$–$20'$ north of Sgr A (Fig. 1.1), the Galactic Centre

Radio arc (GCRA) is one of the most striking radio structure observed in our Galaxy. It is aligned almost perpendicular to the Galactic plane at l=0.18°, while a series of curved structures, the Arches, appear to connect the Arc to the 7′ halo. The GCRA was first resolved into a large number of narrow linear features by Yusef-Zadeh et al. (1984) who (Yusef-Zadeh et al. (1986)) presented an extensive series of images of this region at 20 and 6 cm. These filamentary structures show strong polarisation with no line emission and are therefore nonthermal synchrotron sources. Most of these filaments have a flat or slightly inverted spectral index Anantharamaiah et al. (1991). Several prominent HII regions cross and appear to interact with the GCRA filaments suggesting in situ particle acceleration via magnetic reconnection between a large-scale magnetic field and magnetic fields in a molecular cloud (e.g., Serabyn & Morris (1994)) associated with the HII region. Lasenby et al. (1989) has observed this NTF in HI absorption, and their observation indicates that it is actually located near the GC and is not a projection effect by any object located outside the GC.

(ii) Sgr C: The Sgr C complex consists of an NTF and a HII region located ≈1′ south of the NTF (Fig. 1.1). This complex was studied in detail by Liszt (1985) while LaRosa et al. (2000) studied the spectral index across the filament. At the far eastern end of the filament, the thermal emission from the Sgr C HII region dominates and the spectral index is flat with α=0.02. Beyond the HII region, the spectral index remains essentially constant at approximately −0.5.

(iii) G0.08+0.15: This NTF is located just north of Sgr A East (Fig. 1.1) and is south of the GCRA. It is referred to as the northern thread. It runs through the arched filaments and almost merges with the diffuse GCRA emission at its far northern extension. This filament appears extremely narrow in high resolution images. has a width of 4″, which corresponds to a linear size of 0.15 pc (Lang et al. 1999b) and a linear extent of 11.9′ at 90 cm, corresponding to a length of at least 29.4 pc at the distance of the GC (LaRosa et al. 2000). Its spectral index is –0.6 (LaRosa et al. 2000).

(iv) G359.96+0.096: This filament, known as the southern thread (Fig. 1.1), connects to and appears to emanate from the Sgr A complex. In the 20 cm image, this thread shows considerable substructure consisting of several distinct filaments braided together and its spectral index $\alpha \sim -0.6$ (LaRosa et al. 2000).

(v) G359.79+0.17: This object appears to be an isolated filament (Fig. 1.1) and has a curved morphology reminiscent of a partial shell. It has been clearly seen to bifurcate into, at least, two major strands in the 20 cm image (Lang et al. 1999b). Its length derived from the 90 cm image is approximately 15 pc (LaRosa et al. 2000). Its spectral index $\alpha \approx -0.6$ (Anantharamaiah et al. 1991).

(vi) G359.54+0.18: This source is another example of an apparently isolated filament (Fig. 1.1). It is considerably shorter than the others, extending only 12 pc (Yusef-Zadeh et al. 1997a). Yusef-Zadeh et al. (1997a) have established that this is indeed a magnetic structure with a high degree of polarisation. From the 6 cm image, they have also shown that the source consists of several sub-filaments that overlap near its midpoint (17h43m50s, –29°14′). Staguhn et al. (1998) have suggested that this filament is interacting with two molecular clouds, one at its extreme eastern end and the other one to the east of the peak brightness. Its spectral index $\alpha \approx -0.8$ (Anantharamaiah et al. 1991).

(vii) G359.1−0.2 (Snake): The Snake is an unusual NTF (Fig. 1.1), first noticed in the MOST (843 MHz) Galactic Centre survey (Gray et al. 1991). It is the only filament that exhibits abrupt changes in direction/shape. As derived from the 20 and 35 cm images, the Snake is also the longest NTF, traversing a distance of roughly 60 pc (Gray et al. 1995).

(viii) G358.85+0.47 (Pelican): This source is located approximately a degree ($\sim$150 pc in projection) southwest of Sgr A. It is the only filament that has abrupt changes in direction or kinks. It was first noticed in the high dynamic image at 90 cm made by LaRosa et al. (2000). Follow-up observations of this source by Lang et al. (1999a) at shorter wavelengths have confirmed it to be a NTF. This is the only known NTF parallel

to the Galactic plane [2].

(ix) G359.85+0.39 (Cane): This is a newly discovered system of isolated nonthermal filaments located ≈0.5° northwest of Sgr A. Unlike other isolated NTFs which show subfilaments, braiding of subfilaments and flaring at their ends, these filaments are simple linear structures and resemble the parallel bundled filaments in the GCRA. However, the most unusual feature of these filaments is that the 20/90 cm spectral index uniformly decreases as a function of position, in contrast to all other NTFs in the Galactic centre (LaRosa et al. 2001). They explained the variation of spectral index by a curved electron energy spectrum embedded in a diverging magnetic field.

1.2.1.4 HII regions

Due to their thermal spectrum and the detection of radio recombination lines from them, three prominent extended objects Sgr D, Sgr B and Sgr E complex (Fig. 1.1) are observed within the central 2° region of the GC are identified as HII regions. Here, we briefly discuss some of the observed properties of these HII regions.

It should be noted here that various GC source complexes like Sgr E, C, and perhaps A are associated with the molecular analog of the HI 'rotating nuclear disk', i.e., they appear along a locus of rotationally permitted velocities showing a strong velocity gradient (at least at $l < 0.5°$). Sgr B complex (consists of Sgr B1 and B2) have velocities noticeably below that of the rotation signature (whose gradient abruptly and prematurely ends at $l > 0.5°$, partly as an artifact of the warped inner-galaxy gas distribution, (see Burton & Liszt 1992)). Sgr D has a very modest velocity indeed, but nonetheless is not a local object (Liszt 1992).

(i) Sgr D: Located at l=1.13°, b=–0.11°, its emission is sharply bounded and appears strikingly similar in size (diameter ≈ 7′) to that of the adjacent SNR. The radio recom-

[2] Recently, Nord et al. (2003) have published a list of 18 new candidate NTFs in the GC region, and Larosa et al. (2003) confirm 4 more NTFs. Many of these new NTFs and the candidate ones are oriented randomly with respect to the Galactic plane.

bination line (RRL) is centred at –19 km s^{-1}, but the formaldehyde absorption spectrum against this source extends up to +125 km s^{-1} (Downes et al. 1980), thereby suggesting it to be located in or beyond the GC region (Liszt 1992). Recent 74 MHz observation of the GC region by Brogan et al. (2003), however, indicates that at least the extended emission associated with this source must be located on the near side of the GC, and is likely to be located on the near side of the CMZ.

(ii) Sgr B: Single-dish radio continuum images at a resolution of a few arcminutes show that the Sgr B complex consists of two strong peaks surrounded by a large-scale ($15'$) halo elongated along the Galactic plane (Bieging 1976). The two main components are Sgr B1 (G0.5–0.0) and Sgr B2 (G0.7–0.0). Sgr B1 and Sgr B2 have similar flux densities at 20 cm. The emission from Sgr B1 arises from a wealth of extended bright rim and shell-like structures. One of these features is a bar of ionised gas approximately 6 pc in length. The presence of these large structures might be the result of individual compact HII regions having expanded and coalesced over time. Thus, Sgr B1 may be an evolved star-forming region (Mehringer et al. 1992). Sgr B2 (G0.7–0.0) is a well-studied massive star-forming region located $\sim$100 pc in projection from the Galactic centre. The Sgr B2 molecular cloud is quite exceptional. It has a mass of 5×10^6 $M_\odot$ (Lis & Goldsmith 1990), making it one of the most massive molecular clouds in the Galaxy. The density in the core of the cloud is $\sim10^5$ cm^{-3} (Cummins et al. 1986). Many interstellar molecules were detected here for the first time. High resolution radio continuum measurements show that Sgr B2 is composed of several compact and ultracompact HII regions (Benson & Johnston 1984). Using VLBI techniques, Reid et al. (1988) used one group of H_2O masers in Sgr B2 to determine the distance to this star-forming region, which is estimated to be 7.1 ± 1.5 kpc. RRL studies indicate that the ionised gas in this region has velocities predominantly in the range of 50–75 km s^{-1} (Roelfsema et al. 1987).

(iii) Sgr E: Located at $l \sim 358.4^\circ - 359^\circ$, this complex is believed to be an active star-

forming HII region-molecular cloud complex located some 200 pc away from the GC. Caswell & Haynes (1987) report a recombination line at –209 km s^{-1} from this region. Broad CO emission line at comparable velocities have been detected (Liszt 1992).

1.2.2 Interstellar Medium

The emission from our Galaxy's centre peaks in several wave-bands. Line emission from the molecular CO increases sharply in the central few hundred pc, indicating large amount of molecular gas. The central one degree region is also quite bright in radio and infrared continuum emission. The Galactic Centre is obscured at optical and UV wavelengths by a line of sight interstellar extinction of nearly 30 visual magnitudes, but becomes visible again at energies above 1 keV (Morris & Serabyn 1996) due to emission mostly from hot ionised gas in the region. X-ray line emission also peaks at the Galactic Centre (GC) (Koyama et al. 1989). Recent high resolution observations with the Chandra X-ray observatory has indicated that the earlier detection of diffuse X-ray emission is composed of many compact sources (Muno et al. 2003) superposed on a background diffuse emission probably caused by large amount of hot gas with temperatures of $\sim 10^7$ K. This compact and luminous nuclear region, hereafter designated the central molecular zone or CMZ (to distinguish this largely molecular region from the more extensive 'HI nuclear disk' in which it is embedded), produces 5–10% of our Galaxy's infrared emission and accounts for roughly 10% of our Galaxy's molecular gas content (Mezger 1978; Mezger & Pauls 1979). We discuss below further details of this region.

1.2.2.1 Kinematics of HI features near the GC

Within a radius of 4 kpc in the Galaxy, there is an abrupt disappearance of the neutral gas disk, characterised by adherence to the Galactic plane and an almost circular motion outside the 4 kpc radius. The HI gas in the central region shows systematic velocity pattern, but with large deviation from pure circular motion. At a distance of about 3

kpc from the GC is the prominent velocity feature known as the ‘expanding 3-kpc arm’ (Rougoor 1964). This feature has a velocity of –53 km s^{-1} near l=0°. It is observed continuously over $-22^\circ \leqslant l \leqslant 10^\circ$ near the Galactic plane, and is located at the near side of the GC. No counterpart of this feature is known at the far side of the GC. On scales of 200 to 1500 pc, the gas distribution is believed to lie in a plane which is inclined with the Galactic plane. The observed velocities usually have substantial components of both circular and noncircular motions. The highest velocity feature observed near l=0° is interpreted as arising from a ‘nuclear disk’ of HI in rapid rotation around the centre (Rougoor & Oort 1960). Within the central 200 pc of the Galaxy, most of the gas exists in the molecular form, and the fraction of HI in these dense molecular clouds is ∼1% (Liszt et al. 1983). The HI associated with the near side of the 180-pc molecular ring gives rise to the –135 km s^{-1} HI feature near l=0°. HI at high positive velocities (∼150 km s^{-1}) has also been observed, which could originate either from the far side of the molecular ring (Oort 1977) or from different HI features (Cohen & Davies 1979).

1.2.2.2 The Central Molecular Zone

The structure of the CMZ is best studied by high-resolution observations of the CO molecule (Bania 1977; Liszt & Burton 1978; Bally et al. 1987, 1988; Oka et al. 1998). Within the ‘4-kpc molecular ring’ of the Galaxy, a region consisting of both molecular and atomic gas markedly tilted with respect to the Galactic plane is observed (Morris & Serabyn 1996). Except the central 200 pc of the GC, the emissivity of CO in this region is low (Scoville et al. 1987) reflecting an average molecular surface density of 5 $M_\odot$ pc^{-2} in the HI nuclear disk (Burton & Liszt 1992), which is a mixed molecular/atomic layer that occupies the region inside of our Galaxy’s ‘4-kpc molecular ring’. At a radius of about 200 pc, a transition occurs to a largely molecular, high-density ($\gtrsim 10^4$ cm^{-3}), high volume filling factor ($\gtrsim$0.1) medium containing 5×10^7 $M_\odot$ of gas (Bally et al. 1988). Such densities are usually found only in molecular cloud cores, with small net filling

factor, but in the CMZ, stable clouds require such densities to withstand tidal shearing (Guesten & Downes 1980). The clouds in the CMZ also show significantly elevated temperatures (30–200 K, typically 70 K; (Huettemeister et al. 1993), and high internal velocity dispersions (15–50 km s^{-1}) comparable to the intercloud velocity dispersion. The distribution and kinematics of the gas in the CMZ are inconsistent with both axial symmetry and uniform circular rotation (Bally et al. 1988). The distribution is such that roughly three quarters of the dense molecular gas is located at positive longitudes, three quarters is at positive velocities, and large radial and vertical motions are present in a significant fraction (30%) of the gas (Bally et al. 1988). On the basis of molecular kinematics, it is possible to divide the CMZ gas into two components:

(i) A high-velocity (130–200 km s^{-1}), quasi-continuous ring structure surrounding the nucleus and having a radius ($\approx$180 pc) suggesting a location at the outer boundary of the CMZ. The kinematics of this ring (hereafter referred to as the '180-pc molecular ring') and its tilt relative to the Galactic plane (see Fig. 1.3) are continuous with those of the exterior HI nuclear disk, indicating that this structure likely marks the location of an HI/H_2 transition (Binney et al. 1991). (ii) Inside of this 'boundary' lies the mass-dominant molecular component. This component consists of a lower velocity ($\lesssim$100 km s^{-1}) population of dense and massive molecular clouds. This cloud population (which includes the clouds associated with the Sgr A–Sgr E HII regions) lies close to the true Galactic plane and is referred to as the Galactic centre 'disk population' (Morris & Serabyn 1996). One massive molecular cloud, having a velocity of 50 km s^{-1} (also known as the 50 km s^{-1} cloud), is located adjacent to the Galactic centre in projection. It is associated with the bright, central Sgr A complex (Ekers et al. 1983; Pedlar et al. 1989). However, due to our location in the Galactic disk, the true geometric arrangement of these clouds and structures remains doubtful.

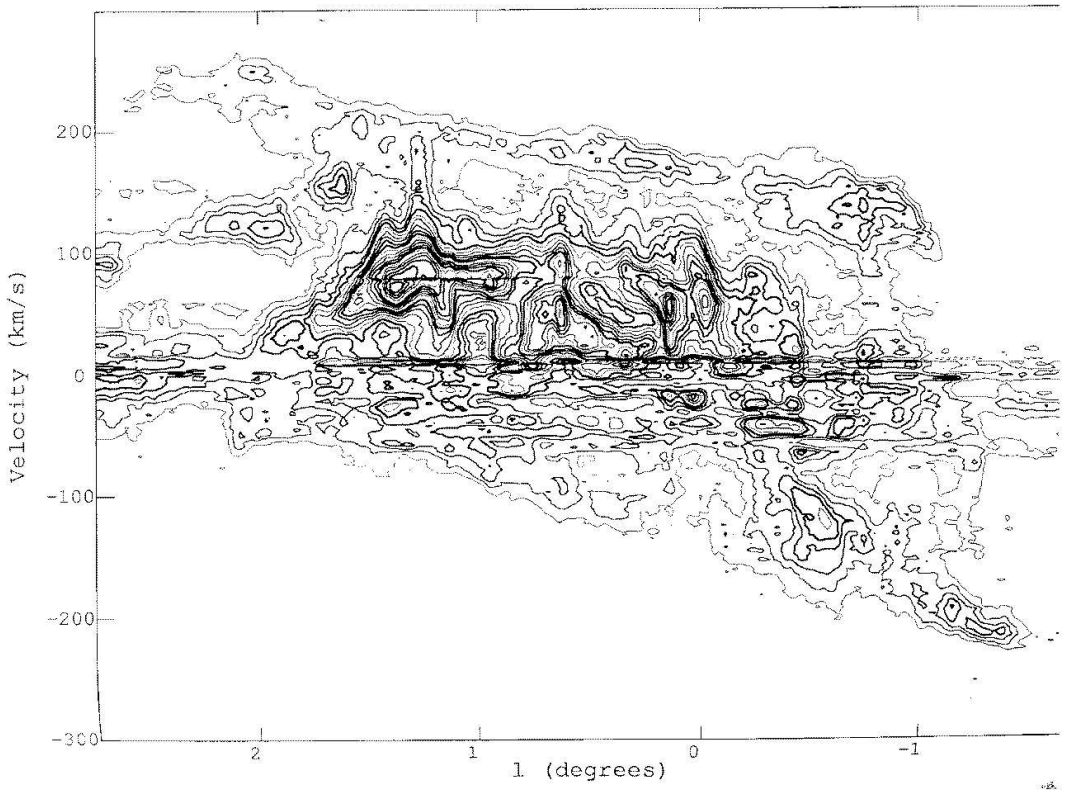

Figure 1.3: 12CO J=1−0 emission contours in a position-velocity plane in which position extends along the line from l, b = 2.5, -0.333 to -2.0, 0.1333, from the AT&T Bell Labs survey (Uchida et al. 1996). This line, tilted by 6° with respect to the Galactic plane, was chosen to reflect the tilt of the plane containing the 180-pc molecular ring. Contour units are 1.4, 2.8, 4.4, 6.2, 8.2, 10.4, . . . K.

1.3 Some unsolved problems at the GC

The three dimensional source distribution in the GC region is complex, which makes the identification of the objects and the physical processes operating in the region is difficult to understand. Despite high resolution studies of this region at different frequencies, many difficulties remain in establishing and explaining the properties of the discrete sources and the ISM, some of which we discuss below.

1.3.1 Sgr A*

Sgr A* was discovered by Balick & Brown (1974), and due to its proximity to the dynamical centre of the Galaxy, it has attracted considerable attention from the time of

its discovery. This object has now been extensively studied from radio to X-ray wavelengths (see Melia & Falcke 2001, and the references therein). Though the observational data strongly associates Sgr A* with the 2.6×10^6 $M_\odot$ black hole at the centre of the Galaxy (Genzel et al. 1996; Ghez et al. 1998; Reid et al. 1999), there are several questions that remain unanswered. Compared to AGNs, this object is extremely underluminous at all wavelengths, radiating at $\sim 10^{-10}$ times its Eddington luminosity. Its flux density is known to vary at higher radio frequencies and the flux density variations appear to have a periodicity of 106 days (Zhao et al. 2001). Though no linear polarisation has been detected at radio frequencies, circular polarisation from this object has been detected at radio frequencies (Bower et al. 1999). Sgr A* has not been detected below 1 GHz and observations by Davies et al. 1976 at 408 MHz and Pedlar et al. 1989 at 330 MHz provides upper limits on its flux density at those frequencies. It could have a low frequency turnover below 1 GHz, but the nature of the turnover has never been clarified in detail (Melia & Falcke 2001). Recently, Nord et al. (2004) claim to have detected Sgr A* at 330 MHz. However, the average brightness of the $7'$ halo seen towards Sgr A* at 330 MHz is $\sim$ 100 mJy/Beam (with the beamsize used in their map), which is comparable to the claimed peak intensity of Sgr A* (Fig. 2 in Nord et al. 2004). The $7'$ halo could be located in front of the Sgr A complex (Pedlar et al. 1989), and presence of any small scale structure in the halo along Sgr A* can mimic its claimed detection. Therefore, detection of Sgr A* at 330 MHz remains provisional.

1.3.2 Sgr A West

As explained in Sect. 1.2.1.1, the Sgr A West is comprised of three arm like features of ionised gas embedded in a halo of ionised gas with an extent of $1.5'$. There has been proper motion (Yusef-Zadeh et al. 1998) and recombination line study of the ionised gas (Roberts et al. 1996), which suggests that the ionised gas is in orbit around the Galactic centre. The Northern arm of Sgr A West could be a manifestation of the infalling stream

of dust and gas towards Sgr A* (Morris & Serabyn 1996). If this picture is correct, then Sgr A West and Sgr A* are spatially related. However, their spatial relationship is yet to be unambiguously established.

1.3.3 Non-thermal filaments

(i) As described in Sect. 1.2.1.3, the NTFs are unique objects seen only towards the central 1° region of the Galactic Centre. With more sensitive observations, fainter NTFs are discovered, some of which are further away from the Galactic Centre (GC) (e.g., Pelican) than expected before. Therefore, due to lack of highly sensitive observation with high resolution of the present surveys beyond the central 2° of the GC, NTFs in these regions may have remained undetected. Any detection of NTFs beyond the central $\sim 1^\circ$ will provide evidence against their present models of origin, and maintenance.

(ii) Since the NTFs are seen only towards the central 1° region of the GC, it is believed that these NTFs are close to the GC. However, out of nine known NTFs, the line of sight distances to all but two remains unknown, and these seven NTFs could be located anywhere along the line of sight.

(iii) As discussed in Sect. 1.2.1.3, the magnetic field strength in the NTFs are believed to be ~ 1 mG. It has been suggested that magnetic field of this strength is prevalent all over the central ∼few hundred pc of the GC Yusef-Zadeh & Morris (1987b). On the other hand, if there is a local enhancement of magnetic field along the NTFs, a strong confining mechanism is required to prevent them from expanding at the Alfven speed and thus disappearing on a time scale of 10^3 years, which is much faster than the time needed to establish the currents necessary to generate the structure in the first place (Morris & Serabyn 1996). Therefore, a large scale mG field appears to be a necessary requirement. However, Shore & Larosa (1999) argues that the NTFs are difficult to maintain if they are anchored to any specific place in the region (i.e., static), but are anchored to molecular clouds moving at high velocities (i.e., they are dynamical struc-

tures) As such, they are local amplification of an otherwise weak field due to encounters with the cloud and not directly connected to any static global field, and the classic Magneto Hydro Dynamic (MHD) instabilities do not limit the aspect ratio as they would for a static equilibrium field (Shore & Larosa 1999). Therefore, it appears that we do not yet know whether the mG magnetic field is globally prevalent in the GC or is only locally present near the NTFs.

(iv) Eight out of nine known NTFs appear to be almost perpendicular to the Galactic plane. However, the NTF Pelican (G358.85+0.47) lies along the Galactic plane. This suggests that the field lines might change their orientation from being perpendicular to the Galactic plane near the GC to being parallel to the plane beyond one degree from the GC, as seen mostly in the rest of the Galaxy. However, if the NTFs are manifestations of some peculiar local environments, our understanding of the magnetic field in the GC region remains incomplete.

1.4 Attempting to resolve these problems and plan of the thesis

Some of the mysteries in the GC region can be resolved by further observations. In this section, we briefly discuss these new observations, which have been performed as part of this thesis and are explained in detail in the subsequent chapters.

1.4.1 High resolution observations of the GC at 620 MHz

As described in Sect. 1.3.1, Sgr A* has not been detected below 1 GHz and observations by Davies et al. 1976 at 408 MHz and Pedlar et al. 1989 at 330 MHz provide upper limits on its flux density. It could have a low frequency turnover below 1 GHz, but the nature of the turnover has never been clarified in detail (Melia & Falcke 2001). Therefore, observations at frequencies between 1 GHz and 408 MHz will provide valuable information on its low frequency spectrum, which can clarify the physical processes

involved in causing its low frequency turnover. If the non-detection of Sgr A* at 408 MHz or below is caused by free-free absorption due to Sgr A West HII region being in front of it, the estimated flux density of Sgr A* will change, which can be described by $I = I_0 \exp(-\tau)$, where I is the estimated flux density at frequency ν, τ is the free-free optical depth and I_0 is the actual flux density of the object at frequency ν, which can be estimated from its spectral index and the flux density measured at higher frequency. It is well known that the optical depth due to free-free absorption is given by,

$$\tau = \int 0.2 n_e^2 T_e^{-1.35} \nu^{-2.1} dL$$

. Where, n_e is the electron density and T_e is the electron temperature. The above equation shows that at high frequencies, when the optical depth is small the spectrum of a HII region is almost flat, being proportional to $\nu^{-0.1}$. However, at low frequencies, when the optical depth is large ($\tau >> 1$), the spectrum is essentially of a black body given by the Rayleigh-Jeans law, being proportional to ν^2. At intermediate frequencies, the spectrum turns over from being essentially flat at high frequencies to one which is inverted at low frequencies. By fitting the equation shown above to the available multi-frequency data, it is possible to estimate the optical depth of the HII region at 620 MHz, and hence determine whether the non-detection of Sgr A* below 1 GHz is due to free-free absorption by Sgr A West. As in item (ii) of the previous section, this will also provide the relative line of sight location of Sgr A* with respect to Sgr A West, which will help to clarify whether the Northern arm of Sgr A West is manifestations of the infalling stream of dust and gas towards Sgr A*. Therefore, we have carried out 620 MHz observations of this region with the GMRT. In Chapter 2, we describe these observations, the results and its consequences.

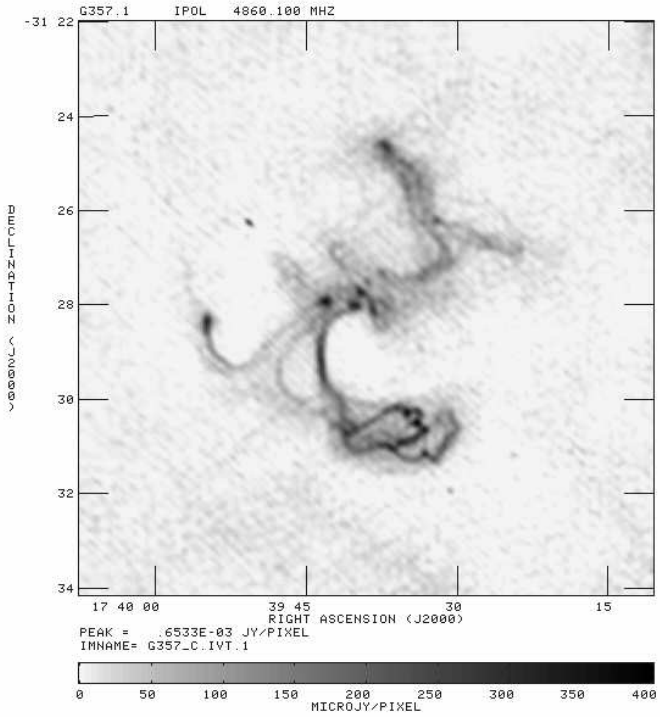

Figure 1.4: 4.8 GHz continuum image of the source G357.1-0.2 (Gray 1996)

1.4.2 Low frequency observations of suspected SNRs with filamentary structures near the GC

As described in Sect. 1.3.3 item (i), search for NTFs beyond the central 1° region of the GC are important to verify the hypothesis that they only form within $\sim 1^\circ$ of the GC. For this purpose, we observed with the GMRT at 330 MHz, 2 filamentary structures located $\approx 3^\circ$ away from the GC, which were suspected to be either (i) NTFs or (ii) part of suspected SNRs in the region. One of these filamentary structures G357.1–0.2 was identified by Gray (1996). The 5 GHz image of this object is shown in Fig. 1.4 (Gray 1996).

The peculiar morphology of G357.1–0.2 makes it difficult to uniquely identify it. It has a steep spectral index of –0.5 between 5 and 1.4 GHz and a maximum polarisation fraction of 60%, indicating non-thermal emission. As mentioned before, its morphology indicates that it could be (i) an NTF as seen near the GC or (ii) an extragalactic source

or (iii) a Crab like SNR. Since low frequency observation can distinguish SNRs from other objects, and HI absorption can constrain its distance, this source was selected for observation with the GMRT at 330 and 1420 MHz. The other filamentary structure was identified in both continuum and polarised emission from the NVSS map by us (Fig. 1.5), and is located in the field of the suspected SNR G3.1−0.6 (Gray 1994a). This filamentary structure could either be part of this suspected SNR, or a candidate NTF located 3° away from the GC. To clarify the nature of this object, we observed this source at 330 MHz with the GMRT.

About a degree away from G357.1–0.2 is located the peculiar object known as the Tornado nebula (Sect.1.2.1.2, item (vi)), which also has extensive filamentary structures. To clarify the nature of this object at low frequency and to constrain its distance, we have observed this object at 330 MHz and in HI absorption using the GMRT.

In Chapter 3, we describe these observations, the results and its consequences.

1.4.3 Constraints on distances to GC NTFs from HI absorption

Absorption by line of sight HI features, whose velocities and distances are known provide constraints on the distance to the NTFs. In Sect. 1.3.3 item (ii), we mentioned that except for two NTFs (Radio-arc and the Snake), the line of sight distances to 7 other NTFs are unknown. Therefore, HI absorption studies of other NTFs are required to constrain their distances. We have conducted HI absorption studies towards three NTFs Sgr C, G359.79+0.17 and G359.54+0.18 using the GMRT. These NTFs have high surface brightness and are located in less confused region of the GC, thereby allowing enough signal to noise ratio to estimate the HI absorption depth. In Chapter 4, we describe these observations, the results and its consequences.

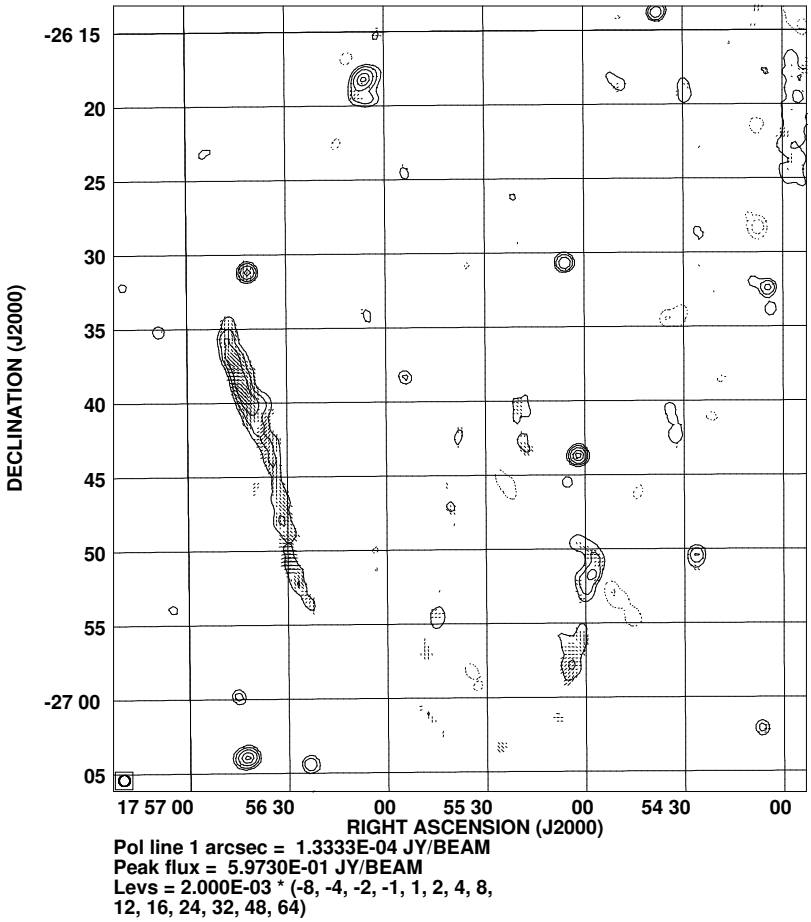

Figure 1.5: NVSS map of the field G3.1–0.6. The polarisation vectors are superposed on the continuum map (in contour).

1.4.4 Magnetic field near the GC: Faraday rotation measure observations of extragalactic sources

Magnetic fields can be strong enough to have a significant influence on the dynamics and evolution in the central region of our Galaxy. Magnetic pressure can contribute significantly to the overall pressure balance of the interstellar medium (ISM) and can even influence the scale height of the gas (Beck et al. 1996). A relatively high systematic magnetic field in the GC region is believed to be responsible for the creation and maintenance of the unique NTFs (Morris et al. 1996, and references therein). Therefore, measurement of the magnetic field geometry and strength in the central part of the

Galaxy is important for estimating its effect on the GC ISM and on the discrete objects. However, other than the central 200 pc region, no systematic study has been made to estimate the magnetic fields in the inner 5 kpc region of the Galaxy (Davidson 1996). As described in Sect. 1.3.3 item (iv) of the previous section, these estimates within the central 200 pc region are mainly based on the observations of these NTFs, and it is not clear that these estimates represent the field strengths in the GC ISM.

The Faraday rotation measure (RM) is the integrated line of sight magnetic field weighted by the electron density (RM=$0.81\times\int n_e B_{||} dl$, where n_e is the electron density, $B_{||}$ is the line of sight component of the magnetic field, and the integration is carried out along the line of sight). Therefore, if a model of electron density is available, observations providing Faraday RM towards the extragalactic sources seen through the Galaxy are well suited to estimate the average magnetic fields prevailing in the ISM. We have systematically studied 64 suspected extragalactic sources seen through the central $-6^\circ < l < 6^\circ$, $-2^\circ < b < 2^\circ$ region of the Galaxy for polarisation, and estimated the Faraday rotation measure (RM) towards the polarised sources. In Chapter 5, we describe these observations and in Chapter 6, we discuss the results of these observations and its consequences.

1.4.5 Summary

In Chapter 7, we summarise the outcome of this thesis, and discuss about possible future scope of work in these areas.

Chapter 2

Observations of the Galactic Centre at 620 MHz with the GMRT

2.1 Introduction

The central region of our Galaxy appears to be comparatively much weaker than a typical Active Galactic Nuclei (AGN). However, some of the activity seen in the region could classify it as a mild AGN. The Galactic Centre (GC) being located two orders of magnitude closer than the nearest galaxy (Andromeda), can be studied at a much greater spatial details, than is possible for other galaxies. Because of this advantage, we can identify unique objects like the Radio-arc consisting of linear parallel filaments (Yusef-Zadeh et al. 1984). The Galactic Centre probably presents the most compelling evidence of a supermassive black hole at the centre of a galaxy.

The Galactic Centre (GC) region has been observed at radio wavelengths with high resolution ($\sim$ arc seconds) using the Very Large Array (VLA) at 2 cm (Yusef-Zadeh & Wardle 1993), 6 cm (Ekers et al. 1983), 20 cm (Pedlar et al. 1989) and 90 cm (Pedlar et al. 1989; Anantharamaiah et al. 1991; LaRosa et al. 2000) and several interesting sources have been identified in the region. In the map of the central $15'$ of the Galaxy (Fig. 2.1), the following sources are identified.

(i) At the dynamical centre of the Galaxy is the 2.6×10^6 $M_\odot$ black hole candidate (Ghez et al. 1998), which coincides with a compact nonthermal radio source known as Sgr A*.

(ii) Around Sgr A* is the HII region Sgr-A West (Ekers et al. 1983), whose morphology resembles a face-on spiral galaxy. (iii) Near Sgr-A West is Sgr-A East, which is believed to be a supernova remnant (SNR). (iv) A $7'$ halo, which has been proposed to be a mixture of thermal and non-thermal emission (Pedlar et al. 1989) can also be identified in this region.

Since Sgr A* is associated with the nearest supermassive black hole and could be a prototype for such black holes in extra galactic AGNs, it has attracted considerable attention since its discovery (Balick & Brown 1974). This object has now been studied from radio frequencies to X-rays (see Melia & Falcke 2001, and the references therein). Though the observational data strongly associates it with the 2.6×10^6 $M_\odot$ black hole at the centre of the Galaxy (Genzel et al. 1996; Ghez et al. 1998; Reid et al. 1999), there are several questions that remain unanswered. Compared to AGNs, this object is extremely underluminous at all wavelengths, radiating only 10^{-10} times its Eddington luminosity. Its flux density at frequencies $\gtrsim$1.4 GHz exhibits variability and at 8.6 and 22 GHz has a periodicity of 106 days (Zhao et al. 2001). Though no linear polarisation has been detected at radio frequencies, circular polarisation from this object has been detected (Bower et al. 1999). Sgr A* has not been detected below 1 GHz and observations at 408 MHz (Davies et al. 1976) and at 330 MHz (Pedlar et al. 1989) provide upper limits on its flux density. Sgr A* probably has a low frequency turnover below 1 GHz, but the nature of the turnover has never been examined in detail (Melia & Falcke 2001). Recently, Nord et al. (2004) claim to have detected Sgr A* at 330 MHz. However, the average brightness of the $7'$ halo seen towards Sgr A* at 330 MHz is $\sim$ 100 mJy/Beam (with the beamsize used in their map), which is comparable to the claimed peak intensity of Sgr A* (Fig. 2 in Nord et al. 2004). The $7'$ halo could be located in front of the Sgr A complex (Pedlar et al. 1989), and presence of any small scale structure in the halo along Sgr A* can mimic its claimed detection. Therefore, detection of Sgr A* at 330 MHz remains provisional.

In high resolution radio images (Fig. 2.1) Sgr A West comprises of three arm like features of ionised gas embedded in a halo of ionised gas which has an angular extent of about 1.5′. Proper motion (Yusef-Zadeh et al. 1998) and recombination line studies of the ionised gas (Roberts et al. 1996) suggest that the ionised gas is in orbit around the Galactic centre. Along the Northern arm, the gas appears to flow away from us. If this is taken as an indication of gas falling in towards Sgr A*, then this would imply that the Northern arm is located in front of Sgr A*. Whiteoak et al. (1983) have suggested Sgr A* to be located in front of Sgr A West, Liszt et al. (1983) detected 40–60 km s^{-1} HI absorption against Sgr A*, but not against Sgr A West. Liszt et al. (1983) suggests that it is due to patchiness of the HI screen. Clearly, the relative location of Sgr A* with respect to Sgr A West is ambiguous.

Sgr A East appears to have a shell like structure at higher radio frequencies. However, it is not clear whether Sgr A East originates from activity at the Galactic centre, or is just a chance superposition of a supernova remnant along the line of sight. Mezger et al. (1989) has estimated that if Sgr A East is a remnant of a supernova which had exploded directly into a giant molecular cloud, then an event of at least 4×10^{52} ergs of total energy would be required to produce the observed radio emission.

It is quite evident from the above that the three dimensional source geometry in the GC region is complex, which makes identification of the objects and the understanding of the energetics in the GC region difficult. Therefore, it is important to constrain the line of sight location of the objects.

If there is an opaque screen in front of the source, the distance to which is known, then the distance to the source can be estimated. Since HI is present all through the Galaxy, and since its velocity due to Galactic rotation in different directions and distances can be estimated, absorption by HI have traditionally been used to constrain source distances. Unfortunately, Galactic rotation cannot be used to constrain the distances to sources towards the GC ($l \approx 0^{\circ}$). There are certain high velocity HI features at

the GC, the distances to which is known from the GC, and absorption by these features can be used to constrain distance to sources (Roy 2003). However, the probability of finding such a feature located between two objects is quite small, and consequently use of HI absorption to find the relative location of objects in the GC is very limited.

Nevertheless, due to free-free absorption at low radio frequencies, regions of ionised hydrogen (HII region) tend to get optically thick, and absorption against another continuum object can be used to constrain their relative location. This technique has successfully being used to constrain the relative location of Sgr A West with respect to Sgr A East (Pedlar et al. 1989). However, Sgr A* was not detected at 90 cm by Pedlar et al. (1989), and its relative location with respect to Sgr A West is uncertain.

Based on the observations of Pedlar et al. (1989), the optical depth (τ) of the Sgr A West complex at 620 MHz is expected to be $\sim$1 and even if Sgr A* is located behind Sgr A West, it may be possible to detect it. Detection of Sgr A* at 620 MHz will constrain its location with respect to Sgr A West, and also provide an important constraint on its low frequency spectrum. Observations at this frequency will also be useful to constrain the spectral indices between 1.4 GHz and 330 MHz of other interesting objects like Sgr A East and the $7'$ halo in the region.

We have observed the central half a degree region of the Galaxy using the 620 MHz band of GMRT. Previous observations between 1.4 GHz and 330 MHz either lacked good *uv*-coverage (Davies et al. 1976), or had low resolution (Downes et al. 1978; Little 1974; Mills & Drinkwater 1984). Observations with resolutions better than about quarter of an arc minute is required to separate Sgr A* from the background emission. The GMRT in 620 MHz band has an effective resolution of about $7''$, and is well suited for the purpose. In Sect. 2.2, we describe the observations and data analysis. The results of these observations are presented in Sect. 2.3, and we discuss about possible implications of the results in Sect. 2.4. A summary of these are presented in Sect. 2.5.

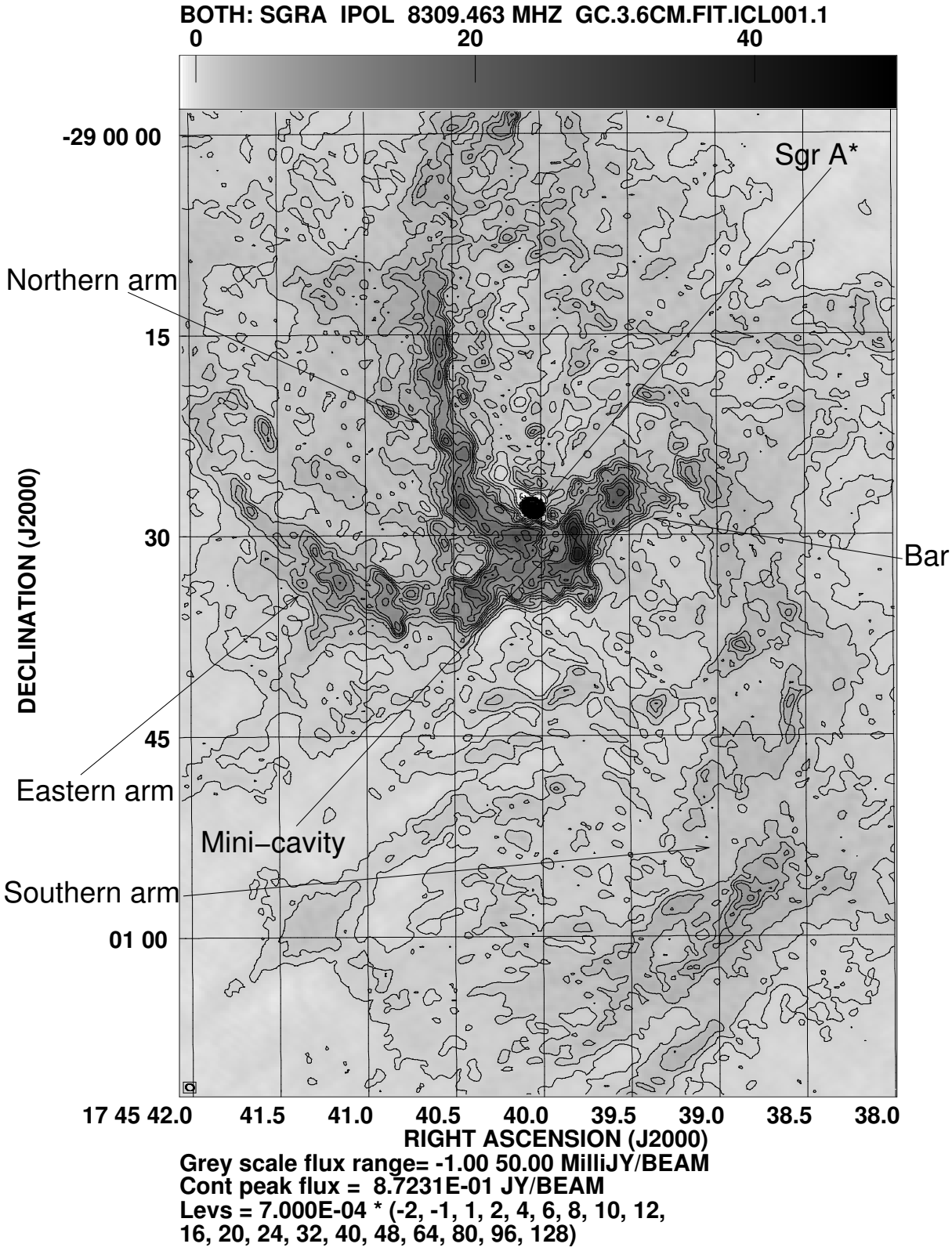

Figure 2.1: 8.4 GHz VLA map of Sgr A West (Roberts & Goss 1993). The resolution is $0.62'' \times 0.51''$, with beam position angle of 73°. The rms noise is about 0.13 mJy/beam.

2.2 Observations and data reductions

The observations were carried out with the Giant Metrewave Radio Telescope (GMRT) at 620 MHz with a nominal bandwidth of 16 MHz on Aug 31 & Sep 21, 2001 and at 580 MHz in June 2002. The field centre was set at RA (J2000)=17h46m07s, DEC (J2000)=$-28^{\circ}57'02''$. All the observations were carried out in the spectral line mode with 128 frequency channels, which is the default mode of the GMRT correlator. 3C48 and 3C286 were used as primary flux density calibrators. We have followed Baars et al. (1977) for the absolute flux density calibration. The source 1751-253 was used as a secondary calibrator, and was observed every 25 minutes during the observations. The source 1714-25 was used for the bandpass calibration, and was observed once in an hour.

Due to the presence of other confusing sources in the field of view (FWHM=$44'$ at 620 MHz), 1751-253 is not a good calibrator at 620 MHz. However, the second nearest calibrator 1714-25 is 10° away from the GC, and our observations made till the end of the year 2000 using phase transfer from 1714-25 yielded maps of the GC field, which had poor dynamic range, probably due to ionospheric phase variation. We, therefore used 1714-25 as a secondary calibrator, and imaged the sky intensity distribution in the field containing 1751-253. The resultant map was further improved by phase only Self-calibration, and used as a model to calibrate the target field of the GC.

At the time of these observations, automatic measurements of system temperature (T_{sys}) had not been implemented at GMRT, and increase of T_{sys} from the calibrator field to the target source affects the source visibility amplitudes in the default observing mode (i.e., when the Automatic Level Control in the system is turned on), and we employed the following method to correct for the T_{sys} variation. We estimated the ratio of the total power, on the target source and the calibrator 3C48 at 620 MHz. Since this ratio was quite similar (within 10%) for almost all the antennas, rather than multiplying the antenna based gain, we multiplied the final map of the source intensity distribution by

this number.

While observing at 580 MHz, the Automatic Level Control (ALC) was turned off. In this case, the T_{sys} variations do not directly affect the visibility amplitudes (see Appendix-C), and a correction is not required. The absolute flux density scale using the first method (i.e., at 620 MHz) is believed to be accurate to about 10%, while, it is expected to be accurate to better than 5% with ALCs off (i.e., at 580 MHz) (the 620 MHz observations were performed about an year earlier than the 580 MHz observations, and this technique was not considered at that time).

The data were processed within Astronomical Image Processing System (AIPS) using standard programs. Bad data (interference in some frequency channels, spikes and drop outs due to electronics, etc) were identified and flagged using FLGIT. The data were also checked for antenna or baseline based problems, which were also flagged. The spectral visibility data were bandpass calibrated. After calibration and editing, a pseudo-continuum database of 3 frequency channels (each of width 3.7 MHz) were made from the central 11 MHz of the observed 16 MHz band. This was adequate to avoid bandwidth smearing within the primary beam. Images of the fields were formed by Fourier inversion and Cleaning (IMAGR). The initial images were improved by self-calibration. However, subsequent amplitude and phase Self-cals failed to improve the dynamic range of the maps. Therefore, phase only Self-cals were used to produce the final images. The GC field shows large scale emission, which cannot be properly mapped due to lack of *uv*-spacings less than 90λ. Therefore, we applied a small weight factor (0.05) to *uv*-data with *uv*-spacings less than 700λ while performing phase self-calibration.

To improve the deconvolution of the extended emission, we made the final image using Multi-resolution Clean (Wakker & Schwarz 1988), which has been explained in Appendix-A. Since the strong emission is seen mostly near the central 10′ region of the GC, and we are interested in sources located only within this region, deconvolution of the dirty image using a single field was deemed adequate. The GMRT map at 620

MHz (Fig. 2.2) has a dynamic range of about 150, and is limited by systematics (for a discussion on possible reasons of dynamic range limitations, the reader is referred to Appendix-B).

2.3 Results

The GMRT image has been made with data with *uv*-spacings greater than 100λ. Therefore, objects larger than 30′ cannot be imaged, and objects larger than about 15′ will suffer from lack of zero-spacing flux density. The 620 MHz map of the GC field is shown in Fig. 2.2. For comparison, we have reanalysed the 1.4 GHz VLA A, B, C and D array archival data acquired and presented by Pedlar et al. (1989). After self-calibration, the final map using the data from the A, B, C and D array has been made with Multi-resolution Clean. A total of 9 fields were Cleaned with the 3-D imaging technique (see, Synthesis Imaging in Radio Astronomy II, Lecture 19 by R. A. Perley) as available with the AIPS task IMAGR. The 1.4 GHz map is shown in Fig. 2.3. On the larger scale, the prominent non-thermal filamentary structure Radio-arc (Yusef-Zadeh et al. 1984) (shown in the figure) is clearly visible. The Radio-arc appears to be joined with the Sgr A complex by the Arched filament (Yusef-Zadeh & Morris 1987c) which is thermal in nature. Due to the use of 3-D deconvolution and Multi-resolution Clean, the 1.4 GHz map appears to have a better fidelity than the map in (Yusef-Zadeh & Morris 1987b). As described in Yusef-Zadeh & Morris (1987b), several narrow filamentary features can be seen in the 1.4 GHz map. Most of the filamentary structures like Radio-arc and the ‘threads’ run perpendicular to the Galactic plane. However, one additional ‘thread’ like feature near RA (J2000)=17h45m22.7s, DEC=$-29^{\circ}04'22''$ labelled new ‘thread’ (U), which is parallel to the Galactic plane has been identified. To the best of our knowledge, this ‘thread’ like feature has not been detected before. Though not visible in Fig. 2.2 due to poor signal to noise ratio, it is marginally visible in the GMRT 620 MHz map,

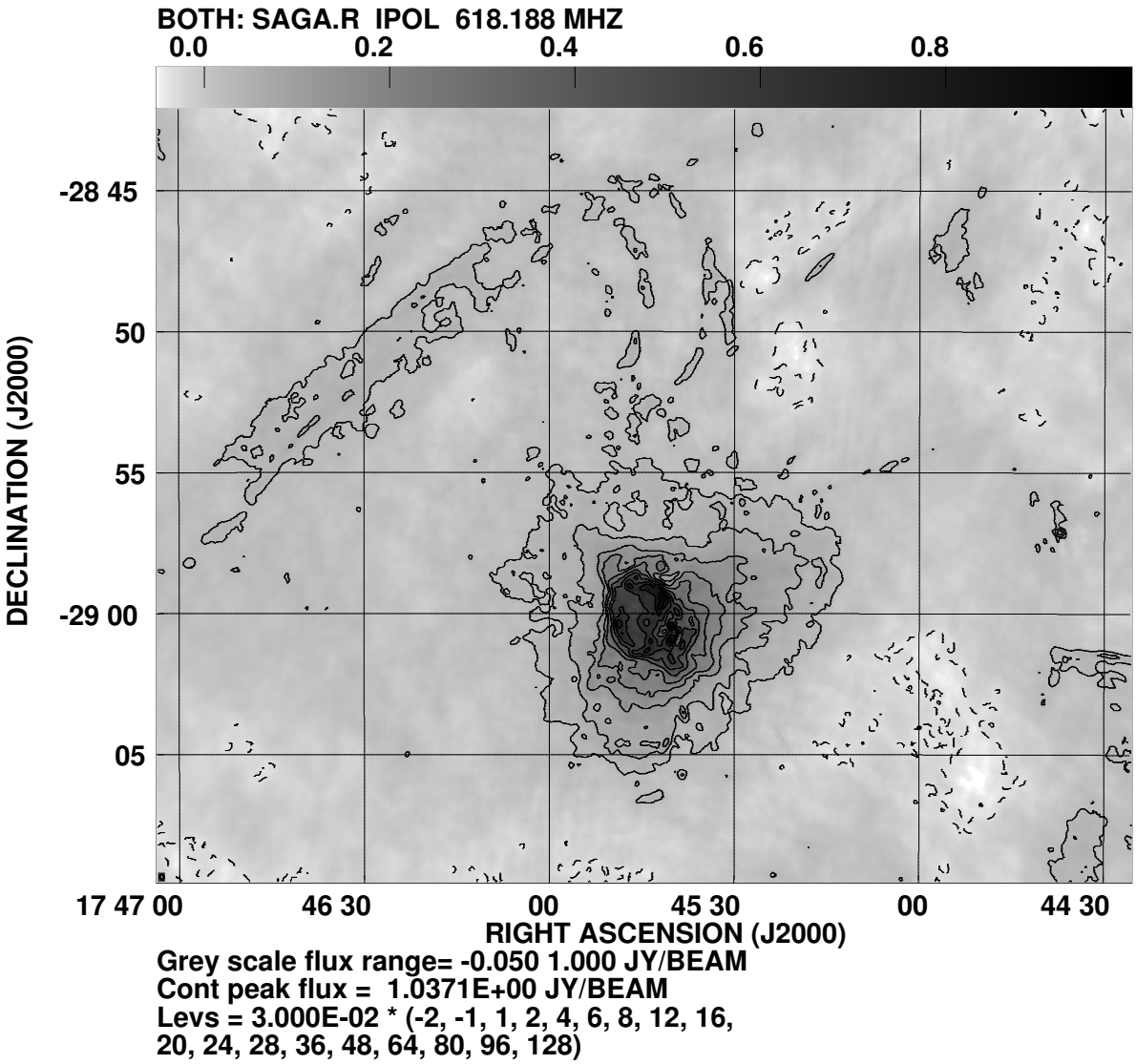

Figure 2.2: 620 MHz GMRT map of the GC region. The resolution is $11.4'' \times 7.6''$, with beam position angle of 7.7°. The rms noise is about 6.5 mJy/Beam.

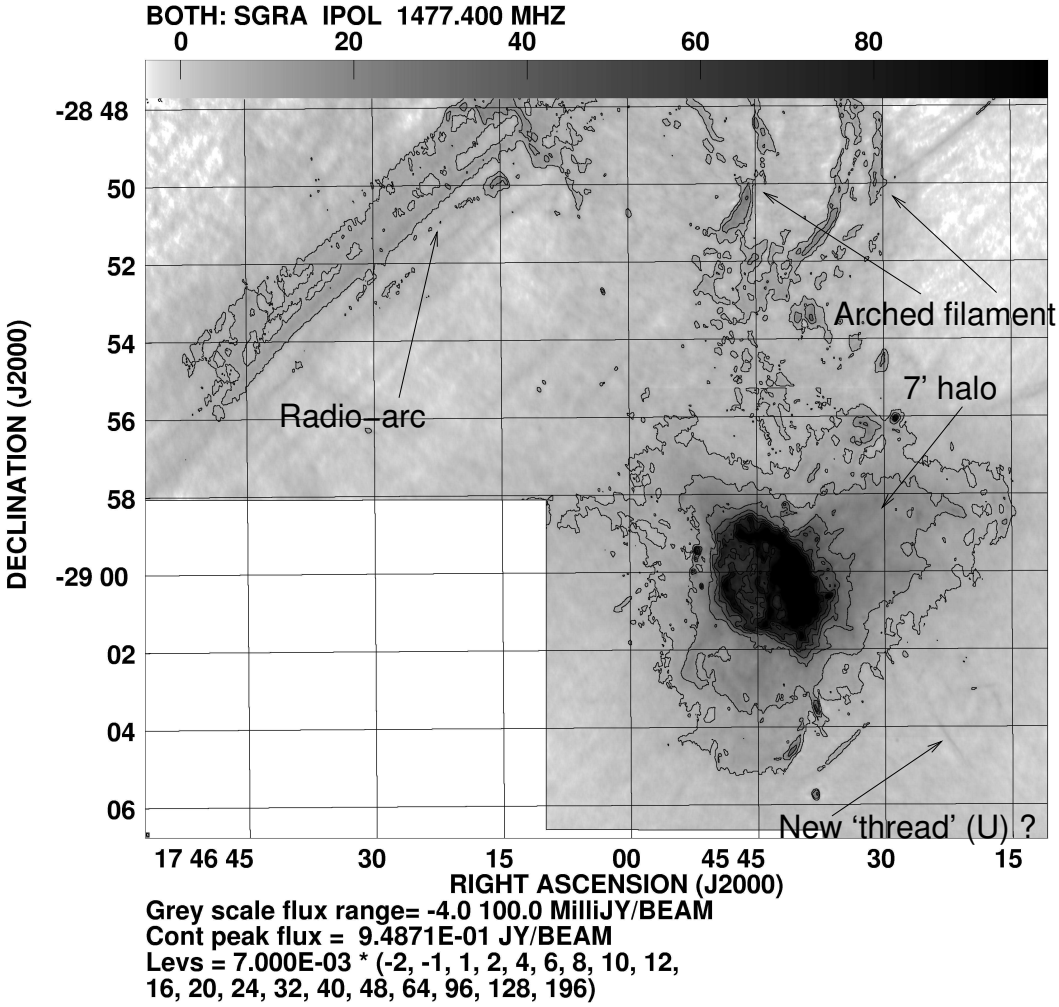

Figure 2.3: 1.48 GHz map made from the archival VLA data of the GC region. The resolution is $4.8'' \times 2.8''$, with beam position angle of 11.2°. The rms noise is about 1.2 mJy/Beam.

when seen in Grey scale on the Computer monitor. We name this feature as thread 'U', and future polarisation observation can confirm whether it falls into the category of non-thermal filament in the region.

We concentrate on the central 15′ region in the rest of this chapter. We show the central 15′ region of the Galaxy at 620 MHz, 1.4 GHz, 4.8 GHz and 330 MHz in Fig. 2.4, Fig. 2.5, Fig. 2.6 and Fig. 2.7 respectively to enable a detailed study. All the images are convolved to an uniform angular resolution of $11.''4 \times 7.''6$ with beam position angle of 7.7°. Around Sgr A*, the strong emission at 1.4 GHz is the Sgr A West HII region, which has three prominent spiral arms which is clearly seen in the 4.8 GHz map of the same region (Fig. 2.6). There is almost one to one correspondence between the strong thermal emission at 4.8 GHz (Yusef-Zadeh 1989), and a drop in the total intensity at 620 MHz, indicating that the thermal emission is getting optically thick near 620 MHz. There is considerable difference in the structure of Sgr A West between the 4.8 and 1.4 GHz map. At 4.8 GHz, the three armed spiral structure part of Sgr A West appears to be brighter than the thermal halo. However, at 1.4 GHz, the halo has similar brightness as the spiral structure, indicating that the emission from the spiral structure has significant optical depth at 1.4 GHz. At 330 MHz, the entire Sgr A West region appears to have turned over (Fig. 2.7) (Pedlar et al. 1989). The shell-like emission feature known as Sgr A East is clearly identified in all the maps. This shell of size about $2' \times 3'$ appears to be sitting on a roughly triangular shaped halo of size $\sim 7'$. Along this shell, from north to south, as shown in Fig. 2.4, we notice a narrow strip of emission, which is also seen in the 1.4 GHz and 4.8 GHz map of the same region. There is another weak emission feature (RA=17h45m44.7s DEC=-29°00') nearly circular in shape in the 620 MHz map (Fig. 2.4). Part of this feature is also seen in the 330 MHz VLA map (Fig. 2.7), which Pedlar et al. (1989) describes as a linear feature elongated along the north-south direction. An emission feature $\approx 30''$ south of Sgr A* can be seen in the 620 MHz gray scale map. This feature was identified by Pedlar et al. (1989), who suggested that it is

associated with Sgr A East.

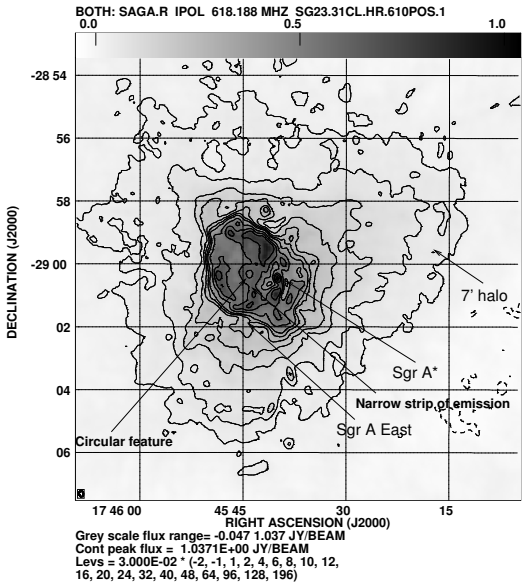

Figure 2.4: 620 MHz GMRT map of the central 15′ region of the Galaxy. The resolution is 11.4″ × 7.6″, with beam position angle of 7.7°. The rms noise is about 6.5 mJy/Beam.

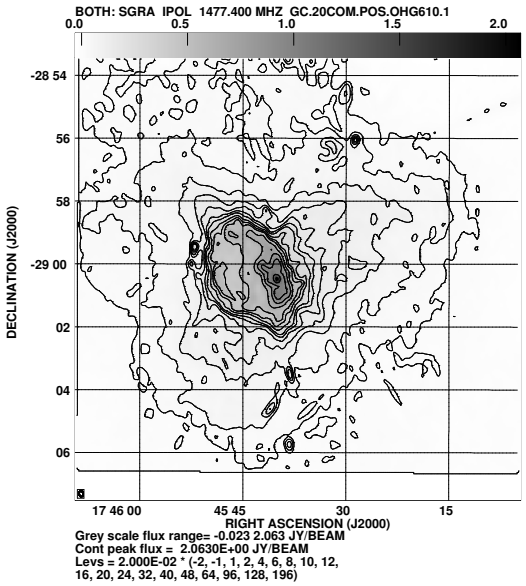

Figure 2.5: 1.4 GHz map of the central 15′ region of the Galaxy. The resolution is 11.4″ × 7.6″, with beam position angle of 7.7°. The rms noise is about 5 mJy/Beam. This map is made from the archival VLA data of Pedlar et al. (1989)

From the 1.4 GHz map, we estimate a total flux density of 320±40 Jy for the Sgr A complex (i.e., including Sgr A West, Sgr A East and the 7′ halo), while the corresponding flux density at 620 MHz is 360±40 Jy, and at 330 MHz is 330±50 Jy. We note that our estimated total flux density of this region at 1.4 GHz is consistent with the estimated flux density of 328 Jy by (Yusef-Zadeh & Morris 1987b). However, it is inconsistent with the estimated flux density of 487±30 Jy by Pedlar et al. (1989). Since we have reanalysed the data of Pedlar et al. (1989) and the estimated flux density matches with Yusef-Zadeh & Morris (1987b), it appears that the estimated total flux density provided by Pedlar et al. (1989) is in error. The temperature of the Galactic background (∼1000 K at 330 MHz) is similar to or less than the equivalent temperature of the noise (about 1000 K at 330 MHz) in the map and we can neglect the effect of the Galactic background in the

estimation of the flux density of the sources.

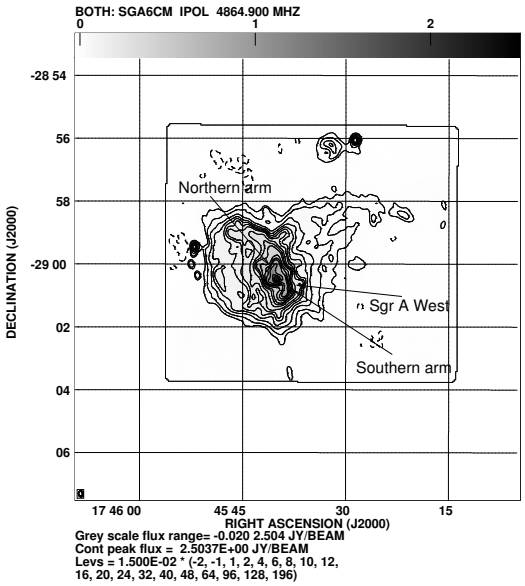

Figure 2.6: 4.8 GHz VLA map (Yusef-Zadeh 1989) of the central 15′ region of the Galaxy. The resolution is 11.4″ × 7.6″, with beam position angle of 7.7°. The rms noise is about 4 mJy/Beam.

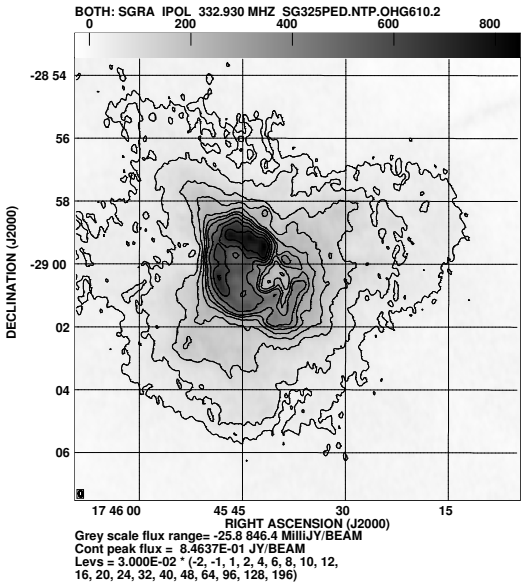

Figure 2.7: 330 MHz map (Pedlar et al. 1989) of the central 15′ region of the Galaxy. The resolution is 11.4″ × 7.6″, with beam position angle of 7.7°. The rms noise is about 6 mJy/Beam.

2.3.1 Estimating flux density of the individual sources in the Sgr A complex

In Fig. 2.4, there are four sources, Sgr A*, Sgr A West, Sgr A East and the 7′ halo, which appear to overlap along the line of sight. Because of this overlap, extracting individual flux densities is non-trivial. In this section, we first try to estimate the flux density of Sgr A West, Sgr A East and the 7′ halo. The flux density of Sgr A* is estimated in the next section. Since, the flux density of Sgr A* at radio freqencies is $\lesssim$1 Jy, and the three other sources in the Sgr A complex have flux densities $\geq$ 10 Jy, its effect on the estimated flux densities on the three sources will be neglected.

The estimated flux density per synthesised beam near the position of Sgr A West at 330 MHz is close to, but not below, the mean level of the 7′ halo (Pedlar et al. 1989).

Therefore, the 7′ halo is likely to be located in front of the Sgr A West. We took crosscuts at several orientations across the 7′ halo through the location of Sgr A*. From the crosscuts, we estimate the intensity of the 7′ halo at the position of Sgr A East to be 0.18 Jy/beam at 620 MHz and 1.4 GHz, and 0.11 Jy/beam at 330 MHz. A typical crosscut at 1.4 GHz and 620 MHz is shown in Fig. 2.8. The background emission is quite small at 4.8 GHz, where it gets partially resolved due to lack of zero spacing flux density, and we estimate about 0.012 Jy/beam as its contribution at this frequency. After subtracting these intensities of the 7′ halo from the corresponding maps, the flux density of Sgr A East and West were estimated. The combined flux density of Sgr A East and West as enclosed by Sgr A East shell is 62±3 Jy at 4.8 GHz, 108±16 Jy at 1.4 GHz, 112±16 Jy at 620 MHz and 110±14 Jy at 330 MHz. By subtracting these flux densities from what is estimated for the Sgr A complex (i.e, Sgr A West, Sgr A East and 7′ halo) we measure the contribution by the 7′ halo at these frequencies. Flux densities of these sources are listed in Table 2.1. We note that Pedlar et al. (1989) includes the halo around Sgr A East, while estimating its flux density. However, we use its prominent shell as the boundary of Sgr A East.

To estimate the spectral index of Sgr A East, we try to avoid any contamination of its flux density due to Sgr A West located close to it. Therefore, we exclude a region of our 620 MHz map, where strong emission from Sgr A West could be seen at 4.8 GHz. Flux density of Sgr A East estimated in this way is 24±1.4 at 4.8 GHz, 59±6 Jy at 1.48 GHz and 91±9 Jy at 0.33 GHz. In Table 2.1, we list the flux density of Sgr A East.

2.3.1.1 Flux density of Sgr A*

While estimating the flux density of Sgr A*, we reduced the confusion due to the extended emission by imaging with only those visibilities having *uv* distance $>7\ k\lambda$. The flux density estimated from the image plane is about 0.5 ±0.1 Jy. We note that even after applying a lower *uv* cutoff, there is significant background confusion within a beam of

Table 2.1: Flux densities of the sources in the Sgr A complex (Jy)

Frequency (GHz)	Sgr A complex	$7'$ halo	Sgr A East†
4.8	–	–	24±1.4
1.48	320±40	212±40	59±6
0.62	360±40	248±40	78±8
0.33	330±50	220±50	91±9

† While estimating the flux density of Sgr A East, the region of the map, where emission from Sgr A West is seen at 4.8 GHz has been excluded.

size $7.5'' \times 4''$. This confusion causes an uncertainty of about 0.1 Jy in the estimated flux density. We also estimated the flux density of this object from the *uv* visibilities. We first applied appropriate phase shift such that Sgr A* is at the phase centre. Every one hour of *uv*-data were averaged vectorially, which ensures that the sources away from the centre have little contribution to the visibility amplitude. After rejecting data with *uv*-distance shorter than 15 kλ, an elliptical Gaussian model was fitted as a model for Sgr A* (using UVFIT). The flux density estimated in this way is also 0.5 Jy. The major and minor axis of the Gaussian fit is $3.8''\pm0.4''$ and $1.8''\pm0.6''$ respectively with a position angle of $93\pm4^\circ$, which is consistent with its expected scatter broadened size of $3.4'' \times 1.8''$ estimated from Lo et al. (1998) at this frequency. In order to check the goodness of the fit, we divided the *uv*-data by the model. If the model matches with the data, then the real part of the visibility after division should be close to unity, which is the case as seen in the plot shown in Fig. 2.9. From the plot, the estimated error on the flux density is estimated to be about 20%, or 0.1 Jy, which is similar to what was estimated from the image plane. We also imaged this object from the 580 MHz data. The flux density estimated at this frequency matches (within the error-bar) to what is estimated at 620 MHz.

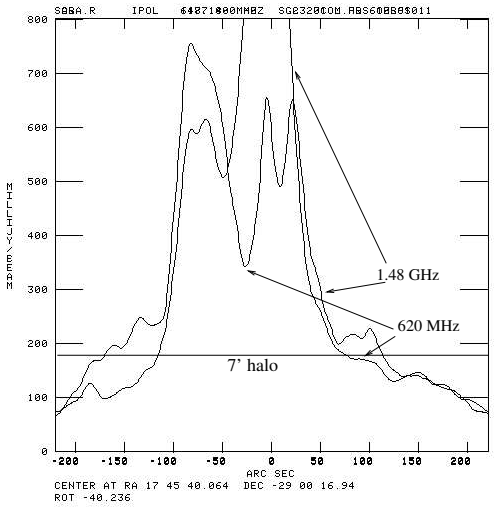

Figure 2.8: Flux density/Beam of one of the Cross-cut taken across the 7′ halo from the 620 MHz and the 1.4 GHz map.

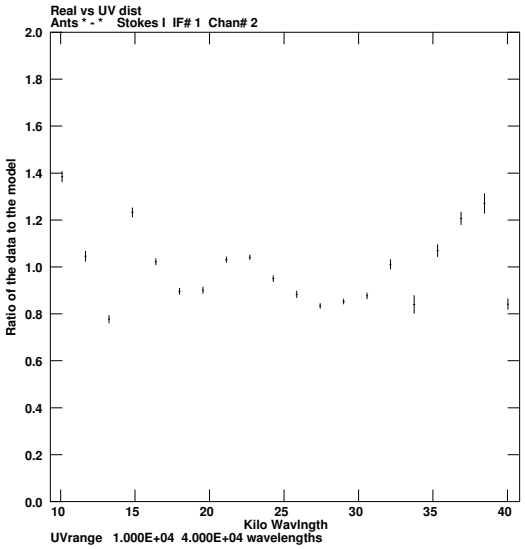

Figure 2.9: The ratio of the *uv*-data to the model of Sgr A*. Sgr A* is modelled as an elliptical Gaussian with major axis of size $3.8'' \pm 0.4''$, minor axis $1.8'' \pm 0.6''$ with a position angle of $93 \pm 4^{\circ}$.

2.3.2 Spectral index distributions

A spectral index map of the GC region (Fig. 2.4) made between 1.4 and 0.62 GHz is shown in Fig. 2.10. The figure was directly derived from the images shown in Fig. 2.4 and Fig. 2.5. The spectral index of the central region consisting of Sgr A West shows a positive spectral index, indicating that the emission from the HII region has turned over at 620 MHz. There are three compact HII regions at the eastern boundary of Sgr A East, which also have turned over at 620 MHz. The spectral index changes smoothly from positive near Sgr A West to slightly negative in the 7′ halo. The spectral index of Sgr-A East is almost flat. Near the edge of the 7′ halo, the spectral index becomes steeper.

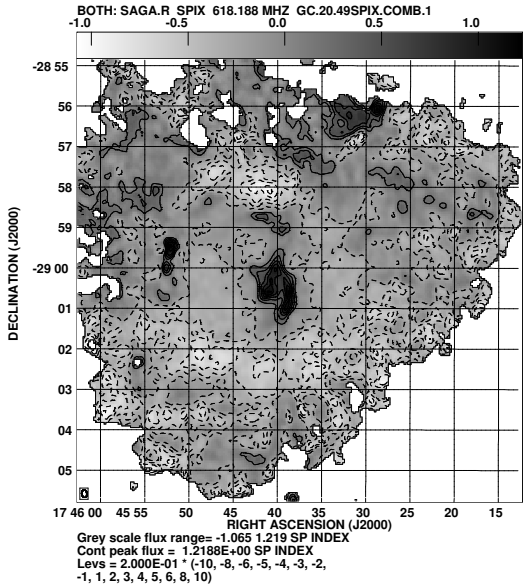

Figure 2.10: Spectral index map of the Sgr A Complex made from the division of the 1.4 GHz and the 620 MHz map of the region.

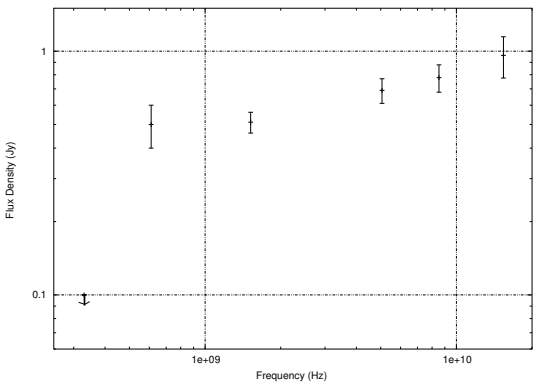

Figure 2.11: The spectrum of Sgr A* from 300 MHz to 20 GHz. Except the 330 (Pedlar et al. 1989) and 620 MHz measurements, all the other data points are taken from Melia & Falcke (2001)

2.3.3 Emission measure and temperature of the ionised gas in Sgr A West HII region

In this section, we estimate the density and temperature of ionised hydrogen in Sgr A West. Pedlar et al. (1989) estimated these parameters by assuming a constant electron temperature across Sgr A West. However, due to the availability of high resolution data between 8.5 and 0.3 GHz at 5 different frequencies, we can study the variation with position within the HII region the electron temperature (T_e), the emission measure ($\int n_e^2 dL$, where L is the path length through the ionised medium) and the background non-thermal flux density due to Sgr A East. We have convolved the 8.5 GHz, 4.8 GHz, 1.4 GHz, 620 MHz and 330 MHz maps to a common resolution of $11.4'' \times 7.6''$, with beam position angle of $7.7^\circ$from which the $7'$ halo contribution was removed (see Section 2.3.1). T_e and $\int n_e^2 dL$ have been estimated for 5 different regions in Sgr A West, which are shown in Fig. 2.12.

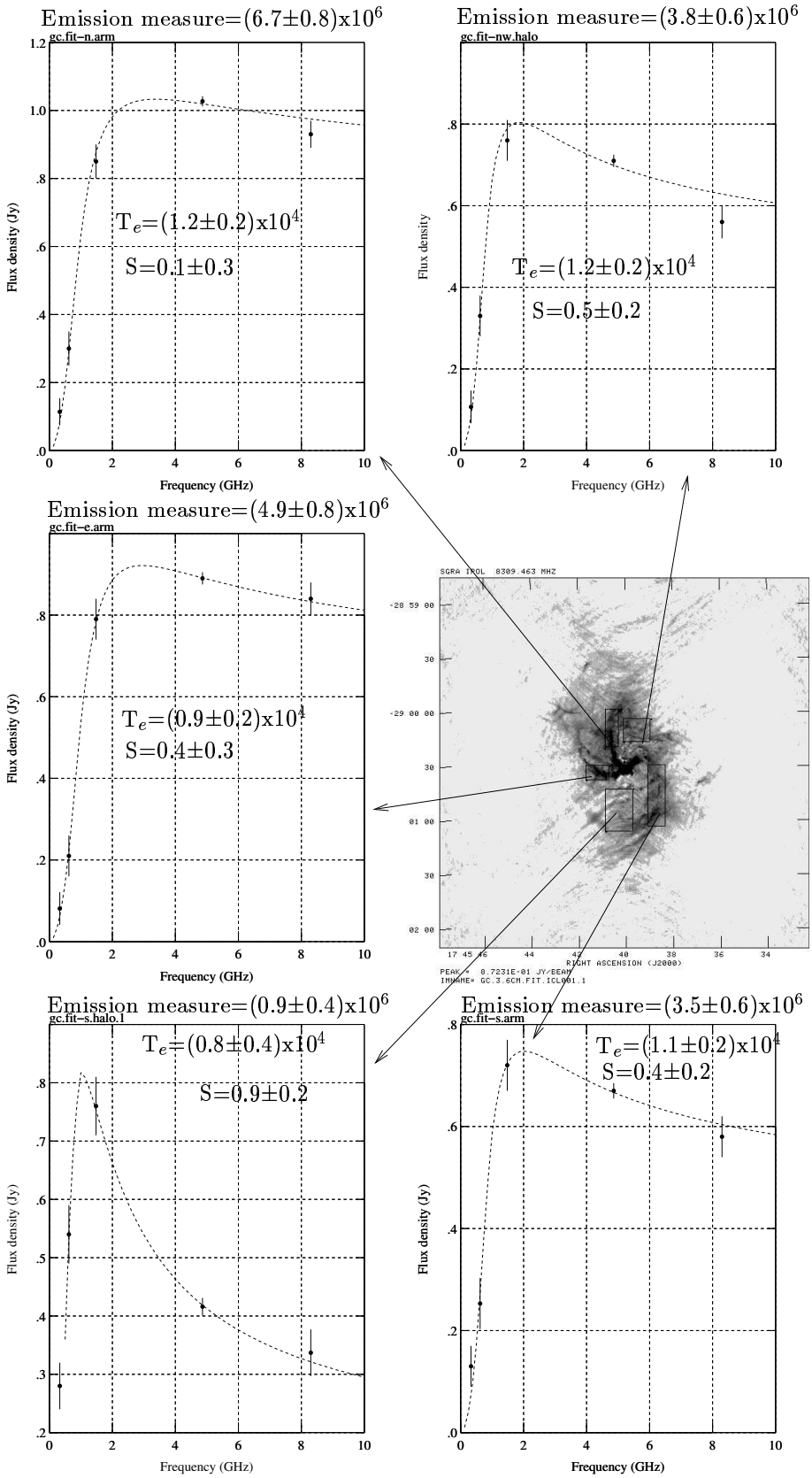

Figure 2.12: Estimated electron temperature and the emission measure from the fit at different parts of the Sgr A complex shown in the figure.

The observed flux density towards Sgr A West is the sum of non-thermal emission from Sgr A East located behind, and its own thermal emission. The observed flux density from Sgr A East can be expressed as $S\nu^{\alpha} \times exp(-\tau)$, where S is the flux density of the background source at 1 GHz, τ is the free-free optical depth at a frequency of ν GHz and α is the spectral index. The estimated flux density due to free-free emission is $[2 kT_e \times (1-\exp(-\tau)) \times \nu^2 \times \Delta\Omega]/c^2$. Where, $\Delta\Omega$ is the synthesised beam size. From the radiative transfer equation, we can express the estimated flux density per synthesised beam as

$$I_\nu = S\nu^{\alpha} \times \exp(-\tau) + [2kT_e \times (1-\exp(-\tau)) \times \nu^2 \times \Delta\Omega]/c^2.$$

τ is given by

$$\tau = \int 0.2 n_e^2 T_e^{-1.35} \nu^{-2.1} dL$$

From Table 2.1, we estimate the spectral index of Sgr A East to be -0.76 between 4.8 and 1.4 GHz, which is similar to that estimated by Goss et al. (1983); Ekers et al. (1983). However, its spectral index between 1.4 and 0.33 GHz is -0.3 (Sect. 2.4.1). Therefore, by assuming the spectral index of Sgr A East to be the same in different parts of the object, we used the spectral index of the background non-thermal emission to be -0.8 between 8.4 and 1.0 GHz, and -0.3 between 1.0 and 0.33 GHz. Finally, the average intensity per synthesised beam estimated from each of the regions (Fig. 2.12) at different frequencies are least square fitted with the expression for I_ν given above.

The 330 MHz emission observed below the eastern and southern arm region (shown within box E), is significantly higher than obtained from the estimates made at other frequencies. Therefore, we excluded this measurement from the fit for this region. We suggest that the spectral index of the foreground non-thermal halo in this region is steeper than the mean spectral index of the $7'$ halo, which could have caused an excess emission at 330 MHz.

From the model fit for the northern, eastern and southern arm, and the diffuse halo,

the electron temperature is found to be within 8,000–12,000 K, which is higher than the reported value of 7000 K by recombination line observation (Roberts & Goss 1993). They assumed the emitting gas to be in local thermodynamic equilibrium (LTE), and that pressure broadening is negligible. However, the estimate of T_e from the continuum spectrum, anchored at the low frequencies by the GMRT measurements, is free from any such assumptions and provide a more accurate value.

The emission measure of Sgr A West halo located below the 'bar' and the eastern arm is about a factor of 5 lower than that estimated for the three arms ($\approx 5\times10^6$ cm^{-6} pc). Consequently, its optical depth at 620 MHz is close to 1, whereas the optical depth of the three arms are about 3–4. The non-thermal emission from Sgr A East in this region is significantly higher than the estimates made at other parts of the HII region.

2.4 Discussion

2.4.1 Low frequency spectral index of Sgr A East and the 7′ halo

Pedlar et al. (1989) estimates the spectral index of Sgr A East between 4.8 and 1.4 GHz to be about -1.0. However, their estimate of its flux density at 330 MHz was a factor of 4 less than what is expected from its high frequency spectral index and the flux density measurement. To account for this anomaly, they proposed that the 7′ halo is a mixture of thermal and non-thermal gas, and its free-free optical depth at 330 MHz is $\sim$1. It is located in front of Sgr A East and hence partially absorbs the emission from Sgr A East. If this was the case, then at 620 MHz, the optical depth of the 7′ halo would be $\sim$0.26. However, at this frequency, the emission from Sgr A East would have been about 2.4 times stronger than at 1.48 GHz, and hence the observed flux density would have been 1.8 times stronger than what is observed at 1.48 GHz. However, from Table 2.1, the estimated flux density at 620 MHz is only 1.3 times than what is estimated at 1.48 GHz, which cannot be explained by free-free absorption. The flux density of

Sgr A East at 1.48, 0.62 and 0.33 GHz is well fitted by a power law with a spectral index of -0.3 ± 0.1. From Table 2.1, we estimate its spectral index between 4.8 and 1.4 GHz to be -0.76 ± 0.1. This indicates that there is a break in the spectral index of Sgr A East at about 1 GHz, and the change of spectral index about the break frequency is about 0.5.

We note that there are several Galactic supernova remnants (SNRs), for which spectral breaks have been observed. These include old SNRs like Cygnus loop and HB9 (Denoyer 1974), S147 (Kundu et al. 1980), G33.2$-$0.6 (Reich 1982). For these SNRs, break in the cosmic ray energy spectrum could play a role (Denoyer 1974). Spectral breaks have also been observed in plerionic type of SNRs like 3C58 (Green 1994), G76.9+1.0 (Landecker et al. 1997), G357.1$-$0.2 (Roy & Rao 2002), where a sudden cut off in the energy supply from the pulsar could have caused the observed spectral break (Green 1994). However, Sgr A East is likely to be in the adiabatic expansion phase (Pedlar et al. 1989), which implies that it is not a very old (age $\lesssim 10^4$ years) SNR. No pulsar is known in its vicinity. From the standard synchrotron model (Kardashev 1962) and using a magnetic field of 3.5 mG as measured by Yusef-Zadeh et al. (1999), we estimate that a change of spectral index by $\approx$0.5 could occur at 1 GHz if its age is $\sim 10^4$ years.

Based on the discussions above, we believe that the emission from Sgr A East is not significantly absorbed at 330 MHz by any line of sight thermal gas, and consequently, there is no need to model the $7'$ halo as a mixture of thermal and non-thermal gas. From the flux density of the $7'$ halo (Table 2.1) and assuming its flux density at different frequencies to follow a power law, the estimated spectral index between 1.4 and 0.33 GHz is -0.05$\pm$0.2. From the data given in Pedlar et al. (1989), the spectral index of the $7'$ halo at frequencies above 1.4 GHz is estimated to be about -0.6 (Pedlar et al. (1989) used a model consisting of thermal and synchrotron emission and estimate the non-thermal emission to have a spectral index of -0.7). Therefore, its spectrum also appears to have a break around 1 GHz. Similarity in spectral properties indicates that the $7'$ halo is likely to be related with Sgr A East. If the magnetic field in the halo is also

similar to what is estimated in Sgr A East, then its age could also turn out to be $\sim 10^4$ years.

The flux density of the Sgr A Complex at 160 MHz as observed by Dulk, G. A. & Slee (1974) could be explained by a foreground screen of ionised hydrogen with emission measure $3\times\ 10^4$ cm^{-6} pc (T_e=6000 K), which causes an optical depth of $\sim$1 at 160 MHz and about 0.2 at 330 MHz. Such low density HII regions (n_e $\sim$10, and size $\sim$100 pc) are believed to be responsible for the Galactic ridge radio recombination lines (Anantharamaiah 1985).

2.4.2 Low frequency spectral index of Sgr A*

While the high radio frequency spectrum of Sgr A* is well established, the spectrum below 1.4 GHz is not well determined. At 1.4 GHz, the flux density of Sgr A* (Zhao et al. 2001) is about 0.5 Jy and its spectral index between 1.4 and 8.5 GHz is +0.17 (Melia & Falcke 2001). Davies et al. (1976) found the flux density of Sgr A* at 960 MHz to be a factor of 2 less than at 1.6 GHz and suggested that it has a low frequency turnover around 1 GHz. This appears to be confirmed from their upper limit of 50 mJy at 408 MHz and the 100 mJy upper limit set by Pedlar et al. (1989) at 330 MHz. However, Nord et al. (2004) at 330 MHz estimate a total flux density of 330 $\pm$120 mJy from the known position and expected size of Sgr A*. The recent flux density estimates of Sgr A* at 620 and 330 MHz raises questions about earlier measurements. Based on the average flux density of Sgr A* at 1.4 GHz (Zhao et al. 2001) and its known spectrum between 1.4 and 8.5 GHz, we expect a flux density of 0.47 Jy at 1010 MHz and 0.44 Jy at 620 MHz, which are consistent with our measurements within the error-bars. The observed spectrum of Sgr A* from 300 MHz to 20 GHz is shown in Fig. 2.11. From the spectrum it is apparent that a factor of two lower flux density at 960 MHz (Davies et al. 1976) can be explained only by assuming Sgr A* to be variable at this frequency. Falcke (1999) finds a modulation index of 6% at 8.3 and 2.5% at 2.3 GHz, which indicates that the

intrinsic variability of Sgr A* is rather low at low radio frequencies (Melia & Falcke 2001). Therefore, interstellar scintillation (ISS), the time scale of which is ∼few years towards Sgr A* at 1 GHz, is likely to cause any significant variability. The observations in the 620 MHz band cover a span of nearly an year and no significant variation (∼ 20%) could be detected. Our measurements rule out any turnover near 1 GHz and indicate that any turnover has to be at frequencies less than 580 MHz. The upper limits at 408 MHz, however, pose problems for this picture, as this would suggest the flux density of Sgr A* at this frequency could have been much less few decades back. We have re-examined the 408 MHz upper limit by Davies et al. (1976) and found that their analysis has not taken account of scatter broadening of Sgr A* (about 8″ at 408 MHz) and the corrected upper limit at 408 MHz could be as high as ≈ 2.5 Jy.

At frequencies of a few GHz to 620 MHz, the observed spectral index of Sgr A* is nearly flat. For extragalactic flat spectrum sources, it is believed that there are multiple components in emission and peak radiation from different components occur at different frequencies to make the overall spectrum appear nearly flat (Cotton et al. 1980). Though the Advection-dominated accretion flow (ADAF) model of emission from Sgr A* fails to explain the observed low frequency emission, ADAF along with self-absorbed synchrotron emission either from a relativistic Jet (Yuan et al. 2002), or from a small fraction of relativistic electrons embedded in the accretion flow (Yuan et al. 2003) could explain the observed spectrum of Sgr A* from X-ray ranges to radio frequencies up to 620 MHz. If we consider the flux density estimated at the position of Sgr A* at 330 MHz (Nord et al. 2004) as the observed upper limit, its estimated spectral index between 620 and 330 MHz is inverted and is $>$0.66. This low frequency turnover could be due to an enhancement in the optical depth of synchrotron emission or internal/external free-free absorption.

2.4.3 Location of Sgr A*

At 620 MHz, Sgr A West shows evidence for free free self-absorption. In Fig. 2.12, we have shown the model fits for the electron density and temperature in different parts of the ionised gas. Sgr A* is located slightly above the junction of the bar and the northern arm. Therefore, this object is seen along the line of sight of the diffuse gas located north of the bar like feature. From the fit shown in Fig. 2.12, we estimate an optical depth of this ionised gas in Sgr A West region to be 2.5 ± 0.5. If Sgr A* was located behind Sgr A West, then its flux density would have been attenuated by a factor of 10. However, the spectral index of Sgr A* between 620 MHz and 1.4 GHz is roughly the same as between 1.4 GHz and 8.5 GHz showing no effect of free free absorption by Sgr A West. This indicates that Sgr A* is located in front of Sgr A West. It is possible to invoke alternate scenarios like sharp enhancement of the 620 MHz flux density of Sgr A* to compensate for the absorption due to Sgr A West or a hole in Sgr A West along the line of sight to Sgr A*, but these appear to be unlikely. Sgr A* is located slightly north of the junction of the Northern arm and the bar like feature of Sgr A West. From the high resolution 3.6 cm map (resolution $\approx 0.5''$) of the region (Fig. 2.1) (Roberts & Goss 1993), we notice the presence of weak emission likely to be emitted from the diffuse ionised gas which becomes optically thick at 620 MHz. Any hole in this ionised gas has to be smaller than $1''$ which is unlikely. Thus, Sgr A* is located in front of Sgr A West.

2.5 Summary

Observations of the GC region at 620 and 580 MHz with the GMRT and a comparison with the existing observations made at other radio frequencies have provided us several important details about the region:

(i) For the first time, the SNR Sgr A East is shown to display a break in its spectral characteristics. It has a spectral index of about -0.76 at frequencies above 1.4 GHz.

However, between 1.4 and 0.33 GHz, its spectral index is about -0.3, indicating that its spectral index changes by $\approx$0.5 at $\approx$1 GHz.

(ii) Using the standard synchrotron model and the break in its spectrum, we estimate the age of Sgr A East to be about 10^4 years.

(iii) Emission from the $7'$ halo also shows similar break in the spectrum, which suggests that Sgr A East and the $7'$ halo are physically associated.

(iv) Sgr A* has been detected at 580 MHz, which is the lowest frequency unambiguous detection, and the estimated flux density at this frequency is consistent with what is expected from its higher radio frequency spectral index and the flux density. This indicates that there is no low frequency turnover of its emission above 580 MHz.

(v) The optical depth of the Sgr A West HII region is estimated to be about 2.5 at 620 MHz. Though Sgr A* is located along the same line of sight, the emission from it undergoes no absorption by this HII region, which indicates that Sgr A* is located in front of Sgr A West.

2.6 Appendices

2.6.1 Appendix-A: Multi-Resolution Clean

'Clean' normally uses a point-source component model and finds and subtracts one component at a time. In maps consisting of small-diameter objects ($\sim$a few synthesised beam) this has been found to work well. But, for extended objects (size $>$10 synthesised beam), the subtraction of a point source at one pixel produces sidelobes of the Dirty beam on the neighbouring pixels. Spurious peaks created by the sidelobes are picked up by Clean and the intensity distribution on the Cleaned map appears 'corrugated' (i.e, parallel stripes in the 'Clean map') (Wakker & Schwarz 1988). The 'corrugation' in the image occur at spatial frequencies that have not been measured (holes in the u-v plane). Therefore, the clean map that is produced is consistent with the measured data but is not

a realistic brightness distribution, and this can become important for observations with incomplete *uv* coverage. This effect is described in detail by Schwarz, U. J. 1984, in Indirect Imaging, ed. J. A. Roberts, p255.

For extended objects with low surface brightness, when the signal becomes comparable to the noise in the map, Clean cannot distinguish between signal and the noise, and as a result deconvolution of the extended emission from the Dirty map does not proceed well.

The Multi-Resolution (MR) Clean (Wakker & Schwarz 1988) attempts to avoid the corrugation and low signal to noise issues by using Clean-components with different diameters during deconvolution (Wakker & Schwarz 1988). MR Clean uses a smoothed image and beam, and a difference image and difference beam, doing a standard point-model Clean on each but appropriately subtracting the components found in one image from the other at every iteration. Smoothing the Dirty image corresponds to a taper in the uv-plane so that only the shorter spacings are used. The smoothing is so chosen that the holes in the uv coverage (often *uv* coverage becomes sparse with increasing uv-distance) lie outside the tapered region and since the smoothed map has no major holes in the *uv* plane of relevance, the corrugation no longer occurs (Wakker & Schwarz 1988).

To examine possible imaging artefacts in our GC map, we used the Clean components as in the 1.4 GHz GC map (Fig. 2.5) within the $7'$ of the Centre as a model, which is shown in Fig. 2.13. By taking inverse Fourier Transform of these components, sampling them at *uv*-points corresponding to the GMRT *uv* coverage and using the standard Clean, we get the map shown in Fig. 2.14. The extended emission of the $7'$ halo while clearly visible, appears ‘corrugated’ and breaks up into small components.

To reduce the problem of ‘corrugation’ on the image, we used the same model visibility data and made a map using the MR Clean as implemented in AIPS, which is shown in Fig. 2.15. For this image we used two different resolutions with one being a point model and the other being a Gaussian with a FWHM of $85''$ respectively. The

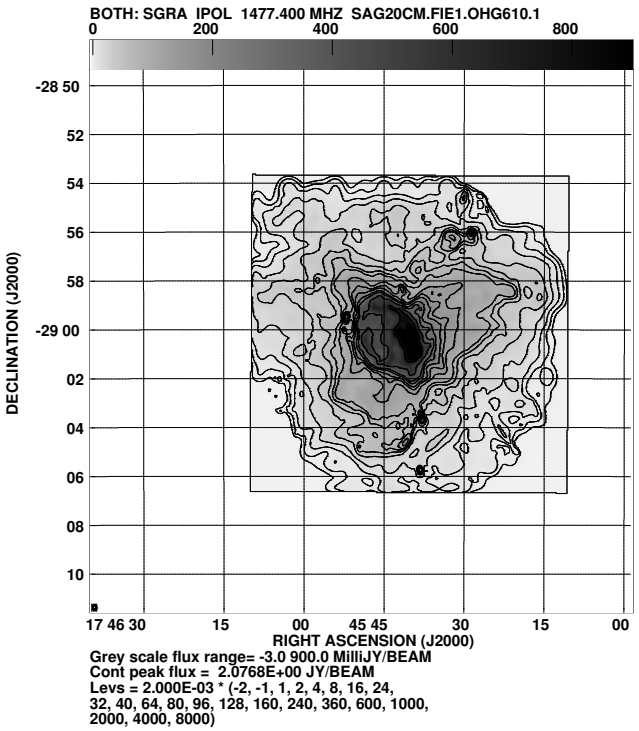

Figure 2.13: A model of the GC using the Clean components within about $7'$ of the Galaxy. The restoring beam is $11.4'' \times 7.6''$, with beam position angle of 7.7°.

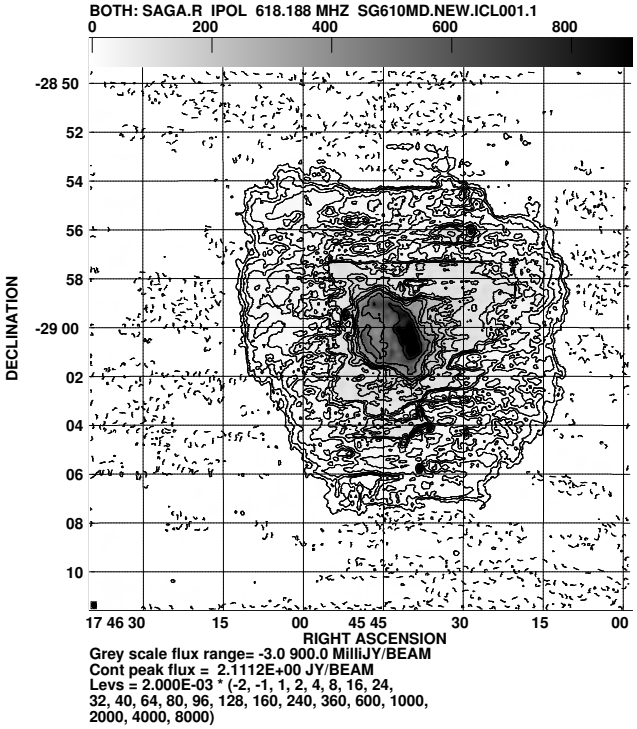

Figure 2.14: A map deconvolved using Standard Clean. The uv-data was generated using the Fourier transform of the Clean components of the map shown above. The restoring beam is $11.4'' \times 7.6''$, with beam position angle of 7.7°.

extended emission of the $7'$ halo in this map appears smooth and quite similar to the one seen in the input model. If we define the dynamic range as the ratio of the measured peak flux density, and the rms flux density estimated from the region where no Clean components in the model were located, then the estimated dynamic range is about 10^4. Therefore, we have used this technique to image the GC using the GMRT data.

2.6.2 Appendix-B: Possible causes of dynamic range limitation of the GC map at 620 MHz

The theoretical noise expected in our 620 MHz GC map is $\sim 100\mu$Jy. However, the actual noise in the map (Fig. 2.2) is about 6.5 mJy, and is limited by dynamic range. This is most likely caused by non-ideal behaviour of the hardware in the system. Here we discuss some of them, which are believed to contribute significantly in reducing the

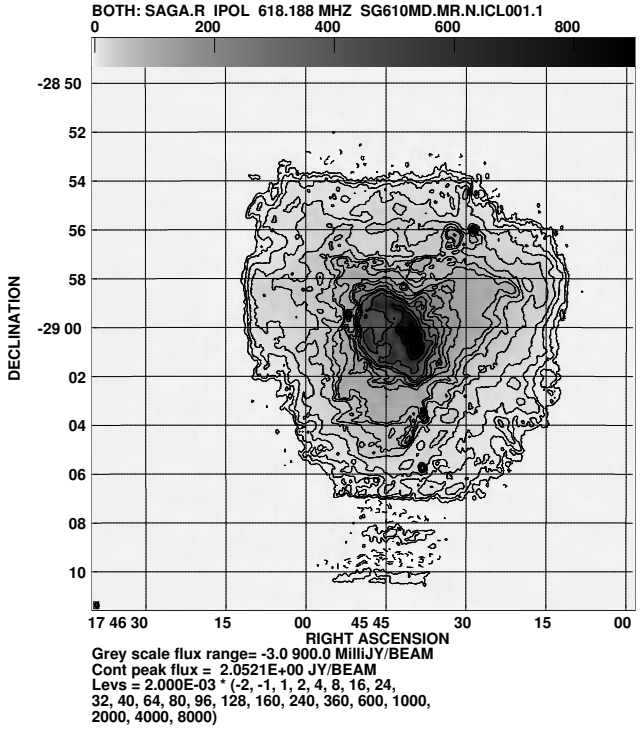

Figure 2.15: This map is produced from the same data as used in the previous map, but deconvolved with MR Clean. The corrugations seen in the previous map have almost vanished

dynamic range of the map.

2.6.2.1 Pointing errors of the antennas

The Fourier Transform relation of the visibility ($V(u,v)$) and the source intensity distribution

$$V(u,v) = \int\int A(l,m)I(l,m)\exp[-2\pi i(\mathrm{ul}+\mathrm{vm})]\,\mathrm{dl}\,\mathrm{dm}$$

assumes that the source intensity ($I(l,m)$) and the antenna reception pattern ($A(l,m)$) does not vary during the observation. However, if due to pointing errors the angular distances of the sources from the pointing centre of the antennas change during the observations, the apparent intensities of the sources in the field can vary with time. Under these conditions, a simple Fourier inversion of the $V(u,v)$ to retrieve the source intensity distribution is not valid.

If the source is compact, so that the pointing error is equivalent to a change in the overall antenna gain, amplitude self-calibration can be expected to correct this problem. However, for extended emission like in the GC field, amplitude self-calibration will not work since the correction is different for different parts of the field.

During our observations using GMRT, we have noticed that the pointing error of the antennas by a few arc-minutes is quite common during observations and the pointing centre of some of the antennas showed jumps of up to $\sim 6'$ after transit. In order to examine the effect of such pointing error in our map, we considered a simple model where during the first half (3.5 hours) of observations there is no pointing error associated with the antennas, but during the second part of the observation, all the antennas have a pointing error of $6'$. In order to generate model data for this case, we restored the Clean components of the model used in Fig. 2.13 with a high resolution beam ($4.8'' \times 2.8''$ with position angle of 11°). For the first part of the observations, we Fourier transformed the map, and sampled them at *uv*-points corresponding to a model uv-data generated using all the 30 antennas of the GMRT. However, for the second part of the observations, before applying inverse Fourier transform, we multiplied the map with the primary beam pattern of the antennas at 620 MHz with an offset of $6'$ from the phase centre. Finally, the data sets of the first and second half of the observations were combined and Fourier transformed. The resultant map is shown in Fig. 2.16, which has been deconvolved using the MR Clean. The source could not be deconvolved properly from the dirty map and the map is limited by a dynamic range of about 10^3, which highlights the dynamic range achievable with the kind of pointing error model we have considered. It should be noted that the model considered is a worst case scenario and in reality this effect will be less since the pointing errors on different antennas are random and are usually much less than the $6'$ that was assumed.

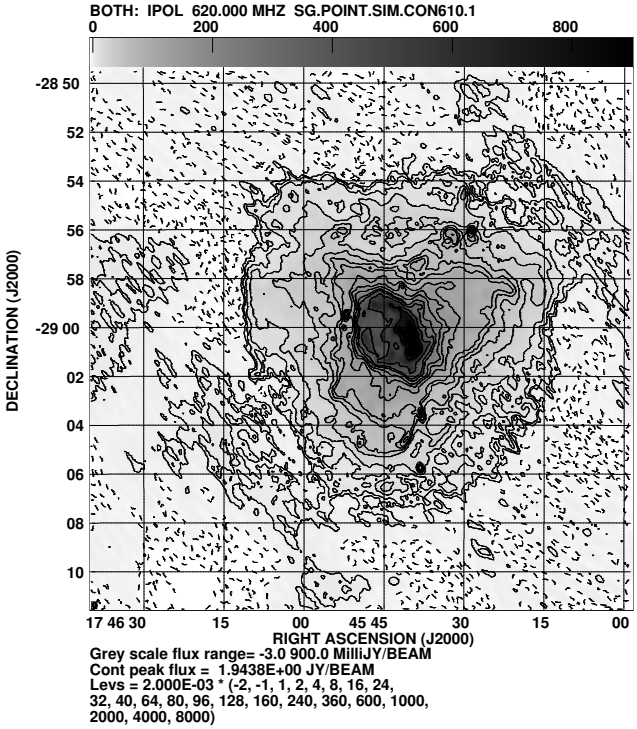

Figure 2.16: Effect of 6′ pointing error of the antennas in reducing the dynamic range. The pointing error was introduced after zenith crossing of the source. See text for details.

2.6.2.2 Calibration errors

The Fourier transform relation between the visibilities and the source intensity distribution is obtained by assuming that the visibilities used for Fourier transform represent the true visibilities. However, the observed visibilities are obtained by means of amplification of the signal received at the antennas, conversion to lower frequency signal, transmission through cables, and correlated from each antenna pair by a correlator. The recorded ensemble of numbers, called the observed visibility data in general, differs from the desired true visibilities.

The calibration procedure tries to estimate the true visibilities from the observed. In Sect. 2.2, we have described how periodic observation of calibrators (having known structure and flux density) are used to estimate the instrumental gain and hence the true visibilities. However, if the gains of the antennas change in timescales shorter than the

interval between the calibration observations, this kind of calibration cannot yield the true visibilities. Short time scale variations in the effective antennas gain can occur due to the electronics chain itself and due to phase variations caused by the ionosphere. The refractive index (ε) of plasma is related to the electron density (n) by

$$\varepsilon = 1 - \frac{4\pi \mathrm{ne}^2}{m_e w^2},$$

where, ω is the observing circular frequency ($2\pi\nu$), e is the charge and m_e is the mass of an electron. Since change in the electron density implies change in the effective path length ($\varepsilon \times$ geometrical path length) through the medium, and the ionospheric patch through which different antennas receive signals from the source can be different, the ionosphere can produce phases that vary with both position and time for different antennas. This change of phase during observations can be corrected by self-calibration (see, Synthesis Imaging in Radio Astronomy II, Lecture 10 by Cornwell & Fomalont). The GC map at 620 MHz has been self-calibrated to correct for this change of phase during the observations. The change in instrumental phase also gets corrected by self-calibration. It should, however, be noted that the standard self-calibration assumes an isoplanatic patch which is infinite in size. Consequently, if the ionospheric phase is a function of the elevation and azimuth angle of the sources, current self-calibration cannot fully correct for the extra phase introduced by the ionosphere.

The observed visibilities, if normalised by the self correlations to give the cross correlation coefficients, are proportional to the antenna efficiency and inversely proportional to the equivalent system temperature (T_{sys}) (see, Interferometry and Synthesis in Radio Astronomy by Thompson, Moran & Swenson; Chapter 6.2), which includes the effective temperature of the antennas (T_{ant}) due to the radiation received from the sky and the equivalent temperature of the electronics system (T_{elec}) (i.e., T_{sys}=T_{elec}+T_{ant}). While observing sources near the Galactic plane at metre wavelengths, the radiation received from the sky contributes significantly to T_{sys}. Moreover, the calibrators are typically

selected to be a few degrees away from the Galactic plane. Therefore, the T_{sys} while observing the calibrator and the target source is different and unless corrections are made for it, can cause a systematic underestimation of the true visibilities of the sources close to the Galactic plane. As described in sect. 2.2, in one of our observations, we have tried to correct for this T_{sys} variation by scaling the map (and all visibilities) by a constant correction factor. However, variations in T_{elec} and the efficiencies among different antennas can cause the T_{sys} to be different for different antennas. Given that $T_{ant} \sim 500$ Kelvin, while observing the GC at 620 MHz, and $T_{elec} \sim 100$ Kelvin, gain variations of $\sim 10\%$ from the mean value can occur in some of the antennas. Therefore, we have tried to understand the effect of amplitude errors on our map by simulations.

We have used the model shown in Fig. 2.13 to generate the uv-data corresponding to 30 antennas of the GMRT. In this model uv-data, we multiply the antenna based gains of the antennas by random numbers spread uniformly about 1.0 with rms value of 0.1 (the antenna based gains are assumed to be constant with time). The resultant map made using IMAGR and deconvolved with MR Clean is shown in Fig. 2.17. We notice that there are systematic pattern generated due to amplitude errors introduced by us, and the dynamic range of the map is reduced to $\sim$250.

The errors in the amplitude gain can also be corrected with self-calibration of both phase and amplitude. However, we found that the GC map at 620 MHz did not improve while keeping the antenna based amplitude and phase as free parameters during self-calibration. Therefore, we have performed only phase self-calibration to the 620 MHz GC map.

2.6.3 Appendix-C: Keeping the visibility amplitudes constant when the system temperature (T_{sys}) changes

To perform GMRT observations such that T_{sys} variations have minimal effect on the observed visibilities, the following procedures were adopted. This is especially useful

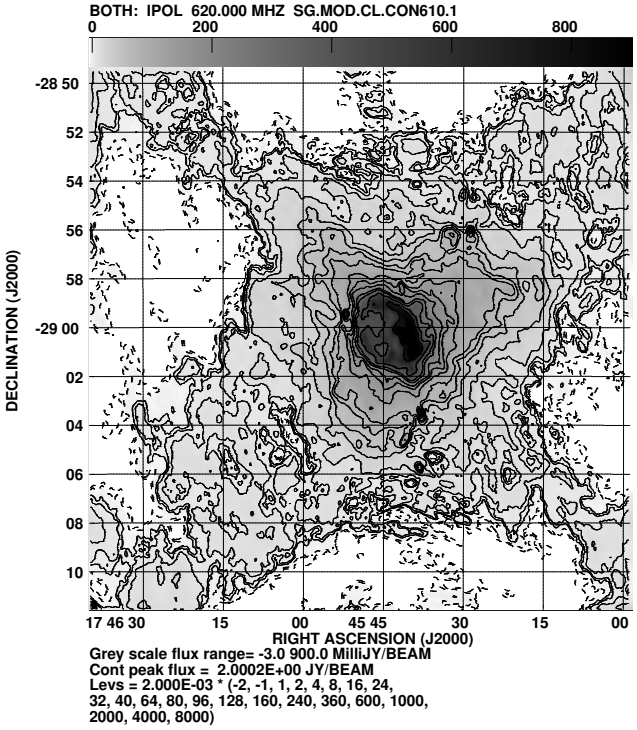

Figure 2.17: Effect of amplitude gain errors of the antennas on the map. The gain errors are taken to be random with rms value of 0.1 (10%)

when the antenna temperature during observation is quite high ($\gtrsim$30 K).

The Automatic Level Control (ALC) is a negative feedback device that keeps the output power of the antennas at the optimal levels. As a result, any increase in the input power reduces the gain of the amplifiers. This keeps the total power output of the system almost constant. However, when any change in the T_{sys} takes place (i.e., while observing sources in the Galactic plane at low frequencies), as explained in the previous section, amplitude gain of the amplifiers changes, and this in turn changes the visibility amplitudes. Therefore, switching off the ALCs avoids the problem. However, when the ALCs are off, an increase in the T_{sys} produces excessive output power, and the antenna based electronics can get saturated. So, when the ALCs are off, the system Gains have to be adjusted in a fashion that the antenna based electronics do not get saturated. This is usually achieved by changing the amplitude gains of all the antennas using attenuators,

such that the output power of all the antennas at the beginning of observation are equal to their default values. Since, T_{sys} is maximum when the sky temperature is maximum, this needs to be performed while observing the strongest source (in our observation, T_{sys} was maximum while observing the GC field).

Avoiding variation in visibility amplitudes also requires using the unnormalised cross-correlation data, where the cross-correlation coefficients between different antenna pairs are not normalised by the total power of the antennas. It is shown in the next appendix that within the observing band, if the antenna efficiency (η) is a function of frequency channel, then if the cross-correlated data is normalised, variation of the antenna temperature will cause a change of bandshape. Therefore, avoiding division by the total power serves both the purposes described above.

2.6.4 Appendix-D: Variation of spectral bandshape estimated from normalised cross correlated data due to change in antenna temperature (T_{ant})

The shape of the instrumental bandpass (bandpass function) is normally determined by observing a suitably strong calibrator during observations. It is assumed that the shape of the instrumental bandpass is independent of the source position in the sky. Here we show that if normalised cross correlated data are used to estimate the true visibilities, this assumption is no longer true while observing sources near the Galactic plane at low radio frequencies.

It is known that the T_{sys} is the sum of T_{elec} and T_{ant}, and T_{ant} is directly proportional to the antenna efficiency (η). Therefore, if η is a function of frequency (ν), then both T_{ant} and T_{sys} are functions of ν. As normalised visibilities are directly proportional to η and inversely proportional to T_{sys}, it implies that the bandpass function is proportional to $\frac{T_{ant}(\nu)}{T_{elec}+T_{ant}(\nu)}$. Since the bandpass calibration is performed with a calibrator typically away from the Galactic plane, the $T_{ant}(\nu)$ may be small and neglected in the denominator.

However, $T_{ant}(\nu)$ is substantial while observing any source in the Galactic plane at low radio frequencies ($\lesssim$1.4 GHz). As the relationship of the bandpass function with $T_{ant}(\nu)$ is non-linear, it changes the overall shape of the bandpass function.

As an example, we consider the antenna efficiency (η) to fall from 0.6 at the centre of the observing band to 0.4 at the edge of the observing band. Assuming T_{elec}=70 K, and the sky temperature (T_{sky}) at the Galactic plane to be 200 K, the normalised bandpass function at the centre of the band is proportional to $\frac{\eta T_{sky}}{T_{elec}+\eta T_{sky}} = 0.63$, and is proportional to 0.53 at the edge of the band. However, while observing a bandpass calibrator away from Galactic plane, the T_{ant} is negligible, (T_{elec} is assumed to be independent of ν) the bandpass function is proportional to ν. However, if this bandshape is used to correct the visibilities of the spectral line data of the target source, the true visibilities at the edge of the observing band will be overestimated by about 25 % with respect to the centre of the band.

Chapter 3

GMRT observations of suspected SNRs with filamentary structures near the Galactic Centre

3.1 Introduction

The long narrow non-thermal filaments (NTFs) observed in high resolution radio-continuum maps are unique features seen towards only the central $\sim 1^\circ$ region of our Galaxy. These structures are less than 1 pc in width, but extend up to 30 pc in length. With the exception of the NTF called the Pelican (Lang et al. 1999a), which is nearly parallel to the Galactic plane, all other NTFs are oriented perpendicular to the Galactic plane to within 20° [1]. The morphology of the NTFs suggests that they reflect the local magnetic field direction and radio polarisation evidence supports this notion (Morris & Serabyn 1996, and references therein). By equating the apparent turbulent pressures within clouds (or the ram pressure associated with presumed cloud motion relative to the field) to the magnetic pressure, as a minimum condition on the strength of the magnetic field, Yusef-Zadeh & Morris (1987a) have estimated that the magnetic field strength within the NTFs is of the order of milliGauss.

With more sensitive observations, fainter NTFs are discovered, some of which are

[1] Recently, Nord et al. (2003) have published a list of 18 new candidate NTFs in the GC region, and Larosa et al. (2003) confirm 4 more NTFs. Many of these new NTFs and the candidate ones are oriented randomly with respect to the Galactic plane.

further away from the Galactic Centre (GC) (e.g., Pelican) than expected before. Therefore, it may be possible to detect NTFs a few degrees away from the GC, which will provide crucial information on their distribution and the effect of the GC environment on their origin and maintenance. On the other hand, lack of their detection beyond the central $\sim 1^\circ$ of the GC will strongly argue for the dense molecular cloud and strong magnetic field in the central 180 pc of the GC to be responsible for the creation and maintenance of the NTFs.

We shortlisted 2 filamentary structures located $\approx 3^\circ$ away from the GC, which were suspected to be either (i) NTFs or (ii) part of suspected SNRs in the region. One of these filamentary structures was noticed by us in the NVSS map (Condon et al. 1998) in both continuum and polarised emission (Fig. 1.5). This object is located in the field of the suspected SNR G3.1–0.6 (Gray 1994c) and could either be part of this suspected SNR, or a candidate NTF located 3° away from the GC.

The other filamentary structure G357.1–0.2 was identified by Gray (1996) (see Fig. 1.4). Its peculiar morphology makes it difficult to draw any unique identification for this object. Based on its steep spectral index between 1.4 and 5 GHz, and highly polarised emission, Gray (1996) suspected that it could be (i) an NTF as seen near the GC or (ii) an extragalactic source or (iii) a Crab like SNR.

Since low frequency observation can distinguish SNRs from other objects, and HI absorption can constrain its distance, this source was selected for observation with the GMRT at 330 and 1420 MHz.

Shell type SNRs can be distinguished from other diffuse sources in our galaxy by their ring like morphology and non-thermal synchrotron emission which is characterised by a steep power law and polarised emission. The other class of SNRs, known as the plerions, are characterised by their filled centre or blob-like morphology, a comparatively flat spectrum and at high radio frequencies, can show a much higher linear polarisation fraction than the shell type SNRs. However, due to changing orientation of the magnetic

field and large Faraday depolarisations within the sources, polarised emission is not detectable for many SNRs and therefore measurements of their low frequency flux density and spectral indices are often the only way to detect synchrotron emission. The Giant Metrewave Radio-Telescope (GMRT) (Swarup et al. 1991) with its large collecting area and high resolution at low radio-frequencies is an ideal instrument for such studies.

Therefore, to clarify the nature of the filamentary structure in the field of the candidate SNR G3.1−0.6 (Field I) and the filamentary structure G357.1–0.2 (Field II), we observed these sources at 330 MHz with the GMRT. We also have done HI absorption study of G357.1–0.2.

The field centre (Field II) during the observation of G357.1–0.2 was chosen in a way so that two more suspected SNRs G356.3−0.3, G356.6+0.1 are also located in the field of view. In the $-5^\circ \leq l \leq 5^\circ$, $-2.5^\circ \leq b \leq 2.5^\circ$ region of the Galaxy, 13 SNRs had been identified before the MOST Galactic Centre survey (MGCS). The MGCS (Gray 1994c) detected another 17 candidate SNRs in the region. These detections, if confirmed, indicate the number density of SNRs in the GC region to be twice than that in the rest of the Galaxy (Gray 1994b) and could link enahnced star formation in the dense environment of the GC with higher number density of SNRs in the region. In view of the above, we attempted to verify the nature of some of these objects in the MGCS.

Near the edge of the field of view of G357.1–0.2 is located the peculiar object known as the Tornado nebula, which also has extensive filamentary structures. This is the sixth brightest object in the Milne (1979) catalogue. It has a very unusual structure and its classification as a supernova remnant has been questioned (Becker et al. 1985). Some authors have noted its similarity with extragalactic head-tail sources (Weiler & Panagia 1980), or a new class of Galactic head-tail object (Becker & Helfand 1985). Another intriguing suggestion is that G357.7-0.1 is powered by an object ejected from the nearby SNR (G359.0-0.9) which lies only 1° from the symmetry axis of G357.7−0.1. This scenario, however, would require such a runaway pulsar or X-ray binary to have a transverse

velocity >2000 km s^{-1}, which is considered unlikely (Gray 1994d). The discovery of an OH (1720 MHz) maser coincident with G357.7-0.1, however, suggests that it is a Galactic SNR (Yusef-Zadeh et al. 1996a).

In spite of its steep spectral index of about -0.5 above 1 GHz, its classification as a shell type or a filled centre type is somewhat uncertain (Shaver et al. 1985). Interferometric high-resolution observations have been performed at 1.4 and at 5 GHz band using the VLA (Shaver et al. 1985; Becker & Helfand 1985). However, it has not been studied below 1.4 GHz. The Tornado nebula as seen in the GC map at 330 MHz (Larosa et al. 2000) is distorted due to its large distance from the GC and the consequent bandwidth smearing, and due to large uncertainty in primary beam correction, its flux density is not estimated at 330 MHz (LaRosa et al. 2000).

Therefore, to clarify the nature of this object at low frequency and to constrain its distance, we have observed this object at 330 MHz (Field III) and in HI absorption using the GMRT. In order to compare its spectrum with an extragalactic source and to put an upper limit on its distance, we also observed in HI absorption an extragalactic source G356.9+0.1 seen close to the line of sight of Tornado nebula.

In Sect 3.2, we discuss observational strategy and calibration. The results of our observations have been described in Sect 3.3 and in Sect 3.4, we discuss about the morphology, spectral index, distance and other physical properties of the objects observed by us. In Sect 3.4.5, we present a list of compact sources seen within the field-of-view and also an estimate of their flux densities at various radio frequencies. We draw the conclusions in Sect 3.5.

3.2 Observations and data reduction :

The GMRT consists of thirty antennas, each of diameter 45 metre, distributed over a region of about 25 kilometres, with fourteen of the antennas placed within a diameter of

about one kilometre and the remaining arranged in 3 arms each of length 14 km, shaped as an irregular Y. This arrangement provides the necessary *uv* coverage for mapping both compact and extended sources. The ratio of the longest to the shortest baseline is around 500 with the shortest projected baseline being about 50 metres.

The present observations were made when the GMRT was still being commissioned and often all the 30 antennas were not available. Table 3.1 give details of our observations. While observing the filamentary structure near the suspected SNR G3.1−0.6, the centre of the Field I was set at l=3.2° and b=−1.0°. The source 1830−21 was used as both phase and amplitude calibrator.

While observing the Field II, the centre of the field was set at l=356.8°, b=−0.1°, so that all the 3 objects, G356.3−0.3, G356.6+0.1 and G357.1−0.2 were observed within the primary beam of the antennas (FWHM=88′ at 330 MHz). We have also carried out an HI absorption study towards G357.1−0.2, and G356.9+0.1. While observing this field, the source 1822−096 was observed as the amplitude calibrator and 1701−299 which was nearby at the same declination as the field being observed, was used as phase calibrator. The amplitude and phase calibrators were observed every 30 minutes.

To observe the Tornado nebula, the centre of Field III was set at l=357.5°, and b=−0.1°, the source 1822−096 was used as the amplitude and bandpass calibrator and 1701−299 which was nearby as the field being observed, was used as phase calibrator.

All the observations were carried out in the spectral line mode with 128 frequency channels, which is the default for the GMRT correlator. For the 330 MHz observations, a bandwidth of 16 MHz was used while for the 21 cm spectral line observations, which needed better frequency resolution, the total bandwidth was reduced to 4 and 2 MHz, giving a frequency resolution of 32 and 16 kHz respectively. For the 330 MHz observations, 1830−36 was observed initially for 20 minutes as a flux density and bandpass calibrator. Long term monitoring of this calibrator at 843 MHz using MOST has shown the modulation index (ratio of the standard deviation to the mean value of the flux den-

Table 3.1: Details of our observation

Galactic coord. of the pointing Centre *(l, b)*	RA (J2000)	Dec (J2000)	Frequency (MHz)	Date	Observing time (hours)	Available antennas
003.2−1.0	17 57 00.1	−26 40 01	330	1999 Jun 25	6	27
356.8−0.1	17 38 11.4	−31 42 26	330	1999 Aug 01	3.5	24
357.2−0.2	17 39 40.6	−31 28 01	1420.6	2000 Feb 26	3.5	15
357.5−0.1	17 40 00.7	−31 10 02	330	2000 Apr 28	5.0	25
357.5−0.1	17 40 18.6	−30 59 52	1420.6	2001 May 24	3.5	27
356.9+0.1	17 37 44.2	−31 31 15	1420.3	2000 Oct 07	0.5	26
356.9+0.1	17 38 00.0	−31 26 00	1420.4	2002 Dec 26	2.5	25

sity from the different epochs) to be 0.016 (Gaensler & Hunstead 2000), which is well within the expected uncertainty of $\pm$ 15% in determining our absolute flux density scale (Baars et al. 1977). From the VLA calibrator manual (Perley 2001) we have taken the flux density of this calibrator as 28 Jy at 330 MHz and 6.9 Jy at 1420 MHz.

At the time of these observations, automatic measurements of system temperature (T_{sys}) were not implemented, the T_{sys} towards the calibrators and the SNR fields were estimated using the 408 MHz all sky map (Haslam et al. 1982), and then scaled to 330 MHz assuming a spectral index of -2.6. The measured visibilities were corrected for this T_{sys} variations towards various sources (the typical correction factors between the target source and the secondary calibrator was $\sim$3). In this chapter, we follow the convention of $F(\nu) \propto \nu^{\alpha}$, i.e., for steep spectral index, the magnitude of α will be negative.

3.2.1 Calibration

The data were processed within AIPS using standard programs. Bad data (interference in some frequency channels, spikes and drop outs due to the electronics, etc) were identified and flagged using FLGIT. The data were also checked for bad antennas or baseline based problems which were also flagged. The spectral visibility data were bandpass calibrated. For the 330 MHz data, a pseudo-continuum database of 4 frequency channels (each of width 2 MHz) were made from the central 64 frequency channels of the

observed 16 MHz band. This was adequate to avoid bandwidth smearing within the primary beam. Images of the fields were formed by Fourier inversion and Cleaning (IMAGR). The initial images were improved by self-calibration. CLEAN maps of the compact sources in the Field I and II made by using only the data with *uv*-distance greater than 150 λ were used to self-calibrate the data using CALIB with a *uv*-range of 0.8−15 kλ.

For a better imaging of the extended structure in the Field G3.2−1.0, we made a high resolution map with a lower cutoff of the *uv* range at 400 wavelengths. The Fourier transform of the CLEAN components of the sources in this map was then subtracted from the *uv* data and one more map was made with no lower cutoff in the *uv* range. This map was then deconvolved using MEM. The CLEAN components which were subtracted earlier were added back to the resulting image to produce the final image of the SNR. This technique has typically yielded an RMS noise one and half times smaller than that obtained using the standard CLEAN. To minimise the effect of non-coplanar baselines, the high resolution CLEAN images were made for both the fields at 330 MHz using the multi-facet technique available in the newer versions of the AIPS task 'IMAGR'. However, to make the images of the Field-II, the above procedure was not required and we used standard CLEAN to remove the side-lobes of the synthesised beam. All the GMRT maps presented in this chapter have been corrected for the primary beam pattern of the antennas.

We have also performed an HI absorption study with the GMRT towards the candidate SNR G357.1−0.2, Tornado nebula and the compact source G356.9+0.1. 1748−253 was used as the phase calibrator and 3C287 as the bandpass calibrator. Since, the bandpass pattern of the antennas change appreciably as a function of frequency, we have not used frequency switching for the bandpass calibration, but have chosen a bandpass calibrator (3C287) with a high Galactic latitude, so that the effect of Galactic HI absorption on its spectra is less than 1% (Dickey et al. 1978). We observed 1830−36 as the flux

density calibrator. The HI absorption profiles towards G357.1−0.2 was obtained using 128 frequency channels over a bandwidth of 4 MHz, whereas the HI profile towards G356.9+0.1 was obtained over a bandwidth of both 2 and 4 MHz. The resultant velocity resolution is 6.6 km s^{-1} towards G357.1−0.2 and 3.3 km.s^{-1} and 6.6 km s^{-1} towards G356.9+0.1. To make the channel maps, standard AIPS task (UVLSF) was used to subtract a constant corresponding to the continuum from the visibility data. The GMRT has an FX correlator, for which 'Gibbs ringing' due to any sharp feature in the spectrum dies away much faster ($sinc^2$ response to a sharp pattern, which has a peak side-lobe of 5%) as compared to an XF correlator. Therefore, we have not applied any spectral smoothing to our data. Also, the variation of the line frequency introduced by the Earth's rotation during the observing period being much smaller than the frequency channel width, we have not applied any Doppler corrections.

3.3 Results

3.3.1 Field I:

The candidate SNR G3.1−0.6 identified during the MOST 843 MHz survey is located in this field. In the MOST (Fig. 3.1) and NVSS maps (Fig. 3.2), which are at higher frequencies, the source appears as a collection of filamentary structures, but, in the GMRT maps at 330 MHz (Fig. 3.3 & Fig. 3.4) extended emission that connects up the filaments which form part of a shell is clearly seen even in the high resolution maps. The overall shape of this suspected SNR is best seen in the GMRT low resolution map in Fig. 3.4 which shows that the radio shell is visible all around except in the northeast of the object. There is general agreement between the structures seen in the MOST and GMRT maps. However, the 330 MHz map also shows appreciable diffuse emission towards the west (feature marked C in Fig. 3.3). The eastern part of the shell as evident in the low resolution image (Fig. 3.4), seems to be quite narrow and appears like a filament in our

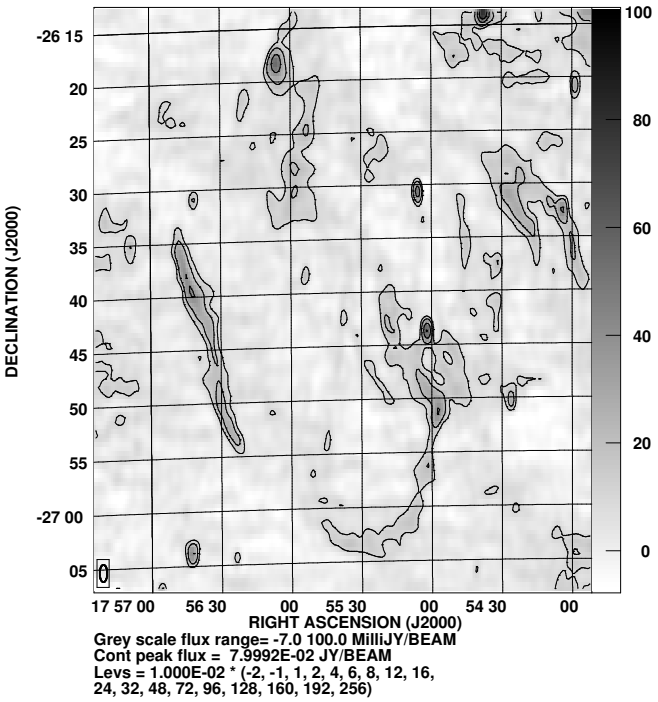

Figure 3.1: MOST image of G3.1−0.6 at the original resolution of $1.6' \times 0.7'$ along PA 0.1°. The RMS noise is 4.5 mJy/beam.

high resolution image (feature marked A in Fig. 3.3). The filamentary structure appears to be connected (Fig. 3.4) with G3.1−0.6, and most likely to be part of its shell. It is also seen in the NVSS (Condon et al. 1998) map (Fig. 3.2). However, the NVSS maps are produced from snapshot observations and due to a comparatively poor *uv*-coverage in their data, the extended structures were not properly imaged in their map. The GMRT 330 MHz maps indicate an additional small shell like feature at the southern part of the larger shell that can be clearly seen in Fig. 3.3 (feature marked B).

From the GMRT image, the total flux density of this object at 330 MHz is 14 ± 3 Jy, while at 843 MHz, the flux density is reported to be 6.5 Jy (Gray 1994c). However, flux density estimated from both maps can suffer from zero-spacing problems due to the large size of $(28' \times 49')$ of G3.1−0.6. The filamentary structure near the eastern side is sufficiently small (Fig. 3.3), and would not to suffer from any significant zero-spacing problem. The spectral index estimated for the filamentary structure is -0.62 ± 0.12. This

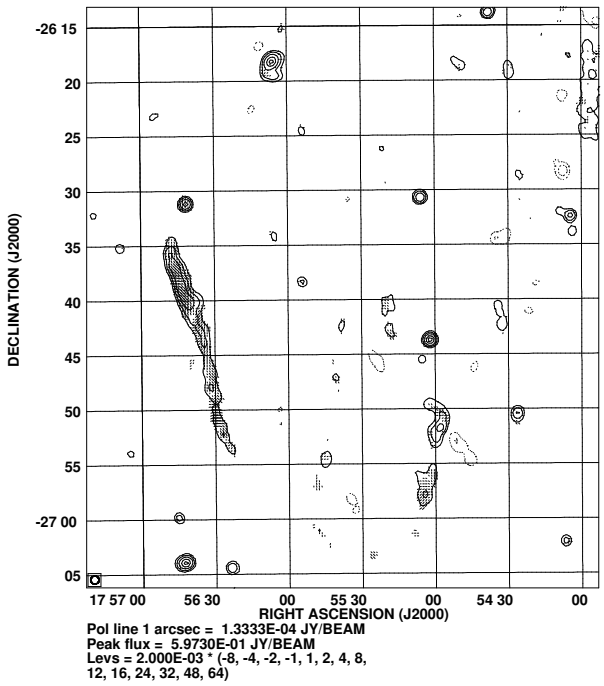

Figure 3.2: NVSS map of G3.1−0.6 at the original resolution of $45''$. The filamentary structure at the eastern side is polarised. The RMS noise in the map is 0.5 mJy/beam.

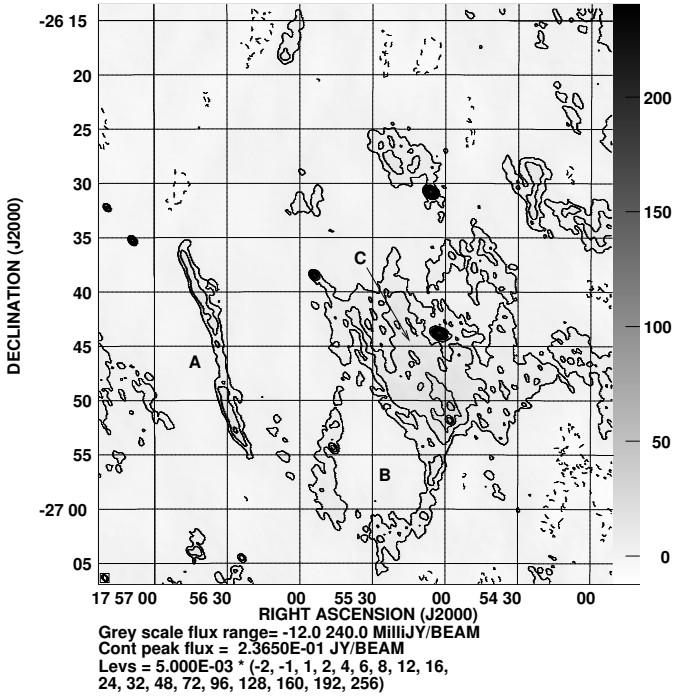

Figure 3.3: GMRT high resolution image of G3.1−0.6 at 330 MHz. The resolution is $37'' \times 25''$ along PA 41° and the RMS noise in the map is 1.7 mJy/beam.

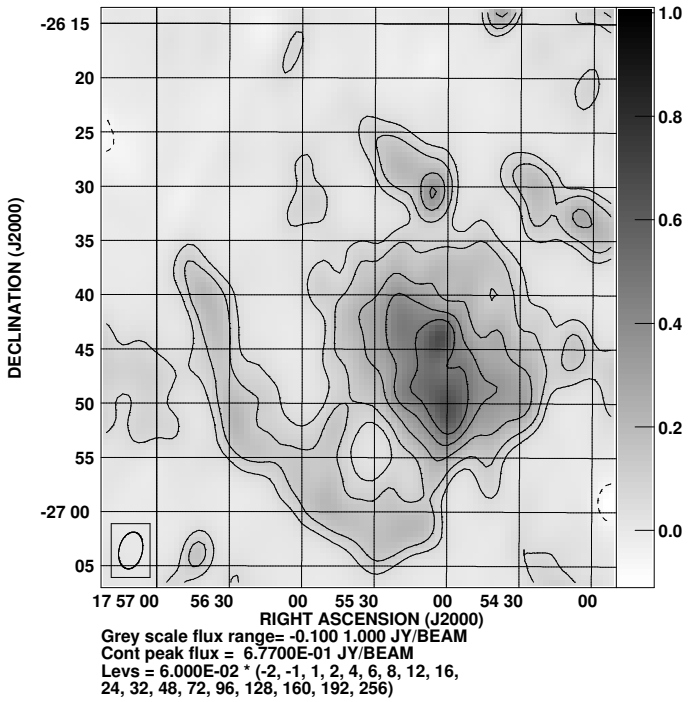

Figure 3.4: GMRT low resolution image of G3.1−0.6 at 330 MHz. The resolution is $3.4' \times 2.1'$ along PA -13° and the RMS noise in the map is 12 mJy/beam.

structure shows about 20% polarisation in the NVSS map. The diffuse emission at the western part of the remnant also has a steep spectral index. We have examined the 8.35 GHz NRAO single dish map (Langston et al. 2000) of this region. We could not identify it, and place an upper limit of 2 Jy for this object. Hence, the spectral index of the object is steeper than −0.64. We summarise the observed parameters of G3.1−0.6 in Table 3.2. It should be noted that the co-ordinate of this object in Table 3.2 is different from (Gray 1994c). GMRT maps indicate that the centre of this object is located further south of the co-ordinate given for this object in Gray (1994c). From Table 3.2, its estimated Galactic Co-ordinate is, l=3.1°, b=−0.7°. However, as the object has already been designated as G3.1−0.6, following the IAU convention, we do not intend to rename it and will continue to use its name as G3.1−0.6 in the rest of this chapter.

Table 3.2: Observed parameters of G3.1−0.6 and G356.8−0.0

Object name (G$l\pm b$)	RA (J2000)	Dec (J2000)	Size ($'$)	Type	S_{843MHz} (Jy)	S_{330MHz} (Jy)	Spectral index
G3.1−0.6	17 55 40	−26 39 30	28×49	Shell	6.5	14 ±3	≤ -0.64
G356.8−0.0	17 38 00	−31 37 41	52×72(?)	Shell	–	30	≤ -0.34

3.3.2 Field II:

This region has been investigated previously by Gray (1994c) using the MOST at 843 MHz. Three candidate SNRs, G356.3−0.3, G356.6+0.1 and G357.1−0.2 were reported and the MOST image of these objects are shown in Fig. 3.5. This field is much more complex than Field I and further there are a number of complications due to the proximity of the 'Tornado nebula' which has a large flux density. The GMRT low resolution map of this field at 330 MHz is shown in Fig. 3.6. The prominent features of this field are (a) the strong source at the northeastern edge of the map which is identified with the Tornado Nebula, (b) a strong unresolved source G356.9+0.1 (RA=17h37m44.0s, Dec=$-31^\circ31'14''$ (J2000)) which with higher resolution has three components (Fig. 3.10) and shows a non-thermal spectrum (Table 3.5), indicative of a background extragalactic source and (c) two extended objects which have considerable fine structure. The large extended emission is located to the south of the extragalactic source G356.9+0.1, which appears to be curved has been detected for the first time. The other extended emission to the east of the extragalactic source coincides with the MOST candidate SNR G357.1−0.2, though the extent of its emission at 330 MHz is larger than that in the MOST maps. This second extended source almost touches the southern emission and they appear to be part of a single large shell, the northern part of which is missing.

It should be noted that interferometric observations which lack zero and short-spacings, can preferentially pick-up small scale structures from extended Galactic emission and hence can show structures in the map which are not genuine entities. These small scale

variations in the Galactic background emission generally create structures with both positive and negative flux densities in the map plane, which finally increases the RMS noise in the map. However, in Fig. 3.6, the first contour level is 0.1 Jy/beam, 5 times higher than the RMS noise and at that level, no extended region of negative flux density can be seen. Therefore, we believe that the two extended objects seen in our map are genuine in nature.

In the absence of the northern part of the shell, we can only speculate about its actual extent to the north. If the conceived shell is formed by the line joining G357.1−0.2 with G356.6+0.1, then, the shell has a size of $52' \times 55'$. However, it appears to us that the northern extent of the shell is upto the object seen at RA=17h38m00s, Dec=$-31^{\circ}05'$, and consequently the shell has a size of $52' \times 72'$ centred at G356.8−0.0. We designate this conceived shell by its galactic co-ordinate of G356.8−0.0. The flux density calculated over the two extended objects at 330 MHz is 30Jy. However, this should be taken with caution since we are likely to underestimate its flux density due to missing short spacings.

A composite of the MOST maps within this field is given in Fig. 3.5, along with the NVSS map of this region (Fig. 3.7). The MOST suffer from zero-spacing problems for objects larger than half a degree which, coupled with further dynamic range limitations due to the nearby strong source (Tornado nebula) could have resulted in their inability to image the large extended structure (G356.8−0.0) and to identify smaller scale structures within the extended emission as separate SNR candidates (equivalent to a 'high frequency spatial filtering'). The NVSS map of the field has serious short spacing problems and it is not surprising that the extended emission is not seen in it. Single dish maps at high frequencies do not have this problem, but since the extended emission has low surface brightness, it is often difficult to detect it. The extended emission is not seen in the 8.35 and 14.35 GHz NRAO single dish maps (Langston et al. 2000), from which we set an upper limit on the flux density of 9.4 Jy at 14.35 GHz and 10 Jy at

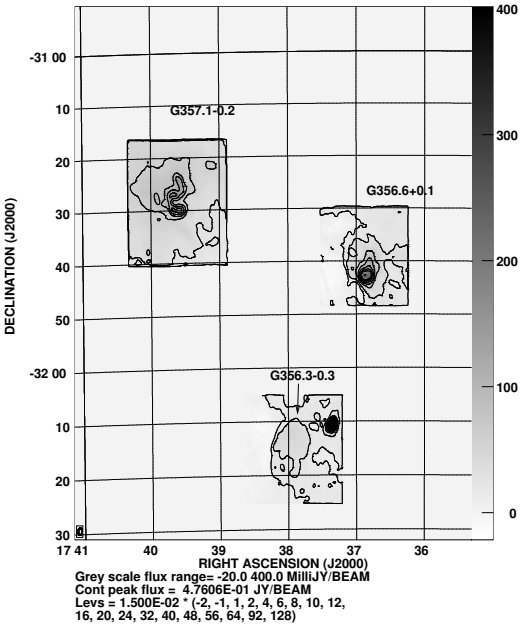

Figure 3.5: A composite of the MOST 843 MHz maps of the 3 suspected SNRs G356.3−0.3, G356.6+0.1 and G357.1−0.2 at the original resolution of $1.3' \times 0.7'$ along PA 0.1°. The RMS noise in the map is $\approx$ 6 mJy/beam.

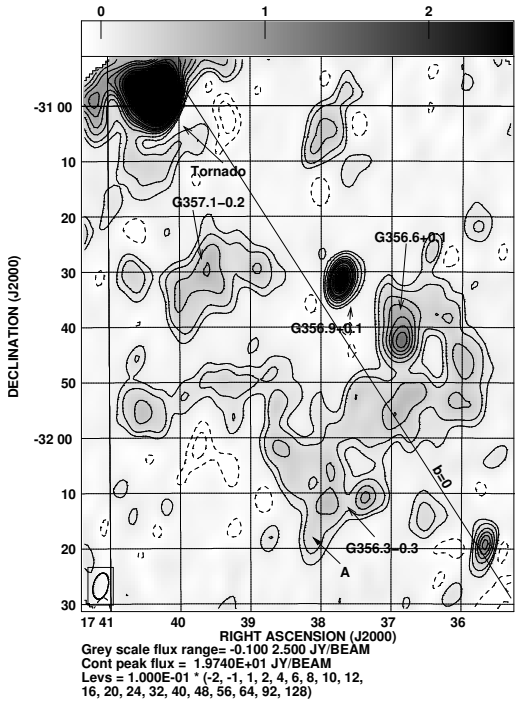

Figure 3.6: GMRT low resolution map of the Field II at 330 MHz. The resolution is $4.8' \times 2.7'$ along PA -14° and the RMS noise in the map is 20 mJy/beam.

8.35 GHz. It should be noted that Langston et al. used a median filter of size 67′ to remove the extended background emission. However, since the area enclosed by the shell is significantly smaller than the filter diameter, removing the extended background is not expected to cause any appreciable underestimation of the flux density. If we combine the 330 MHz results with the upper limits from Langston et al., we find that the spectral index of the shell like structure is steeper than −0.34. Based on the above, we suggest that G356.8−0.0 could be an old SNR shell, which has started breaking up near G357.1−0.2, possibly due to interaction with the surrounding ISM.

The observed parameters of this shell have been summarised in Table 3.2. We compare the observed properties of these sources at different frequencies in the discussion below.

(i) G356.3−0.3:

In the MOST image, this SNR candidate appears as a circular object of size 10′. However, the GMRT map as shown in Fig. 3.8, there is no discrete source at this position. In the GMRT low resolution map (Fig. 3.6), this object is located on the extended structure, which we have interpreted as part of a larger shell. In the NVSS map, a small partial shell structure can be identified (not clear in Fig. 3.7) near the eastern boundary of G356.3−0.3 (RA=17h38m and Dec=−32°15′), which also coincides with the southern edge of G356.8−0.0 (feature marked 'A' in Fig. 3.6) in the 330 MHz map. We suggest that the partial shell structure in the NVSS map is due to a lack of short *uv*-spacings, which results in a 'high frequency spatial filtering' of the feature 'A' shown in Fig. 3.6. Based on the above, we conclude that G356.3−0.3 is likely to be part of the larger shell (G356.8−0.0) like structure. The total flux density calculated for this object from the MOST image after background subtraction is 2 Jy. From the same region, the estimated flux density at 330 MHz (Fig. 3.6) is ≈1.5 Jy, and is 0.1 ± 0.02 Jy at 1.4 GHz (Fig. 3.7).

(ii) G356.6+0.1 :

This suspected SNR candidate (Gray 1994c) appears as a featureless elliptical emission

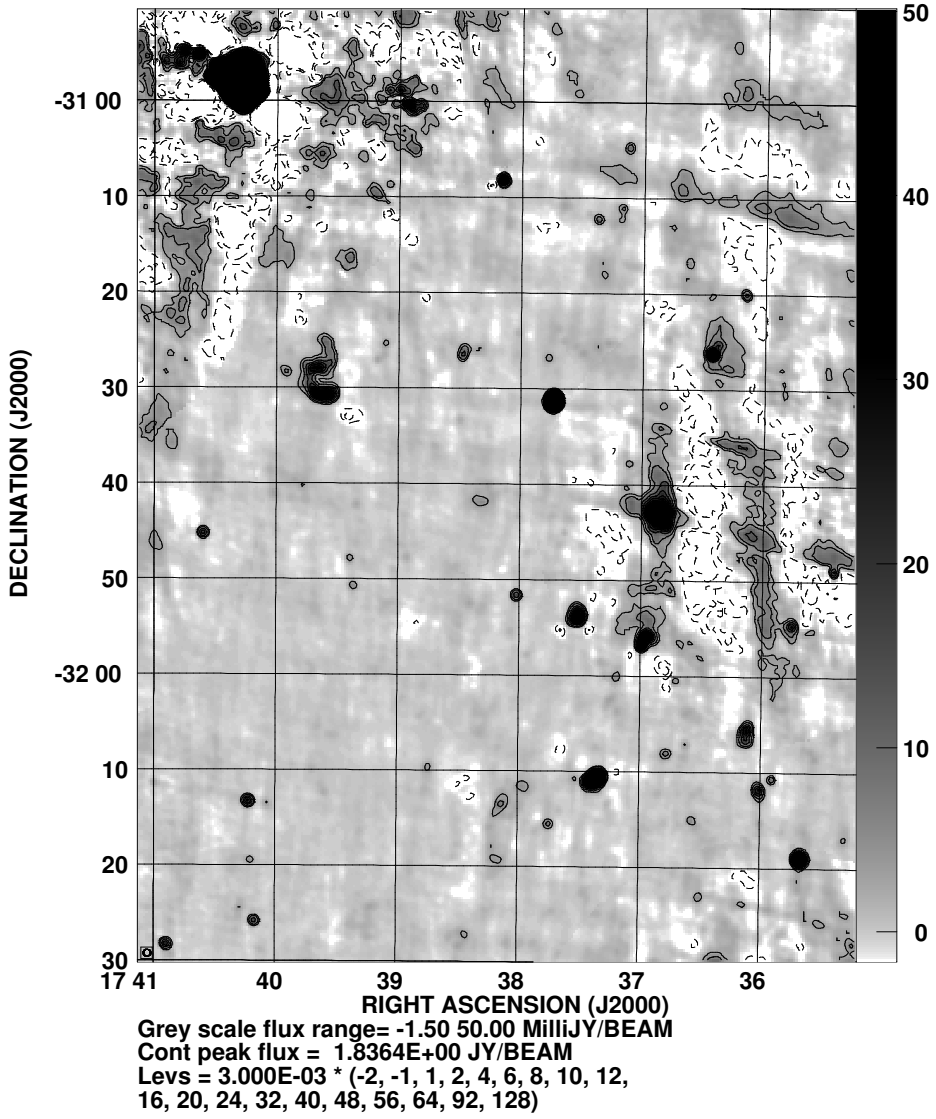

Figure 3.7: NVSS 1.4 GHz map of the Field II at the original resolution of 45″. The RMS noise in the map is 0.8 mJy/beam.

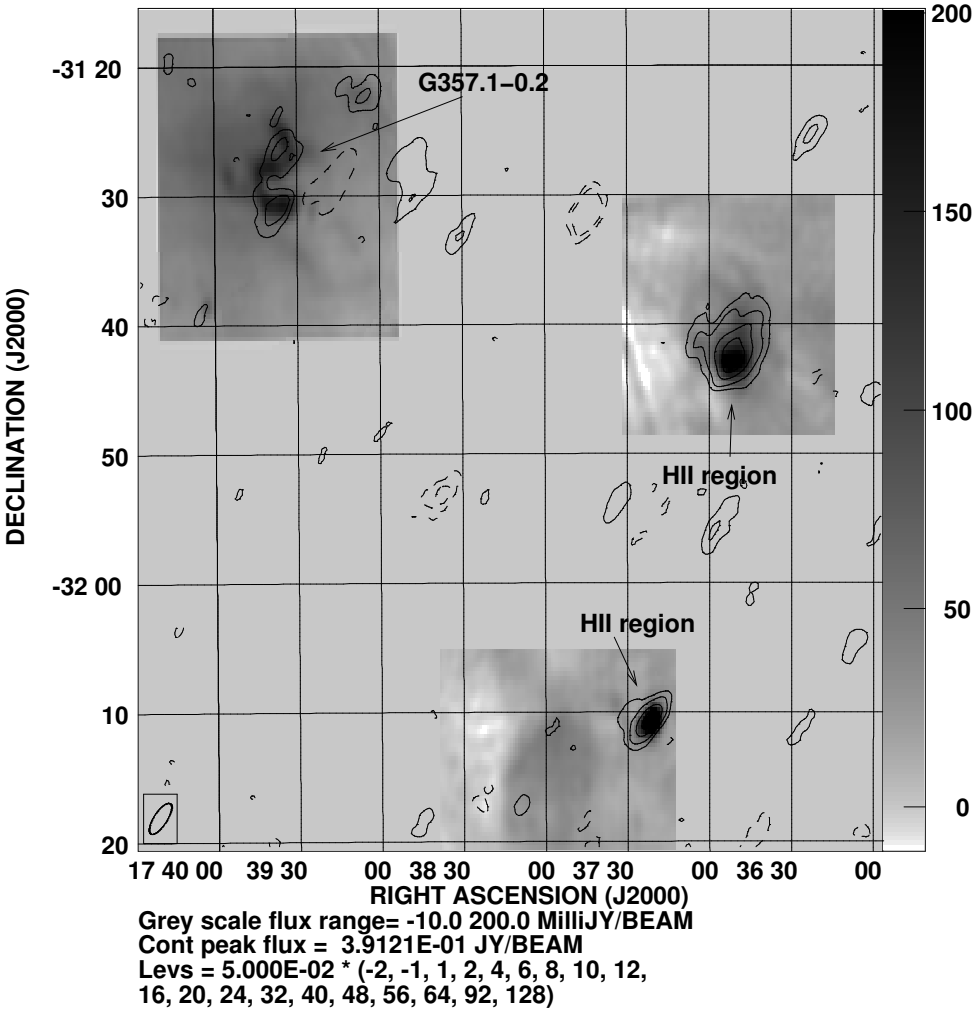

Figure 3.8: GMRT 330 MHz map of the Field II in contour overlaid on the MOST 843 MHz Gray scale map of the same region. The MOST Gray scale map has been presented at the original resolution of $1.3' \times 0.7'$ along PA 0.1°. The GMRT 330 MHz contour map has a resolution of $2.8' \times 1.0'$ along PA -33° and the RMS noise in the map is 17 mJy/beam. The GMRT map was made by first subtracting the CLEAN components of the compact sources from the *uv* data and a lower *uv* cutoff of 230 λ was applied to the data before Fourier Transforming and CLEANING.

with a central compact HII region in the MOST image. As the extended emission surrounding the HII region is not visible in the IRAS images, this was classified as an SNR candidate. The GMRT image also is similar but the extended emission seems associated with the large shell like structure discussed before. After excluding the HII region, we estimate a flux density of 2.2 Jy for this source at 330 MHz. From the MOST image, the corresponding flux density is 1.7 Jy. In NVSS, the central HII region is visible, but the extended emission has stripes due to the lack of shorter *uv* spacing required to image it. The flux density of the central HII region as estimated from the NVSS, the MOST and the GMRT image do agree to within $\pm$ 20%, the estimated flux density being 1.2$\pm$0.2 Jy at 330 MHz. As the extended emission around the HII region has a non-thermal spectrum and appears to be part of the large shell like structure G356.8$-$0.0, we suggest it to be a smaller-scale structure within G356.8$-$0.0 and not a discrete SNR. The central HII region can well be an unrelated background object.

(iii) G357.1$-$0.2:

In the 843 MHz map, G357.1$-$0.2 shows a bi-annular structure of a few arc-minutes with a halo of emission surrounding it. In the 330 MHz low resolution map shown in Fig. 3.6, the bi-annular structure is not distinguishable, but there is an extended emission of size $15'$ at the same place. To search for this structure, we first subtracted the strong sources in the region from the *uv* data and resolved out the extended emission by using a lower *uv* cutoff of 230 λ, while re-imaging the region. The resultant contour map is shown in Fig. 3.8, where, the MOST map has been overlaid on it in gray scale. There is indeed seen some emission at the position of the bi-annular structure of the MOST image (The nearby negative is the result of missing zero-spacing flux density resulted from our attempt of resolving out the extended emission of size $15'$). From the GMRT image, we estimate a flux density of 0.49 $\pm$ 0.15 Jy for this object. From the MOST image, we estimate a flux density of 1.2 Jy at 843 MHz for this object after background subtraction.

As noted by (Gray 1994c), this region of the MOST image is suspected to be affected by the base-level fluctuations caused by the nearby strong source (Tornado nebula). As a check, we have estimated the flux density of the surrounding 15′ halo region from their 843 MHz map to be about 10 Jy. But, from the GMRT image, the estimated flux density is only 5.0±1.0 Jy at 330 MHz (Fig. 3.6). Further, the upper limit of the flux density measured from the 8.35 GHz NRAO single dish map (Langston et al. 2000) is 1.0 Jy for this region. The above measurements clearly indicate that there is a problem in explaining the flux density as measured at 843 MHz, as, neither an HII region (any significant free-free absorption at 330 MHz can be ruled out) nor a mixture of thermal and non-thermal emission can explain the estimated flux density at 843 MHz. Therefore, it seems that the flux density measurements of this region from the MOST image is badly affected by the background uncertainty and hence we have not used the flux density of 1.2 Jy calculated for the bi-annular structure at 843 MHz any further in this chapter.

From our HI data of this source we have made a continuum map using the line free channels (Fig. 3.9), which gives us a flux density of 0.67±0.1 Jy for this object at 1.4 GHz. From the NVSS map at 1.4 GHz, the estimated flux density is 0.45±0.03 Jy. To resolve this difference, we re-mapped the same region by using the calibrated *uv* data of the NVSS (available in the web). The estimated flux density for this object after applying the primary beam correction is found to be 0.7 ± 0.1 Jy, in agreement with our measurement.

This source has also been observed by Gray (1996) using the VLA at 5 GHz (DnC array) and 1.4 GHz (CnB array). This object shows several filamentary structures. Between 5 and 1.4 GHz, most parts of the structure show a spectral index of −0.5, though, there is a variation of spectral index from −0.3 to −0.6. The structures seen at 5 GHz are highly polarised and display a polarisation fraction of upto 60% (Gray 1996). Therefore, the emission mechanism from the source is synchrotron in origin. We further discuss its properties in the following sections.

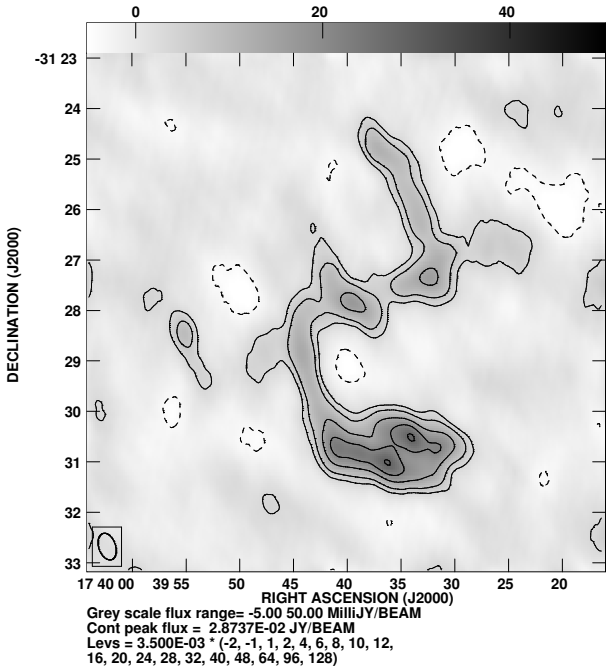

Figure 3.9: GMRT 21 cm map of G357.1−0.2. The resolution is $33'' \times 20''$ along PA 19° and the RMS noise is 1.5 mJy/beam.

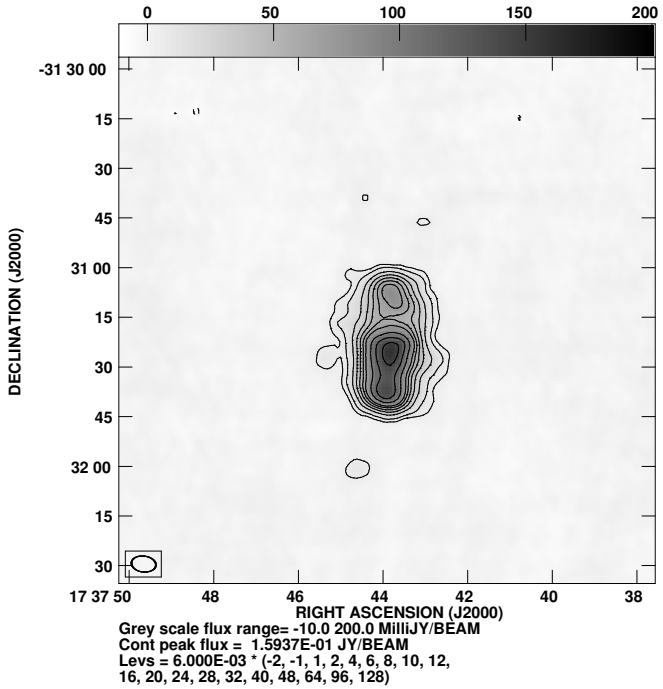

Figure 3.10: GMRT continuum map of G356.9+0.1 at 21 cm. The resolution is $7.4'' \times 4.8''$ along PA 83° and the RMS noise is 1.7 mJy/beam.

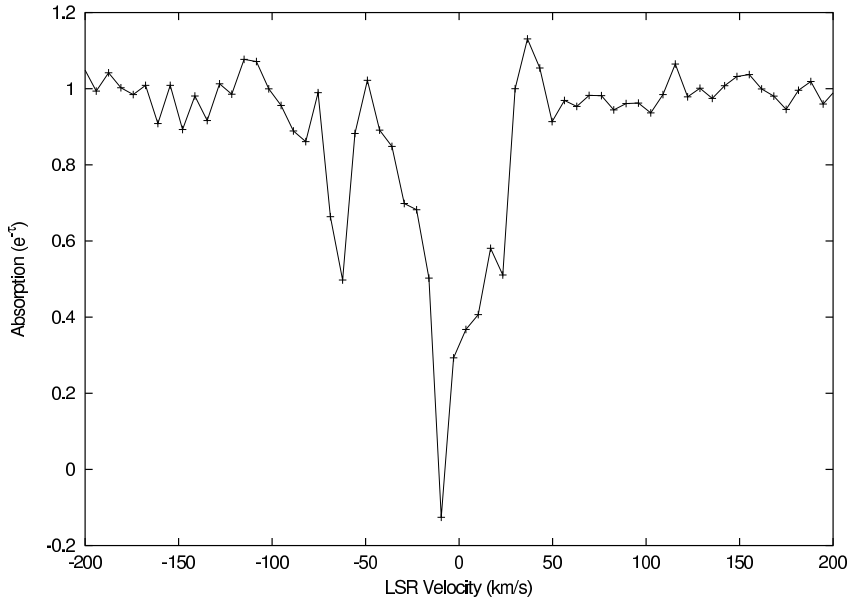

Figure 3.11: HI absorption spectra towards G357.1−0.2. The spectra was made by integrating over a rectangular region of the line maps, where strongest continuum emission from the source is observed.

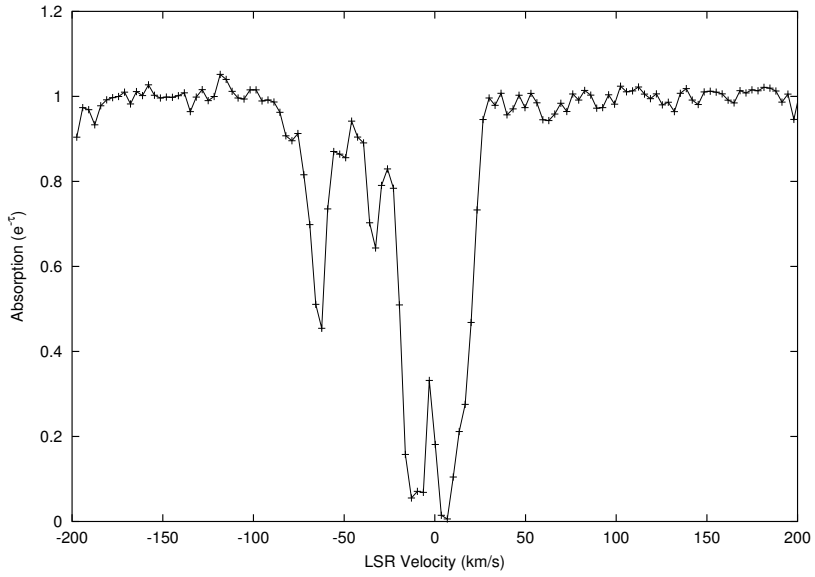

Figure 3.12: HI absorption towards G356.9+0.1

3.3.3 HI absorption towards G357.1−0.2 :

In Fig. 3.11 is shown the normalised spectrum of the source, where, the y-axis represents the estimated absorption ($e^{-\tau}$, where, τ is the optical depth). Within $\pm$20 km s^{-1} of the LSR velocity, the RMS noise is 0.07 of the absorption profile (i.e., $e^{-\tau}$), but, for the frequency channels located outside the above LSR velocity range, the RMS noise is 0.035. The HI emission from the Galactic plane increases the system temperature for the frequency channels located within $\pm$20 km s^{-1} of the LSR velocity, causing an increase in the RMS noise for the frequency channels located in the above range. In our map of G357.1−0.2, HI emission was also found to increase the confusion limit for the frequency channels located within the above velocity range. To reduce the effect of HI emission from the extended structure along the line-of-sight gas, we applied a lower *uv* cutoff of 500 λ before imaging the spectral-line *uv* data. We have also tried to identify any small scale HI emission associated with this source from our line maps. However, no evidence was found in this regard. The source G357.1−0.2 is seen in absorption near the LSR velocity −10 and −62 km s^{-1}. The absorption near the −62 km s^{-1} arises from the '3 kpc arm' (for which $V_{LSR} \approx -60$ km s^{-1}) indicating that this source is located at least at a distance of more than 6 kpc from us (the GC is $\approx$ 8.5 kpc away from us). The absorption near the −10 km s^{-1} is quite narrow with the velocity width (FWHM) $\sim$ 28 km s^{-1} (Fig. 3.11). For comparison, we have also observed the compact object G356.9+0.1 located near the centre of our 330 MHz map, in HI absorption at 1420 MHz. This object appears to have three components in our high resolution 1.4 GHz continuum map (Fig. 3.10) and is likely to be an extragalactic source. The absorption spectrum towards this source is shown in Fig. 3.12 (the RMS noise in the spectra is 0.02 for the frequency channels located within $-20 \geq V_{LSR} \leq 20$, and is $\approx$0.01 outside this range.). As expected, this object is seen in absorption against the '3 kpc arm'. At LSR velocity of −33 km s^{-1}, one more absorption line can be seen against this source which

is not observed towards G357.1−0.2. The HI absorption profile shows a large velocity width (FWHM ∼40km s^{-1}) near the LSR velocity of 0 km s^{-1} towards this object.

Similar broad absorption features have been observed for the extragalactic sources seen through the Galactic Centre region, e.g., 1748−253, G0.537+0.26 (Dickey et al. 1983) and G359.87+0.18 (Lazio et al. 1999), which are believed to be caused by an anomalous velocity cloud located behind the Galactic Centre. As the absorption FWHM towards G357.1−0.2 is significantly lower as compared to G356.9+0.1, we think that this object is likely to be a galactic source. However, the full width of absorption towards this object is quite similar to G356.9+0.1, which suggests that G357.1−0.2 may be embedded within the positive velocity cloud located behind the Galactic Centre, which gives rise to much deeper absorption profile towards G356.9+0.1 because of the longer path length towards this extragalactic source.

3.3.4 Field III:

This field contains the object known as the Tornado nebula whose peculiar morphology can be seen in the 330 MHz GMRT map of this object shown in Fig. 3.13.

It has a bright core like structure (marked ‘A’), and is surrounded by emission, which is more prominent towards east. Two filament like structures (marked ‘B’ and ‘C’) are seen east of the core. Two more linear structures (marked ‘D’ and ‘E’) are seen towards the eastern side of these two filamentary structures. Diffuse emission appears to “break-out” towards the east (linear extent ∼6′), with a position angle of about 65° from North, and its direction is the same as the linear structures ‘D’ and ‘E’, suggesting that these structures act like a wall of a chimney to define the direction of any possible flow of material from the core to outside region. For comparison, we also show the 1.4 GHz map of this object (Fig. 3.14) made with VLA (Shaver et al. 1985), which is convolved to the same resolution as in Fig. 3.13. The two maps agree in fine details pretty well. However, the small diameter source (marked ‘F’ in Fig. 3.14) seen at 1.4 GHz map is

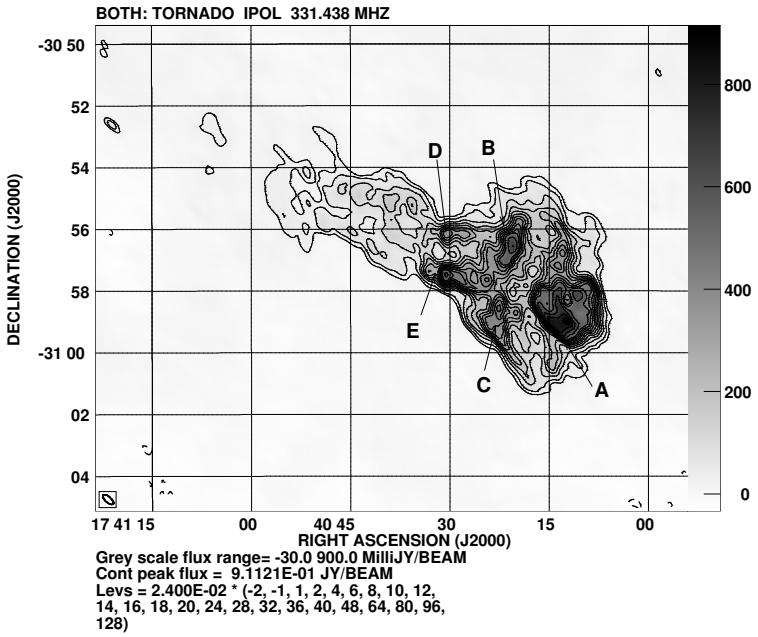

Figure 3.13: 330 MHz GMRT map of the Tornado nebula with a resolution of $26'' \times 11''$ and position angle 47.7°. The rms noise is 5 mJy/Beam.

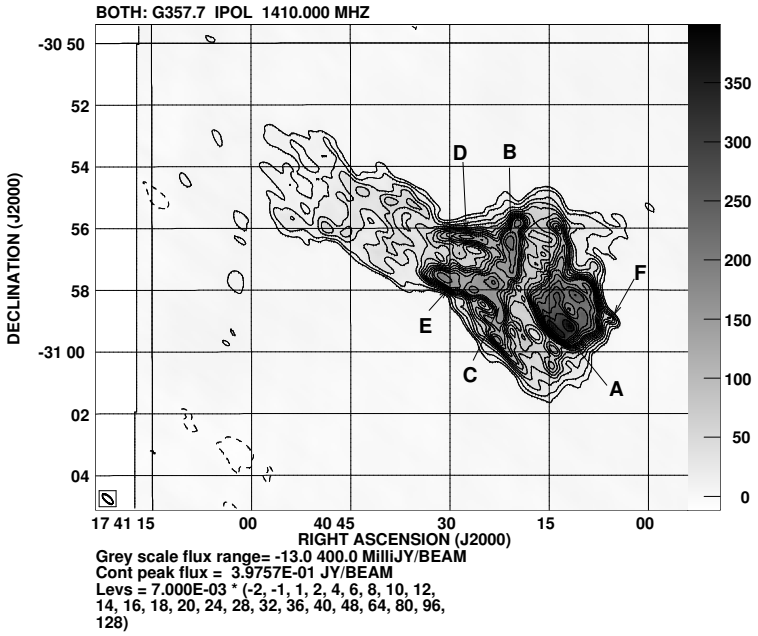

Figure 3.14: 1.4 GHz VLA map of the Tornado nebula (Shaver et al. 1985) with a resolution of $26'' \times 11''$ and position angle 47.7°. The rms noise is 1.5 mJy/Beam.

not seen in the 330 MHz.

The flux density of the Tornado nebula is estimated to be 81 $\pm$ 12 Jy at 330 MHz, and 33 Jy at 1.4 GHz, implying an average spectral index of -0.63 ± 0.1 between 1.4 and 330 MHz, which is consistent with previous estimates of -0.53 ± 0.02 (Shaver et al. 1985).

The small diameter source near the core of the nebula has a flux density of 0.030 Jy at 1.4 GHz (Shaver et al. 1985). However, its non-detection at 330 MHz and a 1 σ upper limit on its flux density of 0.012 Jy indicates that the emission from this object to turn over at frequencies below 1.4GHz.

We have tried to identify any spatial variation of spectral index within this nebula and used two different procedures to identify these variations.

(i) To highlight spectral variation of the small scale filamentary structures with larger surface brightness, we follow a procedure called Spectral Tomography that has been applied to analyse the spectra of Tycho's SNR (Katz-Stone et al. 2000). Mathematically, a set of images $M_t(\alpha_t)$ is constructed where

$$M_t(\alpha_t) \equiv M_{1.4} - M_{0.33}\left(\frac{\nu_{1.4}}{\nu_{0.33}}\right)^{\alpha_t}$$

where $M_{1.4,0.33}$ are the images at 1.4 and 0.33 GHz. If a component has spectral index α_t, it will disappear with respect to its surroundings in image M_t. If a component has spectral index greater than α_t, it will be oversubtracted and have negative brightness. If a component has spectral index less than α_t, it will be undersubtracted and have positive brightness. Since this source has an average spectral index of -0.63 between 1.4 GHz and 330 MHz, we call features with spectral index steeper than -0.73 as steep and flatter than -0.5 as flat. Two such figures from the sets of images with spectral index steeper than -0.73 and flatter than -0.5 are shown Fig. 3.15 and Fig. 3.16 respectively.

We notice that the filamentary structure D and part of E has spectral index flatter than -0.5. The eastern part of B has a flatter spectral index, while the western part of it has

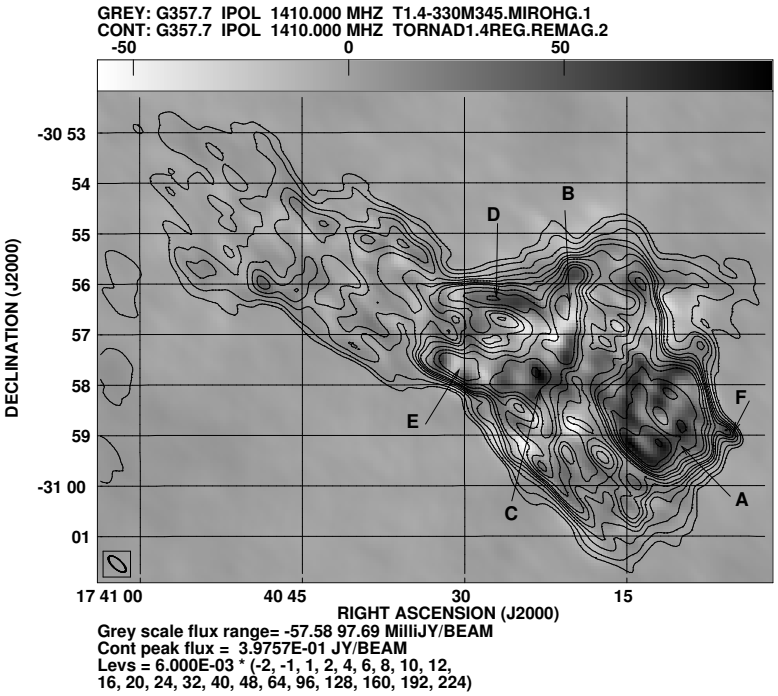

Figure 3.15: A representative spectral tomography image of the Tornado nebula between 1.4 GHz and 330 MHz. Bright areas have radio spectral indices steeper than -0.73. The contour map is the 1.4 GHz continuum map shown in Fig. 3.14

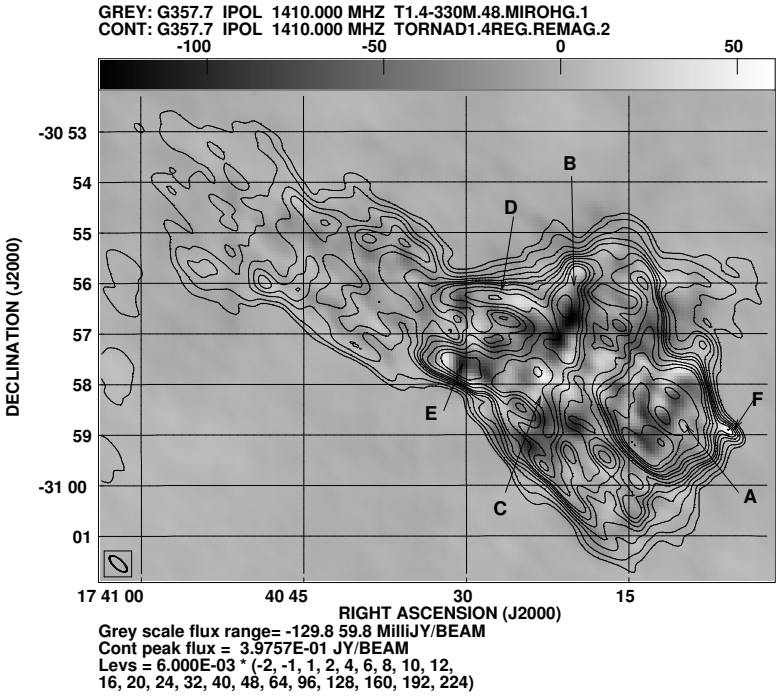

Figure 3.16: Another representative spectral tomography image between 1.4 GHz and 330 MHz. In this image, intensity scale is reversed so that bright areas have spectral indices flatter than 0.5 and the dark areas steeper indices. The contour map is the 1.4 GHz continuum map shown in Fig. 3.14

a steeper spectral index.

(ii) Interferometer maps made with different uv-coverage often suffer from base-level difference. This is essentially caused by the extended background emission to be improperly represented due to lack of zero spacing flux densities. The uv-coverage of the VLA 1.4 GHz map (Shaver et al. 1985) is different from that of the GMRT map at 330 MHz. Since part of the diffuse emission has brightness quite comparable to the background, determination of spectral indices of extended emission of the nebula by direct division of the maps can cause significant error. To avoid this problem, a standard procedure is to plot the flux densities of each pixel from one map against the other, and a straight line fit can then account for the difference in background level (also known as the T-T plot).

In Fig. 3.17, we show such plots for 4 different parts of the nebula. The estimated spectral indices of these regions are within 0.1 of the mean spectral index of the nebula (-0.62), thereby indicating the large scale emission to have similar spectral indices across the nebula. The spectral index of the core 'A' appears to be flatter than (2 σ significance) the average spectral index of the nebula.

3.3.4.1 HI absorption spectrum towards Tornado nebula and G356.9+0.1

In Fig. 3.18 is shown the normalised HI spectrum weighted by the square of the continuum to maximise the signal to noise ratio in the spectrum. Within $\pm$20 km s^{-1} of the LSR velocity, the RMS noise in the absorption profile (i.e., $e^{-\tau}$) is 0.008, but, for the frequency channels located outside the above LSR velocity range, the RMS noise is 0.005. We note that the systematics in the bandshape can also be of similar magnitude and features with absorption depth $\leq$0.02 occupying a single frequency channel may not be real features. In order to reduce the confusion due to large scale HI emission along our line of sight, part of which gets resolved out due to lack of short spacings of the interferometer, we have rejected *uv*-data with *uv*-distance less than 500 λ before

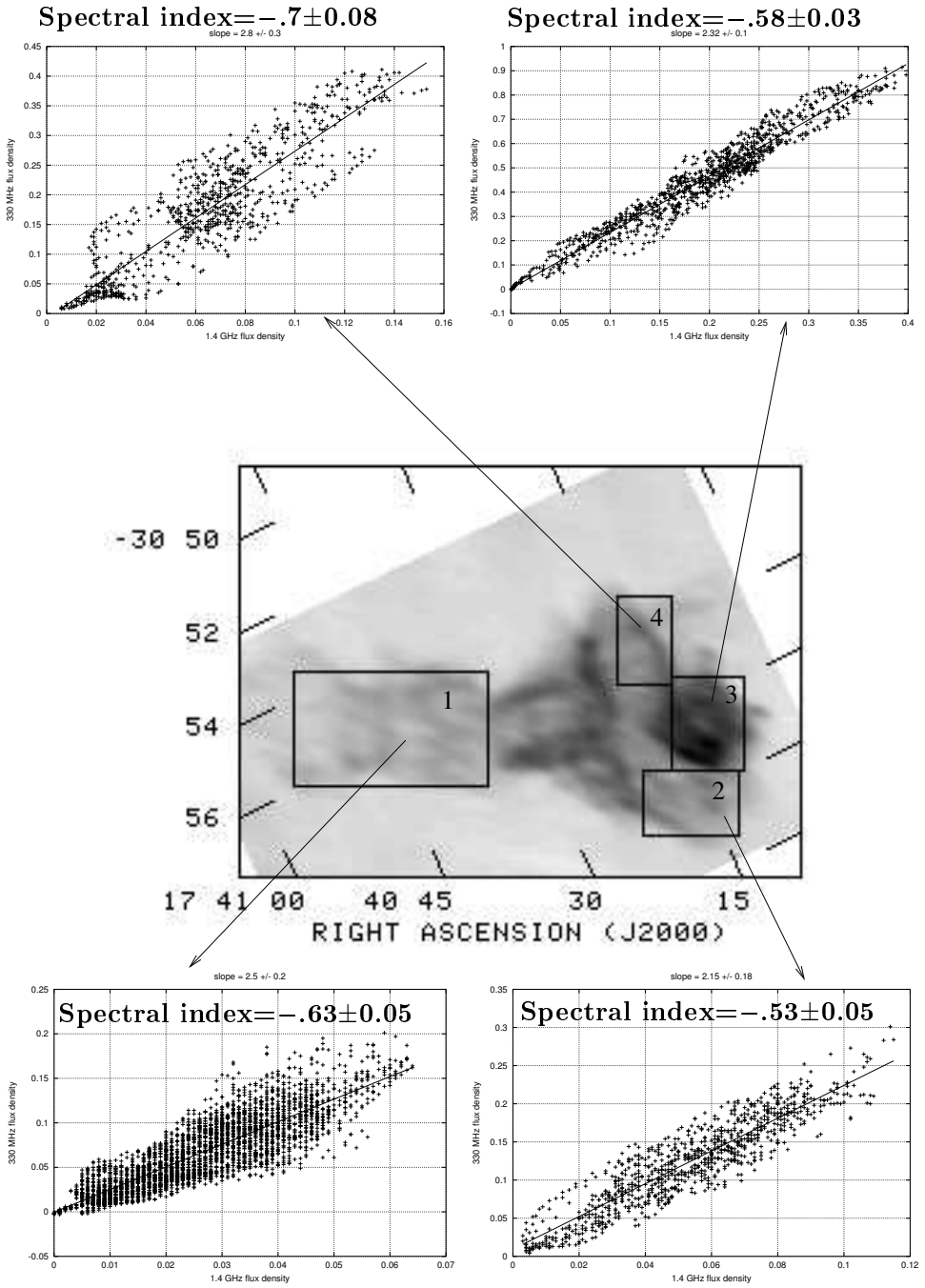

Figure 3.17: Spectral indices of some of the extended emission features in the Tornado nebula. The plots show the flux densities of each pixel from 330 MHz map (y-axis) map against the 1.4 GHz map (x-axis) for parts of the nebula as shown by arrows. The spectral indices have been estimated from the slope of straight line fit to the data points shown in the plots.

imaging.

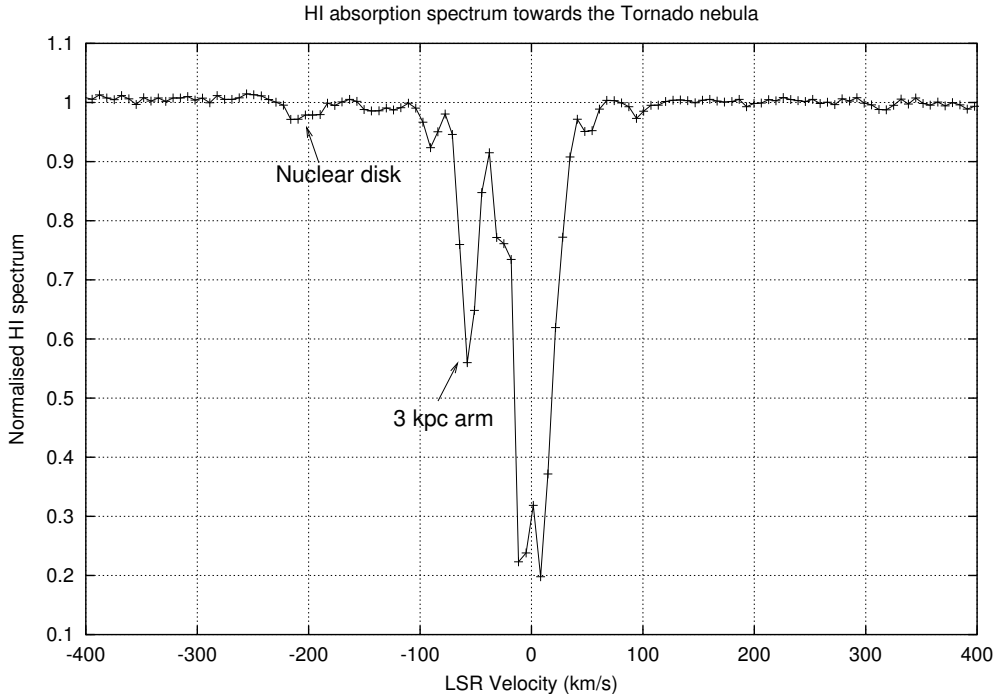

Figure 3.18: HI absorption spectrum towards the Tornado nebula. The absorption profile across the object have been averaged after applying a weighting factor proportional to the square of the continuum intensity, which maximises the signal to noise ratio in the spectrum. The rms noise in the spectrum with $|$ LSR velocity $| > 20$ km s^{-1} is 0.005.

Several absorption lines are identified in its spectrum (Fig. 3.18). The prominent absorption near '0' km s^{-1} is due to the line of sight gas. When 'l' is close to zero, there is velocity crowding near '0' km s^{-1} of velocity. The FWHM of this absorption profile is $\sim$40 km s^{-1}. At positive velocities, there are two weak absorption feature, with one at 50 km s^{-1} and the other at 94 km s^{-1}. At negative velocities, the prominent absorption feature at -60 km s^{-1} is due to the 3 kpc arm, which has a velocity close to the velocity observed at this longitude. The absorption feature at -93 km s^{-1} is quite narrow. The other high negative velocity feature is observed at a velocity of -200 km s^{-1} which has a line-width of about 40 km s^{-1}. The HI absorption spectrum towards the extragalactic source G356.9+0.1 is shown in Fig. 3.19. Within $\pm$20 km s^{-1} of the LSR velocity, the RMS noise in the absorption profile (i.e., $e^{-\tau}$) is 0.013, but for the

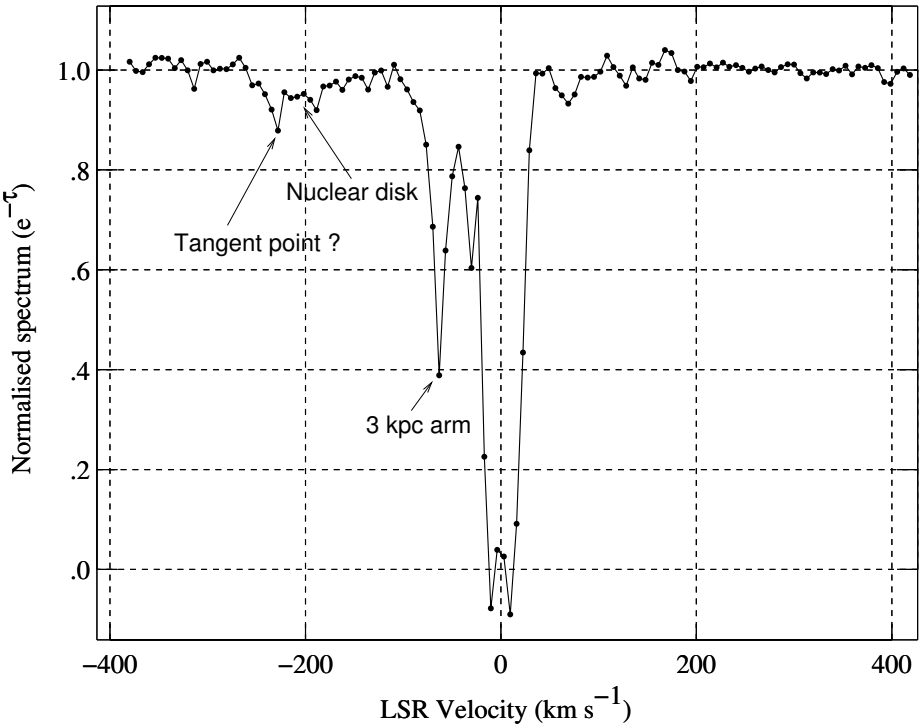

Figure 3.19: HI absorption spectrum towards the suspected extragalactic source G356.9+0.1. The rms noise in the spectrum with $|\text{LSR velocity}| > 20$ km s^{-1} is 0.008.

frequency channels located outside the above LSR velocity range, the RMS noise is 0.008. The HI absorption profile is quite similar to what is seen towards the Tornado nebula, with absorption at negative velocities of -63 km s^{-1} due to the 3 kpc arm, and wide absorption line near -200 km s^{-1}. The absorption at high negative velocities appear to continue up to -250 km s^{-1}, whereas the HI absorption towards the Tornado nebula is observed up to -223 km s^{-1}.

3.4 Discussions:

3.4.1 G3.1−0.6 (Field I):

3.4.1.1 Distance:

From the present observations, only the Σ-D relation can be used to estimate its distance. We used the modified Σ-D relation ($\Sigma_{1\ \mathrm{GHz}} = 2.07 \times 10^{-17} \times \mathrm{D}^{-2.38}$ W.m^{-2}.Hz^{-1}.sr^{-1}) by Case & Bhattacharya (1998), which is expected to yield distance to individual SNRs with an error ∼40%. Using a flux density of 6 Jy for this object at 1 GHz and a diameter of 39′, we estimate a distance of 7.7 kpc for this object, which indicates that it can even be located near the Galactic Centre region.

It should be noted that the Σ-D relation is essentially derived by assuming the environments of the SNRs into which expansion occurs are similar. It is believed that the Σ-D relation overestimates the diameter of SNRs located at higher Galactic latitudes (Caswell & Lerche 1979). This phenomenon is thought to be related with intrinsic decrease of the surface brightness of the SNRs due to a lowering of magnetic field at higher Galactic latitudes. However, the magnetic field in the GC region is expected to be much higher than the Galactic disk, which can result in a higher intrinsic surface brightness of the SNRs in the region. Hence, the use of Σ-D relation to estimate the distance or linear-diameter of the SNRs located in the GC region can result in underestimating these parameters. For example, the distance estimated by using the Σ-D relation (Case & Bhattacharya 1998) for the SNR Sgr A East (G0.0+0.0) is 3.3 kpc. However, it is thought to be actually located behind the GC (i.e., at a distance of ≥ 8.5 kpc) (Pedlar et al. 1989).

3.4.1.2 Morphology:

G3.1−0.6 shows two ring like structure in our high resolution map with the smaller ring being located towards the south. Possible explanations of the observed morphology are (a) the SNR itself is the combination of two separate objects, (b) this morphology could

be a result of the expansion of the supernova blast-wave into a cavity having a bi-annular structure created by stellar winds of the progenitor system, (c) the ISM in which the SNR expands has structures which are responsible for such a morphology.

Given the high density of SNRs in the Galactic Centre region, the suggestion that two SNRs lie close to each other is not unreasonable. There are at present 15 known SNRs within the central 50 square degree area of the Galactic Centre region and the probability of the centre of one the SNRs to be within 0.5° of another is $\sim$7.5%, which is not negligible. This hypothesis can be discarded if the two shells can be shown to have different distances, ages or spectral index. The spectral indices estimated from the 330 MHz and the 843 MHz map for the two shells are not very different and we cannot rule out the two SNR hypothesis, though, we prefer the case of an anisotropic ISM as described below.

It is now known that the slow wind from the red super-giant star (RSG) possess axial symmetry (Blondin et al. 1996). Manchester (1987) proposed that expansion of an SNR into such a medium can produce a double ringed morphology. Gaensler et al. (1998) have shown for the SNR G296.8$-$0.3, the asymmetric cavity as created by the RSG wind of the progenitor star has a typical size of $\sim$5 pc. However, if G3.1$-$0.6 is placed at a distance of 7 kpc, it would have a linear size of 80 pc. Therefore, RSG wind can be ruled out as one of the possible reason for the double ring structure.

Finally, we consider the case of an anisotropic ISM being responsible for the shape of the SNR. It has been argued that the SNRs G166.0+04.3 (VRO 42.05.01) (Pineault et al. 1987), G350.0$-$02.0 (Gaensler et al. 1998) and G296.8$-$0.3 (Gaensler et al. 1998) represents the case of a supernova shock re-energising a tunnel and then propagating on to the other side to form a second shell. We find that the morphology of the SNR G3.1$-$0.6 can also be explained on the basis of the above model. In order to explain the model, we depict the main two ring structures in a schematic diagram as shown in Fig. 3.20.

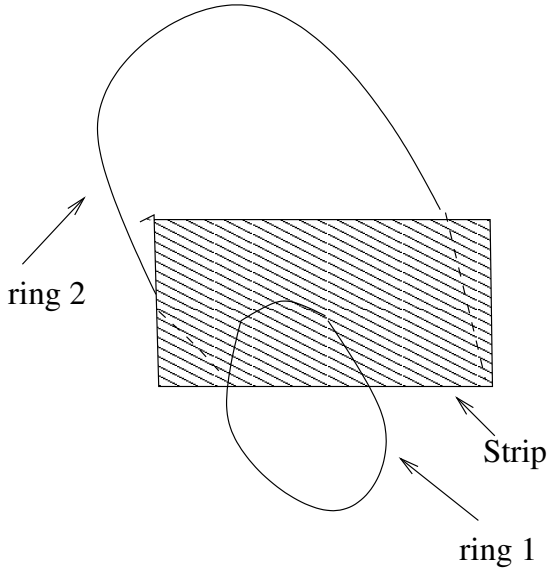

Figure 3.20: A sketch of the morphology of the SNR G3.1−0.6

(i) There is a smaller ring of emission ('ring 1'), which in the absence of the other structures would appear as a typical SNR (feature B in Fig. 3.3).

(ii) A strip of emission running west from the eastern side of the SNR (feature marked C and the weak emission towards the eastern edge of Fig. 3.3) which, we suggest corresponds to a tunnel of much lower density. On encountering such a region, an expanding shock will energise it, rapidly propagating both across the tube and up and down its length. As this process continues, electrons in the walls are shock-accelerated and emit synchrotron radiation (Pineault et al. 1987) giving a linear structure as observed here. This is quite similar to the case of the SNR G296.8−0.3.

(iii) A comparatively larger ring ('ring 2'), located north of ring 1 (corresponding to the large ring structure in Fig. 3.4). Ring 2 is fainter than ring 1 (as seen in Fig. 3.3) and extends much beyond the boundary of the ring 1 in the north. This ring has a poorly defined outer edge especially towards the north, which suggests that it represents a region of break-out into an adjacent cavity. This cavity itself could have been created in the past by some other energetic phenomena. In this case, the shock after being re-energised in the low density tunnel, will expand rapidly to take the shape of the cavity (Braun &

Strom 1986). For the SNRs G166.0+04.3 (VRO 42.05.01) and G350.0−02.0, all the above three components are located in the plane of the sky. Whereas for G296.8−0.3, the explosion site, the low density tunnel and the second shell all lie roughly along the line of sight. We suggest that SNR G3.1−0.6 may be quite similar to the case of G296.8−0.3 (Gaensler et al. 1998), where all the three components lie along the line of sight.

3.4.1.3 Spectral index and polarisation:

Non-thermal steep spectral index, polarised emission and shell morphology clearly identifies G3.1−0.6 to be a shell type SNR. The detection of polarised emission suggests that the magnetic field in the region is well organised.

3.4.2 G356.8−0.0 (Field II):

There are two extended curved emission seen in the map of this region. Following the discussion in Sect. 3.4.2, both of these objects appears to be part of a single large shell named as G356.8−0.0. Its non-thermal spectral index and a partial shell like morphology suggests the large shell like structure to be of an old SNR. However, due to its low surface brightness, its flux density at higher frequencies are poorly determined. As a result, its spectral index (≤ -0.34) is not well constrained.

With the available data, only the Σ-D relation can be used to estimate its distance. With an assumed spectral index of -0.5, the estimated flux density of this object is 20 Jy at 1 GHz. The modified Σ-D relation as developed by Case & Bhattacharya (1998), yields an estimated distance of 4.4 kpc for this SNR candidate. However, due to the short-spacing problem and the inherent uncertainty in the Σ-D relation itself, this distance may be uncertain by as much as a factor of three. The large shell shows kinks at different places and also seems to have broken up near G357.1−0.2, suggesting it to be an old SNR. Assuming an expansion velocity of 50 km s^{-1} and its angular size of 60′ at

Table 3.3: Observed parameters of G357.1−0.2

Galactic Coords ($l \pm b$)	RA (J2000)	Dec (J2000)	Size ($'$)	$S_{1.4GHz}$ (Jy)	S_{330MHz} (Jy)	Spectral Index (5/1.4)	Spectral Index (1.4/0.330)
357.1−0.2	17 39 38	−31 28 57	8×7	0.67±0.1	0.49±0.1	−0.5	0.2 ±0.2

a distance of 4.4 kpc, we use the Chevalier (1974) formula t=1.5 x 10^5 D v^{-1} to estimate its probable age. The calculated age is 2.4×10^5 years, which is an old age for an SNR.

3.4.3 Bi-annular source G357.1−0.2 (Field II):

The flux density of this object at 330 MHz along with its flux density measured at 1.4 GHz shows a slightly inverted spectral index of +0.2 ± 0.2. However, between 5 and 1.4 GHz, it has a spectral index of ~ -0.5. This indicate a break in its spectral index near 1 GHz with a difference of 0.7 between its high and low frequency spectral index. The peculiar morphology makes it difficult to draw unique identification for this object. Highly polarised emission at 5 GHz, however, shows the emission to be non-thermal in nature. As noted by Gray (1996), this object can be identified with (i) an extragalactic source, (ii) filamentary structure as seen close to the GC or (iii) a Crab like SNR. Compact cores of extragalactic sources often show a flat spectral index, which turns over at low radio-frequencies $\sim$ 100 MHz due to the synchrotron self-absorption. However, the extended components have a steep spectral index and shows relatively low level of absorption only at very low frequencies. As this object is extended, our determination of a turn over of its spectra below 1 GHz argues against the object being a typical extragalactic source. Also, its HI absorption spectrum suggests it to be galactic. Filaments near the Galactic Centre have not been reported to show any spectral break and therefore, it is unlikely to be a Galactic Centre filament. Within the observational error, this object has a flat or slightly inverted spectrum at low radio frequencies. A slightly inverted spectrum, if correct, can be a result of line of sight free-free absorption by diffuse foreground HII region. We argue below that optical depth (τ) due to free-free absorption cannot be more

than 0.2 at 330 MHz towards this object.

(i) Any line of sight structure of size larger than $40'$ will get resolved out in our map. However, we can estimate the free-free absorption coefficient by using the 408 MHz map of Haslam et al. (1982), which is equivalent to $\tau \leq 0.17$ at 330 MHz.

(ii) HII region of size $\leq 40'$ and optical depth ≥ 0.001 should be visible in our map above the noise level. As nothing of that sort is visible, we can rule out any perceptible line of sight absorption by a moderate size HII region (the $15'$ extended structure around the bi-annular source shows a non-thermal spectrum and from its emission measure at 8.35 GHz, the estimated optical depth due to free-free absorption at 330 MHz is found to be negligible).

(iii) The bi-annular structure itself is unlikely to have any associated HII region. It was selected as a candidate SNR due to its low IR/Radio luminosity (Broadbent et al. 1989).

Hence, the change in spectral index for this object seems to be intrinsic in nature. Breaks in spectral indices were earlier observed for a few Galactic SNRs like Cygnus loop and HB9 (Denoyer 1974), S147 (Kundu et al. 1980), G33.2−0.6 (Reich 1982), 3C58 (Green 1994) G76.9+1.0 (Landecker et al. 1997). However, only S147, G33.2−0.6 and G76.9+1.0 show break at metre wavelengths. From its irregular morphology and the spectral break, we suggest that G357.1−0.2 may be a Crab like SNR. The pulsar B1739−030 is located $2'$ away, but, there is no indication that it is associated with this object.

It is also possible that G357.1−0.2 is associated with the large suspected SNR which we have named as G356.8−0.0. G357.1−0.2 shows HI absorption by the 3 kpc arm. This implies a distance of more than 6 kpc from us for this object. The distance of the large SNR G356.8−0.0 could also be similar ($\sim$ 4.4 kpc from Σ-D relation). However, the large SNR apparently being a shell type remnant (expected spectral index ~ -0.5), an association with an object of different spectral type seems unlikely. We suggest that

G357.1-0.2 may be a crab like SNR, where the energy transfer from the pulsar has stopped in the past, giving rise to a steeper spectral-index at higher radio-frequencies due to synchrotron aging. The estimated parameters for G357.1−0.2 are summarised in Table 3.3.

3.4.4 Tornado nebula

Shocks and eddy motions at Rayleigh-Taylor instabilities are thought to provide the necessary acceleration mechanism and magnetic field enhancement to produce the synchrotron emission (Gull 1973). Therefore, the filamentary structures seen in the map of Tornado nebula is likely to indicate local shock, which causes higher electron density or magnetic field or both leading to more synchrotron emission from these regions.

If the compression due to the shock is large, the spectral index of the emission will be comparatively flat. Behind the shock (reverse shock), rarefaction takes place, and emission from these regions can be steep (Bell 1978). Therefore, in filamentary structures of the Tornado nebula, which may be created due to local shock can show spectral variation.

An alternate scenario for the spectral variations within SNRs is internal inhomogeneities. In the case of a curved electron energy spectrum with varying magnetic field strengths can lead to correlated variation of spectral index with brightness. A detailed analysis of SNR HB 9 has shown that this is a reasonable scenario for the outer regions of that remnant (Leahy et al. 1998). If the electron energy spectrum hardens at lower frequencies, regions in which the magnetic field is higher than the surroundings will both appear brighter and have a flatter spectrum than the surroundings.

In Tornado nebula, we do not find any global pattern of steeper or flatter spectral index with filamentary structures. However, we do find that some of the filamentary structures in the nebula have spectral indices different than the average spectral index of the nebula, which we discuss here. In Sect 3.3.4, it is shown (Fig. 3.16) that the

filamentary structure D, eastern part of B and E have flatter spectra. From Spectral tomography maps we have identified that these regions have spectral indices flatter than -0.5. From Fig. 3.17, we identify that the Southern edge of the core (marked A in Fig. 3.17) also has a flatter spectrum. As discussed above, it is possible that in these regions the Mach number of the shock is high, which results in flatter spectrum. The western part of B could be the region of reverse shock, and spectrum is steeper than -0.73 (Fig. 3.15). However, the internal inhomogeneities could also have given rise to this variation in spectral indices.

The spectral indices of the extended emission as seen in Fig. 3.17 is quite close to the average spectral index of the nebula. Especially, the diffuse tail of the nebula do not show any significantly steep spectrum, which was likely if it would have been an extragalactic head-tail source. The typical variation of the spectral index is about 0.1 from the average, which is consistent with what is seen in several SNRs like the Kepler's SNR (DeLaney et al. 2002), Tycho's SNR (Katz-Stone et al. 2000), G39.2–0.3 and G41.1–0.3 (Anderson & Rudnick 1993).

3.4.4.1 Distance

As shown in Sect 3.3.4.1, we detect several HI absorption lines against this nebula, indicating it to be located beyond or embedded within these HI features. Based on single dish HI absorption profile, Radhakrishnan et al. (1972) showed this nebula to be located beyond the 3 kpc arm. Cohen (1977) tentatively detected HI absorption due to the Nuclear disk feature (Rougoor & Oort 1960) near the GC. Since the absorption by the Nuclear disk was weak, they could not rule out instrumental artefacts as a cause of this absorption. However, our observations clearly show the absorption by the Nuclear disk, which is observed in emission at a velocity of about -200 km s^{-1} (Cohen 1977). Since the Nuclear disk is known to be located within a few hundred pc of the GC, it puts a lower limit on its distance.

The extragalactic source G356.9+0.1 located about a degree away also shows HI absorption by the Nuclear disk. However, we notice a marked increase in HI absorption depth almost by a factor of 2 at a velocity of -230 km s^{-1} (marked 'tangent point') towards this source, which indicates that the gas rotating around the GC (assumed to be circularly symmetric in the Nuclear disk) intersects our line of sight tangentially at this velocity. This leads to velocity crowding and consequent increase in the absorption depth at this velocity. However, no such increase in the optical depth of the Tornado nebula near this velocity has been observed, thereby suggesting that the Tornado nebula is located at a distance less than the 'tangent point'. We also note that the line width (about 60 km s^{-1}) towards this extragalactic source is significantly higher than what is observed towards the Tornado nebula (about 40 km s^{-1}), thereby supporting the suggestion regarding its location at a distance less than that of the GC, which strongly argues against any suggestion of it being located outside the Galaxy.

Table 3.4: Compact sources in the field centred on G3.2−1.0

Name	RA (J2000)	DEC (J2000)	Peak (Jy/Beam)	Total (0.33 GHz) (Jy)	Total (1.4 GHz) (Jy)	Distance from centre (′)	Comment
2.442 – 0.701	17 54 02.0	-27 12 02	0.030	0.056	0.003	50.9	
2.546 – 0.917	17 55 06.6	-27 13 13	0.056	0.102	0.0137	41.6	
2.548 – 1.309	17 56 38.5	-27 24 56	0.055	0.120	0.038	45.1	Double
2.596 – 1.315	17 56 46.3	-27 22 38	0.067	0.095	0.019	42.7	
2.596 – 1.086	17 55 52.6	-27 15 45	0.236	0.405	0.120	38.6	TX=0.397
2.603 – 0.774	17 54 40.9	-27 05 56	0.026	0.032	0.0014	40.3	Pulsar ?
2.749 – 1.518	17 57 54.5	-27 20 46	0.025	0.023	0.011	42.5	
2.773 – 1.274	17 57 00.7	-27 12 15	0.035	0.053	0.0086	32.2	
2.798 – 0.596	17 54 26.1	-26 50 26	0.046	0.068	0.012	35.8	
2.816 – 1.091	17 56 23.8	-27 04 29	0.030	0.060	0.010	25.7	
2.833 – 1.218	17 56 55.8	-27 07 26	0.057	0.070	0.021	27.4	
2.838 – 0.708	17 54 57.7	-26 51 46	0.023	0.034	0.012	29.6	
2.859 – 1.147	17 56 42.6	-27 03 55	0.051	0.135	0.038	24.1	
2.893 – 0.884	17 55 45.9	-26 54 15	0.019	0.021	0.007	21.7	
2.924 – 1.304	17 57 28.1	-27 05 18	0.009	0.010	0.0014	26.0	
2.937 – 0.352	17 53 48.5	-26 35 49	0.033	0.059	0.008	42.9	
2.961 – 0.656	17 55 02.2	-26 43 48	0.093	0.203	0.030	26.5	Double
2.988 – 1.304	17 57 36.7	-27 01 57	0.012	0.020	$<$0.001	23.4	
3.016 – 0.372	17 54 03.8	-26 32 22	0.056	0.064	0.011	40.0	
3.022 – 1.584	17 58 46.6	-27 08 34	0.019	0.032	0.014	37.1	
3.026 – 1.186	17 57 14.2	-26 56 25	0.010	0.018	0.0016	16.7	
3.044 – 1.136	17 57 05.2	-26 53 59	0.007	0.005	0.004	14.0	
3.110 – 1.189	17 57 26.4	-26 52 11	0.018	0.048	0.007	13.5	Double
3.136 – 0.775	17 55 53.5	-26 38 22	0.033	0.043	0.014	14.8	NV=0.004

Name	RA (J2000)	DEC (J2000)	Peak (Jy/Beam)	Total (0.33 GHz) (Jy)	Total (1.4 GHz) (Jy)	Distance from centre (′)	Comment
3.157 – 0.556	17 55 05.6	-26 30 39	0.136	0.157	0.026	27.1	NV=0.015
3.170 – 0.260	17 53 59.1	-26 20 58	0.065	0.096	<0.003	44.7	Pulsar ?
3.323 – 0.991	17 57 08.8	-26 35 10	0.030	0.028	0.004	5.43	
3.347 – 0.324	17 54 37.6	-26 13 47	0.099	0.240	0.042	41.2	Double, NV=0.019
3.384 – 0.999	17 57 19.2	-26 32 13	0.016	0.018	0.003	8.93	
3.434 – 1.077	17 57 43.8	-26 31 59	0.055	0.072	0.024	12.7	
3.505 – 1.116	17 58 02.5	-26 29 27	0.070	0.105	0.031	17.5	
3.565 – 1.009	17 57 45.7	-26 23 08	0.010	0.013	0.002	19.7	
3.572 – 1.551	17 59 52.6	-26 38 59	0.013	0.016	<0.001	38.6	Pulsar ?
3.595 – 1.566	17 59 59.1	-26 38 12	0.038	0.058	0.020	40.1	
3.621 – 1.348	17 59 12.0	-26 30 22	0.015	0.019	0.048	31.1	
3.630 – 1.090	17 58 13.1	-26 22 10	0.178	0.210	0.054	24.2	
3.663 – 0.320	17 55 19.4	-25 57 17	0.040	0.120	0.050	48.3	Double, NV=0.005
3.717 – 0.938	17 57 49.4	-26 13 06	0.013	0.010	0.002	29.1	
3.721 – 0.841	17 57 27.5	-26 09 59	0.011	0.022	<0.001	30.6	
3.727 – 0.240	17 55 09.6	-25 51 34	0.029	0.039	<0.0015	54.3	Pulsar ?
3.746 – 1.222	17 58 59.2	-26 20 05	0.091	0.174	0.058	33.3	Double
3.748 – 0.802	17 57 22.1	-26 07 23	0.018	0.026	0.003	33.0	
3.889 – 1.122	17 58 55.1	-26 09 40	0.016	0.025	0.007	39.8	
4.027 – 1.301	17 59 54.9	-26 07 49	0.026	0.027	0.012	50.7	

Table 3.5: Compact sources in the field centred on G356.8−0.1

Name	RA (J2000)	DEC (J2000)	Peak (Jy/beam)	Total (0.33 GHz) (Jy)	Total (1.4 GHz) (Jy)	Total (5 GHz) (Jy)	Distance from Centre (′)	Comment
356.001 + 0.022	17 35 40.4	-32 18 54	0.606	1.31	0.397(NV)	0.114	48.5	TX=1.01
356.018 + 0.428	17 34 06.2	-32 04 52	0.129	0.26	0.032	0.0062	56.5	TX=0.286
356.379 + 0.004	17 36 42.5	-32 00 23	0.076	0.139	0.005	0.005	26.2	Double
356.394 + 0.338	17 35 25.2	-31 48 49	0.140	0.184	0.061	0.015	35.9	
356.433 − 0.044	17 37 02.2	-31 59 12	0.033	0.055	<0.0015	—	22.2	
356.463 − 0.014	17 36 59.5	-31 56 43	0.073	0.16	0.21(NV)	0.0083	20.7	Double
356.580 + 0.567	17 34 59.3	-31 32 00	0.042	0.073	0.031	—	42.0	
356.597 − 0.739	17 40 13.4	-32 13 08	0.206	0.33	0.042	—	40.2	
356.655 − 0.152	17 38 01.6	-31 51 26	0.069	0.081	0.047	14.4	9.37	
356.805 − 0.310	17 39 02.0	-31 48 53	0.035	0.065	<0.001(NV)	—	12.6	
356.830 + 0.360	17 36 26.3	-31 26 05	0.295	0.415	0.18	0.026	27.5	TX=0.739
356.837 + 0.378	17 36 23.0	-31 25 09	0.046	0.067	0.0185	—	28.7	
356.884 + 0.465	17 36 09.6	-31 19 58	0.084	0.102	0.028	—	34.3	
356.906 + 0.081	17 37 44.0	-31 31 14	1.837	3.75	2.24 (NV)	0.487	12.5	TX=3.50
356.965 − 0.074	17 38 29.7	-31 33 12	0.044	0.043	0.002	—	10.0	Pulsar ?
357.036 − 0.559	17 40 36.2	-31 45 06	0.098	0.140	0.043	—	30.9	
357.067 − 0.401	17 40 03.0	-31 38 29	0.033	0.042	<0.002	—	24.1	
357.098 − 0.220	17 39 24.5	-31 31 07	0.069	0.060	<0.0015	—	19.2	Pulsar
357.134 + 0.316	17 37 22.6	-31 12 07	0.043	0.046	0.018	0.005	31.9	
357.280 + 0.211	17 38 09.4	-31 08 06	0.206	0.301	0.154	0.02	34.2	
357.437 − 0.519	17 41 26.4	-31 23 25	0.312	0.470	0.222	—	45.6	TX=0.369
357.452 − 0.597	17 41 47.3	-31 25 07	0.144	0.201	0.047	—	49.0	
357.809 − 0.299	17 41 29.2	-30 57 29	0.093	0.12	0.085	0.020	61.7	

3.4.5 Compact sources in the field of view:

Our 330 MHz maps allow us to image compact sources in the field of view. The sources were searched from our high resolution (beam-size $\approx 15-20''$) maps of the Field I and II. A total of 44 sources have been identified from the field G3.2−1.0, and 23 sources from the field G356.8−0.1. Due to twice better sensitivity in the map of the first field, we could detect almost a factor of two higher number of sources in the field G3.2−1.0. We have presented the parameters for the sources in Table 3.4 for the field G3.2−1.0 and in Table 3.5 for the field G356.8−0.1. In Table 3.4, (Field centred at l=3.2, b=−1.0) column-1 shows the Galactic Co-ordinate of the object, columns 2 and 3 give the Right Ascension and Declination (J2000) of the object respectively and columns 4 and 5 give the peak and total flux density at 330 MHz. Column 6 gives the total flux density of the object at 1.4 GHz. Column-7 lists the distance of the object from the pointing centre of the fields and column-8 gives any comments about the source. In the last column (Comments), 'TX' denotes the flux density of the object as measured by the Texas Survey at 365 MHz. The flux density of these sources at 1.4 and 5 GHz have been quoted from the VLA Galactic plane survey (Becker et al. 1994; Helfand et al. 1992; Zoonematkermani et al. 1990) along with the NVSS map at 1.4 GHz. NVSS observations being of much higher sensitivity than the Galactic plane survey, many sources from our map which are absent in the Galactic plane survey were found to have counterpart in the NVSS map. Also, to estimate flux density for the extended sources, we have preferred the NVSS maps to minimise any zero-spacing problem. The sources for which the 1.4 GHz flux density is quoted from the NVSS, an entry of '(NV)' is given beside the numerical value of the total flux density. For Table 3.5 (field centred at l=356.8, b=−0.0), the columns 1 to 6 have the same meaning as above. However, column-7 indicates the source flux density at 5 GHz and column-8 indicates the distance of the object from the pointing Centre. Column-9 shows any comments about the objects. In Table 3.5, the 1.4 GHz

flux density is estimated for most of the objects from the NVSS map. The sources for which the 1.4 GHz flux density have been quoted from the Galactic plane survey, the corresponding NVSS flux density has been given in the last column (Comments) by 'NV=flux'. The Galactic plane survey being of intrinsically higher resolution, we have compared the source positions in both of our 330 MHz maps with respect to the above survey. The typical positional error of the sources were found to be ≈4-5″, part of which is caused by systematic offset for all the sources.

The flux density quoted for the sources in our list can be affected by two kinds of errors. The first is due to an error in the absolute flux density scale, where, all the sources will be affected by this error. We expect, the error in our flux density scale to be within ±15%. The second kind of error in the flux of the objects can be caused by the primary beam pattern of the antennas. Though, our maps have been corrected by multiplying the maps by the inverse of the primary beam pattern, any error in pointing and in determining the primary beam pattern will persist. Only the sources which are located near the FWHM (88′ at 330 MHz) or beyond will get seriously affected by this type of an error. In our list of sources, the objects which are located close or beyond the FWHM of the antennas can have an estimated flux density which may be off even by 20−40% of their absolute flux density due to this error. Hence, the flux density for these sources should be treated with caution.

Most of the sources in our list show a non-thermal steep spectral index and is expected to be background extragalactic sources. A few sources having non-thermal spectra also have a double-lobed morphology. These sources are almost certainly to be extragalactic. Four sources from Field I (G2.603−0.774, G3.170−0.260, G3.572−1.551 and G3.727−0.240) (Table 3.4) and one source from Field II (G356.965−0.074) (Table 3.5) appears to be compact and have a spectral index steeper than −1.9. We classify these sources as pulsar candidates.

3.5 Summary

Our observations of four suspected supernova remnants close to the Galactic Centre region have resulted in:

(a) Confirmation that G3.1−0.6 (Gray 1994c) is supernova remnant. This was the largest suspected SNR ($28' \times 49'$) detected during the Molonglo Galactic Centre survey. We estimate a spectral index of ≤ -0.64 for this object. In the NVSS map, the narrow filamentary part at the eastern region of the shell is found to be polarised upto a level of 20%. This indicate an ordered magnetic field in the region. The Σ-D relation indicates a probable distance of 7.7 kpc from us for this object. The object has a two shell morphology which we interpret as due to expansion of the SNR into an anisotropic ISM.

(b) The detection of two curved extended structures in the Field II, which appears to be part of a large shell like structure (size $\approx 52' \times 72'$) centred at G356.8−0.0, and having a total flux density of 30 Jy at 330 MHz. A comparison of our map with single dish maps at 8.35 and 14.35 GHz constrains its spectral index to be steeper than −0.34. The shell type morphology and a non-thermal spectral index suggest it to be a supernova remnant. Observations at even lower frequency is recommended to better constrain its spectral index. Using Σ-D relation, a probable distance of 4.4 kpc has been estimated for this object. It appears to be a very old supernova remnant.

(c) We find that the three previously suspected supernova remnants, G356.6+0.1, G356.3−0.3 and G357.1−0.2 (Gray 1994c) are located on an extended object, which appears to be part of a large shell as described above. We suggest that G356.6+0.1 and G356.3−0.3 are actually parts of this large shell which were accidentally identified as separate objects in the MOST survey.

(d) The peculiar morphology and the spectral index of the object G357.1−0.2 suggests that it is a separate supernova remnant along the same line of sight of the large shell (G356.8−0.0). It appears to be a plerionic type of supernova remnant with a spec-

tral break around 1 GHz and is located at a distance of more than 6 kpc from us.

(e) We have made spectral tomographic maps of the Tornado nebula between 1.4 GHz and 330 MHz. We find that a few of the filamentary structures appear to show spectral index variations, which could either be explained by difference in the conditions of electron acceleration at the site of shocks, or a curved electron energy spectrum. Overall variation of the spectral index of the extended features across the nebula is consistent with what is seen in other SNRs.

(f) Using HI absorption towards the Tornado nebula, it can be placed in or beyond the central few hundred pc of the Galactic Centre. Comparison of its HI spectrum with what is observed for the suspected extragalactic source G356.9+0.1 indicate that the Tornado nebula is located at the nearer side of the GC, which for the first time puts an upper limit on its distance.

Chapter 4

Constraints on distances to Galactic Centre non-thermal filaments from HI absorption

4.1 Introduction

The long narrow non-thermal filaments (NTFs) observed in high resolution radio-continuum maps are unique features seen towards only the central $\sim 2^\circ$ region of our Galaxy. These structures are less than 1 pc in width, but extend up to 30 pc in length. With the exception of the NTF called the Pelican (Lang et al. 1999a), which is nearly parallel to the Galactic plane, all other NTFs are oriented perpendicular to the Galactic plane to within 20° (Morris & Serabyn 1996, and references therein) [1]. Except for NTF G359.79+0.17, which has a curved morphology reminiscent of a partial shell, all other NTFs have a linear structure. The spectral indices of these structures range from -0.8 to +0.3 (where $S_\nu \propto \nu^\alpha$) (Anantharamaiah et al. 1991) and they are found to be highly polarised at centimetre wavelengths (Morris & Serabyn 1996). Since these NTFs remain straight despite interaction with nearby molecular clouds, it is believed that the molecular clouds and the NTFs are in pressure equilibrium, which indicates a magnetic field strength of a few milliGauss inside the NTFs (Yusef-Zadeh & Morris 1987a). Magnetic fields of

[1] Recently, Nord et al. (2003) have published a list of 18 new candidate NTFs in the GC region, and Larosa et al. (2003) confirm 4 more NTFs. Many of these new NTFs and the candidate ones are oriented randomly with respect to the Galactic plane.

comparable strengths are thought to be present in the central molecular zone (CMZ) located within $\sim$ 200 pc of the centre of the Galaxy (Morris & Serabyn 1996). Before any attempt is made to relate the magnetic field in the NTFs with the processes occurring in the Galactic Centre (GC), it is necessary to establish that these NTFs are actually located in the GC region and are not chance superpositions of foreground or background objects (Lasenby et al. 1989). HI absorption towards the GC 'Radio-arc' (Lasenby et al. 1989) and the 'Snake' (Uchida et al. 1992b) have indicated that they are located close to the GC, but the distances to the remaining NTFs are not constrained.

An intriguing fact that has been noticed for all the well-studied NTFs is the interaction between the NTF and molecular clouds (Morris & Serabyn 1996). It appears that the presence of an HII region near the place of interaction plays a role in the creation and maintenance of the NTFs (Serabyn & Morris 1994; Staguhn et al. 1998; Uchida & Guesten 1995). CO observations have indicated the presence of high velocity molecular clouds; -65 km s^{-1} and -130 km s^{-1} towards Sgr C (Liszt & Spiker 1995). It is believed that the HII region located just south of the NTF (known as the Sgr C HII region) is actually embedded in the -65 km s^{-1} cloud (Liszt & Spiker 1995; Kramer et al. 1998). Two dense molecular clouds are reported to be associated with the NTF G359.54+0.18. One of the clouds having a velocity of -140 km s^{-1} is located near the bent portion of the NTF ('E' in Fig. 4.8). The other cloud with a velocity of -90 km s^{-1} is located close to the eastern edge of the NTF (Staguhn et al. 1998). However, these reported associations are based on their proximity in the sky plane, and the spatial association of the corresponding objects has yet to be established.

In this chapter, we present new HI absorption measurements towards three NTFs, Sgr C, G359.54+0.18 and G359.79+0.17 made with the Giant Metrewave Radio Telescope (GMRT). These observations not only constrain the distances of these objects, but also test the association of some of the clouds mentioned above with the corresponding NTFs. These three NTFs are located to the south and south west of the Sgr A complex, and high

resolution radio continuum observations have confirmed the characteristic properties of each of the NTFs: Sgr C (Liszt & Spiker 1995), G359.54+0.18 (Bally & Yusef-Zadeh 1989; Yusef-Zadeh et al. 1997b) and G359.79+0.17 (Lang & Anantharamaiah, in preparation).

Due to velocity crowding near Galactic longitude l=0°, Galactic rotation cannot be used to constrain the distances to these NTFs. Therefore, in this chapter, detection of absorption by known HI features has been used to provide constraints on the distances to the NTFs. Since an interferometer resolves the extended HI emission features, no information about the emission features are obtained from our observations. However, absorption by these features against the continuum source can be observed with an interferometer. Therefore, in this section, we briefly summarise the distances and the velocities of the HI features identified from single dish HI emission observations towards the NTFs under study (e.g. Cohen & Davies 1979), which we will refer to later in this chapter. Near the Galactic longitude of 359.5°, two high velocity HI emission features known as the 'Nuclear disk' (Rougoor & Oort 1960) and the 'Molecular ring' (Scoville 1972) have been found. The 'Nuclear disk' shows high negative velocity ranging from ≈ -160 to -200 km s^{-1}, whereas the 'Molecular ring' has a velocity of ≈ -135 km s^{-1}. Both these features are believed to be nearer than the GC and located at a distance of few hundred parsecs from it (Cohen & Davies 1979). The emission from the '3 kpc arm' (Rougoor 1964) located at a distance of $\approx$ 5.1 kpc from the Sun is identified at a velocity near -53 km s^{-1}. At positive velocities, emission near 135 km s^{-1} is seen due to the HI features 'XVI' and 'I' (Cohen & Davies 1979), both of which are thought to be located behind the GC. While the feature 'XVI' is likely to be located within a few hundred parsecs of the GC (Cohen & Davies 1979), the feature 'I' is thought to be 2 kpc behind the GC (Cohen 1975).

In Sect 4.2, we discuss the observations and data reduction. The results from our observations are presented in Sect 4.3 and their consequences are discussed in Sect 4.4.

Finally, the conclusions are presented in Sect 4.5.

4.2 Observations and data reduction

The GMRT (Swarup et al. 1991) consists of thirty antennas, distributed over a region of about 25 km, with fourteen of the antennas located within a diameter of about one km and the remaining arranged in 3 arms each of length 14 km, shaped as an irregular Y. This arrangement provides the necessary *uv* coverage for mapping both compact and extended sources. The ratio of the longest to the shortest baseline is $\approx$ 500 with the shortest projected baseline being $\approx$ 50 metres. Table 4.1 give the details of our observations. All the observations were carried out in the default spectral line mode with 128 frequency channels. A bandwidth of 4 MHz was used to observe G359.54+0.18 and G359.79+0.17 which gave a velocity coverage of $\pm$400 km s^{-1} with a resolution of 6.7 km s^{-1}. The Sgr C complex was observed with a bandwidth of 2 MHz ($\pm$ 200 km s^{-1}) and 4 MHz ($\pm$ 400 km s^{-1}). In all the observations, 3C286 was observed as a primary flux density calibrator, 3C287 as the bandpass calibrator and 1748-253 as the secondary calibrator. The bandpass pattern of the antennas change appreciably as a function of frequency. Therefore, we have not used frequency switching for the bandpass calibration. Instead, we have chosen a bandpass calibrator (3C287) with a high Galactic latitude, so that the effect of Galactic HI absorption on its spectra is less than 1% (Dickey et al. 1978). During our observations, the automatic measurements of system temperatures were not implemented. However, since in this chapter we are not concerned with the absolute value of the flux density, we have applied an approximate correction by scaling the flux density of all the fields by the ratio of the estimated flux density (157 mJy) of the small-diameter source G359.87+0.18 (Lazio et al. 1999) at 1.55 GHz to the flux density that we have estimated from our map (ratio $\approx$ 2.5). All the maps presented in this chapter have been corrected for the primary beam pattern of the antennas.

Table 4.1: Details of our observation

Source Name	RA (J2000)	Dec (J2000)	Frequency (MHz)	Band-width (MHz)	Date	Observing time (hour)	Ante-nnas
Sgr C	17 44 33.8	−29 28 02	1420.4	2	2000 Oct 06	1	27
Sgr C	17 44 33.8	−29 28 02	1420.4	2	2000 Oct 08	2	27
Sgr C	17 44 33.7	−29 28 00	1420.6	4	2001 May 24	2.5	28
G359.79+0.17	17 44 30.9	−28 59 50	1420.6	4	2001 May 24	3.0	26
G359.54+0.18	17 43 48.3	−29 11 26	1420.6	4	2001 May 25	3.5	28

The spectral visibility data were processed using standard NRAO AIPS programs. Bad data due to antenna-based or baseline-based problems were flagged using UVFLG. The data were then calibrated and images of the fields were formed by Fourier inversion and CLEANing (IMAGR). To reduce the effect of comparatively large-scale structures in HI along the line of sight, we have done a high-pass filtering while making the maps of the three NTFs. Since the NTFs are oriented almost along the east-west direction (i.e. along u), we have filtered out data having $v \leq 2000\lambda$ and $u \leq 4000\ \lambda$, because of which any 2-D structure that has a size-scale $\geq 1.5'$ will not be visible and linear structures of length $\leq 10'$ can only be imaged. We have used the AIPS task UVNOU to implement this data filtering in u and v. The visibility data were then used to generate the continuum and line images. The continuum map of Sgr C NTF made using the above procedure is shown in Fig. 4.1. Since the Sgr C HII region is extended, we have applied a lower uv cutoff of 1 kλ to the visibility data before making the line and the continuum maps (Fig. 4.2). During observation of G359.79+0.17, the GC was located just outside the half power width of the GMRT primary beam. Hence, to minimise the sidelobe response of the GC in the image of the NTF G359.79+0.17, 3-D imaging (available in the recent versions of IMAGR) was used.

Before making the channel maps, the AIPS task UVLSF was used to subtract a constant term across the frequency channels corresponding to the continuum from the visibility data. The GMRT has an FX correlator, for which 'Gibbs ringing' due to any sharp feature in the spectrum dies away much faster ($\propto \mathrm{sinc}^2$) than in a XF correlator. There-

fore, we have not applied any spectral smoothing to our data. The variation in the line frequency introduced by the earth's rotation during the observing period is estimated to be much smaller than the frequency channel width and so we have not applied any Doppler corrections to the data. It should be noted here that the RMS noise quoted for each spectrum is the noise estimated from the corresponding images (i.e., from image plane) and are applicable for only |velocity| $\geq$ 20 km s^{-1}. For |velocity| $\leq$ 20 km s^{-1}, due to emission from the HI gas along the line of sight (velocity crowding occurs when $|l| \approx 0^{\circ}$), the system temperature increases and the typical RMS noise is 1.6 times higher than the quoted values. The systematic error in our spectra ($e^{-\tau}$, where τ is the optical depth) is believed to be less than 0.05.

4.3 Results

In this section, we present the absorption spectra towards the target sources and identify the velocity of the HI absorption features. In all the spectra, unless otherwise stated, the X-axis represents the velocity in km s^{-1} and Y-axis represents the transmission (I/I_0), where I is the observed flux density of the background source at the given frequency and I_0 is the actual flux density of the source. We also assume the spin temperature of the atomic hydrogen to be much less than the brightness temperature of the background source and in that case $I/I_0=e^{-\tau}$. All the velocities quoted in this chapter are expressed with respect to the Local Standard of Rest and the GC is assumed to be at a distance of 8.5 kpc. As is well known, the HI column density is related to its optical depth by the formula, N_H=1.8 $\times 10^{18} \times T_S \times \int \tau dv$, where, N_H is the column density of the atomic hydrogen, T_S is the spin temperature and $\int \tau dv$ is the velocity integrated optical depth. We use this relation to calculate the HI column density from the observed optical depth.

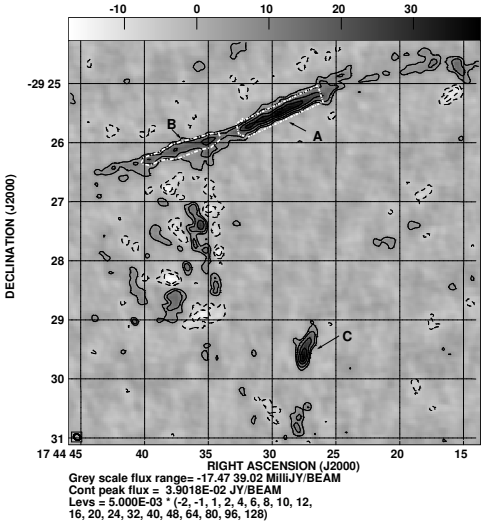

Figure 4.1: Continuum map of the Sgr C NTF at 1.4 GHz after high pass filtering. The image has a resolution of 7 x 6 arcsec^2, along PA=56°. The Sgr C HII region is resolved out. RMS noise in the map is 1.6 mJy beam^{-1}.

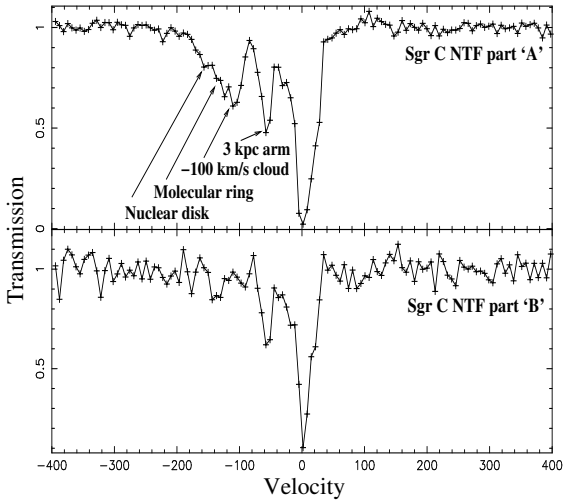

Figure 4.3: HI absorption spectrum towards the central bright part and the eastern part (marked 'A' and 'B' in Fig. 1 respectively) of the Sgr C NTF. The bandwidth is 4 MHz. RMS noise in the two spectra is 0.027 and 0.063 respectively.

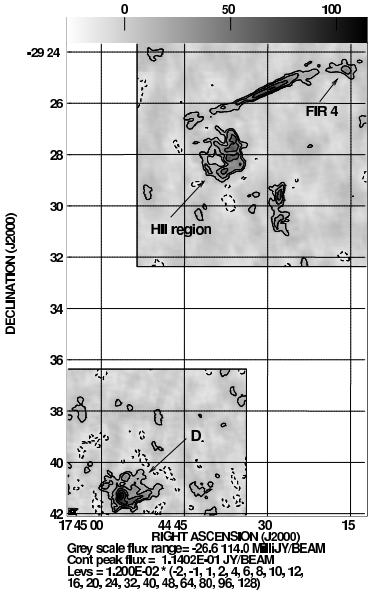

Figure 4.2: Continuum map of the Sgr C region at 1.4 GHz with a resolution of 10 x 8 arcsec^2, along PA=56°. This is a composite map and shows the Sgr C HII region along with few other sources in the field of view. The rms noise is 4.0 mJy beam^{-1}.

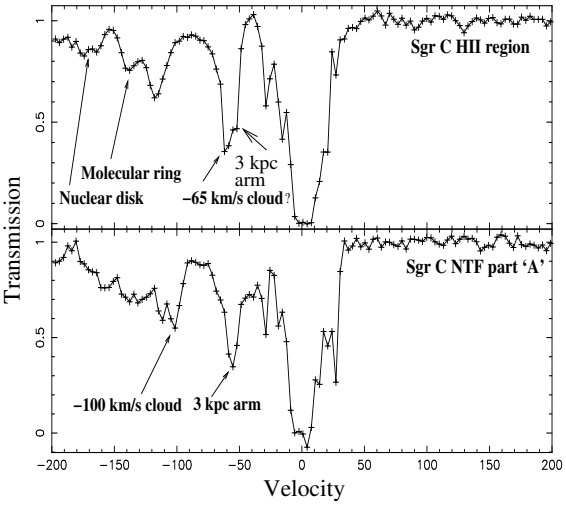

Figure 4.4: HI absorption spectrum towards the Sgr C HII region (Fig. 2) and the central bright part (marked 'A' in Fig. 1) of the Sgr C NTF. The bandwidth is 2 MHz. RMS noise in the two spectra is 0.021 and 0.034 respectively.

4.3.1 Sgr C

The absorption spectra towards various parts of the object (Fig. 4.1 & Fig. 4.2) are shown in Fig. 4.3 and 4.4. Fig. 4.3 shows the absorption spectrum towards parts 'A' and 'B' (see Fig. 4.1) of the NTF. The spectrum towards part 'A' shows several absorption features at negative velocities in addition to the absorption feature at 0 km s^{-1} (line-width $\approx$ 30 km s^{-1}). A strong absorption feature near -54 km s^{-1} is seen due to HI absorption by the '3 kpc arm'. A broad absorption feature is seen between -100 km s^{-1} and -200 km s^{-1}, with an almost linear decrease in optical depth from $\approx$ 0.5, at -100 km s^{-1}, to $\approx$ 0.0, at -200 km s^{-1}.

The spectrum taken towards part 'B' of the NTF (Fig. 4.3) appears markedly different. The absorption width of the 0 km s^{-1} feature appears to be narrower ($\approx$ 25 km s^{-1}) than that observed towards 'A'. Absorption due to the '3 kpc arm' is also seen. However, except for a weak 4σ absorption feature at -137 km s^{-1}, the wide absorption feature between -100 and -200 km s^{-1} is not seen.

The absorption spectrum towards the Sgr C HII region with a resolution of 3.3 km s^{-1} is shown in Fig. 4.4. For comparison, the spectrum of part 'A' having the same velocity resolution is also plotted. Both the spectra show similar absorption features with a few differences, which we note here. Towards the HII region, the broad absorption feature seen between -100 and -200 km s^{-1} shows at least three main components centred at -118 km s^{-1}, -138 km s^{-1} and -175 km s^{-1} with optical depth of $\approx$0.5, 0.3 and 0.2 respectively. The absorption depth at these velocities are similar to what is seen towards part 'A' of the NTF. However, the absorption feature near 0 km s^{-1} is broader towards the HII region (line-width $\approx$ 33 km s^{-1}). The HII region shows a feature at -61.5 km s^{-1}, in addition to the absorption by the '3 kpc arm' observed near -54 km s^{-1} in both the spectra. However, Part 'B' of the NTF being weaker than part 'A' in radio continuum, absence of the -61.5 km s^{-1} feature could not be verified against 'B'.

4.3.2 HI absorption spectra towards objects located in the field of Sgr C: source C, D and FIR-4

Fig. 4.5 shows the spectra towards source 'C' ('3' in Liszt & Spiker (1995)), source 'D' and FIR-4 (Fig. 4.2). The spectrum towards the source 'C' is similar to what is seen towards the Sgr C HII region, but, in place of the wide absorption feature between -100 and -200 km s^{-1} (Fig. 4.4), two absorption lines are observed at -123 km s^{-1} and -170 km s^{-1}. Since the continuum emission from the HII region FIR-4 is weak, its absorption spectrum is noisy. However, we identify HI absorption at -135 km s^{-1} (5 σ detection) and at -183 km s^{-1} (4 σ detection) towards FIR-4. CO emission has been observed towards the source 'C' and FIR-4 at -123 km s^{-1} and -135 km s^{-1} respectively (Oka et al. 1998). On the other hand, the spectrum towards the southern HII region 'D' (Fig. 4.2), ('1' in Liszt & Spiker (1995)) located just outside the half power width of the GMRT antennas is markedly different. Except the strong absorption near the 0 km s^{-1} (line-width $\approx$ 30 km s^{-1}), no other absorption feature could be identified towards this object.

4.3.3 NTF G359.79+0.17 and G359.87+0.18

The continuum image at 20 cm of the field of NTF G359.79+0.17 is shown in Fig. 4.6. The absorption spectrum integrated over the NTF is plotted in Fig. 4.7. The strong absorption near 0 km s^{-1} has a line-width of $\approx$ 24 km s^{-1}. No absorption feature at positive velocities is seen towards this source. However, at negative velocities, an absorption feature can be seen at -26 km s^{-1}, and a weaker feature at -58 km s^{-1}, which coincides with the line of sight velocity of the '3 kpc arm'.

Fig. 4.7 also shows the absorption spectrum towards the extragalactic source G359.87+0.18. Strong absorption near 0 km s^{-1} with a line-width of $\approx$ 40 km s^{-1}, and absorption at -53 km s^{-1} are observed. Lazio et al. (1999) have observed HI absorption against G359.87+0.18, and the aforementioned features match with their spectrum. However,

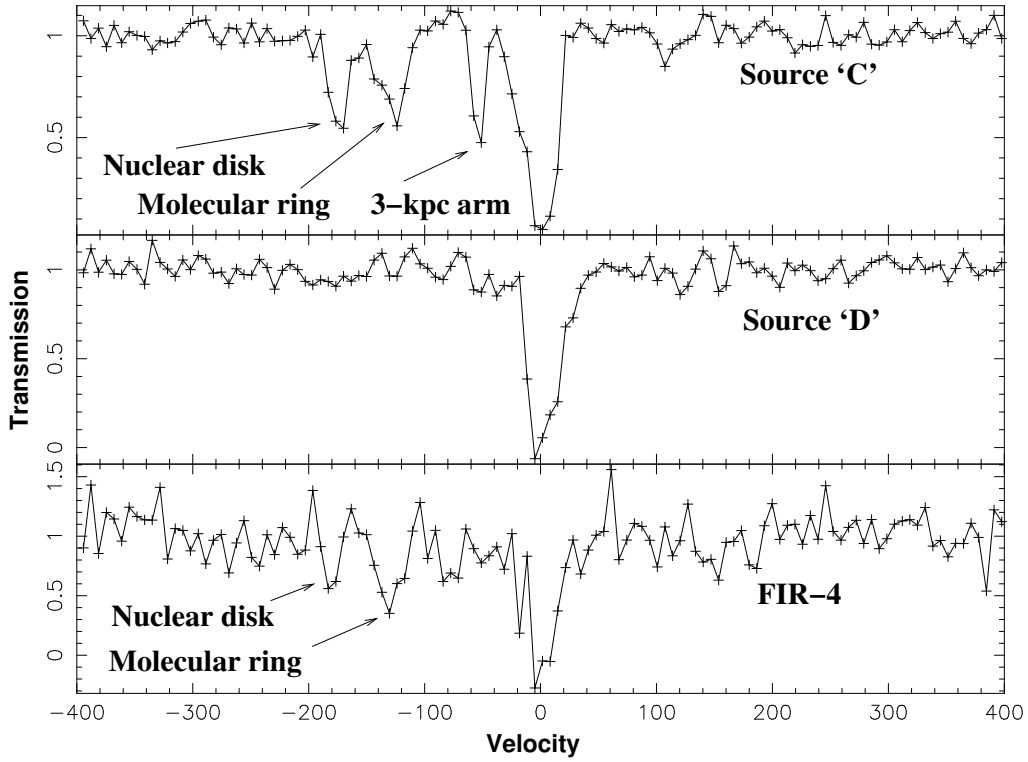

Figure 4.5: HI absorption spectrum towards the source 'C' (Fig. 4.1), 'D' (Fig. 4.2) and FIR-4, located in the field of Sgr C. The bandwidth is 4 MHz. RMS noise in the three spectra are 0.078, 0.05 and 0.2 respectively.

the present observations have a wider velocity coverage than Lazio et al. (1999) and we detect an additional absorption feature at +140 km s^{-1}.

4.3.4 NTF G359.54+0.18

The continuum image of the NTF G359.54+0.18 is shown in Fig. 4.8 and the absorption spectrum integrated over the NTF is plotted in Fig. 4.9. The absorption spectrum is quite similar to the one seen towards G359.79+0.17, with components at -26 km s^{-1} and -53 km s^{-1}. The strong HI absorption near 0 km s^{-1} has a line-width of $\approx$ 24 km s^{-1}. Staguhn et al. (1998) have found a dense molecular cloud at -140 km s^{-1} near the bent portion of the NTF (position of the molecular cloud is denoted by 'E' in Fig. 4.8). HI spectrum taken towards this region of the NTF (denoted by 'F' in Fig. 4.8) shows absorption (Fig. 4.9) at this velocity (4σ detection). Staguhn et al. (1998) also

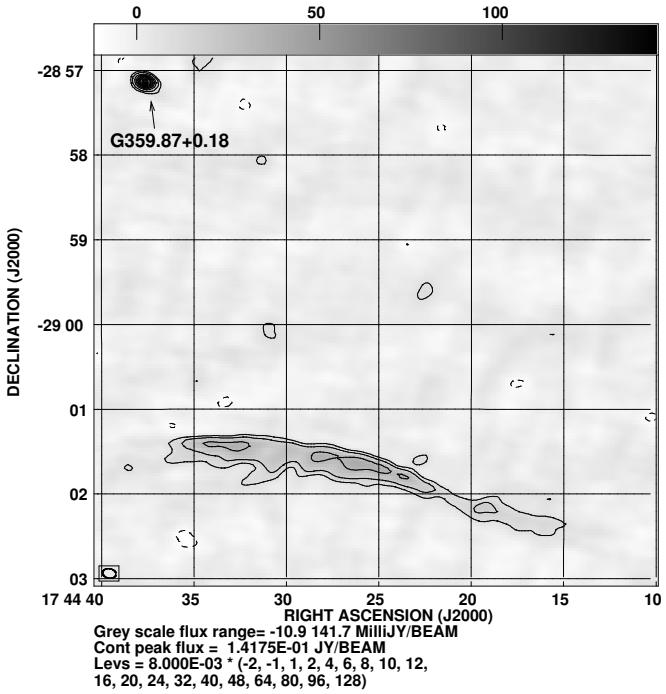

Figure 4.6: Continuum image of the NTF G359.79+0.17 at 1.4 GHz with a resolution of 9.7 x 6.7 arcsec^2, along PA=79°. The rms noise is 3.0 mJy beam^{-1}.

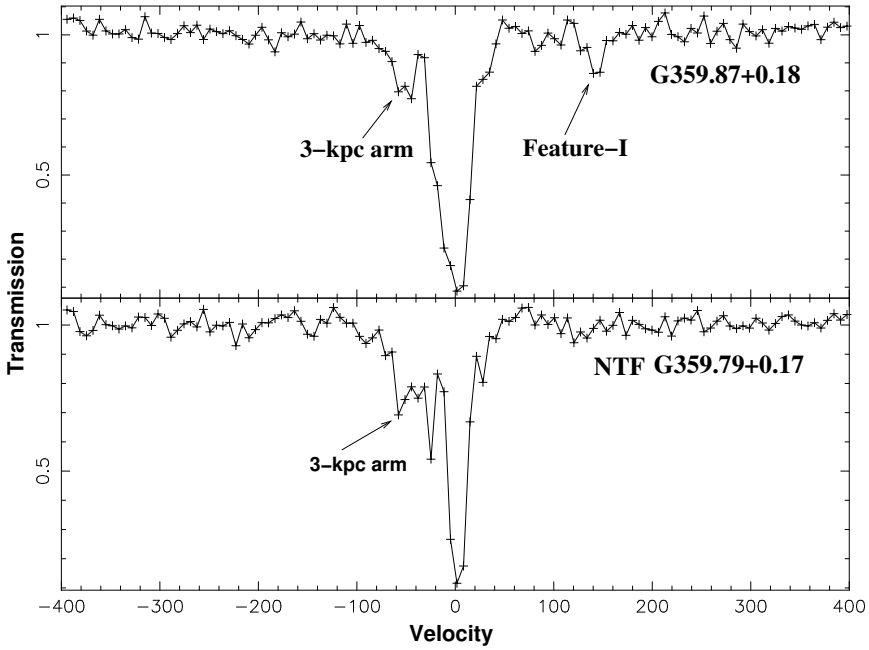

Figure 4.7: HI absorption spectrum towards the extragalactic source G359.87+0.18 and the NTF G359.79+0.17. The bandwidth is 4 MHz. RMS noise in the two spectra are 0.028 and 0.026 respectively.

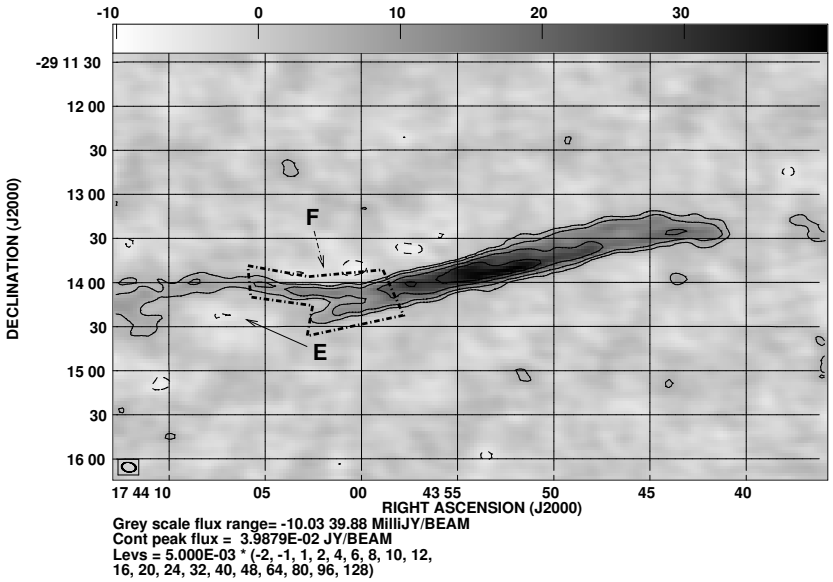

Figure 4.8: Continuum image of G359.54+0.18 at 1.4 GHz with a resolution of 9.6 x 6.4 arcsec^2, along PA=79°. The rms noise is 1.7 mJy beam^{-1}.

detected another molecular cloud near -90 km s^{-1} near the eastern edge of the NTF (not seen in Fig. 4.8). Since the eastern edge of the NTF G359.54+0.18 is faint in radio-continuum, no useful HI absorption spectrum could be obtained.

4.4 Discussion

4.4.1 Identification of HI features & constraints on the distances to the NTFs

Identification of HI absorption feature is performed by comparison with features of known velocities. Absorption indicates that the continuum source is located on the far side of the HI cloud and thereby provides a constraint on the distance to the continuum source. The velocities and the distances of the known HI emission features towards the three NTFs studied here have been discussed in Sect. 4.1 and summarised in Table 4.2, which will be used to constrain the distances to the NTFs.

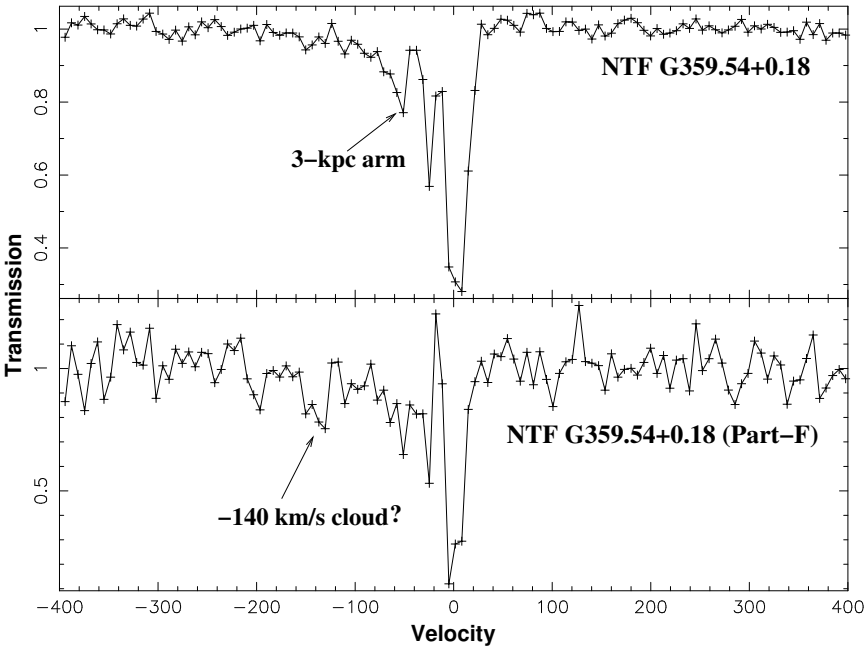

Figure 4.9: HI absorption spectrum integrated over the NTF G359.54+0.18 and towards a smaller portion of the NTF where it bends (region 'F' in Fig. 4.8). The bandwidth is 4 MHz. RMS noise in the two spectra are 0.025 and 0.1 respectively.

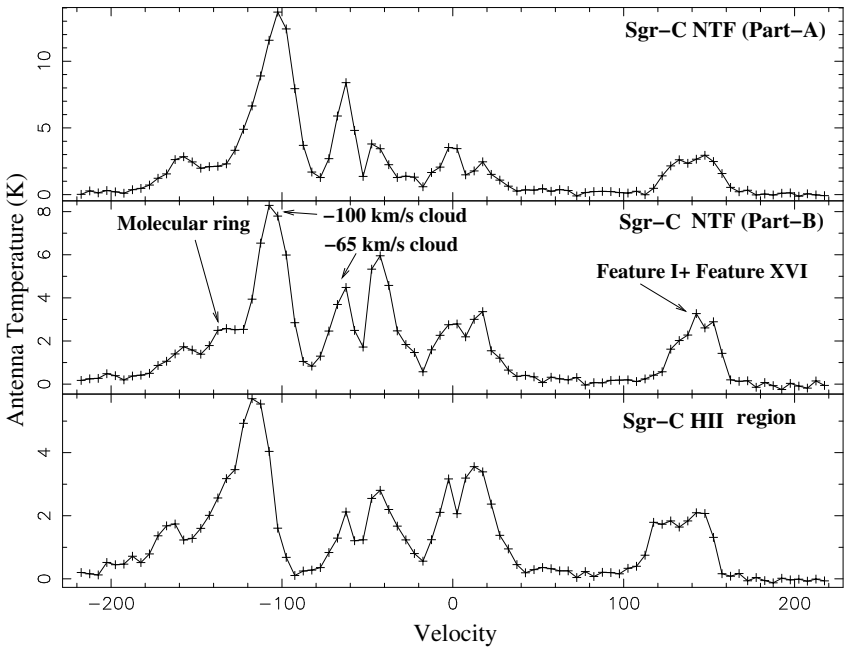

Figure 4.10: CO emission spectra towards the central part (top panel) (marked 'A' in Fig. 4.1) and the eastern part of the NTF (middle), along with the spectrum taken towards the Sgr C HII region (bottom) (Data courtesy Oka et al. (1998)).

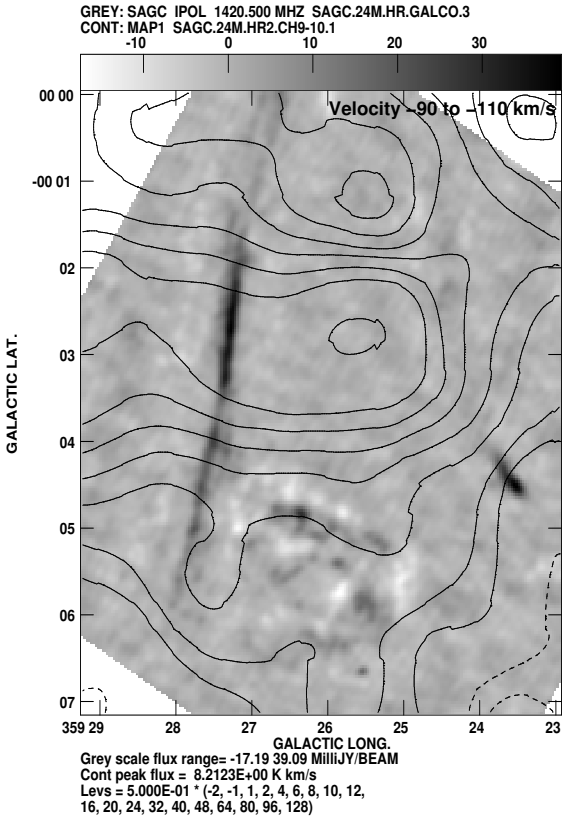

Figure 4.11: CS emission (contours) averaged over a velocity range of -110 to -90 km s^{-1} superimposed on a grey scale radio-continuum image of the Sgr C NTF in Galactic co-ordinate. CS data courtesy Tsuboi et al. (1999)

Table 4.2: Velocities and distances of the HI emission features

Name of the HI feature	Velocity km s^{-1}	Distance kpc	References for Distances
'0 km feature'	-30 to 30	Unknown	
'3 kpc arm'	-53	5.1	Cohen & Davies (1976)*
'Molecular ring'	≈ -135	$\lesssim 8.5$	Cohen & Davies (1979)
'Nuclear disk'	≈ -170	$\lesssim 8.5$	"
'XVI'	+135	$\gtrsim 8.5$	"
'I'	+135	10.5	Cohen & Davies (1976)

* Distance of '3 kpc arm' corrected for a Galactic Centre distance of 8.5 kpc rather than 10 kpc.

4.4.1.1 Sgr C

Due to absorption by the line of sight HI gas and velocity crowding near $l = 0^{\circ}$, strong absorption is observed near 0 km s^{-1} in all spectra towards the Sgr C NTF and the HII region discussed in Sect. 4.3.1. Absorption by the '3 kpc arm' is observed at -54 km s^{-1} towards the Sgr C NTF and the HII region (Fig. 4.3 and 4.4). However, the broad absorption feature (Fig. 4.3) identified towards the central part of the Sgr C NTF (marked 'A' in Fig. 4.1) between -100 and -200 km s^{-1} is peculiar. Three distinct absorption features are detected in the same velocity range in the higher resolution spectrum of the HII region in Fig. 4.4. This suggests absorption by clouds whose velocities differ by an amount less than the individual line-width.

Absorption near -138 km s^{-1} is likely to be caused by the HI associated with the 'Molecular ring', which has a line-width of ≈ 40 km s^{-1} in emission (Cohen & Davies 1979). Detection of absorption beyond -160 km s^{-1} indicates absorption by the 'Nuclear disk' (Rougoor & Oort 1960). However, we were unable to identify the -100 km s^{-1} absorption with any known HI emission feature. We believe that this feature was missed due to beam dilution in the low resolution (single dish) HI surveys. We examined the existing CO (Oka et al. 1998) and CS (Tsuboi et al. 1999) emission line maps of this region (spatial resolution $\sim 1'$) made using the 45 m telescope of the Nobeyama Radio Observatory. Since these spectra have a much higher angular resolution than the single dish HI surveys, we attempted an identification of the -100 km s^{-1} feature with a CO or CS feature. The CO spectra towards parts 'A' and 'B' of the NTF and the HII region is shown in Fig. 4.10. Strong CO emission is indeed observed near -100 km s^{-1} (line-width ≈ 20 km s^{-1}). The antenna temperature from part 'A' of the NTF is a factor of 2 higher than part 'B'. The CS spectrum also shows a similar ratio. (CS emission traces dense molecular clouds with density $\sim 10^4$ cm^{-3}, which are typically found in the CMZ). Fig. 4.11 shows a contour image of this cloud in CS emission

(data courtesy Tsuboi et al. (1999)) within a velocity range of -110 and -90 km s^{-1}. Note that the molecular cloud covers almost the whole NTF, although the -100 km s^{-1} absorption is only observed towards part 'A'.

The -100 km s^{-1} molecular cloud has been catalogued by Oka et al. (2001) and by Miyazaki & Tsuboi (2000) (cloud 17 at l=359.48°, b=$-$0.042°). Using the estimated parameters of the cloud (radius $\approx$ 5 pc, mass 7.2×10^4 M$_\odot$), the mean density of this cloud is 3100 H_2 cm^{-3}. Assuming the ratio of atomic to molecular hydrogen is 0.01 (Liszt et al. 1983; Lasenby et al. 1989), the HI column density is 9.3×10^{20} cm^{-2}. We find that an assumed spin temperature of 100 K, and a line width of 20 km s^{-1} explains the observed HI optical depth of $\approx$ 0.5. Hence, we believe that we are observing absorption by HI associated with the -100 km s^{-1} molecular cloud.

Our high resolution spectrum of the Sgr C HII region shows the presence of two spectral features in the range of -50 to -65 km s^{-1}(Fig. 4.4). Liszt & Spiker (1995) have identified a molecular cloud towards Sgr C with a velocity of ≈ -65 km s^{-1}, which they call M359.5$-$0.15. The -54 km s^{-1} feature is identified with the 3 kpc arm, whereas the -61.5 km s^{-1} feature in our HI data is believed to arise from M359.5$-$0.15. The presence of absorption by the molecular cloud M359.5$-$0.15 indicates that the Sgr C HII region is either embedded in or located at the far side of the cloud. This result supports the suggestion of Liszt & Spiker (1995) that the Sgr C HII region (Fig. 4.2) is located in a cavity of M359.5$-$0.15. We note that CO emission near -65 km s^{-1} has been detected towards both part 'A' of the NTF and the HII region (Fig. 4.10). The lack of HI absorption towards part 'A' of the NTF indicates that it is located in the front of the -65 km s^{-1} cloud. Therefore, we believe that the Sgr C HII region is relatively farther away than the Sgr C NTF, which provides evidence against any interaction between the two (see the schematic in Fig. 4.13). Having identified the absorption features in the HI spectrum, here we estimate the distance of the Sgr C complex. Since absorption by the 'Molecular ring' and the 'Nuclear disk' have been detected towards the Sgr C NTF (part

'A' in Fig. 4.10) and the HII region, we can conclude that these objects seen in radio continuum are located at a minimum distance of these HI features. As the 'Molecular ring' and the 'Nuclear disk' are located within $\sim$ 200 pc of the GC, this provides a lower limit of $\approx$8.3 kpc to these objects. We note that despite the emission feature seen in the CO map at $\sim$140 km s^{-1} (Fig. 4.10), no corresponding HI absorption could be detected towards the Sgr C region. The CO emission from the molecular cloud at $\sim$140 km s^{-1} is likely to be associated with the HI features 'XVI' and 'I' and both these features are located at the far side of the GC. Absence of any absorption by the HI associated with these structures indicate that the Sgr C NTF and the HII region are located within a few hundred parsecs at the far side of the GC, which provides an upper limit to their distances.

There appears to be weak absorption (4 σ detection) towards part 'B' of the NTF at -137 km s^{-1} which appears to have been caused by the 'Molecular ring'. Since we expect a much stronger absorption if this part of the NTF is located at the far side of the 'Molecular ring', we suggest that the part 'B' of the NTF is embedded in the 'Molecular ring'. Also, since the 'Nuclear disk' is expected to be located farther away from the GC than the 'Molecular ring'; lack of absorption by this feature may indicate that there is a hole in the 'Nuclear disk' towards part 'B' of the NTF.

4.4.1.2 Objects located in the field of Sgr C: source C, D and FIR-4

The HI spectrum (Sect. 4.3.2) towards source 'C' (Fig. 4.1) shows absorption at -53 km s^{-1}, -123 km s^{-1} and -170 km s^{-1} (Fig. 4.5), which indicates HI absorption by the '3 kpc arm', 'Molecular ring' ('Molecular ring' is expected to have a velocity of ≈ -135 km s^{-1}, which differs in this case by less than the line-width) and the 'Nuclear disk' respectively. HI spectrum of FIR-4 also indicates absorption by the 'Molecular ring' at -135 km s^{-1} and the 'Nuclear disk' at ≈ -183 km s^{-1} (Fig. 4.5). Since the 'Molecular ring' and the 'Nuclear disk' are thought to be located within a few hundred

parsecs of the GC, HI absorption by these two features provides a lower limit of ≈ 8.5 kpc to the distances of the source 'C' and FIR-4. On the other hand, the spectrum taken towards the southern HII region 'D' (Fig. 4.2), shows no absorption near −53 km s^{-1} (Fig. 4.5). Liszt & Spiker (1995) have suggested that source 'D' is a local object due to the absence of non-zero velocity features in the HI spectrum. The absence of any non-zero velocity features in our spectrum also makes us draw a similar conclusion.

4.4.1.3 NTF G359.79+0.17 & G359.87+0.18

HI absorption near +140 km s^{-1} is observed (Fig. 4.7) towards the extragalactic source G359.87+0.18. The HI emission feature 'I' seen in HI (Cohen & Davies 1979) is located ≈ 2 kpc behind the GC and has a line of sight velocity of +135 km s^{-1} at this longitude. The HI feature 'XVI' located a few hundred parsecs behind the GC also has a similar velocity at this longitude. The absorption seen in Fig. 4.7 near +140 km s^{-1} matches closely with the velocity of these two features, which indicates that the absorption is caused by either one or a combination of both these features.

No HI absorption at high positive velocity is detected towards the NTF G359.79+0.17. However, CO emission has been detected near +140 km s^{-1} towards both G359.79+0.17 and the extragalactic source G359.87+0.18 (Fig. 4.12), which indicates that there is no hole in feature 'I' (or perhaps in feature 'XVI') along these directions. Consequently, the upper limit to the distance of the NTF is ≈ 10.5 kpc. The presence of absorption in the spectrum of the NTF up to a negative velocity of −58 km s^{-1} suggests absorption by the '3 kpc arm' and consequently, the lower limit to its distance is ≈ 5.1 kpc of the Sun.

Lazio et al. (1999) suggested presence of a −20 km s^{-1} cloud at the far side of the GC. Presence of a narrow absorption feature −26 km s^{-1} in our data towards the NTF G359.79+0.17 may indicate that it is embedded in this cloud. This cloud could have caused the somewhat wider absorption profile in the spectrum towards the extragalactic source G359.87+0.18 which is observed through a substantially longer line of sight path.

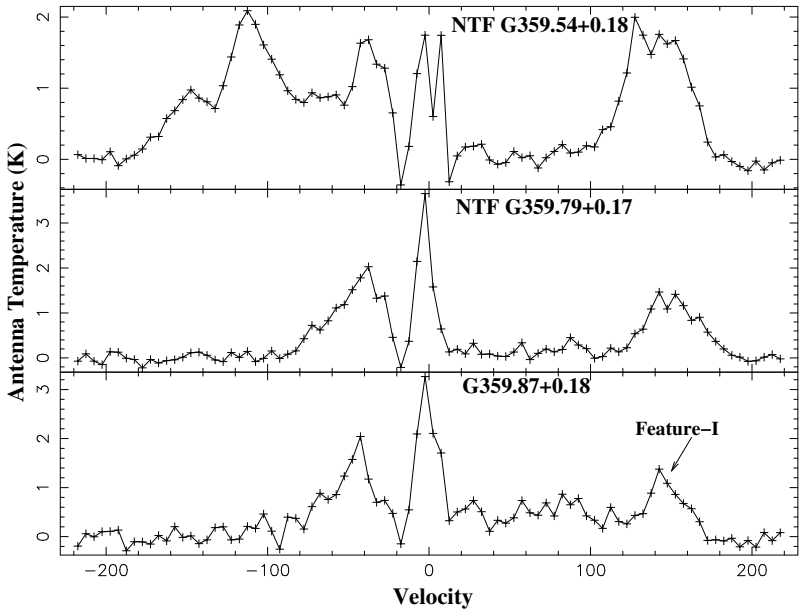

Figure 4.12: CO emission spectrum towards the NTF G359.54+0.18 (top), G359.79+0.17 (middle) and the extragalactic source G359.87+0.18 (bottom). Data courtesy Oka et al. (1998)

4.4.1.4 NTF G359.54+0.18

The spectrum of G359.54+0.18 (Fig. 4.9) is quite similar to that towards the NTF G359.79+0.17. The presence of absorption by the '3 kpc arm' near a velocity of -53 km s^{-1} clearly indicates that G359.54+0.18 is located beyond 5.1 kpc from the Sun. As G359.79+0.17 and G359.87+0.18, CO emission has also been detected towards this NTF at 140 km s^{-1} (Fig. 4.12), but, absence of HI absorption at this high positive velocity indicates that it is located within $\approx$ 10.5 kpc from the Sun. As described in Sect 4.4.1.3, this NTF also seems to be embedded in the -20 km s^{-1} cloud. We could detect weak HI absorption at 4σ level at -140 km s^{-1} (Fig. 4.9) toward part-F of the NTF shown in Fig. 4.8. A dense molecular cloud having the same velocity is also found to be present near this location (Staguhn et al. 1998). Since dense molecular cloud are typically found only in the CMZ, our observations suggest that the NTF G359.54+0.18 is also embedded in or located at the far side of the CMZ.

Table 4.3: HI column densities toward Sgr C, G359.79+0.17, G359.54+0.18 and G359.87+0.18

Column density (cm^{-2})	Central part of Sgr C NTF	Sgr C HII region	G359.79+0.17	G359.54+0.18	G359.87+0.18
N(H) (+155 to +125 km s^{-1})	–	–	–	–	$5.2 \times 10^{18}\ T_s$
N(H) (+35 to −35 km s^{-1})	$1.6 \times 10^{20}\ T_s$	$2.3 \times 10^{20}\ T_s$	$8.8 \times 10^{19}\ T_s$	$6.3 \times 10^{19}\ T_s$	$1.3 \times 10^{20}\ T_s$
N(H) (−77 to −40 km s^{-1})	$3.0 \times 10^{19}\ T_s$	$2.7 \times 10^{19}\ T_s$	$1.8 \times 10^{19}\ T_s$	$1.0 \times 10^{19}\ T_s$	$1.9 \times 10^{19}\ T_s$
N(H) (−90 to −200 km s^{-1})	$4.8 \times 10^{19}\ T_s$	$3.6 \times 10^{19}\ T_s$	–	–	–

4.4.2 HI column densities

We have estimated column densities for the HI feature 'I' (+155 to +125 km s^{-1}), the local foreground HI component (+35 to −35 km s^{-1}), the '3 kpc arm' (−77 to −40 km s^{-1}), and the combined 'Molecular ring' and 'Nuclear Disk' (−90 to −200 km s^{-1}) components towards the NTFs Sgr C, G359.79+0.17 and G359.54+0.18 and the extragalactic source G359.87+0.18. These column densities, expressed as a multiple of the spin temperature 'T_s', are presented in Table 4.3. The velocity limits for the various HI features were determined by visual inspection of the absorption spectra towards these sources. Since we could not separate the absorption by the'Molecular ring' and the 'Nuclear disk', we have quoted their total column densities. Due to the velocity crowding towards the GC, the optical depth of the local line of sight HI gas is large (i.e., $\exp(-\tau) \approx 0$). Therefore, any small error in estimating the optical depth would result in a comparatively larger error in the estimated column densities. Hence, the estimated total column densities of the foreground HI gas should be taken with caution. The column density of the line of sight HI gas (−35 km s^{-1} < velocity < 35 km s^{-1}) shown in Table 4.3 falls by a factor of 2 towards the NTFs G359.79+0.17 and G359.54+0.18 for $|b| \approx 0.2^{\circ}$, which suggests that the scale height of the HI gas at the distance of the GC is $\sim$ 27 pc.

The HI column density estimated from the optical depth towards the 'Snake' (G359.1−0.2) NTF (Uchida et al. 1992b) is 1.1 $T_s \times 10^{20}$ due to the local foreground HI component, 2.3 $T_s \times 10^{19}$ due to the '3 kpc arm', and 2.8 $T_s \times 10^{19}$ due to the 'Molecular ring'. These numbers are comparable (within a factor of two) with our estimated column density towards G359.54+0.18 and G359.79+0.17 given in Table 4.3. We note that the column density as quoted in Table 1 of Uchida et al. (1992b) towards all of their sources are incorrect and 100 times higher than what is found from their quoted optical depth.

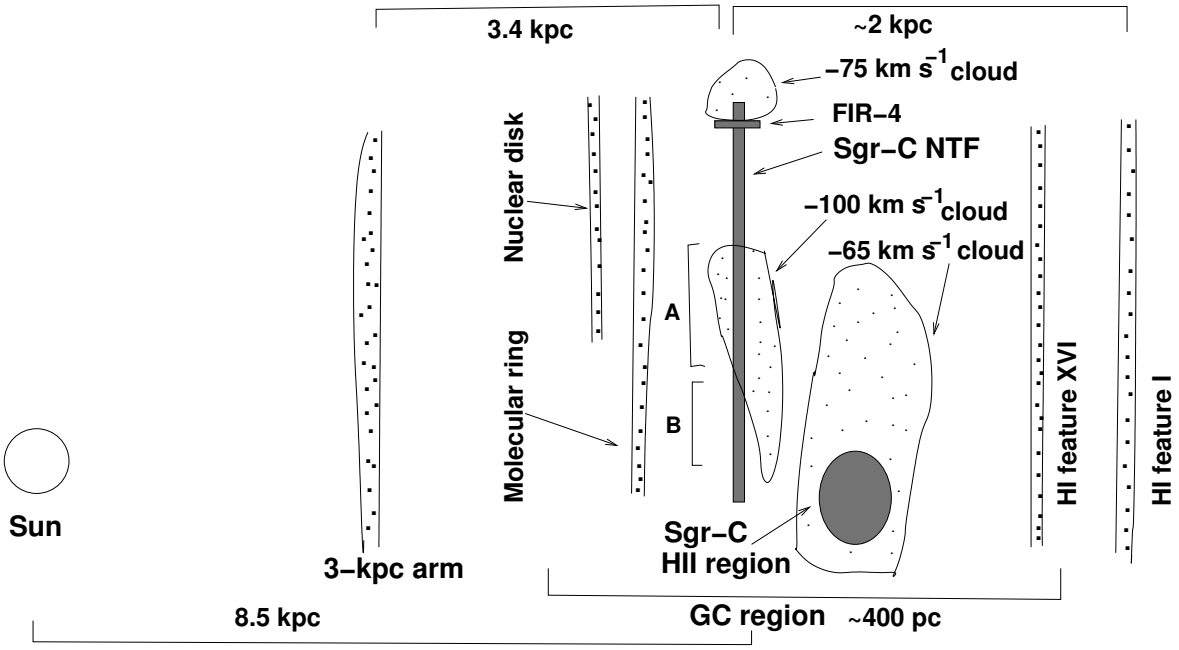

Figure 4.13: Schematic diagram of the Sgr C complex with HI absorbing clouds (not to scale) as seen from bottom of the Galaxy

4.4.3 Interaction of the molecular cloud with the Sgr C NTF

As shown in Sect. 4.3.1, no HI absorption by the -100 km s^{-1} cloud could be identified towards part 'B' of the Sgr C NTF (Fig. 4.3). However, HI absorption by the -100 km s^{-1} cloud could be identified towards part 'A' of the Sgr C NTF. From the ratio of CO brightness and temperature towards part 'A' and 'B' of the NTF (Sect. 4.4.1.1), we expect HI optical depth of $\approx$0.2 towards 'B' in the velocity range of -95 and -125 km s^{-1}, which is 5 times higher than the effective noise in the spectrum. Therefore, if the abundance of atomic hydrogen and the spin temperature (T_s) are the same in different parts of the cloud, HI absorption towards part 'A' and the lack of it towards part 'B' of the NTF can only be explained if 'A' is located at the far side and 'B' is located at the near side of the cloud and the NTF is at least partly embedded within the cloud. In Fig. 4.13, we show a schematic of the Sgr C complex in the GC region, including the relative location of the absorbing clouds about the Sgr C complex.

Here, we consider three possible scenarios that could have led the Sgr C NTF to be

partly embedded within the -100 km s^{-1} cloud.

(i) We first consider the case of the NTF tunnelling through the already existing -100 km s^{-1} cloud after being created. To penetrate the cloud, the high energy electrons in the NTF have to first ionise the neutral gas. With an estimated width of $35''$ (1.4 pc), length $255''$ (10 pc) and equipartition magnetic field of 100 μG (Anantharamaiah et al. 1991) in the NTF, the estimated total energy of the relativistic electrons is $\sim 2 \times 10^{47}$ erg. However, the energy required to ionise even a HI cloud (mean density 3100 cm^{-3}) of length equal to that of the size of the cloud (10 pc) and cross-sectional area equal to that of the NTF is $\sim 3 \times 10^{49}$ erg. Therefore, the energy of the relativistic electrons is less than 1% of the energy required to penetrate the molecular cloud. Hence, unless a tunnel in the cloud already exists, the electrons will not have sufficient energy to support this scenario.

(ii) Next, we consider the case, where the NTF does not penetrate the cloud, but the synchrotron electrons are generated from the ionised surfaces on either side of the -100 km s^{-1} cloud and follow the local magnetic field lines. In the case of the 'Radio-arc', which is comprised of several narrow filaments, the individual filaments appear to either end or begin from the HII region G0.18$-$0.04 (sickle like feature), located near the midpoint of the NTF. Based on the observations of the 'Radio-arc', Serabyn & Morris (1994) have proposed that association of the NTF, molecular cloud and HII region are necessary to explain the generation of high energy electrons forming the NTFs. In Fig. 2c of Liszt & Spiker (1995), we observe two filamentary structures towards the western side of the part 'A' of Sgr C NTF, which merge into a single brighter filament near 'A'. Our observations indicate that the -100 km s^{-1} cloud is associated with the NTF near 'A' (RA (J2000)=17h44m33s, DEC=$-29^{\circ}25'55''$). In this scenario, if the surface of this cloud is ionised, then association of the molecular cloud and HII region with the NTF satisfies the criterion of Serabyn & Morris (1994) to generate it. Here, if the electrons flowing towards part 'A' is at the far side and part 'B' lies at the near side of the

cloud, then the absence of -100 km s^{-1} HI absorption against part 'B' can be explained. However, no such ionised surface of the cloud (as HII region) like G0.18$-$0.04 has been detected near part 'A' of the NTF from the Nobeyama millimetre array observation of this region (Tsuboi et al. 1991) at 22 GHz. Thus, the above scenario also fails to explain the observations.

(iii) Finally, we consider an alternative source of the synchrotron electrons in the Sgr C NTF and the case of collision of the -100 km s^{-1} cloud with this already existing NTF. Liszt & Spiker (1995) proposed that the HII region FIR 4 (Odenwald & Fazio 1984) is associated with the Sgr C NTF, with the HII region acting as the source of relativistic electrons. Fig. 7 in Liszt & Spiker (1995) shows a molecular cloud around this HII region. We note that FIR-4, with its wedge-like morphology, is similar to the HII region G0.18$-$0.04, discussed earlier. The longer side of FIR-4 lies almost perpendicular to the direction of the NTF, thereby suggesting interaction between the NTF and the HII region in a way similar to the Radio-arc. The CS data (Tsuboi et al. 1999) shows a compact dense molecular cloud with a velocity of -75 km s^{-1}, which coincides with the position of FIR-4. However, in the absence of any recombination line detection from this HII region, actual association of FIR-4 and the -75 km s^{-1} cloud cannot be verified. In Sect. 4.4.1.2, it is shown that the lower limit to its distance is ≈ 8.5 kpc, which is consistent with its proposed association with the NTF. Therefore, if we assume that the FIR-4 acts as the source of relativistic electrons to the Sgr C NTF, collision of the -100 km s^{-1} cloud with the central part of the NTF, which causes the NTF to appear partly embedded in the cloud, can also explain the observations. After the collision of the cloud with the NTF, if the magnetic pressure in the NTF would have been less than that of the cloud, the fields could be pinched or disrupted and the flow of high energy electrons towards part 'B' significantly reduced. On the other hand, if the magnetic pressure in the NTF is much larger than the pressure due to the cloud (Yusef-Zadeh & Morris 1987a), then the NTF will remain stable and the cloud may wrap around the NTF.

Here, the flow of electrons from the FIR-4 to part 'B' of the NTF will not be significantly disrupted.

If flow of electrons has stopped in part 'B' (first possibility), then this part of the NTF is likely to show a steeper spectral index. However, the estimated spectral index between 1.6 GHz and 330 MHz is quite flat, which LaRosa et al. (2000) has suggested to be due to the presence of thermal emission from the nearby HII region. In this regard, we note that if the -100 km s^{-1} cloud is moving with a velocity similar to its line of sight velocity in the sky plane, then the collision took place around 5×10^4 years ago. However, to our knowledge, part 'B' of the NTF has been imaged with high resolution and sensitivity only up to a few GHz and at this frequency range, the half-life of synchrotron electrons responsible for the emission in an equipartition field of 0.1 mG (LaRosa et al. 2000) is $\sim 10^5$ years. Therefore, unless the magnetic field is much higher than the equipartition value, no significant steepening of the spectral index may be detectable in the presently available data. Hence, to distinguish between the two cases, future polarimetric observations, which traces the direction of the local magnetic field lines, and can show that whether the magnetic field lines in part 'B' are pinched, will be useful. We prefer the third model, taking into consideration the available information. Since the NTF does not show any change of shape or direction near the place of interaction with the -100 km s^{-1} cloud, the magnetic pressure in the NTF is likely to be more than the pressure of the cloud.

4.5 Summary

HI absorption studies of three NTFs known as the Sgr C, G359.54+0.18 and G359.79+0.17 using the GMRT have yielded the following results:

(a) For the first time, the Sgr C NTF and the HII region are shown to be located within a few hundred parsecs of the GC.

(b) Our study indicates that the Sgr C HII region is either embedded in or located behind the -65 km s^{-1} molecular cloud, whereas the Sgr C NTF is located at the near side of the cloud, which argues against any possible interaction between the two objects.

(c) A molecular cloud with a velocity of -100 km s^{-1} appears to be associated with the central part of the Sgr C NTF, and on the basis of the presently existing data, it appears that the magnetic pressure in the NTF is higher than the pressure due to the -100 km s^{-1} cloud.

(d) HI absorption by the '3 kpc arm' is detected against all the three NTFs, which indicates that the NTF G359.54+0.18 and G359.79+0.17 are located at a minimum distance of 5.1 kpc from the Sun.

(e) Weak HI absorption ($4\,\sigma$ level) at -140 km s^{-1} suggests that the NTF G359.54+0.18 is located at a minimum distance of ≈ 8.5 kpc from us.

(f) The maximum distance of the NTF G359.54+0.18 and G359.79+0.17 is estimated to be 10.5 kpc from the Sun.

The present study extends the number of NTFs that have been found to be located near the GC region to five. With most of the known NTFs now being shown to be near the GC, there remains little doubt that phenomena related to the central region of the Galaxy are responsible for the creation and maintenance of the NTFs.

Chapter 5

Extragalactic sources behind the central region of the Galaxy

5.1 Introduction

Studies of the propagation effects of the interstellar medium on radio sources provide a wealth of information on the physical conditions in the medium. Extragalactic radio sources are particularly valuable as probes of the Galactic ISM. Unlike pulsars, the line of sight towards these sources could pass through distant parts of the Galaxy, thereby allowing to observe the integrated effect of the medium along large ($\sim$20 kpc) line of sight distance. These sources being located randomly in the sky, also sample the ISM in all directions. Unfortunately, such propagation studies near the central $-6^\circ < l < 6^\circ$, $-5^\circ < b < 5^\circ$ region of the Galaxy are hampered by the absence of a well defined sample of extragalactic radio sources in the region. The high obscuration at optical wavelengths and the confusion due to the high concentration of stars at infrared wavelengths have prevented identification of such sources in this region. High angular resolution studies at centimetre wavelengths can identify compact radio sources (Becker et al. (1994) at 5 GHz and Zoonematkermani et al. (1990) at 1.4 GHz), but in the presence of a large number of Galactic sources near the GC, identification of extragalactic sources is non-trivial. Therefore, only about half a dozen extragalactic sources in this region have been identified (Bower et al. 2001).

We have initiated a project to probe the magnetic field and the electron density in the Galactic Centre region by studying the Faraday rotation measure (RM) of a sample of extragalactic sources whose lines of sight pass through this region. To carry out these observations, a reasonably large sample of polarised extragalactic radio sources were required. From the existing literature, we formed a sample of 64 small diameter ($< 10''$) sources, which we have studied with high angular resolution at 4.8 (C band) and 8.5 GHz (X band) with the ATCA and the VLA. All the sources in our sample were studied for linear polarisation taking special care to avoid bandwidth depolarisation up to a RM of 15,000 rad m^{-2}. Though NVSS (Condon et al. 1998) had the capability to detect polarised emission from sources, in the likelihood of high RM (> 350 rad m^{-2}) introduced by the Galactic Centre (GC) ISM, its observing bandwidth of 50 MHz would have caused the extragalactic sources to be bandwidth depolarised. Therefore, our observations for the first time provide reliable estimation of polarisation properties of the sources in the region. These observations have almost an order of magnitude higher sensitivity (in Stokes I) and a resolution up to 3 times higher than the previous VLA Galactic plane survey (GPS), and this high sensitivity coupled with higher resolution has helped to separate the Galactic sources from the sample.

In this chapter, we present the basic data on the morphology, polarisation fraction and the spectral indices of the these sources and based on these properties, we try to separate the Galactic sources from the sample. Out of 64 sources, 60 are identified as possible extragalactic sources and in the next chapter, present their Rotation Measures and draw inferences for the magnetic field in the GC region.

5.1.1 Sample selection

We surveyed the literature and formed a sample of possible extragalactic radio sources in the central $-6^\circ < l < 6^\circ$, $-2^\circ < b < 2^\circ$ of the Galaxy. The sources were selected on the basis of their small scale structure ($\leq 10''$) and non-thermal spectra ($\alpha \leq -0.4$, S(ν)

$\propto \nu^{\alpha}$). For the sources to have detectable linear polarisation and so be useful for the Rotation Measure study, we assumed that the polarisation fraction of the unresolved sources to be greater than 2.5% (Saikia & Salter 1988), and sources with estimated flux density greater than 10 mJy at 5 GHz were selected. The source catalogues used for this selection were VLA maps of the GC region at 327 MHz (LaRosa et al. 2000), the VLA survey of the Galactic plane (GPS) at 1.4 GHz (Zoonematkermani et al. 1990), (Helfand et al. 1992) and at 5 GHz (Becker et al. 1994). Sources observed by Lazio & Cordes (1998a) and the 365 MHz Texas survey (Douglas et al. 1996) were also used for this purpose. The sources, for which no flux density estimates were available at 5 GHz, the flux density at 5 GHz were estimated from the extrapolation of their 1.4 GHz flux density using their spectral indices estimated between 327 MHz and 1.4 GHz. A total of 64 sources were found that satisfied the above criteria.

5.2 Observations and data reduction

A pilot project was initially carried out using the ATCA, where twelve sources were observed with two IF frequencies set at 4.8 and 5.9 GHz. The ATCA consists of six 22-m radio antennas. Five of the six antennas lie along a three kilometre railway track, which is oriented east-west. The sixth antenna lies on a 75-m rail-track three kilometres further west, thus allowing a maximum ATCA baseline of six kilometres. The 6-km configuration of the ATCA was used for the pilot project and subsequent observations. Further observations were made with the ATCA and 24 more sources were observed in the C and X band with IF frequencies at 4.8, 5.3, 5.9 and 8.5 GHz. The bandwidth of all the ATCA observations was 128 MHz. The pseudo continuum mode provides 16 frequency channels across the band and this mode was used for all our observations. Details of the observations are summarised in Table 5.1. Each target source was typically observed for a total of 40–50 minutes in each IF pair. Since the ATCA is nearly an east-west array,

multiple-snapshot mode was used to get a satisfactory *uv*-coverage and each source was observed $\approx$ 10 times equally spaced in hour-angle. The sources 1741-312 and 1748-253 were used as secondary calibrators and 1938-612 was used as primary flux density calibrator. 1938-612 (polarisation fraction $\leq$ 0.2%) was also used for determining antenna based polarisation leakage. The data from the ATCA was based on linearly polarised signals and the calibration and editing of the ATCA data was performed using the Multichannel Image Reconstruction Image Analysis and Display (MIRIAD) package. After calibration, the data were converted to Stokes I, Q, U, V and taken into Astronomical Image Processing System (AIPS) for imaging, self-calibration and further analysis.

We used the VLA in its BnA configuration to observe the comparatively weak sources in the sample. For this purpose, the default continuum mode which provides a single frequency channel of bandwidth 50 MHz in each IF band was used. The selected IF frequencies were 4.635, 4.885, 8.335 and 8.685 GHz. The secondary calibrators used for the observation were the same as in the ATCA observations. Polarisation calibration was performed using the unpolarised source 3C84. 3C286 was used as the primary flux density calibrator and to estimate the instrumental phase difference between the two circularly polarised (RR and LL) signals. Each source was observed for typically 5 minutes at 2 different hour angles. The details of these observations are in Table 5.1. All the data were calibrated and processed using the AIPS package.

5.3 Results

From the ATCA data, 24 sources were found to have at least one polarised component. Maps of these sources are shown in Fig. 5.1. The resolution of each of the ATCA maps are $\approx 6'' \times 2''$, and the typical RMS noise is 0.23 mJy/beam in Stokes I and about 0.15 mJy/beam in Stokes Q and U. From these maps, 7 of the 24 sources are found to have single unresolved component and the rest are either partially resolved, or have more than

Table 5.1: Details of our observation

Date	Telescope	Array	Observing Time (Hour)	Band	Number of sources Observed
06 Feb 2000	ATCA	6A	10	C	12
30 Sept 2000	ATCA	6B	12	C	12
02 Oct 2000	ATCA	6B	12	C	12
06 Oct 2000	ATCA	6B	12	C & X	12
06 Oct 2000	ATCA	6B	12	C & X	12
11 Feb 2001	VLA	BnA	06	C	28
13 Feb 2001	VLA	BnA	06	X	32
12 Apr 2002	ATCA	6B	11	C	08

one component.

From VLA observations, 21 sources were found to have at least one polarised component. Maps of these sources along with 2 polarised phase calibrators are shown in Fig. 5.2. The VLA maps have an angular resolution $\sim 2'' \times 1.5''$, and RMS noise of typically 75 μJy/beam. In these maps, four sources appear to have a single unresolved component.

Maps of the unpolarised sources from the ATCA and VLA observations are shown in Fig. 5.3 and Fig. 5.4 respectively.

The observed properties of the 45 polarised sources and 2 secondary calibrators are presented in Table 5.2, which is arranged as follows. Column 1: the source name using the Galactic co-ordinates (G$l \pm b$). If the source has been observed with the ATCA, then we put 'AT' as superscript in the source name. Sources are arranged with increasing l, with the sources observed with the ATCA being arranged first. Column 2: the component designation ('N' denotes Northern, 'S' denotes Southern, 'E' denotes Eastern and 'W' denotes Western, 'EX' denotes highly extended and 'R' denotes ring type component respectively). Columns 3 and 4: Right ascension (RA) and Declination (DEC) of the radio intensity peaks of the components in J2000 co-ordinates. Column 5: the deconvolved size of the components with their major and minor axes in arcsec and the

position angle (PA) in degrees (arranged as major axis $\times$ minor axis, PA). A few sources have multiple components, which are not well resolved in the 4.8 GHz map. These components are much better resolved in the 8.5 GHz map due to higher resolution. For these sources, we have estimated the size parameters of the components from the 8.5 GHz map, and we put a '*' beside the estimated parameters. Columns 6 and 7: the corresponding peak and total flux density of the components at 4.8 GHz in units of mJy beam^{-1} and mJy respectively. Column 8: total flux density of the component at 4.8 GHz, as estimated by the VLA GPS. Column-9: percentage polarisation of the components. Column 10: estimated spectral index of the components between 8.5 and 4.8 GHz from our observations. A few of the sources are extended over several synthesised beam-widths and for these sources, comparing the integrated flux density of the components are difficult. Therefore, after convolving the 8.5 GHz maps of these sources to the resolution of the corresponding 4.8 GHz maps, we made spectral index maps of these sources. We quote the spectral indices of each of the components from these maps at the position of the peak flux density of the components. For all these sources, we put an 's' beside the estimated spectral indices. Column 11: spectral index between 4.8 and 1.4 GHz. Column 12: spectral index between 1.4 and 0.3 GHz. In Table 5.3, we present the properties of the sources which are found to be unpolarised. This Table is similar to Table 5.2, except that in the absence of polarisation, we have removed the column representing percentage polarisation (column 9 in Table 5.2). For the four HII regions detected, we write in column 12 of this Table, 'HII reg.' in place of spectral indices.

To compute the spectral indices of the sources in Table 5.2, the 1.4 GHz flux density of the sources have been taken from the VLA GPS and the NRAO VLA Sky Survey (NVSS) (Condon et al. 1998). If the estimated flux density of a component in the GPS differs from that in the NVSS by more than 20%, we have put a † mark beside the computed spectral indices. We have visually examined the NVSS maps of these sources, and if we find that the source is not in a confused region of the map, we have used the

flux density from NVSS to compute the spectral index and in that case, we put '(N)' beside the estimated spectral index. For a few of the source, the 1.4 GHz flux density could not be estimated, but its flux density is known at other two frequencies (4.8 and 0.3 GHz). In these cases, we put a '*' in column 11, and put the estimated spectral index between 4.8 and 0.3 GHz in column 12 with '(0.3/4.8)' shown in the next row. The P band flux density of the sources have been taken from the Texas survey at 365 MHz (Douglas et al. 1996). However, the Texas survey is known to have large uncertainty in the estimated flux density. This is especially true near the complex GC region, where lack of good *uv*-coverage drastically increases the problems of imaging. Therefore, if the sources are detected in the GC map at 330 MHz (LaRosa et al. 2000), we have used their flux density to compute the spectral index (column 12 in Table 5.2 and column 11 in Table 5.3) and put 'GC' in parenthesis beside the estimated spectral index. For 5 sources, the flux density at 330 MHz have been taken from Roy & Rao (2002), and we put '(GM)' beside the spectral index in column 12. We have also taken the flux density of 3 sources at 330 MHz from Bhatnagar (private communication) and put '(GM1)' in column 12. Many of the sources resolved at 1.4 GHz and above appear unresolved in the low frequency Texas survey. For these source, we only compare the integrated flux density of the sources between 1.4 and 0.3 GHz, and put '(i)' beside the estimated spectral index in column 12.

5.3.1 Reliability of the estimated spectral indices

It is well known that if the angular size of an object is greater than $\lambda/(2 \times `d')$ (where, angular size is in radian, λ is the observed wavelength, and 'd' is the length of the shortest baseline), then its flux density will be underestimated by an interferometer. This problem is more severe in the GC region, where emission at various size scales may coexist. Since, our observations are performed at comparatively high radio frequencies, the contribution of the extended synchrotron background of the Galaxy is negligible.

Most of these sources have small angular size, and therefore, the problem of missing flux density should be minimal. However, the problem of missing flux density increases with observed frequency, and it can affect the estimated flux density of the extended sources at 8.5 GHz. We could detect extended emission $\sim 10'$ in the 4.8 GHz maps of G353.410-0.360, G355.424-0.809, G355.739+0.131, G356.905+0.082, G358.149-1.675, G358.643-0.034, G359.2-0.8 (Mouse), G359.717-0.036, G0.313+1.645 and G5.791+0.794. Since, the configuration of the interferometric array was the same during our observations at 4.8 and 8.5 GHz, the 8.5 GHz maps of the above 10 sources can suffer from the missing flux density problem. Therefore, to check for any missing flux density at 8.5 GHz, we sampled the Fourier Transform of the CLEAN components of the 4.8 GHz maps of the sources at the *uv*-points of the 8.5 GHz data and made maps (equivalent of mapping the sources at 4.8 GHz using the *uv*-coverage of our 8.5 GHz observations). A comparison of these maps with the corresponding 4.8 GHz map shows that except for G353.410-0.360, G355.739+0.131, G356.905+0.082, G358.643-0.034, G358.149-1.675, G359.2-0.8 (Mouse) and G359.717-0.036, the missing flux density for all the other sources are less than 10% of the total flux. Among the above 7 sources, 4 have been identified as HII regions. The spectral index between 8.5 and 4.8 GHz (Table 5.3) of the 2 remaining extragalactic sources, G356.905+0.082 and G358.149-1.675 have been estimated only for the compact components (hot spots and the central component). Similar technique has also been followed for estimating the spectral index of the Galactic non-thermal source G359.2-0.8 (Mouse).

Due to extended emission and enhanced source confusion near the GC, maps made with radio interferometers suffer quite often from systematic errors. These fields are normally identified and mentioned in published catalogued. However, in the absence of the availability of the maps of the Galactic plane survey and the Texas survey, we consider the effect of the systematic errors in these maps quite uncertain. To check the reliability of the source flux densities in these surveys, we compared the 1.4 GHz flux

densities of our sample sources as estimated by the VLA Galactic plane survey and the NVSS. More than 20% flux density variation was found for about 20% of the sources in our sample. 20% difference in flux density contributes an error of about 0.13 in the estimated spectral indices (assuming the actual spectral index is ~ -0.7) between 4.8 and 1.4 GHz of the sources. We also compared the flux density of the sources, which were detected both in the Texas survey and in the 330 MHz VLA GC map (LaRosa et al. 2000). Twelve sources were found to have counterparts in both the surveys. The flux densities estimated for six of these sources from the Texas survey differ almost by a factor of two than what is estimated from the GC map at 330 MHz. The accuracy of the flux densities estimated from the GC map is expected to be much better than the Texas survey, and therefore, if the P band flux density of a source is estimated from the Texas survey, an error $\sim$0.5 can occur in its estimated spectral index between the L band (1.4 GHz) and the P band (0.3 GHz). We note that other than the missing flux density problem, there are several other factors which could lead to erroneous measurement of the spectral index. In the GC region, insufficient *uv*-coverage can contribute systematic error in the estimated flux densities. Also, since these observations are made at different epochs, source variability could be an additional factor contributing error in the estimated spectral indices. It should, however be noted that at higher radio frequencies (typically above 1.4 GHz), source variability is mostly intrinsic. The central region (core) of active galaxies typically has a flat spectral index, which shows large variability in time scale of days to years. However, most of the sources in our sample have a steep spectral index ($\alpha \leq 0.5$) and lack of core dominated objects in our sample indicates little intrinsic variability ($\leq 10\%$) of the sources. On the other hand, at low radio frequencies, source variability is mostly interstellar in origin, and the typical timescale could be of years. However, interstellar scintillation is most prominent for objects with prominent compact (milli arc-seconds) cores, lack of which in our sample indicates that the low frequency variability of these objects will be quite small ($\leq 10\%$).

Table 5.2: Estimated parameters of the polarised sources

Src Name	Cmp	RA (J2000)	DEC (J2000)	$S_{maj} \times S_{Min}$,PA	S_p	S_t mJy	S_5 mJy	% Poln.	$\alpha_{8.5/4.8}$	$\alpha_{4.8/1.4}$	$\alpha_{1.4/0.3}$
354.740+0.138^{AT}	N	17 31 56.99	−33 18 34.1	0.8×0.0, 146	61	67	52.6	2.6	−1.2	−1.0†	−0.8 (i)
	S	17 31 57.00	−33 18 41.6	4.3×1.6, 0	14	13	”	8	−1.1		
356.000+0.023^{AT}	E	17 35 39.74	−32 18 54.2	2.3×1.2, 103*	30	42	34.7	7	−0.9	−0.8	−1.1 (GM)
	C	17 35 40.15	−32 18 57.0	0.9×0.0, 24*	29	34	79.2	9	−0.6	−0.5	
	W	17 35 40.40	−32 18 59.0	1.3×1.1, 107*	36	38	79.2	6	−1.0	−0.6(i)	
356.161+1.635^{AT}	E	17 29 42.63	−31 18 02.1	3.1×1.0, 81	21	38		5.6	−1.1	−0.7	−0.9 (i)
	W	17 29 43.80	−31 18 05.6	2.4×0.7, 101	44	69		11	−1.0	−0.8	
356.567+0.869^{AT}	N	17 33 44.85	−31 22 33.6	6.1×4.4, 119	11	31			−1.5	−0.55†	−0.9 (i)
	S	17 33 45.82	−31 22 51.2	3.4×1.3, 140	21	46		14	−1.6	−0.65	
356.719−1.220^{AT}	E	17 42 27.41	−32 22 08.3	3.4×2.1, 141	19	30		11	−1.0	−0.8	−0.9 (i)
	W	17 42 27.96	−32 22 15.3	2.0×1.8, 102	24	35		7	−1.0	−0.6	
358.002−0.636^{AT}	C	17 43 17.87	−30 58 18.7	0.4×0.0, 165	277	283		1	−0.4	−0.26	−0.3
358.917+0.072^{AT}	C	17 42 44.00	−29 49 16.0	0.3×0.0, 2	99	101	74	1.5	−1.4	−1.05	−1.2 (GC)
359.388+0.460^{AT}	C	17 42 21.47	−29 13 00.9	0.5×0.0, 178	39	41		3	−0.9	−0.65†	−0.4 (GC)
359.844−1.843^{AT}	C	17 52 30.91	−30 01 06.6	1.4×1.0, 74	154	181		1.6	−0.6	−0.2	−0.9 (GC)
359.911−1.813^{AT}	C	17 52 33.1	−29 56 44.8	0.6×0.0, 01	132	149		4	−0.9	−0.2	−0.9 (GC)
359.993+1.591^{AT}	E	17 39 26.49	−28 06 18.2	1.2×0.0, 176	13	14			−1.2	−0.9	−0.5 (GC)

Source Name	Cmp	RA (J2000)	DEC (J2000)	$Smaj \times S_{Min}$,PA	S_p	S_t mJy	S_5 mJy	% Pol.	$\alpha_{8.5/4.8}$	$\alpha_{4.8/1.4}$	$\alpha_{1.4/0.3}$
	W	17 39 26.94	−28 06 12.6	1.5×0.0,46	11	12		10	−0.8	−0.66	
0.313+1.645^{AT}	E	17 40 00.27	−27 48 11.6	3.4×2.1, 144*	17	32		16	−0.7	−0.6	
	C	17 40 00.65	−27 48 15.9	2.3×0.9, 155*	07	08			−0.1	„	−0.55 (GC)
	W	17 40 01.08	−27 48 22.0	2.3×0.0, 131*	11	21			−1.3	−0.8	
0.537+0.263^{AT}	C	17 45 52.48	−28 20 26.6	2.5×0.0, 175	71	79	121	1.6	0.64	0.44	
1.028−1.110^{AT}	N	17 52 22.51	−28 37 34.1	2.4×0.9, 153	23	26		6	−1.1	−0.8	−1.0 (GC)
	S	17 52 22.81	−28 37 42.1	1.3×0.0, 142	40	45		6	−1.1	−1.0	
1.035+1.559^{AT}	N	17 42 01.90	−27 13 10.3	2.3×0.0, 17	50	67		24	−1.2	−0.73	−0.86 (GC)
	C	17 42 03.42	−27 14 16.3	1.7×0.0, 85	02	02			0.0		
	S	17 42 05.22	−27 15 10.2	3.7×2.6, 119	02	09					
1.505−1.231^{AT}	E	17 53 55.37	−28 15 53.8	1.8×0.8, 109	30	56		17	−1.7	−0.43	−1.3 (i)
	W	17 53 59.21	−28 17 21.3	0.7×0.0, 13	23	25		12	−1.0	−0.7	
2.143+1.772^{AT}	C	17 43 51.24	−26 10 59.6	0.8×0.4, 150	45	48		4.5	−1.5	−1.25	−1.1
4.005+1.403^{AT}	S	17 49 31.68	−24 46 58.5	1.7×0.0, 163	52	71		4	−0.8	−0.7	−0.8 (i)
	N	17 49 32.30	−24 46 45.7		01	03					
4.188−1.680^{AT}	S	18 01 44.34	−26 10 43.6	1.8×0.7, 25	29	44		13	−1.4	−0.5	−1.3 (i)
	C	18 01 45.97	−26 10 17.6	1.4×0.6, 22	06	06			−0.7		
	N	18 01 47.04	−26 10 02.0	6.7×4.2, 16	04	16			<-2.0	−0.84	
4.256−0.726^{AT}	E	17 58 11.76	−25 38 49.1	1.0×0.0, 165	08	09			−0.8	−0.8	−0.84 (i)
	W	17 58 13.00	−25 38 44.7	1.7×0.5, 63	13	17		18	−1.5	−1.0	

Source Name	Cmp	RA (J2000)	DEC (J2000)	$S_{maj} \times S_{Min}$,PA	S_p	S_t mJy	S_5 mJy	% Pol.	$\alpha_{8.5/4.8}$	$\alpha_{4.8/1.4}$	$\alpha_{1.4/0.3}$
5.260−0.754[AT]	C	18 00 31.50	−24 47 21.3	0.7×0.5, 68*; 0.6×0.4, 84*	66	89		10	−0.8	−0.8	−0.45
5.358+0.899[AT]	E	17 54 27.34	−23 52 33.8	1.4×0.0, 8*; 1.7×0.5, 7*	24	45			−0.4	−0.85	−0.95 (i)
	W	17 54 27.78	−23 52 36.2	0.8×0.2, 40*	31	33		6	−1.2	−0.9	
5.511−1.515[AT]	S	18 03 59.28	−24 56 45.6	5.3×1.0, 01	62	85		4	−0.8	−0.6	−1.1
	N	18 03 59.43	−24 56 30.8		02	04				−0.8	
6.183−1.480[AT]	N	18 05 18.04	−24 20 26.7	3.6×1.6, 09	08	10			−0.8	−1.0†	−1.2 (i)
	S	18 05 18.04	−24 20 45.5	3.6×0.9, 08	19	24		14	−1.1	−0.9	
353.462−0.691	C	17 31 55.40	−34 49 59.9	0.4×0.2, 165	98	103		0.6	−0.9	−0.9	−0.7
354.815+0.775	E	17 29 36.26	−32 53 52.1	0.8×0.5, 71	6.8	8.2			−1.2	−1.0	−0.9 (i)
	W	17 29 36.64	−32 53 51.7	0.5×0.4, 176	18.2	20.2		5	−1.4	−1.0	
355.424−0.809	N	17 37 32.54	−33 14 36.7	2.7×1.3, 57	6.5	22		20	−1.0 s	−1.0 (N)	−0.9
	C	17 37 32.07	−33 14 50.7	1.5×1.0, 167	1.0	1.1			−1.0 s		
	S	17 37 31.40	−33 15 10.4	1.5×1.1, 176	11	24		12	−0.8 s		
356.905+0.082	C	17 37 43.79	−31 31 13.7	3.6×0.4, 179	40	43	32	3	−0.1		−0.4 (GM)(i)
357.865−0.996 (1741−312)	C	17 44 23.58	−31 16 36.0	0.1×0.0, 22	369	370		1.4	0.2	0.4†	−0.5 (i)
358.149−1.675	E	17 47 45.32	−31 23 37.4	2.1×1.4, 124	8.9	57		25	−1.0 s	−1.0 (N)	−0.77
	C	17 47 48.13	−31 23 15.2	0.3×0.0, 18	7.4	7.6			0.1 s		

Source Name	Cmp	RA (J2000)	DEC (J2000)	$Smaj \times S_{Min}$,PA	S_p	S_t mJy	S_5 mJy	% Pol.	$\alpha_{8.5/4.8}$	$\alpha_{4.8/1.4}$	$\alpha_{1.4/0.3}$
	W	17 47 50.13	−31 23 03.9	0.7×0.4, 60	13	98		12	−0.8 s		
358.156+0.028	N	17 41 02.91	−30 29 22.1	0.5×0.5, 113	23.7	30	31	13	−0.9	−0.6	−1.0 (GC)
	C	17 41 02.90	−30 29 27.3	0.5×0.0, 04	1.7	1.5			−0.1		
	S	17 41 02.67	−30 29 36.1	1.5×0.7, 39	3.0	4.2	5.2	21	−0.8	−0.86	
358.930−1.197	E	17 47 46.36	−30 28 17.8	1.5×0.9, 27	8.9	22		26	−0.6 s	−0.4 (i)	−1.4 (GC)
	W	17 47 47.54	−30 28 11.7	2.6×1.3, 22	4.5	14.8			−0.7 s		
359.392+1.272	E	17 39 12.44	−28 47 02.7	2.2×1.2, 33	6.9	24.5		16	−0.6	−0.9 (N)	−0.76 (GC)
	W	17 39 13.46	−28 46 53.7	2.8×1.5, 40	5.1	20.4		20	−0.7		
359.2−0.8 (Mouse)	C	17 47 15.78	−29 58 01.0	3.2×2.2, 20	11.3	20.2		13	0.3		−0.3 (GC) (i)
359.604+0.306	E	17 43 28.39	−29 06 47.6	2.8×1.0, 77	2.6	7.7	–		−1.0	*	−0.8 (GC) (i)
	C	17 43 28.77	−29 06 47.0	0.7×0.1, 81	2.5	2.7	3.3		−0.1		(0.3/4.8)
	W	17 43 29.26	−29 06 47.1	1.4×0.9, 14	6.7	10.8	7.6	12	−1.0		
359.710−0.904	E	17 48 27.73	−29 39 10.3	4.0×1.9, 67	2.4	23		23	−1.4	*	−0.75 (GC)
	C	17 48 28.58	−29 39 10.9	0.4×0.0, 52	0.7	0.7			−1.5		(0.33/4.8)
	W	17 48 29.39	−29 39 11.8	5.5×2.5, 90	2.3	23.6		15	−1.7		
359.871+0.179	E	17 44 36.22	−28 57 14.9	1.7×0.0, 78	1.5	2.2		5	−0.8	−0.5 (L)	−0.26 (GC)
	C	17 44 36.84	−28 57 11.5	0.2×0.0, 11	7.9	8.1			−0.8	−0.4	
	W	17 44 37.08	−28 57 09.7		41	46	34		−1.3	−1.0	
0.404+1.061	E	17 42 27.93	−28 02 08.5	0.4×0.1, 130	13.5	14.8		11	−1.3	−1.0†(i)	−0.9 (GC)
	W	17 42 28.25	−28 02 10.9	0.7×0.1, 97	07.5	10.0			−1.3		
1.826+1.070	N	17 45 47.67	−26 49 05.6	1.8×1.3, 176	7.5	20.2		8	−1.3	−0.86	−0.9 (i)

Source Name	Cmp	RA (J2000)	DEC (J2000)	$S_{maj} \times S_{Min}$,PA	S_p	S_t mJy	S_5 mJy	% Pol.	$\alpha_{8.5/4.8}$	$\alpha_{4.8/1.4}$	$\alpha_{1.4/0.3}$
	S	17 45 47.17	−26 49 21.5	0.9×0.0, 08	9.8	16.4		23	−1.0	−0.6	
2.922+1.028	N	17 48 29.18	−25 54 15.8	1.1×0.9, 37	13.8	16.7		6	−1.1 s	−0.8 (i)	−0.94
	S	17 48 29.09	−25 54 18.0	0.6×0.5, 11	21.3	25.4		8	−1.1 s		
3.347−0.327	C	17 54 38.31	−26 13 50.9	1.7×0.9, 168	4.8	10.3	6	20	−1.2	−1.1†	−1.2 (GM)
3.745+0.635 (1748−253)	C	17 51 51.26	−25 24 0.0	0.0×0.0, 0	446	446		2.6	−1.0	−1.0	0.1 (GM1)
3.748−1.221	E	17 58 58.66	−26 20 02.1	0.4×0.0, 27	11.3	12.9		10	−1.3	−1.0†(N) (i)	−0.77 (GM)
	W	17 58 59.75	−26 19 56.8	0.0,0.0, 00	2.8	3.1			0.1		
3.928+0.253	C	17 53 43.37	−25 26 10.3	0.2×0.0, 178	120	122	67.9	2	0.2	*	0.0 (GM1) (0.3/4.8)
4.752+0.255	C	17 55 33.41	−24 43 30.6	1.2×1.1, 143	26	46	33.2	7	−1.3	−1.1†	−0.8
5.791+0.794	E	17 55 48.31	−23 33 21.9	3.1×1.3, 77	17.7	64		17	−1.4 s		
	C	17 55 48.60	−23 33 21.1	1.9×0.0, 77	10.8	13.9		17	−1.0 s	−1.0†(N)	−0.8
	W	17 55 48.82	−23 33 20.5	1.6×1.5, 68	12.7	49		30	−1.3 s		
5.852+1.041	N	17 55 00.75	−23 22 32.4	1.5×0.4, 01	9.2	21.8		12	−1.0	−0.9	−1.1 (i)
	S	17 55 00.80	−23 22 52.0	3.4×1.2, 119	2.8	12.8		24	−1.5	−0.75	

Table 5.3: Estimated parameters of the unpolarised sources

Src Name	Cmp	RA (J2000)	DEC (J2000)	$Smaj \times S_{Min}$,PA	S_p	S_t	S_5	$\alpha_{8.5/4.8}$	$\alpha_{4.8/1.4}$	$\alpha_{1.4/0.3}$
354.719-1.117^{AT}	N	17 36 57.84	−34 00 30.0	0.4×0.0, 01	92	91		−0.8	−0.8	−0.6 (i)
	S	17 36 57.19	−34 00 37.6	1.2×0.0, 01	06	07		−1.2	−1.1	
357.435-0.519^{AT} (357A)	C	17 41 26.32	−31 23 30.3	6.0×2.0, 167	49	73		–	−0.8	−0.6 (GM)
358.982+0.580^{AT} (358B)	C	17 40 54.52	−29 29 50.6	0.3×0.0, 7	44	44		–	−0.6*	−0.5 (GC)
359.568+1.146^{AT} (359B)	C	17 40 07.79	−28 42 03.0	0.4×0.4, 38	113	114		–	−0.5	−0.4 (GC)
358.591+0.046^{AT}	C	17 42 02.71	−30 06 41.7	1.0×0.0, 26	25	25	17	−0.8	−1.0*	−1.1 (GC)
359.546+0.988^{AT}	C	17 40 41.56	−28 48 10.7	0.0×0.0, 0	35	35		−0.8	−0.8*	−0.5 (GC)
0.846+1.173^{AT}	C	17 43 05.43	−27 36 05.2	1.3×0.0, 7	43	46		−0.9	−1.0	−0.8 (GC)
1.954-1.702^{AT}	C	17 56 49.65	−28 07 37.4	0.7×0.0, 171	60	60		−1.6	−1.1*	−0.4
2.423-1.660^{AT}	C	17 57 43.61	−27 42 02.0	0.6×0.3, 11	46	46		−1.1	−0.8	−1.0
4.898+1.292^{AT}	C	17 51 57.26	−24 04 24.9	0.9×0.0, 26	51	52		−1.3	−1.1	−0.9
353.410-0.360	C	17 30 26.14	−34 41 44.9	2.6×2.1, 51	149	469	155	0.0	0.1	HII reg.
355.739+0.131	EX	17 34 34.24	−32 28 34.3	∼12×10, -	28	256	155	−0.1	0.1	HII reg.
358.643-0.034	EX	17 42 29.08	−30 06 34.6	∼20×20, -	07	169	48	−1.2	0.4	HII reg.
358.605+1.440	C	17 36 38.76	−29 21 26.4	0.4×0.0, 17	39	40		−0.8	−0.7	−0.7

Source Name	Cmp	RA (J2000)	DEC (J2000)	$S_{maj} \times S_{Min}$,PA	S_p	S_t	S_5	$\alpha_{8.5/4.8}$	$\alpha_{4.8/1.4}$	$\alpha_{1.4/0.3}$
359.717-0.036	R	17 45 05.08	−29 11 45.0	∼22×20, –	12	198	28	−1.3	–	HII reg.
4.005+0	C	17 54 38.87	−25 27 30.7	1.0×0.0, 165	08	09		−0.8	−0.8	–
4.619+0.288	C	17 55 07.96	−24 49 21.7	0.8×0.3, 10	22	25	21	−1.1	−0.9*	−0.45

5.4 Discussion

5.4.1 Galactic sources

Extended unpolarised structures, typical of HII regions, are seen in the VLA images of the sources G353.410-0.360, G355.739+0.131, G358.643-0.034 and G359.717-0.036. The field of G353.410-0.360 has a small diameter source and extended emission is seen around this object. The small diameter source has a flat spectrum between 8.5 and 4.8 GHz. The small diameter object is well resolved in our BnA array map and so it is unlikely to be the flat spectrum core of a background extragalactic source. Therefore, we believe that it is a Galactic HII region.

The 8.5 GHz BnA array map of G359.717-0.036 (Fig. 5.5) clearly show a partial shell like structure. Extended emission can also be seen around this object. Since shell like structures are seen both for HII regions and SNRs, we have tried to estimate its spectral index accurately. We made a map of this object at 8.4 GHz using the archival VLA data taken near this source using the CD array (Project Code AY68 and the observations were made by Farhad Yusef Zadeh). We also imaged it at 1.4 GHz using the archival Galactic Centre data acquired and presented by Pedlar et al. (1989) using the B, C and D array of the VLA during 1981–1984. The low resolution 8.4 and 1.4 GHz map of this source show that the spectrum of this component is flat, indicating it to be an HII region.

The image of G358.643-0.034 at 8.5 GHz suffers from serious zero spacing problem and consequently, the estimated steep spectral index between 8.5 and 4.8 GHz (Table 5.3) is in error. However, its spectrum between 4.8 and 1.4 GHz is inverted, and it has not been detected in the 330 MHz GC map. Therefore, extended structure and inverted spectrum at low radio frequencies indicate that it is an HII region.

G355.739+0.131 has a flat spectrum between 8.5 and 1.4 GHz and is well resolved. This source is also not detected at 0.3 GHz, which suggests that its spectrum has turned over due to large free free absorption depth at low radio frequencies, indicating it to be

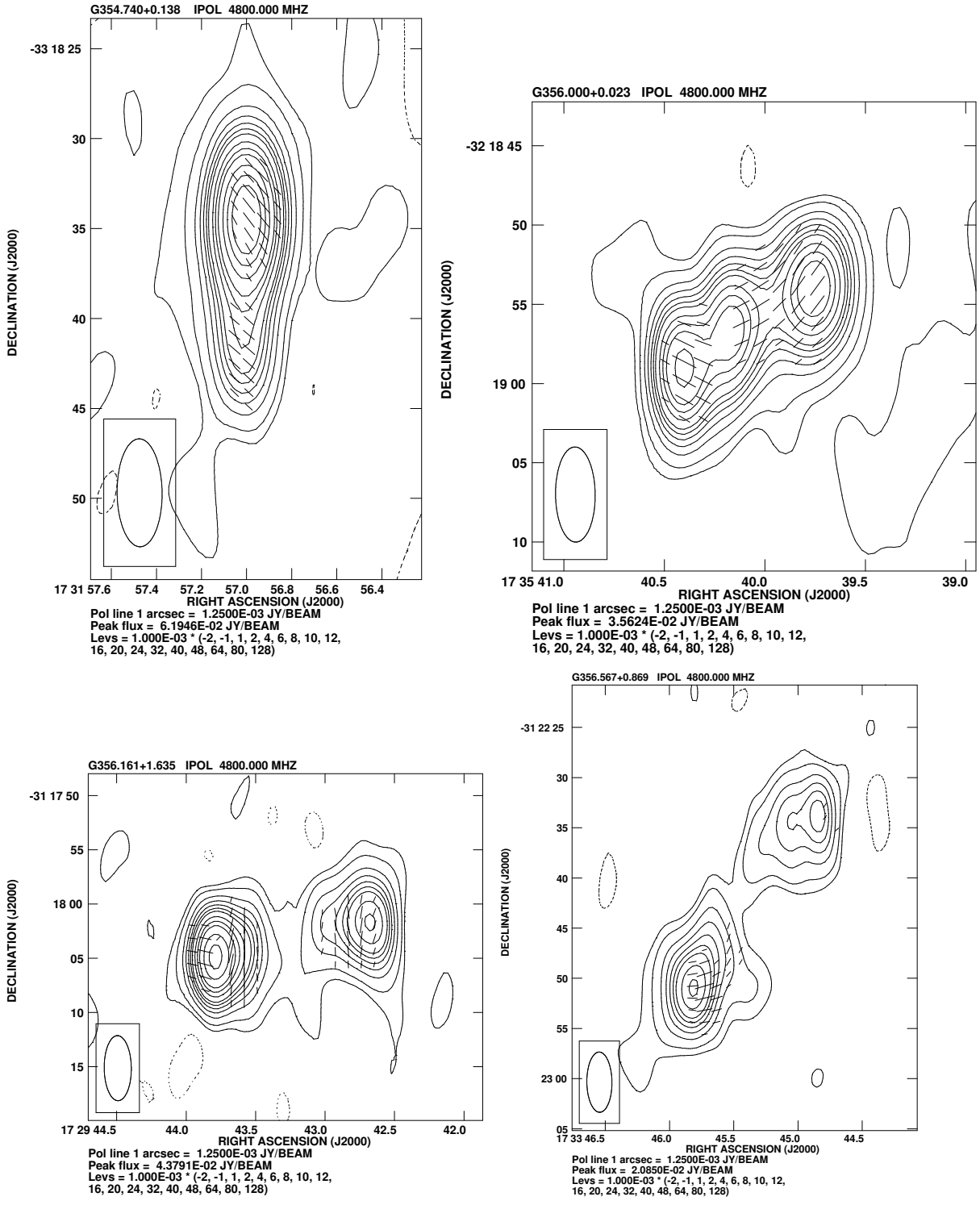

Figure 5.1: 4.8 GHz ATCA continuum maps of the polarised sources with the polarisation vectors superposed on them. Typical rms noise in Stokes I is about 0.23 mJy/beam and about 0.15 mJy/beam in Stokes Q and U. Typical beamsize of these maps are $\approx 6'' \times 2''$.

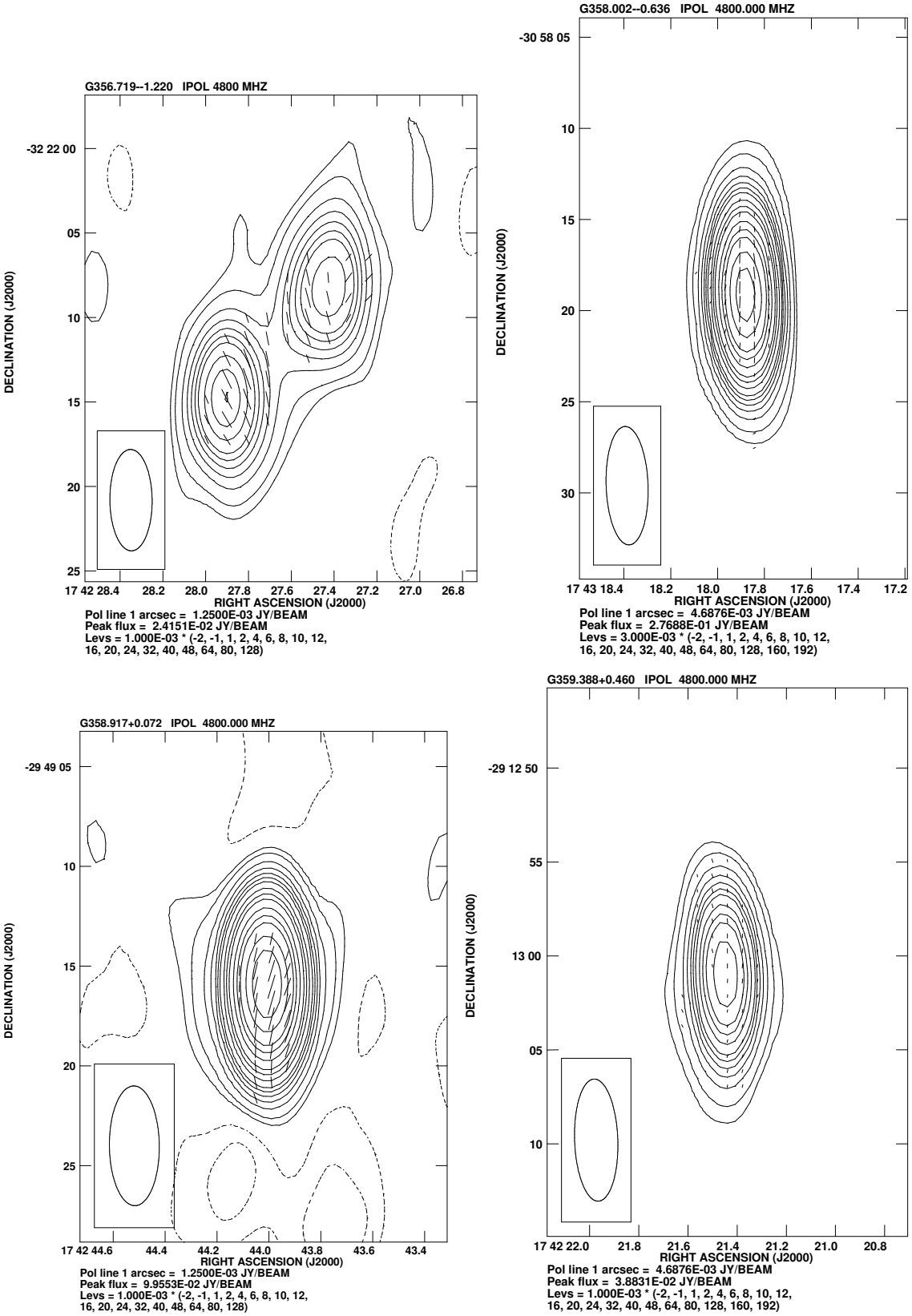

Figure 5.1: Continued

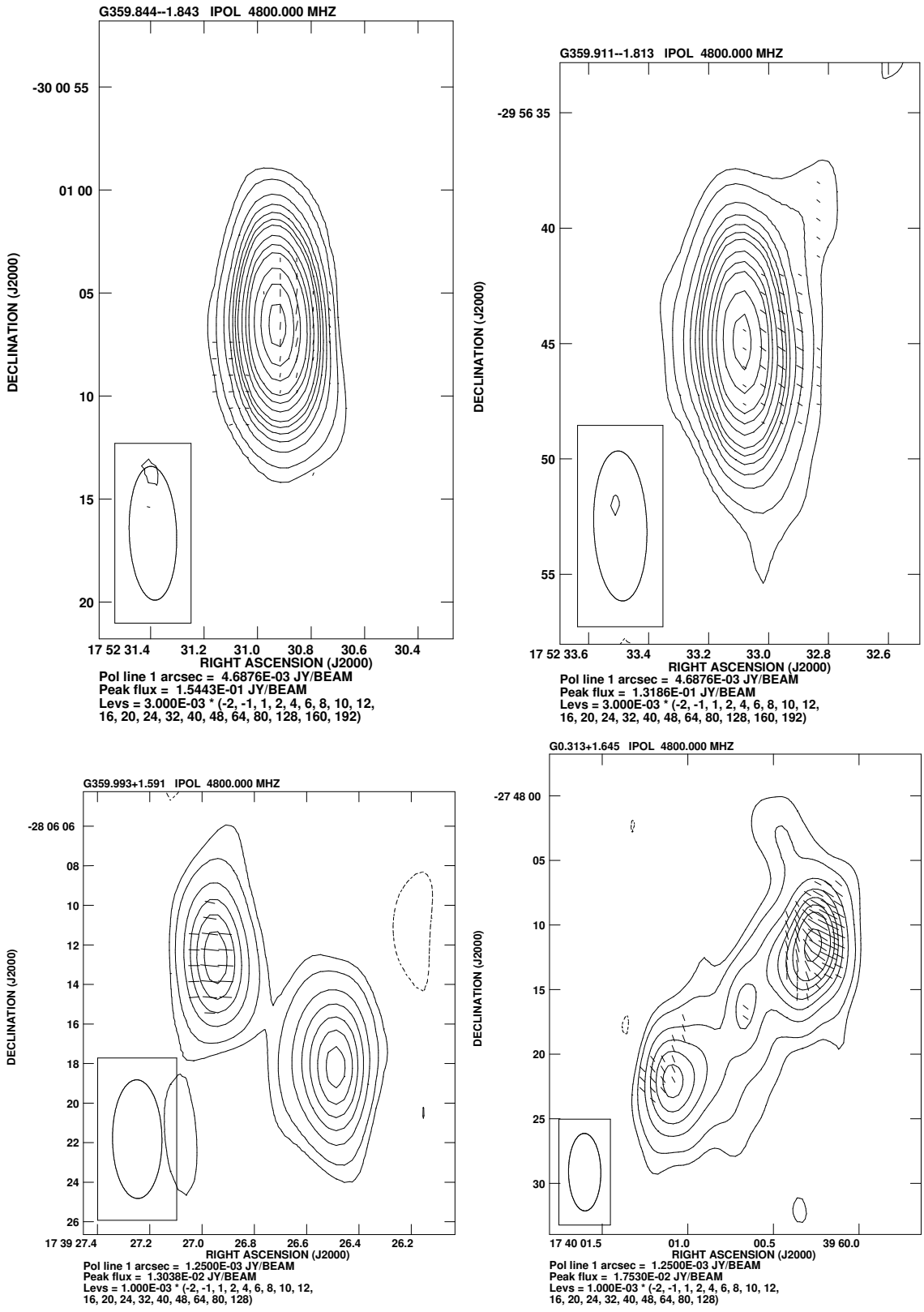

Figure 5.1: Continued

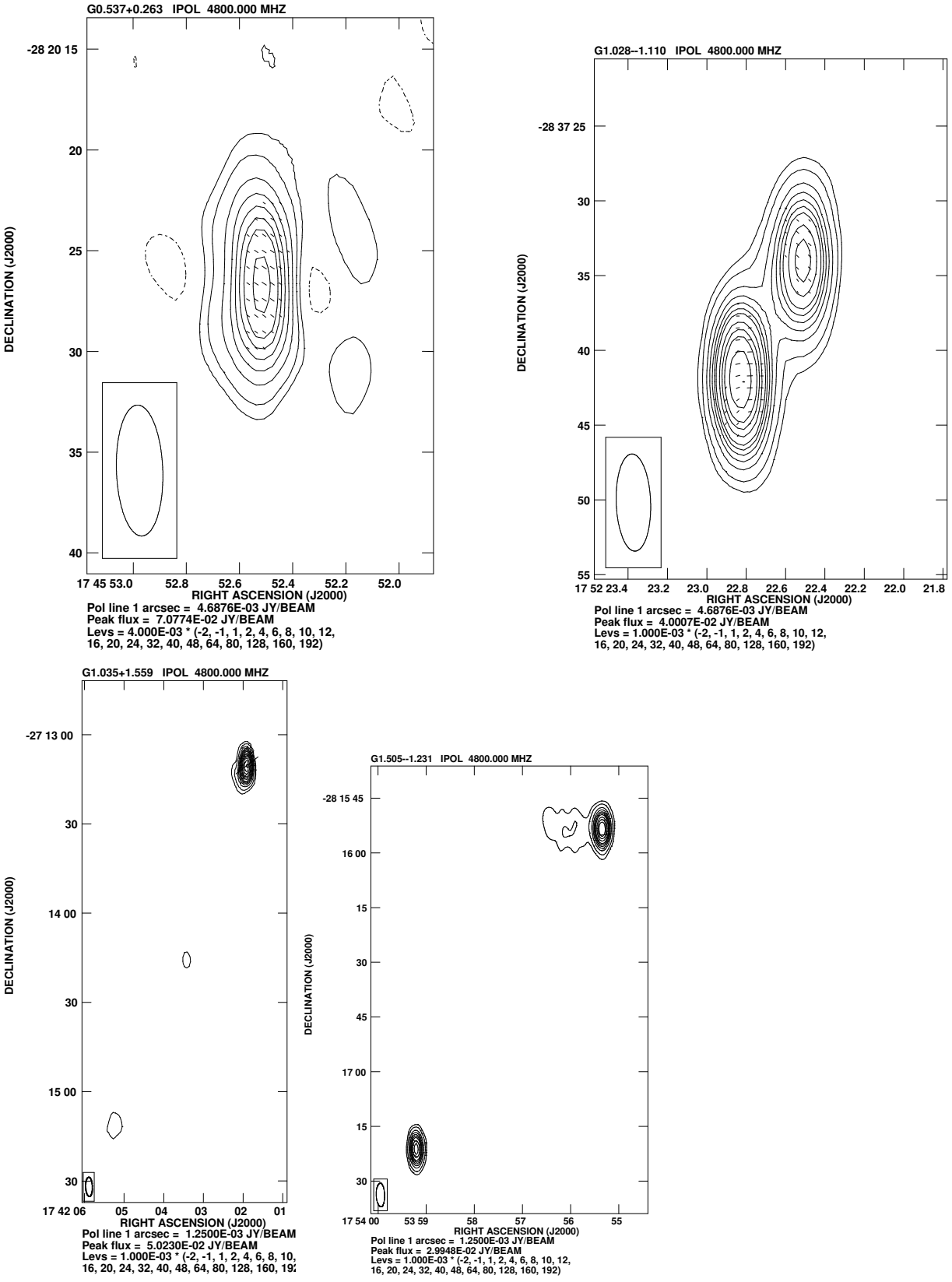

Figure 5.1: Continued

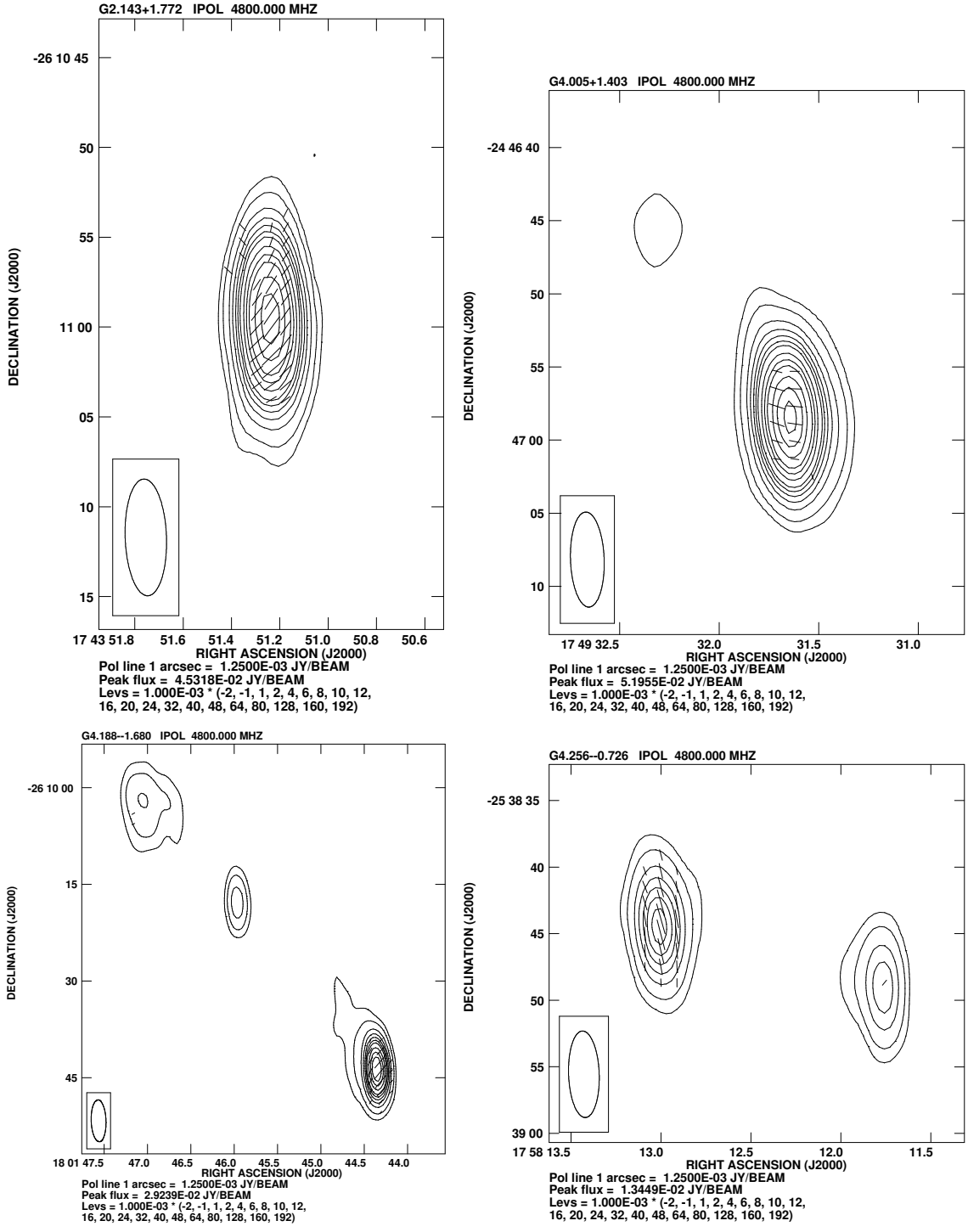

Figure 5.1: Continued

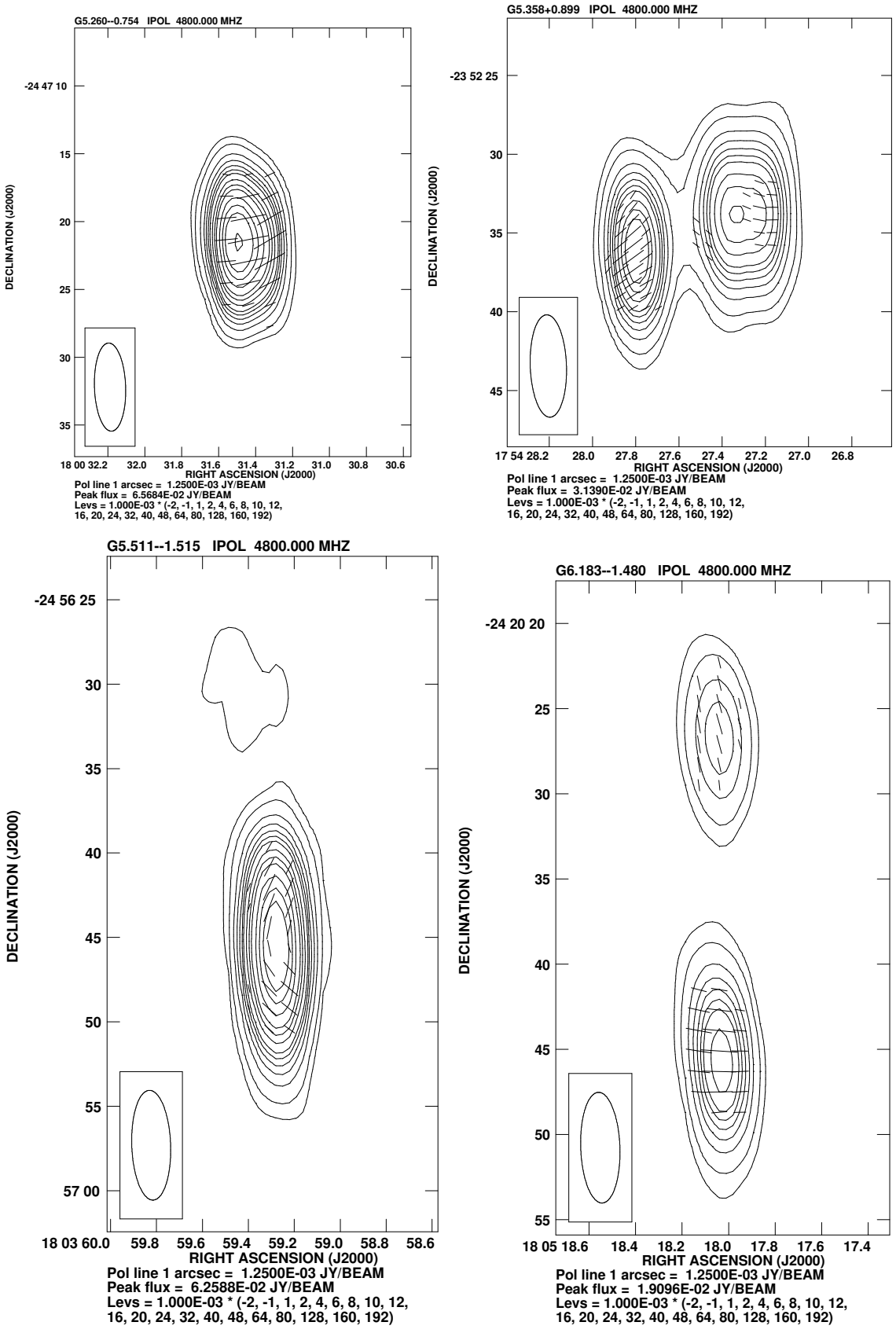

Figure 5.1: Continued

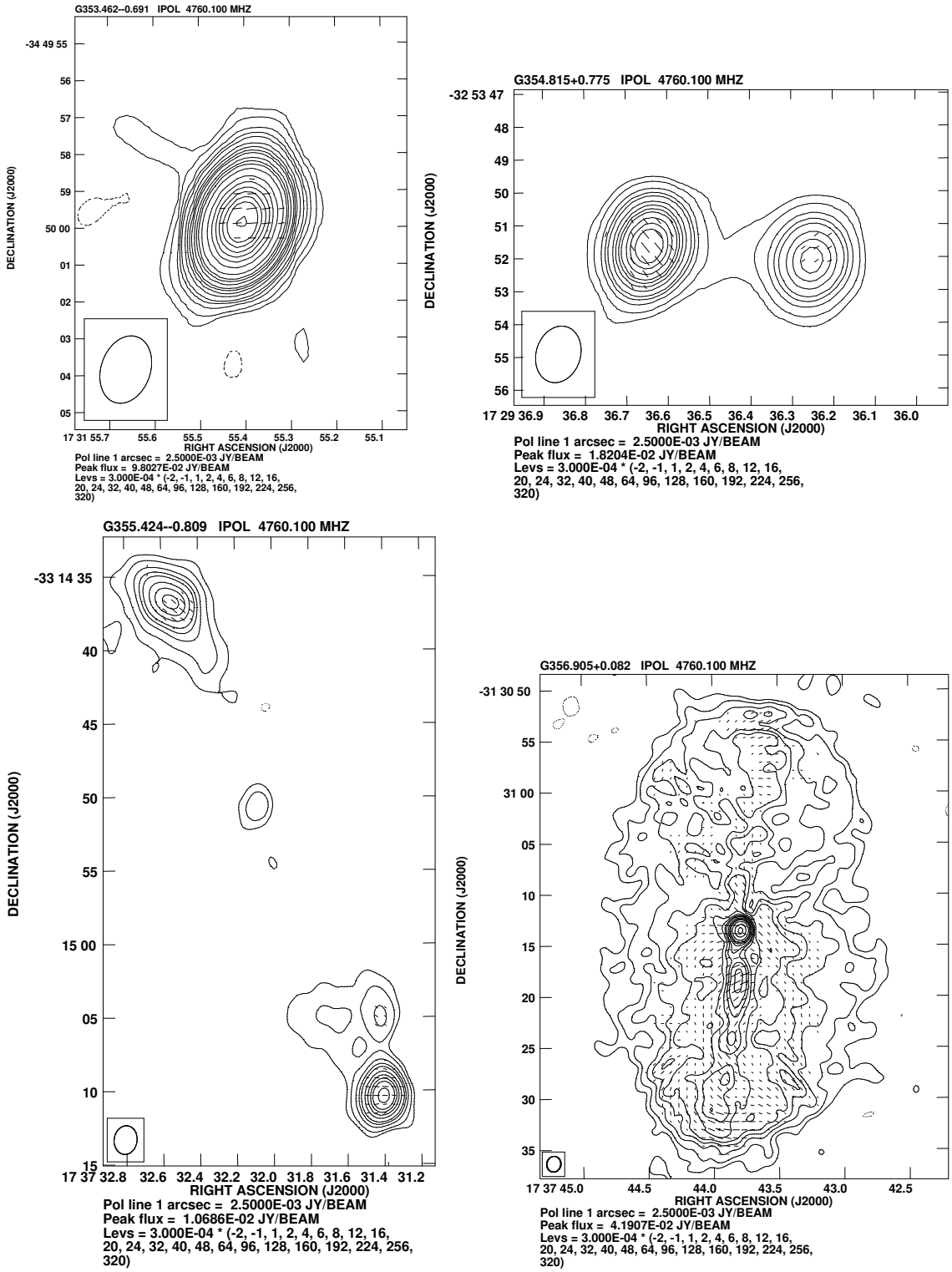

Figure 5.2: 4.8 GHz VLA continuum maps of the polarised sources with the polarisation vectors superposed on them. Typical rms noise in Stokes I is about 90 μJy/beam and about 75 μJy/beam in Stokes Q and U. Typical beamsize of these maps are $\approx 2'' \times 1.5''$.

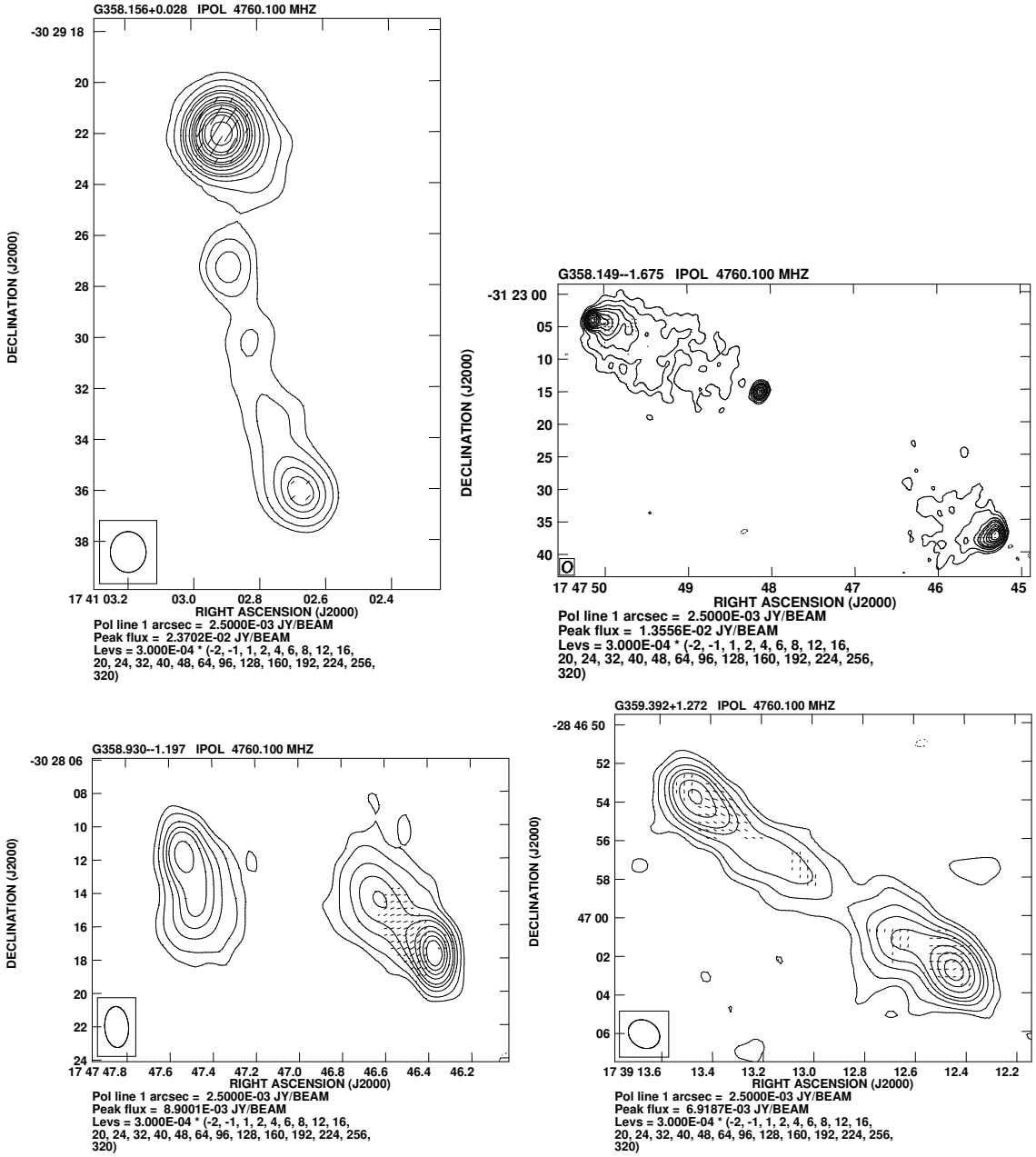

Figure 5.2: Continued

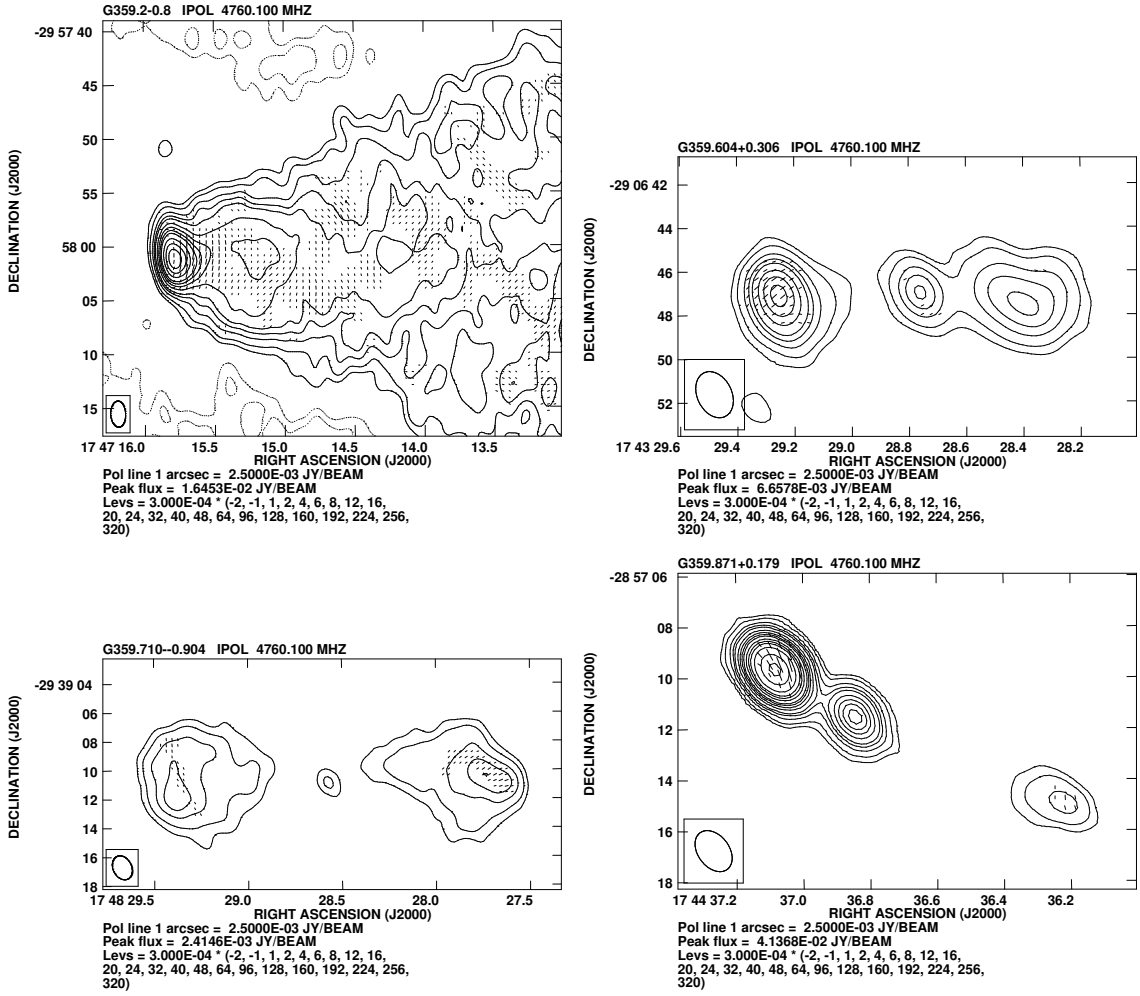

Figure 5.2: Continued

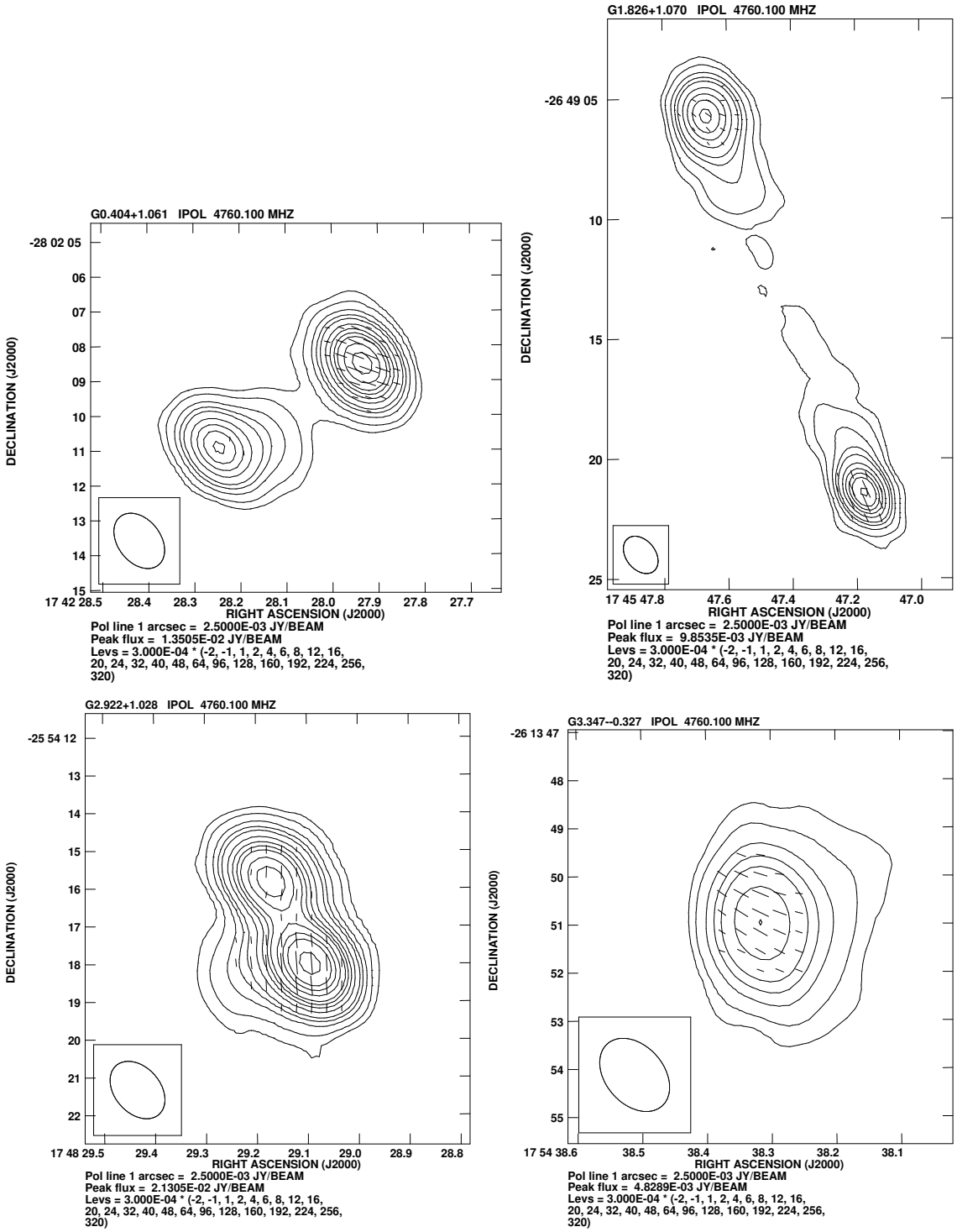

Figure 5.2: Continued

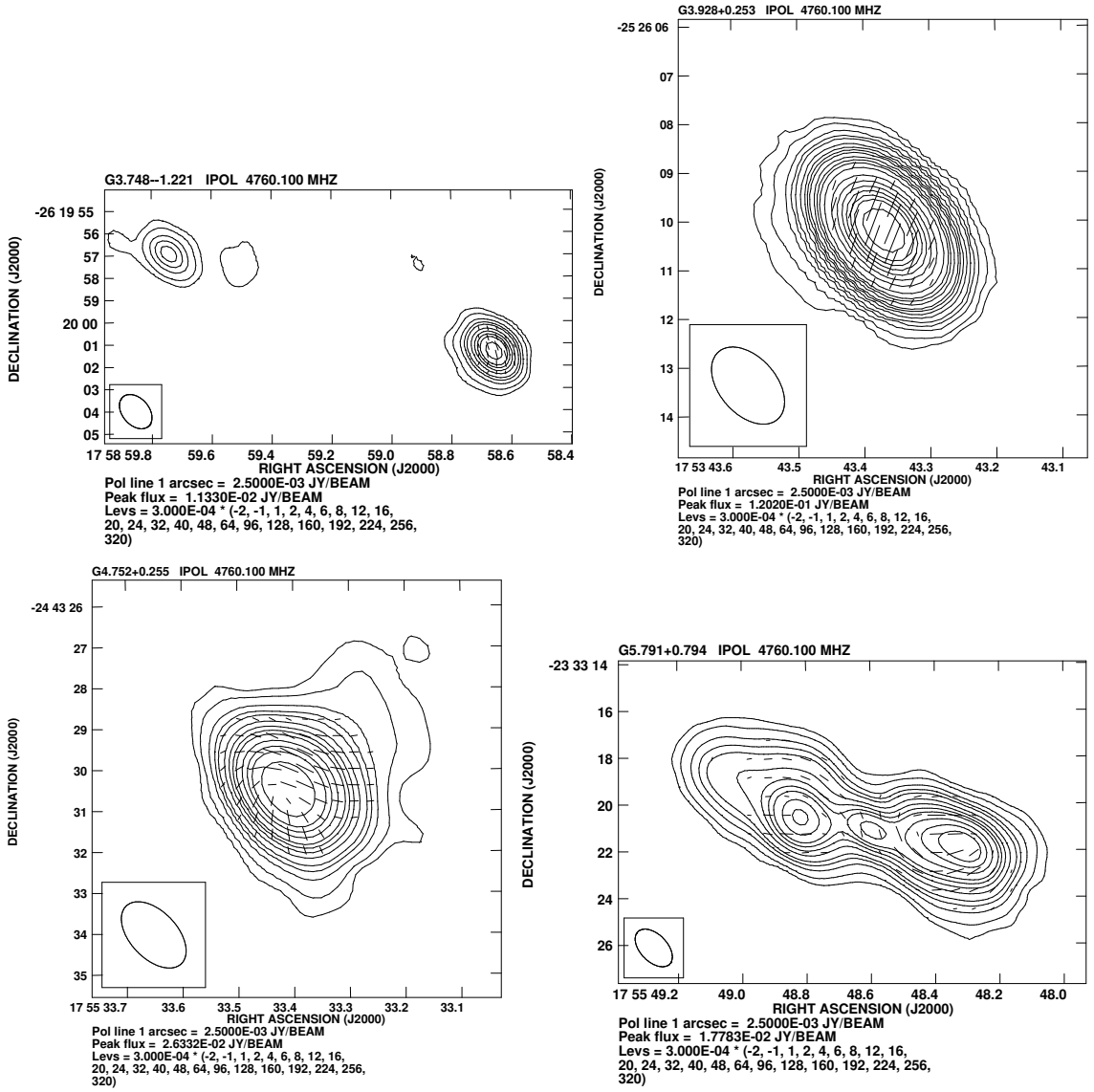

Figure 5.2: Continued

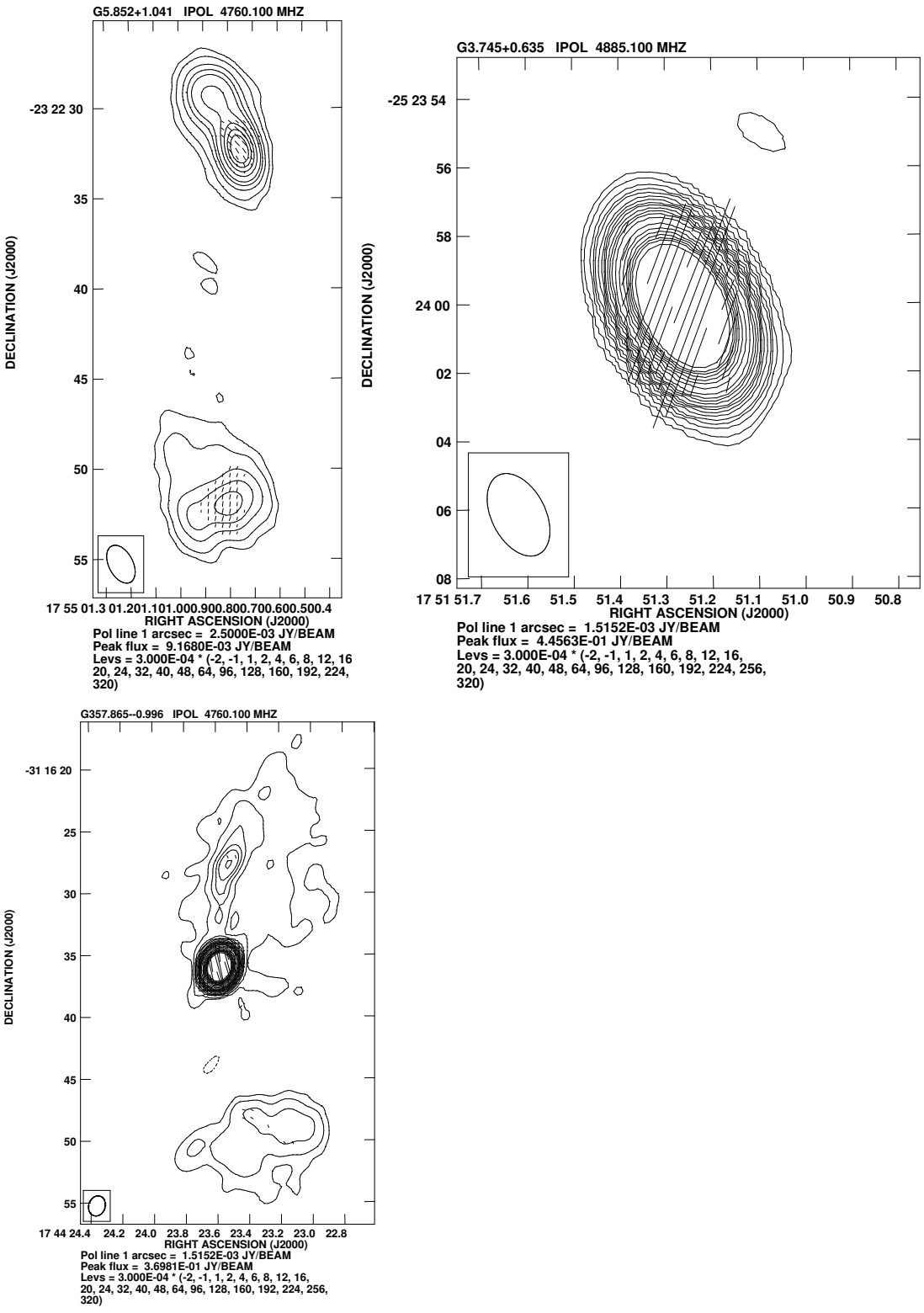

Figure 5.2: Continued

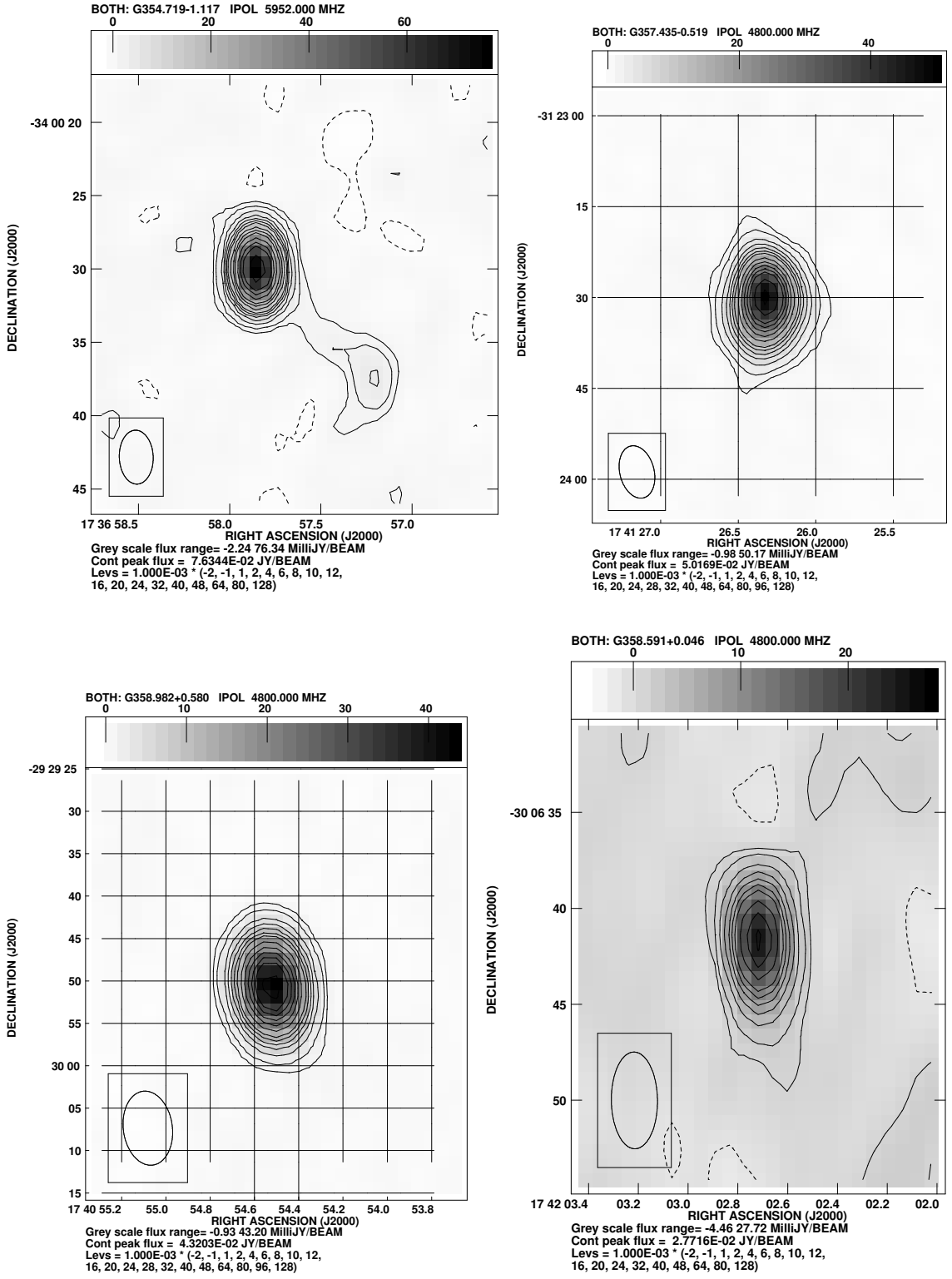

Figure 5.3: 4.8 GHz continuum maps of the unpolarised sources observed with the ATCA. Typical rms noise in Stokes I is about 0.23 mJy/beam, and beamsize $\approx 6'' \times 2''$.

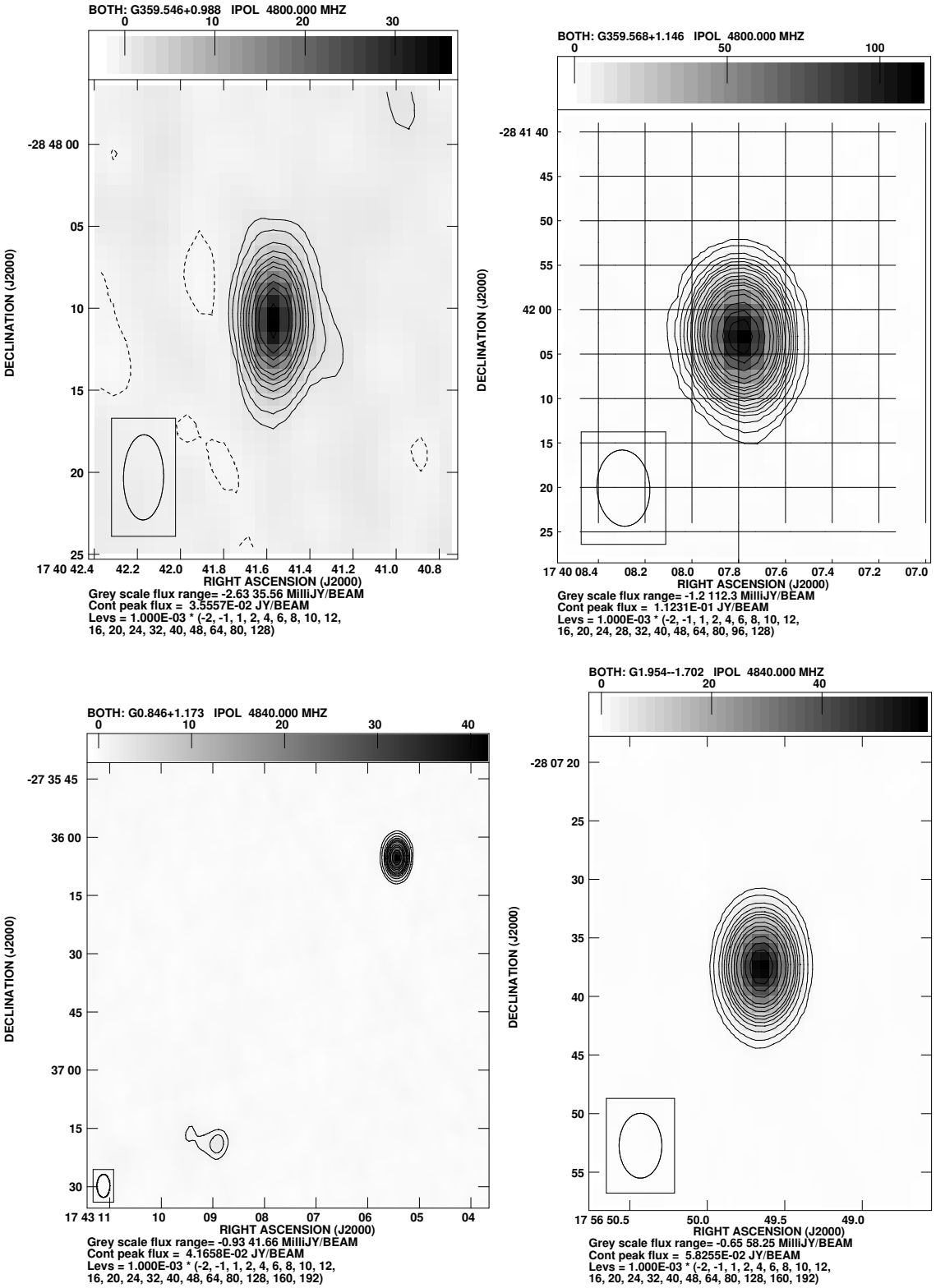

Figure 5.3: Continued

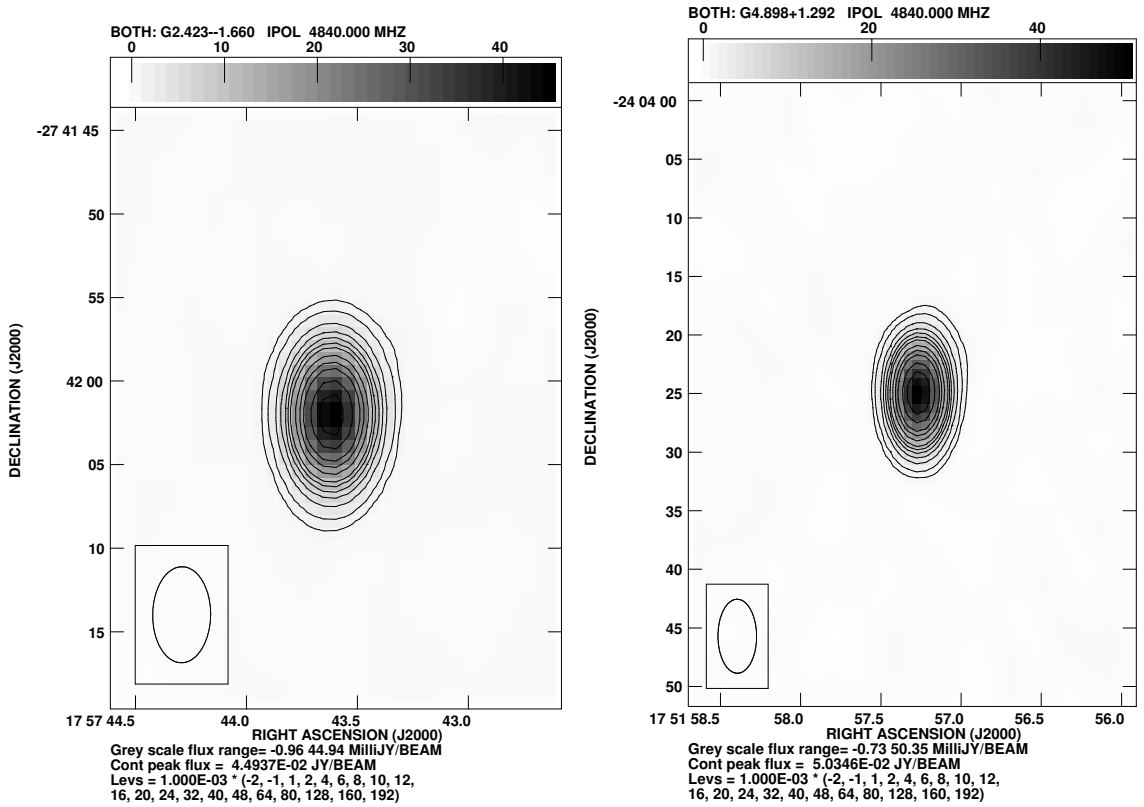

Figure 5.3: Continued

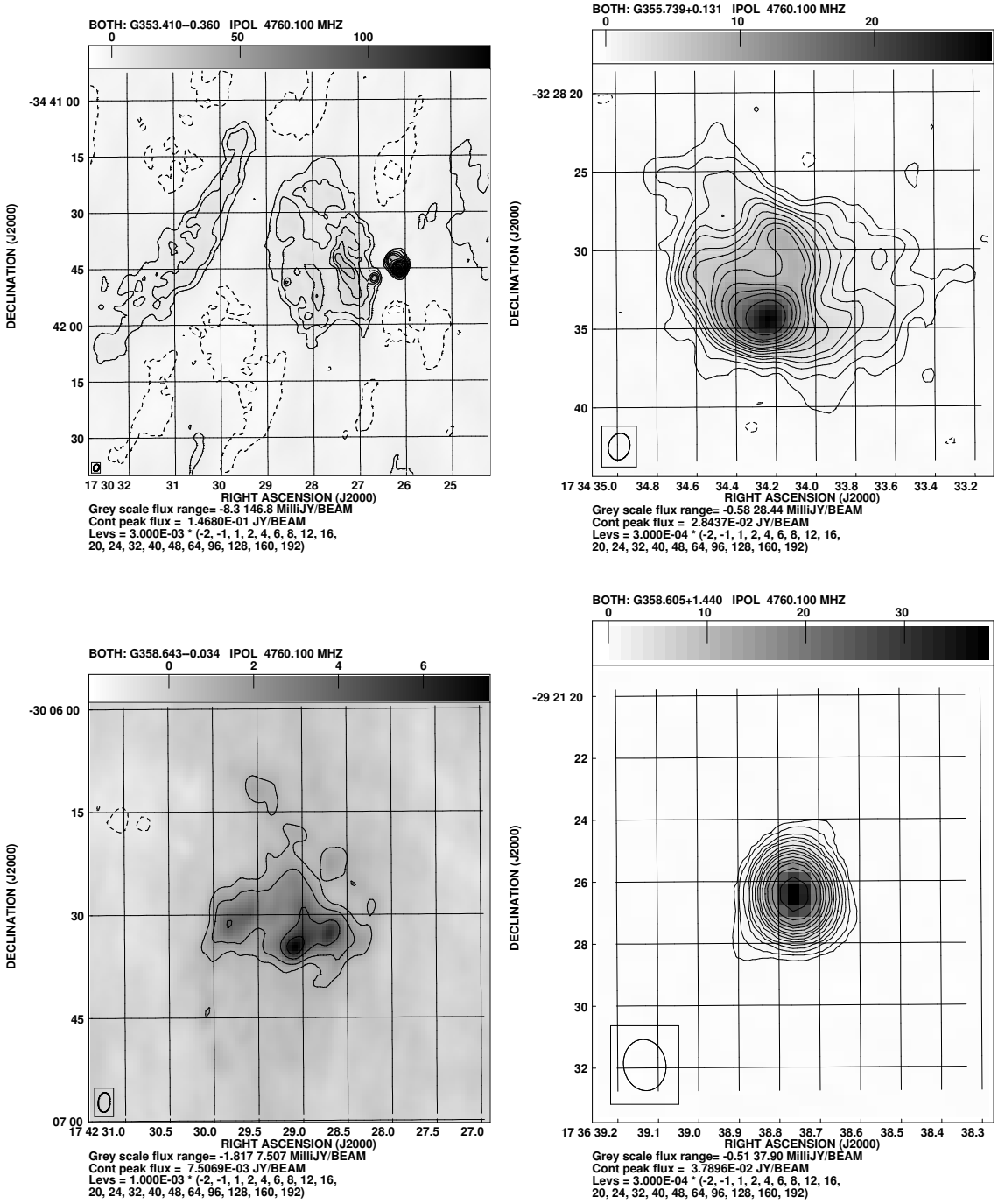

Figure 5.4: 4.8 GHz continuum map of the unpolarised sources observed with the VLA. Typical rms noise is about 90 μJy/beam, and beamsize of $\approx 2'' \times 1.5''$.

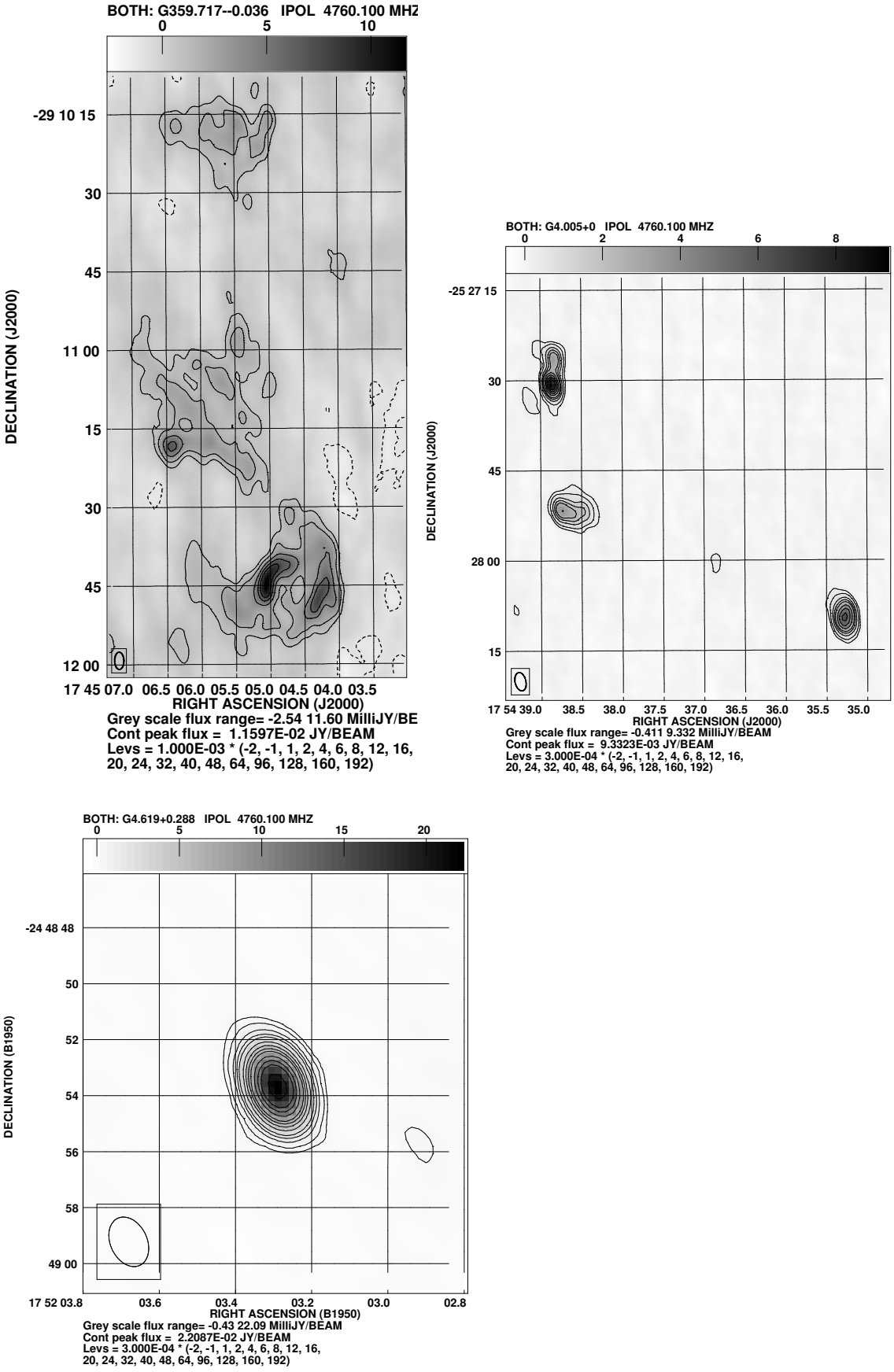

Figure 5.4: Continued

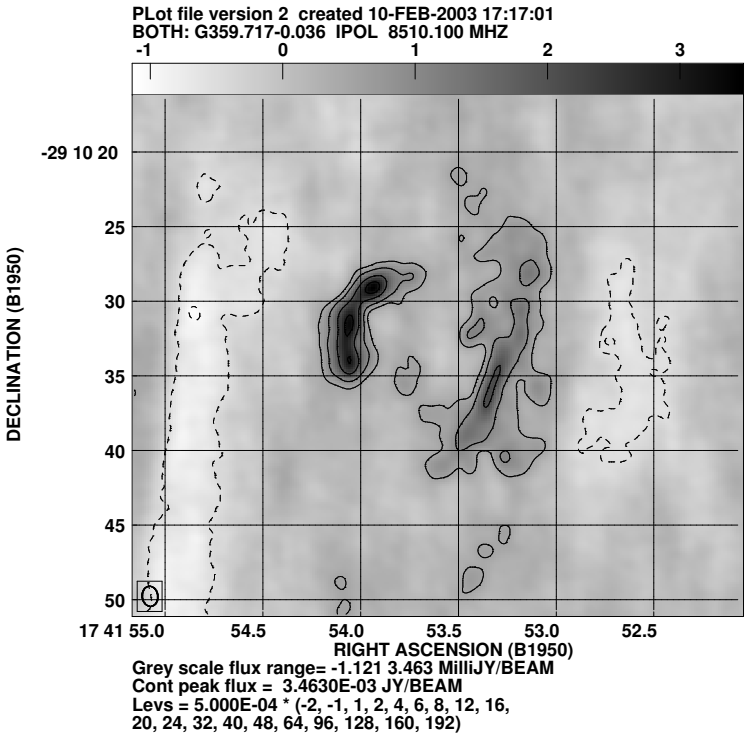

Figure 5.5: 8.5 GHz continuum map of the partial shell like object G359.717-0.036

an HII region.

5.4.2 Are the rest of the sources extragalactic ?

Excluding the sources described above, the rest of the sources observed are either polarised or the deconvolved diameter of the sources imply a brightness temperature greater than 10^3 Kelvin at 4.8 GHz. Except a few small diameter sources, all the other sources have steep spectral indices indicating the emission from these sources to be non-thermal. However, these small diameter sources have flat spectra even at 0.3 GHz. A thermal source with brightness temperature of 10^3 Kelvin at 4.8 GHz will show self absorption at 0.3 GHz (otherwise, the required brightness temperature exceeds 10^5 kelvin). Therefore, source with flat spectrum at 0.3 GHz indicates that the emission from these small diameter sources are also non-thermal. Among these non-thermal source, the object G359.2-0.8 (Mouse) (Table 5.2) (Yusef-Zadeh & Bally 1987; Uchida et al. 1992a) is

known to be a Galactic non-thermal source located within 5 kpc from the Sun. In order to classify the rest of the sources as extragalactic, we need to eliminate the possibility of them being Galactic non-thermal objects.

5.4.2.1 Non thermal emission from Galactic sources

There are several types of Galactic sources, which are known to emit non-thermal emission.

(i) Supernova Remnants (SNRs): These are the remnants of supernova explosion. The electrons in these objects are accelerated to high energies near the expanding shock front. The SNRs are normally spherical in shape, and when projected on the sky appears like a ring for the shell type SNRs, while it appears to be filled with emission in the case of filled centre SNRs. None of the non-thermal objects in Table 5.2 have such a morphology, indicating that there is no resolved supernova remnant among these sources. However, if an SNR is young, it can appear like an unresolved source. Assuming an initial expansion velocity of 3000 km s^{-1}, an SNR at a distance of 10 kpc will expand to an angular size of $6''$ in about 100 years after the explosion. An object of angular size of $6''$ will be well resolved in our maps and should have a ring (for shell type SNR) or filled centre morphology (in case of plerion), the absence of which rules out any SNR older than 100 years in our sample. However, since the expected number of supernova explosion in our Galaxy is believed to be abut 1 in 50 years, the probability of finding one SNR of age less than 100 years in the central 12°x $4^\circ$of the Galaxy is less than 0.1, which suggests that there is no young SNR in our sample.

(ii) Radio Pulsar: Pulsars typically have a very steep spectrum, with spectral indices in centimetre wavelengths varying between -1.5 and -4. They appear unresolved and due to their steep spectrum, very few such pulsars should be detectable at 5 GHz. Since, none of the unresolved sources in our sample have a very steep spectrum, we rule out any pulsar in the list of sources.

(iii) Radio Stars: Normal stars are relatively weak radio emitters. However, some of the stars do emit non-thermal emission. It is shown in Becker et al. (1994) that the highest anticipated radio flux density is $\leq$ 1 mJy at 5 GHz. Since the observed sources have a much higher flux densities, these objects can be ruled out from the list of sources.

(iv) Transient sources: These are highly variable and transient radio sources which include radio counterparts of X-ray sources. The sources in our sample are not only detected in the X and C band from our observations, but also detected in the L band observations during the GPS and the NVSS. These sources are also detected in the P band, and either in the Texas survey or in the 330 MHz GC observations. These observations were separated by days to years and the estimated spectral indices determined between any two bands are quite close to their mean value (differs by less than 0.6). Therefore, the flux densities of these sources have not changed by more than a factor of two about what is expected from their mean spectral indices and the flux densities measured at any particular frequency. This rules out any transient sources from our catalogue.

(iv) Galactic Microquasar: These are stellar-mass black holes in our Galaxy that mimic, on a smaller scale, many of the phenomena seen in quasars (see Mirabel & Rodríguez (1999), and the references therein). For a black hole accreting at the Eddington limit, the characteristic black body temperature at the last stable orbit in the surrounding accretion disk is approximately given by T $\sim$ 2 x $10^7 M^{-1/4}$ (Rees 1984). Therefore, compared to the AGNs, the emission from microquasars are shifted towards higher frequencies, and are usually identified for the first time in X-ray (Mirabel & Rodríguez 1999).

Though, many of the already known 10 microquasars are highly variable, two of these sources, 1E1740.7-2942 (Mirabel & Rodríguez 1999) and GRS 1758-258 (Martí et al. 2002) appears to be persistent sources of both X-rays and relativistic jets. At the radio wavelengths, these two sources appear morphologically similar to typical radio galaxies, which have a central compact component and two extended lobes. There-

fore, based on just morphology, microquasars cannot be separated from the distant radio galaxies. However, as mentioned above, microquasars are believed to have X-ray counterparts. Therefore, we have searched the ROSAT PSPC all sky survey (Voges et al. 1999) catalogue and the catalogue of soft X-ray sources ($|l| \leq 1.5^\circ$, $|b| \leq 2.0^\circ$) in the GC region (Sidoli et al. 2001). Twenty of our sources are also located within the boundary of the ASCA survey of the GC region ($|l| \leq 2.5^\circ$, $|b| \leq 2.5^\circ$) (Sakano et al. 2002). However, none of the radio sources were found to have any counterpart in the catalogues mentioned above. Therefore, it appears that none of the sources we have observed (Table 5.2 & Table 5.3) can be a microquasar.

Therefore, we believe almost all the sources listed in Table 5.2 except the Galactic source Mouse are extragalactic.

5.4.3 Comparison with statistical properties of extragalactic sources

The expected number of extragalactic sources (N) within 1 square arc minute of the sky at 5 GHz with a flux density limit of S mJy (Ledden et al. 1980) is N(>S)=0.032 x $S^{-1.13}$. Therefore, the expected number of extragalactic sources seen through the central $l \times b$ = 12°x 3.6° region of the Galaxy above a flux density limit of 20 mJy at 5 GHz are 168. However, only 60 possible extragalactic sources are identified by us, which indicates that about two third of the extragalactic sources are yet to be identified in the region. The median angular size of these 60 sources is 7.6″, and the median flux density of these sources at 1.4 GHz is 160 mJy. However, in the absence of complete sample, we do not carry out any further statistical comparison with extragalactic sources.

5.5 Summary

We have observed sixty five sources through the central $-6^\circ < l < 6^\circ$, $-2^\circ < b < 2^\circ$ of the Galaxy using the C and X band of the ATCA and the VLA. These observations, for the first time provide information on the polarisation fractions of the background sources

seen through the region. We provide 4.8 GHz maps of all the observed sources, and estimate the angular sizes, spectral indices and polarisation fractions of these sources. From our data, spectral indices of these sources could only be estimated between 8.5 and 4.8 GHz. Therefore, we have used existing catalogues made from the GPS, NVSS and Texas surveys, and computed spectral indices of these sources between 4.8 and 1.4, and between 1.4 and 0.3 GHz. Based on the morphology, spectral characteristics and polarisation properties, we identify 4 Galactic HII regions in the sample. The remaining 61 sources show non-thermal emission. Except the source G359.2-0.8 (Mouse), which is a known Galactic non-thermal source, we compare the properties of the remaining non-thermal sources with the known types of Galactic non-thermal sources like SNRs, radio pulsars, radio stars, transient sources and Galactic microquasar. None of the sources appear to share any characteristic properties of these Galactic non-thermal sources. This lead us to believe that all or most of these non-thermal sources are located outside the Galaxy.

Chapter 6

Magnetic field near the Galactic Centre from Rotation Measure observations of Extragalactic sources

6.1 Introduction:

Magnetic fields can be strong enough to have a significant influence on the dynamics and evolution of the central region of our Galaxy. Magnetic pressure can contribute significantly to the overall pressure balance of the interstellar medium (ISM) and can even influence the scale height of the gas. It can affect the formation and motion of clouds and perhaps mediate in the star formation process (Beck et al. 1996). A relatively high systematic magnetic field in the Galactic Centre (GC) region is believed to be responsible for the creation and maintenance of the unique non-thermal filaments (NTFs) (Morris et al. 1996, and references therein). Therefore, it is important to measure the magnetic field geometry and strength in the central part of the Galaxy.

However, other than the central 200 pc region, no systematic study has been made to estimate the magnetic fields in the inner 5 kpc region of the Galaxy (Davidson 1996). The estimates within the central 200 pc region are mainly based on the observations of the non-thermal filaments (Yusef-Zadeh & Morris 1987c; Anantharamaiah et al. 1991; Gray et al. 1995; Yusef-Zadeh et al. 1997a), and it is not clear that these estimates represent the field strengths in the GC ISM. The estimated RM towards these NTFs

are $\sim$1000 rad m^{-2} (Yusef-Zadeh & Morris 1987c; Anantharamaiah et al. 1991; Gray et al. 1995; Yusef-Zadeh et al. 1997a; Lang et al. 1999b). Since the magnetic pressure in these NTFs overcome the turbulent ISM pressure (otherwise, the NTFs would have bent due to interaction with molecular clouds) Yusef-Zadeh & Morris (1987a) derived a magnetic field strength of about 1 milliGauss in these NTFs. Earlier estimates of the direction of the magnetic field within the NTFs have shown the field lines to be oriented along the length of the NTFs. Since, all the NTFs found within a degree from the GC are oriented almost perpendicular to the Galactic plane, it suggests that the field lines in the surrounding ISM are perpendicular to the Galactic plane (Morris et al. 1996 and the references therein). However, the NTF Pelican (G358.85+0.47) located about a degree from the GC is found to be almost parallel to the Galactic plane. This suggests that the field lines change their orientation from being perpendicular to the plane near the GC, to parallel to the plane beyond one degree from the GC, as seen mostly in the rest of the Galaxy. However, we reiterate that if the NTFs are manifestations of a peculiar local environments (Shore & Larosa 1999), inferences drawn from these observations can be misleading.

Zeeman splitting of spectral lines can yield directly the magnetic field. However, this is sensitive to small scale fields, and hence high magnetic field strengths anywhere along the line of sight can produce Zeeman splitting of spectral lines. Therefore, past estimates of milliGauss magnetic field based on Zeeman splitting (Schwarz & Lasenby 1990; Killeen et al. 1992; Yusef-Zadeh et al. 1996b, 1999) of the HI or OH lines towards the GC could have resulted from local enhancement of field (*e.g.*, near the cores of high density molecular clouds). To estimate any systematic magnetic field in the region, it is necessary to use an observational technique which is sensitive to the large scale field. Galactic objects, being manifestations of favourable local environments, should not be used for this purpose.

The Faraday rotation measure (RM) is the integrated line of sight magnetic field

weighted by the electron density

$$RM = 0.81 \times \int n_e B_{\parallel} dL, \tag{6.1}$$

where, RM is the rotation measure expressed in rad m^{-2}, n_e is the electron density expressed in cm^{-3}, $B_{\parallel}$ is the line of sight component of the magnetic field in μG, and the integration is carried out along the line of sight, with distance expressed in parsec. If a model of electron density is available, observations providing Faraday RM towards the extragalactic sources seen through the Galaxy are well suited to estimate the average magnetic fields prevailing in the ISM. Earlier studies of the large scale Galactic magnetic field was performed by Simard-Normandin & Kronberg (1980); Frick et al. (2001) using RM towards the extragalactic sources. Similar studies have also been performed by estimating RM towards pulsars (Rand & Kulkarni 1989; Rand & Lyne 1994; Han & Qiao 1994). These studies have established that there is one field reversal within and one outside the solar circle. Two more reversals have been suggested by Han et al. (1999). These reversals could be explained by invoking either the bisymmetric spiral model (Simard-Normandin & Kronberg 1980; Han et al. 1999), or by invoking a ring model, where the direction of the field lines reverses in each ring (Rand & Kulkarni 1989). However, no systematic observations of Faraday rotation measures towards extragalactic sources seen through the GC region have been carried out in the past.

We have systematically studied 64 suspected extragalactic sources seen through the central $-6^\circ < l < 6^\circ$, $-2^\circ < b < 2^\circ$ region of the Galaxy. We found that 60 sources are likely to be extragalactic and 45 sources have polarised components (totally 63 polarised components). We could estimate the RM towards 44 sources. To avoid any significant bandwidth depolarisation up to a RM of 1.2×10^4 rad m^{-2}, our observations were carried out at higher radio frequencies using the 4.8 (C band) and 8.5 GHz (X band) band of the ATCA and the VLA. The angular scale over which the magnetoionic medium is coherent near the NTFs has been estimated to be $\sim 10''$ (Gray et al. 1995, Yusef-Zadeh

et al. 1997). Therefore, to avoid any beam depolarisation introduced by the ISM of the Galaxy, these observations have been made with the longer baseline configurations of these telescopes, so that the synthesised beam sizes are considerably smaller than the coherence scale length of the Faraday screen near the GC.

In Chapter 5, we have described the sample sources and the observations. In this chapter, we provide the results and interpretation of the RM observations. The sections in this chapter are arranged as follows. In Sect. 6.2, we provide details of the RM estimation from the data. The results of the the data analysis are presented in Sect. 6.3 and the interpretation of the results are described in Sect. 6.4. Finally, the conclusions are presented in Sect. 6.5.

6.2 Data analysis

Following the editing and calibration discussed in Chap. 5, we converted the data acquired by the ATCA into Stokes I, Q, U, V, and further analysis were carried out using AIPS. The Polarisation angle (ϕ) being given by ϕ=0.5 $\tan^{-1}(U/Q)$ (where, signs of Q and U are considered separately to unambiguously determine the value of ϕ), we divided the Stokes U image by the Q image and estimated the polarisation angle and its error (AIPS task COMB). Finally, the polarisation angle images at 4 frequencies bands was fit to the equation, $\phi = RM.\lambda^2 + \phi_0 + n\pi\lambda^2$ using the AIPS task RM. In this equation, n is an integer, λ is the wavelength, and ϕ_0 denotes the intrinsic polarisation angle (when the observing frequency tends to infinity). The fitted values were rejected, if the RMS residuals exceed three times the expected RMS noise.

Since we had 16 frequency channels per 128 MHz band of the ATCA data, we tried to estimate the RM in two ways by using the AIPS task RM. (i) Since AIPS task RM cannot fit more than four frequency channels to estimate RM, in order to maximise signal to noise ratio as well as to check for high RM in the data, we divided the 4.8 and

5.9 GHz band into 3 equal parts. Polarisation angle were estimated from first and third part of each of these bands, and these were used as input to the AIPS task RM. (ii) If the RM estimated by the previous method is not very high (.i.e., $\leq$ 2000 rad m^{-2}, and was the case for all except one source), data from each of the 4.8, 5.3, 5.9 and 8.5 GHz band were averaged and polarisation angle estimated from each of these bands. These polarisation angle images and their error maps were used as the input to the AIPS task RM.

Five sources, namely G359.604+0.306, G359.710-0.904, G359.844-1.843, G359.911-1.813, and G2.143+1.772 had no detectable polarisation at 8.5 GHz. In order to get a reliable estimate of the RM towards these sources, they were reobserved at 5.0 and 5.6 GHz with the ATCA. The polarised emission from G1.035+1.559 was quite strong, and there was high signal to noise ratio across the multichannel ATCA data to rule out nπ ambiguity. Therefore, it was only observed using the 4.8 and 5.9 GHz band of the ATCA.

We acquired VLA data with single frequency channel per band with a bandwidth of 50 MHz centred at 4.635, 4.885, 8.335 and 8.685 GHz. Polarisation angle estimated from these bands were used as input to the AIPS task RM, which yielded the RM of the sources.

The source G356.905+0.082 (see the previous chapter) has a compact core, which is weakly polarised, and an extended highly polarised halo. Due to zero spacing problem, the image of the halo could have problems at 8.5 GHz. Since the polarised intensity per beam of the core is similar to the contribution by the halo, which has small scale structures in polarised image and is not properly sampled at 8.5 GHz, we could not reliably estimate the RM from the core or the halo. Therefore, we have not provided its RM in Table 6.1.

6.3 Results:

The estimated RM towards 44 sources (65 components) and 2 secondary calibrators are given in Table 6.1, which is arranged as follows:
Column 1: the source name in Galactic co-ordinates (G$l\pm$b). Column 2 & 3: RA (J2000) and DEC (J2000) of the source components. The co-ordinates of these components are based on the peak in the polarised emission and if they do not coincide with the peak in total intensity, the co-ordinate values will be different from what is given in the previous chapter. Following the convenion given in the previous chapter, if two objects are found within 2′ region of the sky, and if these objects are slightly extended towards each other, they are assumed to be part of a single source. Column 4 & 5: the estimated RM and the error in these estimates. Column 6: depolarisation ratio of the components between 8.5 and 4.8 GHz, which is the ratio of the polarisation fraction estimated at 8.5 GHz to that at 4.8 GHz.

The source G359.2−0.8 (Mouse) is a known Galactic non-thermal source. Since this source is known to be within 5 kpc from the Sun (Uchida et al. 1992a), the RM towards this object is expected to be quite small. To check if observations can confirm its low RM, we observed this source. From Table 6.1, its RM is indeed measured to be very small (-5 ± 18 rad m^{-2}). However, since our samples are selected to estimate the RM contribution of the GC region, and this source only samples the local ISM, its RM is not used in any further analysis.

Table 6.1: Estimated RM towards the background sources

Source Name	RA (J2000)	DEC (J2000)	RM (rad m^{-2})	Error on RM	Depolarisation ratio
354.740+0.138^{AT}	17 31 56.96	−33 18 33.72	1193	32	1.4
	17 31 57.00	−33 18 42.12	858	45	1.3
356.000+0.023^{AT}	17 35 40.37	−32 18 59.03	332	25	0.9
	17 35 40.05	−32 18 55.83	436	29	1.1
	17 35 39.74	−32 18 54.23	713	30	0.9
356.161+1.635^{AT}	17 29 43.86	−31 18 04.77	677	27	1.0
	17 29 43.64	−31 18 04.77	685	23	0.7
	17 29 42.71	−31 18 02.37	623	34	1.1
356.567+0.869^{AT}	17 33 45.73	−31 22 50.38	962	25	0.9
356.719-1.220^{AT}	17 42 27.90	−32 22 14.04	−511	37	0.9
	17 42 27.52	−32 22 09.64	−459	41	0.8
358.002-0.636^{AT}	17 43 17.87	−30 58 18.73	1050	27	0.7
358.917+0.072^{AT}	17 42 43.99	−29 49 16.03	4768	88	3.0
359.388+0.460^{AT}	17 42 21.47	−29 12 59.73	−568	29	2.7
359.844-1.843^{AT}	17 52 30.88	−30 01 06.59	−58	47	–
359.911-1.813^{AT}	17 52 32.97	−29 56 44.28	162	47	–
359.993+1.591^{AT}	17 39 26.94	−28 06 12.65	23	65	1.4
0.313+1.645^{AT}	17 40 0.21	−27 48 10.37	−121	22	0.9
0.537+0.263^{AT}	17 45 52.50	−28 20 26.64*	−1169	56	1.4
1.028-1.110^{AT}	17 52 22.81	−28 37 41.31	−65	23	1.5
	17 52 22.51	−28 37 32.51	221	43	1.4
1.035+1.559^{AT}	17 42 1.90	−27 13 9.94	−136	9	–
1.505-1.231^{AT}	17 53 55.37	−28 15 53.77	388	12	1.0
	17 53 59.21	−28 17 21.35	689	24	0.7
2.143+1.772^{AT}	17 43 51.24	−26 10 59.24	158	50	–
4.005+1.403^{AT}	17 49 31.68	−24 46 57.70	458	28	1.2

Source Name	RA (J2000)	DEC (J2000)	RM (rad m^{-2})	Error on RM	Depolarisation ratio
4.188-1.680^{AT}	18 01 44.34	−26 10 43.63	−625	15	1.0
4.256-0.726^{AT}	17 58 12.97	−25 38 44.29	1785	22	1.5
5.260-0.754^{AT}	18 00 31.38	−24 47 21.73	1142	12	1.4
5.358+0.899^{AT}	17 54 27.81	−23 52 36.17	851	29	1.2
5.511-1.515^{AT}	18 3 59.28	−24 56 43.63	321	20	1.3
	18 3 59.25	−24 56 48.03	393	32	0.8
6.183-1.480^{AT}	18 5 18.04	−24 20 45.50	−889	24	1.1
353.462-0.691^{AT}	17 31 55.40	−34 49 59.9	1011	30	2.0
354.815+0.775	17 29 36.653	−32 53 51.88	−102	16	1.2
355.424-0.809	17 37 32.514	−33 14 36.88	611	17	1.1
	17 37 31.413	−33 15 09.56	574	23	1.1
357.865-0.996 (1741-312)	17 44 23.580	−31 16 35.970	1881	2.8	1.3
358.149-1.675	17 47 50.144	−31 23 03.86	−17.4	13	1.1
	17 47 45.300	−31 23 36.21	276	18	1.0
	17 47 45.411	−31 23 38.40	343	24	0.7
358.156+0.028	17 41 02.909	−30 29 22.11	533	6	1.1
	17 41 02.668	−30 29 36.53	467	28	9
358.930-1.197	17 47 46.474	−30 28 17.39	−905	26	1.0
359.392+1.272	17 39 13.384	−28 46 54.08	−318	27	0.8
	17 39 12.505	−28 47 01.35	−271	30	0.9
359.2-0.8 (Mouse)	17 47 15.78	−29 58 01.0	−05	18	1.0
359.604+0.306	17 43 29.266	−29 06 46.736	−504	40	–
359.710-0.904	17 48 29.373	−29 39 08.83	1423	93	–
	17 48 27.686	−29 39 09.76	1470	52	–
359.871+0.179	17 44 37.069	−28 57 09.27	770	14	1.1
0.404+1.061	17 42 27.934	−28 02 08.49	−176	16	1.2
1.826+1.070	17 45 47.185	−26 49 21.48	806	9.5	0.9
	17 45 47.702	−26 49 06.24	638	40	1.6

Source Name	RA (J2000)	DEC (J2000)	RM (rad m^{-2})	Error on RM	Depolarisation ratio
2.922+1.028	17 48 29.121	−25 54 17.97	1563	15	1.0
	17 48 29.150	−25 54 15.97	1510	21	1.5
3.347-0.327	17 54 38.331	−26 13 50.76	−71	21	1.3
3.745+0.635 (1748-253)	17 51 51.26	−25 24 0.05	1291	2	1.4
3.748-1.221	17 58 58.649	−26 20 01.31	1247	18	1.3
3.928+0.253	17 53 43.371	−25 26 10.26	1457	7	0.7
4.752+0.255	17 55 33.409	−24 43 29.77	193	18	1.1
	17 55 33.424	−24 43 31.16	112	24	1.4
5.791+0.794	17 55 48.323	−23 33 22.71	1203	13	1.1
	17 55 48.526	−23 33 21.09	1294	17	0.9
	17 55 48.802	−23 33 18.67	1144	24	0.7
5.852+1.041	17 55 00.749	−23 22 31.56	579	26	1.0
	17 55 00.800	−23 22 52.16	626	33	1.2

6.3.1 Contribution of the intrinsic Faraday rotation to our observations:

When the polarised emission from the source reaches the observer, rotation of the polarisation angle could occur within the source or the Inter Galactic Medium (IGM) or the ISM of the Galaxy. Compared to the ISM of our Galaxy, the electron density of the IGM is very small, and consequently the Faraday rotation introduced by it is negligible. However, if the synchrotron electrons are mixed with thermal electrons at the source or if the ISM of another galaxy or cluster galaxies lies along the line of sight, there can be Faraday rotation outside our Galaxy. From our data, the RM towards the source G358.917+0.072 is found to be the highest with an estimated value of 4768 rad m^{-2}. The plot of the polarisation angle for this source as a function of frequency is shown in Fig. 6.1. The fit to the polarisation angle deviates from the measurement significantly more than the expected noise in the data, and the data can be fitted with comparable (but higher) residuals with one more extra π rotation of the polarisation angle within the 128 MHz observing bandwidth. Consequently, we have estimated the minimum RM, which is quoted above. As discussed by Gardner & Whiteoak (1966); Kronberg et al. (1972); Vallee (1980), the polarisation angle could deviate from the λ^2 law due to the following three mechanisms. (i) If the synchrotron optical depth becomes significant at some frequency, the polarisation direction makes a transition from parallel to perpendicular to the projected magnetic field. (ii) If there are multiple unresolved emission components with differing spectral indices and polarisation characteristics, it can cause complex wavelength dependent variations in polarisation angle. (iii) If there are significant gradients in Faraday rotation across or through the emission region of the source, then also the polarisation angle can have a complex dependence on the observing wavelength. G358.917+0.072 is unresolved in the ATCA map. It could either be a compact steep spectrum (CSS) source (O'Dea 1998), where the parent galaxy could introduce RM, or the source is seen through any cluster or intracluster medium like the

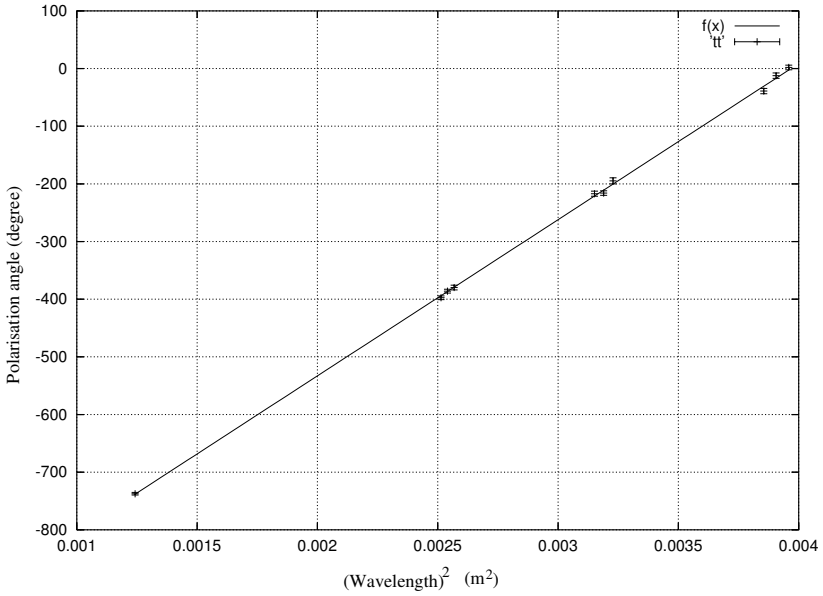

Figure 6.1: Polarisation angle vs. λ^2 plot for the source G358.917+0.072

one suggested for Cygnus-A (Dreher et al. 1987).

The source G358.917+0.072 shows a high depolarisation fraction (3.0 between 4.8 and 8.5 GHz). The distance of the intervening Faraday screen responsible for the depolarisation is likely to be several orders of magnitude more than the GC ISM. As a result, emission from different parts of the source is viewed within one synthesised beam, the linear scale of which is much larger than what is sampled in our ISM. It is likely that in such length scales ($\sim$1 kpc), the magnetic field of the intervening Faraday screen is uncorrelated. As a result, there is differential Faraday rotation within the beam, which gives rise to source depolarisation. Since, differential Faraday rotation increases at lower frequency (Kronberg et al. 1972), the depolarisation fraction for this source is high.

Following the arguments given above, if the polarisation angle of a source deviates from the best fit RM by more than four times of the noise, there could be RM introduced outside the Galaxy and the RM of that source was not estimated. Similarly, we have also estimated the depolarisation fraction between 8.5 and 4.8 GHz for all the components which have detectable polarised emission at 8.5 GHz (Table 6.1). If any of the

component is found to have a depolarisation fraction of more than 1.5, we suspect that there is significant RM introduced outside the Galaxy and those components have not been used any further for estimating RM introduced by the ISM of the Galaxy. Other than G358.917+0.072, two more sources G359.388+0.46 and 353.462-0.691 and one more component of the source G1.826+1.070 were rejected following the criteria given above. We note that the intrinsic RM of most of the extragalactic sources are quite small ~ 10 rad m^{-2} (Simard-Normandin & Kronberg 1980) and the RMs estimated from our sample is quite high (~ 1000 rad m^{-2}), and consequently should have little effect on the results of these observations.

6.3.2 Anomalous RM contribution by Galactic sources

As in Sect. 6.1, strong ordered magnetic fields within Galactic sources can bias the estimated magnetic field in the ISM. Therefore, while selecting the sources, we had inspected the NVSS map at 1.4 GHz (Condon et al. 1998) and the GC map at 330 MHz (LaRosa et al. 2000) for the presence of extended Galactic continuum source along the line of sight (*l*os) of the target sources. Except the source G0.537+0.263 (its RM is included in the plot shown in Fig. 6.2), which is seen close to the HII region Sgr-B1, none of the other polarised sources are seen close to any prominent continuum source in these maps.

6.3.3 Features in the Faraday screen near the GC:

In Fig. 6.2, the RM of all the 41 extragalactic sources which conform to the criteria described before are plotted. In the plot, the positive RMs have been indicated by 'X' and the negative RMs by 'O', and the size of the symbols increases linearly with the $|\mathrm{RM}|$. Clearly, the region is dominated by positive RM, as observed towards most of the sources in both positive and negative Galactic longitude. The observed RMs towards sources with $|b| \leq 1.5^\circ$ are quite high $\sim$1000 rad m^{-2}. Such high RMs have

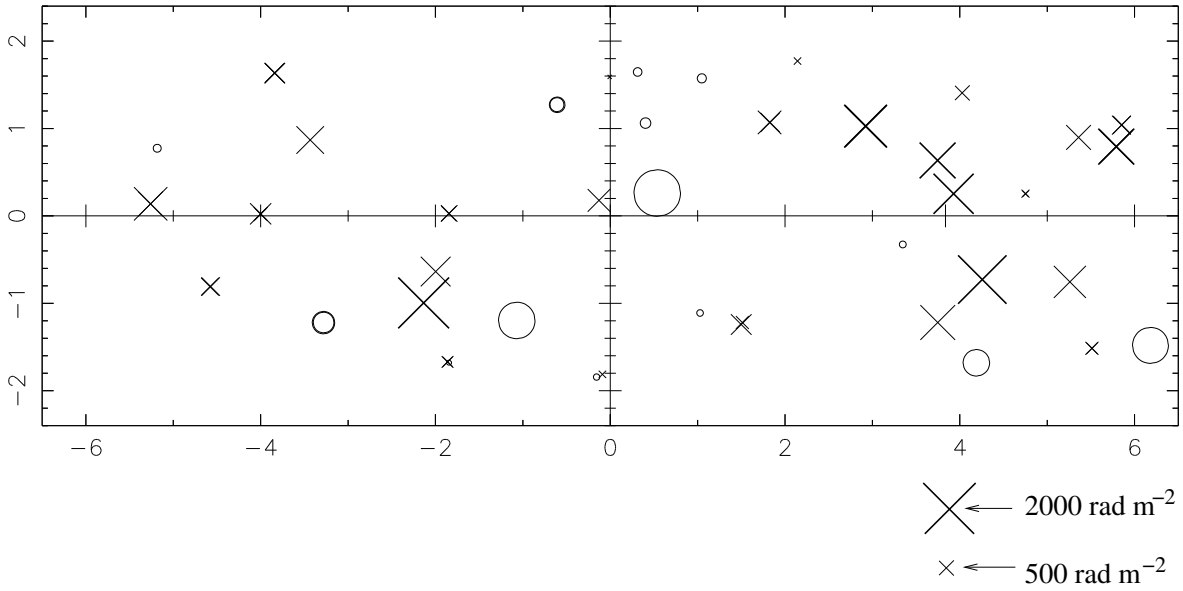

Figure 6.2: Estimated Faraday RM towards the polarised sources in Galactic co-ordinate. The positive values are indicated by 'cross (X)' and negative values by 'circle (O)'. The size of the symbols increase linearly with |RM|.

been observed before in the survey of low latitude extragalactic sources ($45^\circ < l < 93^\circ$, $|b| < 5^\circ$) (Clegg et al. 1992), and is partly due to the passage of the line of sight through large path length of the ISM. The observed RMs in our data do not appear to decrease with distance from the GC. The median RM is estimated to be 467 ± 87 rad m^{-2}, which indicates that there is an ordered large scale magnetic field in the region which points towards us. After subtracting this large scale RM, we checked for the presence of any correlation among the estimated RM towards the sources.

The normalised autocorrelation function is given by (Nissen & Thielheim 1974)

$$f(\theta) = \frac{< \mathrm{RM} . \mathrm{RM}(\theta) >_{\Delta\theta}}{< \mathrm{RM}^2 >},$$

where the numerator is the mean of the products of all pairs of RMs with their median removed in intervals of $\Delta\theta$, θ being the angular separation between the sources in the sky. The autocorrelation function is computed within 0.0° to 0.1°, 0.1° to 0.3°, 0.3° to 1.0°, 1.0° to 3.0° and 3.0° to 10°, and is plotted in Fig. 6.3. As can be seen from the plot, the RMs of sources located beyond 1° from each other are almost uncorrelated. We note

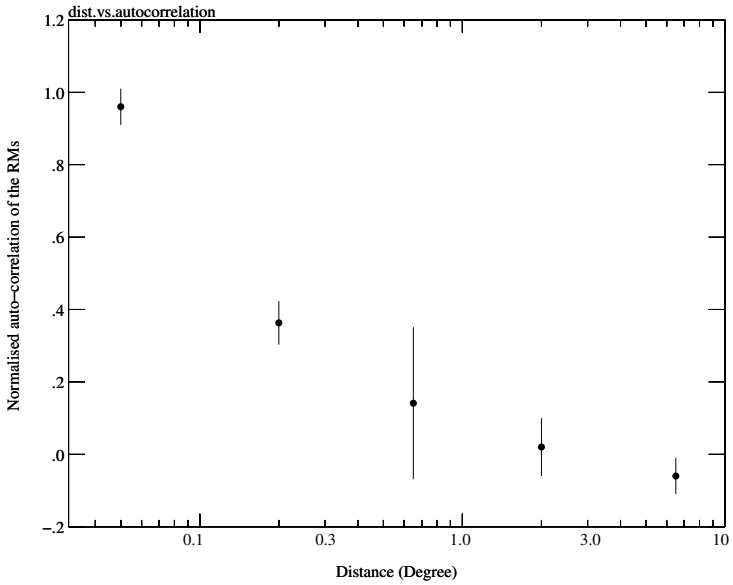

Figure 6.3: Normalised RM autocorrelation function as a function of angular separation

that there is a random component of the magnetic field, the presence of which can be ascertained due to the reversal of sign of the RM towards some of the sources. The rms value of the random component of the estimated RM is 666 rad m^{-2}.

6.4 Discussion

6.4.1 Geometry of the large scale magnetic field

Depending on the physical processes, the large scale magnetic field could either be perpendicular (poloidal) or parallel to the Galactic plane. The large scale magnetic field in the GC region is believed to be poloidal (Morris & Serabyn 1996 and the references therein). If this geometry is correct, then even due to small perturbations like turbulence, there will be a line of sight component of the magnetic field, which will be random, and we should have detected almost an equal number of sources having positive and negative RM. However, from our data, we found the RMs to be mostly positive, which indicates

that the large scale magnetic field is not perpendicular to the plane.

We now compare the results with three different models of the magnetic fields, and see if the results match with the predictions of these models.

(i) Uchida et al. (1985) have proposed a model of the magnetic field, which predicts a toroidal component (along the Galactic plane) of the field near the GC. This magnetohydrodynamic model was made to explain the origin of the Galactic Centre Lobes (Sofue & Handa 1984), which are a limb-brightened radio structure with a size of several hundred parsecs extending from the plane of the Galaxy up toward positive Galactic latitudes (Sofue & Handa 1984). This model predicts separate poloidal-dominant and toroidal-dominant regions within the central few hundred parsec of the GC. Uchida et al. (1985) performed non-steady axisymmetric magnetohydrodynamic simulations in which the field is assumed to be axial at high Galactic latitudes. However, due to the differential rotation of the dense gas near the Galactic plane, the field acquires a component along the Galactic plane. Novak et al. (2003) have made a new submillimeter polarimetric map of the Galactic Centre using the Submillimeter Polarimeter for Antarctic Remote Observations (SPARO). The submillimetre thermal emission can act as a tracer of the dust emission and polarimetric observations detect the orientation of these dust grains, thereby providing the direction of the magnetic fields. In their map, the observed magnetic field are tightly aligned with the Galactic plane and they claim that such alignments provide strong evidence of the existence of this large scale magnetic field along the Galactic plane. From our RM data, large scale magnetic field is observed along the Galactic plane (along the line of sight) and is consistent with one of the predictions of the model.

This model further predicts that the line of sight field in the first (+,+) and third quadrant (-,-) of the Galaxy is towards the observer (positive RM), whereas the field is away from the observer in the second (-,+) and fourth quadrant (+,-) of the Galaxy. Since the RM of five non-thermal filaments (NTFs) have been estimated in the past, the

Table 6.2: RM towards the GC NTFs

Name of the NTF	Estimated RM (rad m^{-2})	Reference	Sign of the RM near peak of continuum	Galactic quadrant	Predicted sign of RM
Northern filament (G0.08+0.15)	100 to 2000	Lang et al. (1999b)	positive	First	positive
Snake (G359.1–0.2)	2000 to 5500	Gray et al. (1995)	positive	Third	positive
359.54+0.18	−370 to −4200	Yusef-Zadeh et al. (1997a)	negative	Second	negative
Pelican (G358.85+0.47)	500 to −1000	Lang et al. (1999a)	negative	Second	negative
Radio-arc (G0.16–0.14)	−2000 to −5500	Yusef-Zadeh & Morris (1987a)	negative	Fourth	negative

direction of the magnetic field in these NTFs can be compared with the prediction of Uchida et al. (1985). Following Novak et al. (2003), the RM towards these NTFs are given in Table 6.2. From the Table, it is clear that the signs of RM towards all these NTFs are consistent with the predictions of magnetohydrodynamic model of Uchida et al. (1985). However, from our observations, the estimated RM towards the sources seen through all the four quadrants of the Galaxy are positive, which indicate that their model is not globally valid in the central 1 kpc region. However, we only have a few sources within 1° of the GC (1° corresponds to 150 pc at the distance of the GC) and due to statistical uncertainty involving small number of measurements, we cannot rule out their model near the GC.

(ii) We consider one more model of the magnetic field, which Rand & Kulkarni (1989) had proposed to explain the large scale geometry of the magnetic fields in our Galaxy. In this model, the magnetic field lines are oriented along circular rings in the Galactic plane. As discussed in Rand & Kulkarni (1989), such a geometry arises in galactic dynamo models of the field, in which a symmetric azimuthal mode is dominant (e.g., Krause (1987)). Reversals of the field as a function of galactocentric radius are also predicted by this model. Theories involving a primordial origin of the field also claim to be able to produce ring fields, but only in the inner regions of galaxies (Sofue et al.

1986). For simplicity, we consider a single ring model of the magnetic field in the GC, along which the regular field lines are oriented. In this model, the sign of the line of sight magnetic field changes with the change of sign of the Galactic longitude. However, we find that the median RM estimated towards the sources with positive Galactic longitude is 579$\pm$131 rad m^{-2}, whereas the median RM towards the sources with negative Galactic longitude is 451$\pm$110 rad m^{-2}. Since, the sign of the median RM does not flip with the sign of the Galactic longitude, a single ring model fails to explain the observations.

(iii) We now consider the GC magnetic field to be part of the large scale magnetic field configuration in our Galaxy. To explain the estimated RM towards the extragalactic sources and the pulsars, Simard-Normandin & Kronberg (1980) and Han et al. (1999) have earlier proposed a bisymmetric spiral model of the magnetic field. In this model, the line of sight component of the fields near the GC can have the same sign on both positive and negative Galactic longitude (see Fig. 6.4). We note that if the magnetic field in our Galaxy is a result of the compression of the primordial magnetic field during the formation of the Galaxy, the net magnetic field of the Galaxy will be non-zero. Indeed, our observations show a net positive magnetic field at the GC region. Therefore, a primordial origin of the magnetic field in our Galaxy is consistent with our observations.

6.4.2 Estimation of the magnetic field from the RM:

In order to estimate the *l*os component of the magnetic field from the RM, a model of the electron density distribution is required. Therefore, we first discuss the available models of the electron density distribution near the GC, and then estimate the regular component of the magnetic field from our data.

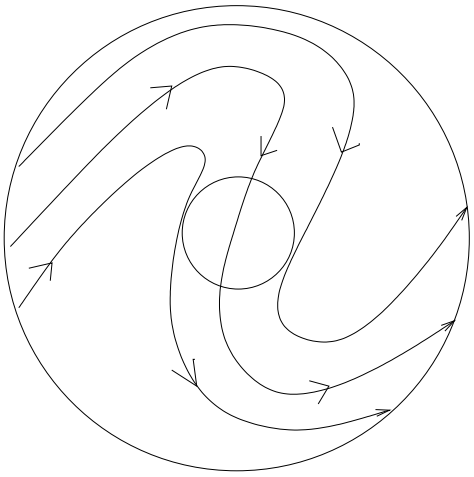

Figure 6.4: A schematic diagram of the bisymmetric spiral structure of the magnetic field in the Galaxy.

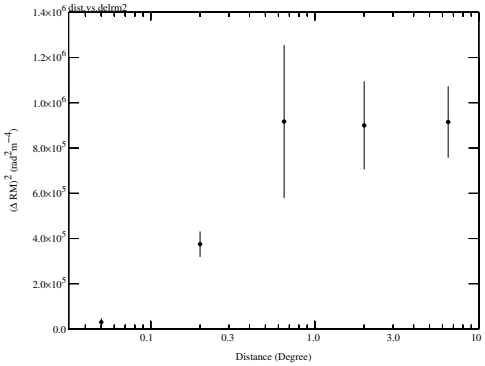

Figure 6.5: Structure function of the RM

6.4.2.1 Electron density distribution in the GC region

A radio signal at frequency ν propagates through the ISM with group velocity $v = c[1 - (v_p^2/v^2)]^{0.5}$, where c is the speed of light in vacuum, $v_p = e[n_e/(\pi m)]^{0.5}$ is the plasma frequency and e and m are the charge and mass of the electron. This causes frequency dependant delay in pulse arrival time, and is related to the dispersion measure ($\int n_e dL$, where, n_e is the electron density and 'L' is the *l*os distance) of the medium. By using pulsars, the dispersion measure can easily be estimated, and if the distance to the pulsar is known, the average electron density along the *l*os can be measured.

The ionised plasma in the ISM causes refraction of the radio waves and in presence of turbulence in the medium, the plasma density fluctuates, causing scattering of the electromagnetic waves. The scattering of the waves causes angular broadening of the sources emitting the electromagnetic radiation (see Rickett (1990) for a review). Using scatter broadening, it is possible to estimate the electron density fluctuation in the ISM, which under certain assumptions is related to the electron density in the ISM.

Using these two methods, Taylor & Cordes (1993) have made a model of the electron density in the Galaxy. However, their model does not include the electron density in the

GC region. Therefore, we consider alternate models of the electron density distribution in the GC region. van Langevelde et al. (1992) showed that there is a region of enhanced scattering towards the central region of the Galaxy. Using constraints based on free-free absorption, they suggested the scattering region to be located at a distance of more than 850 pc from the GC. However, using a likelihood analysis, Lazio & Cordes (1998b) showed that there is a 'hyperstrong' scattering screen ($n_e \sim$10 cm^{-3}) with an angular extent of about half a degree along our *los* towards the GC. They estimate a distance of 133^{+200}_{-80} pc for the screen from the GC. However, the extragalactic source G359.87+0.18 (Lazio et al. 1999) is seen through the 'hyperstrong scattering' region, but has a scattering size of an order of magnitude less than the prediction of the 'hyperstrong scattering' model. Therefore, it appears that either their model underestimates the distance to the screen from the GC, or the source is seen through holes in the scattering screen (Lazio et al. 1999). Bower et al. (2001) have carried out VLBA observations of 3 extragalactic sources and report an intermediate scattering region covering $\gtrsim 5^\circ$ in longitude and $\leq 5^\circ$ in latitude. The estimated scattering size of the 3 extragalactic sources are almost 2 orders of magnitude less than what is predicted by the 'hyperstrong' scattering and about 1.5–6 times more than the prediction by the Taylor & Cordes (1993) model. The scattering size of these extragalactic sources are comparable to the scattering size of the maser sources near the GC (van Langevelde et al. 1992), which suggests that either these sources are viewed through holes in the scattering screen, or the screen is located several kpc away from the GC. Cordes & Lazio (2002) have recently modified the electron density model of Taylor & Cordes (1993), and have included a GC component (based on Lazio & Cordes (1998b)). However, the inner Galaxy component in their model peaks along the '4 kpc molecular ring'. Since, the '4-kpc ring' is visible for $|l| < 30^\circ$, Cordes & Lazio (2002) model does not explain the enhanced scattering observed by Bower et al. (2001) only in the central few degrees of the GC. We believe that other than the GC scattering screen of size 0.5°, there is a region of enhanced scattering covering

$\gtrsim 5^\circ$ in Galactic longitude and $\leq 5^\circ$ in Galactic latitude. However, since the scattering size of a source is a function of the electron density and the clumpiness of the medium, in the absence of further constraints, estimating the electron density of this component is difficult. Since the scattering angle measured by Bower et al. (2001) is 1.5–6 times higher than the prediction from Taylor & Cordes (1993) or Cordes & Lazio (2002), we have taken an electron density 0.4 cm^{-3}, which is twice of the Taylor & Cordes (1993) model for the inner Galaxy. The corresponding dispersion measure due to the inner 2 kpc of the Galaxy is 800 pc cm^{-3}. From the Cordes & Lazio (2002) model, we estimate a dispersion measure of about 800 pc cm^{-3} along the *l*os from the rest of the Galaxy. Therefore, about half of the total dispersion measure along the *l*os originates from the inner few kpc of the Galaxy. It should be noted that at present the dispersion measure of the inner Galaxy component is uncertain by factor of a few.

6.4.2.2 The *los* average magnetic field:

The Faraday rotation measure is defined in Equation 6.1 as

$$RM = 0.81 \int n_e B_{||} dL$$

Where RM is expressed in rad m^{-2}, n_e in cm^{-3} and $B_{||}$ is the component of the regular field along the *los* in microGauss. Measurement of RMs together with an estimate of dispersion measure $(DM) = \int n_e dL$ allows an estimate of $B_{||}$ of the magnetic field. The large scale average magnetic fields estimated by this method will have contribution (i) from the GC region (size 2 kpc), and (ii) from the rest of the Galaxy along the *l*os. We first consider the RM contributed by the magnetic field outside the central 2 kpc region of the Galaxy.

If the large scale magnetic field along the Galactic plane follows a ring like configuration concentric with the GC (Rand & Kulkarni 1989), then the *l*os component of this

field for $|l| \leq 6^\circ$ is estimated to be ≤ 0.2 μG. Therefore, even if we neglect field reversals along the *los*, the contribution of the large scale field of the Galaxy to the estimated RM is $\lessapprox$ 30% (DM 800 pc cm^{-3}). We reach similar conclusion, even if the magnetic field geometry is a bi-symmetric spiral (Simard-Normandin & Kronberg 1980). Therefore, we do not consider the effect of the large scale Galactic magnetic field to the estimated RM any further.

With the estimated median RM of 467 rad m^{-2}, and a DM of 800 pc cm^{-3}, we estimate 0.7 μG to be the average line of sight magnetic field in the central 2 kpc. We note that if there are 'n' field reversals in the GC region, then the estimated field is underestimated by at least a factor of n+1. Therefore, the field strength estimated above should be regarded as a lower limit.

6.4.3 Small scale variations in the RM:

The variations in RM over an angular scale of $\Delta\theta$ are described by the RM structure function $D(\Delta\theta) =< [RM(\theta) - RM(\theta + \Delta\theta)]^2 >$. The structure function is estimated by computing angular separation $\Delta\theta$ and by computing the expectation value of the squared differences of the RM among all pairs of sources within that angular separation. We have binned the data with $\Delta\theta$ 0.0° to 0.1°, 0.1° to 0.3 °, 0.3°to 1.0°, 1.0°to 3.0° and 3.0° to 10°, and the structure function is computed within that interval. The RM structure function is shown in Fig. 6.5. The errorbars in the plot have been estimated by a statistical method known as 'Bootstrap' (Efron 1976). The structure function due to a perfectly uniform field will have a measurable geometrical component due simply to the change in the line of sight component of the field with change in l and b. An observer embedded in an extended homogeneous medium with uniform magnetic field approaching from an arbitrary angle θ_0 sees a rotation measure $RM_0 cos(\theta - \theta_0)$ (Clegg et al. 1992), where RM_0 is the RM towards θ_0. However, it can be shown that the contribution of this geometric component is much less than what is observed in Fig. 6.5. Therefore, we do

not consider this effect any further. It is clear from Fig. 6.5 that as the angular separation tends to zero, the structure function also goes to zero; indicating that the difference in RM originates in our Galaxy, and intrinsic contribution to the RM is negligible. The Galactic ISM is likely to introduce the observed RM. The structure function increases with angular separation from the origin, and at separations of $\sim$0.7° (100 pc) saturates at a value equal to twice the RM variance. If we define the outer scale as the length scale at which the structure function attains half of its maximum value (Rickett 1988), then we estimate an outer scale length of $\approx$30 pc corresponding to an angular scale of 0.3° at an assumed distance of 8.5 kpc. We note that this estimated value of the outer scale is much larger than the estimated outer scale of $\sim 10''$ (0.4 pc) towards the GC NTF G359.54+0.18 (Yusef-Zadeh et al. 1997a) and the Snake (G359.1−0.2) (Gray et al. 1995). This indicates the properties of the Faraday screen near the NTF is very different from the screen that what we have sampled.

6.4.3.1 Comparison with theoretical structure function

The small scale variations in a magnetoionic medium are likely to be related to the electron density fluctuations in the ISM, which have been studied through scattering and scintillation observations (Rickett 1990). The power spectrum of the electron density irregularities can be expressed by

$$P(q) = C_n^2 q^{-\alpha}, q_0 < q < q_i \tag{6.2}$$

Where q is the spatial wavenumber, and α is the spectral index (Rickett 1977). C_n^2 is the normalisation constant of the electron density power spectrum. The quantities q_0 and q_i represent wavenumbers corresponding to 'outer scale' and 'inner scale' of the turbulence respectively.

If this formula remains valid over the range of scale sizes from those responsible for scattering ($\sim 10^8$ cm) to those responsible for Faraday rotation ($\sim 10^{19}$ cm) as has been

suggested by Armstrong et al. (1981), then the statistical contribution to the rotation measure structure function (Simonetti & Cordes 1988) is given by

$$D_{RM}(\Delta\theta) = (2.89 \times 10^5)(C_n^2 L) < B_{||} >^2 (L\Delta\theta)^{5/3} \quad (6.3)$$

Here, $\Delta\theta$ is the angular separation in degrees between the lines of sight probed, $< B_{||} >$ is the systematic component of the line of sight magnetic field strength in microGauss, and L is path length through the turbulent medium in kpc. This expression assumes a Kolmogorov spectrum of density irregularities (i.e, $\alpha = 11/3$). In this equation, the quantity $C_n^2 L$ can be estimated from scattering. The scattering size of an object at 1 GHz is given by

$$\theta_{mas} = 2.24 \left(\int C_n^2 dL \right)^{0.6} \quad (6.4)$$

(Spangler et al. 1986). From Bower et al. (2001), we roughly estimate a scatter broadened size of about 300 milli-arcsec at 1 GHz, which yields $C_n^2 L = 3.5$ m$^{-20/3}$ kpc. Since, $< B_{||} >^2$ has already been estimated in the previous section, if 'L' is known, D_{RM} can be estimated. However, the thickness of the scattering screen (L) is a poorly estimated quantity, and if we take $L = 2$ kpc, then for an angular separation of 0.2°, $D_{RM} = 1.1 \times 10^5$ rad^{2}m^{-4}. The measured structure function at this angular separation is about 3.7×10^5 rad^2 m^{-4} (Fig. 6.5). This indicates that variation in the electron density can only partially account for the RM fluctuation, and magnetic field variation must also contribute to the RM fluctuation. Assuming the fluctuations in electron density and magnetic field to be zero mean isotropic Gaussian random processes having Kolmogorov spectrum and the same outer scale (l_0), Minter & Spangler (1996) have derived the following formula as the structure function of the RM

$$D_{RM} = [251.226(n_e^2 C_B^2 + < B_{||} >^2 C_n^2) + 23.043(C_n^2 C_B^2 (l_0)^{2/3})] \times (L)^{8/3} (\Delta\theta)^{5/3} \quad (6.5)$$

Where n_e is expressed in units of 0.1 cm^{-3}, C_n^2 in 10^{-3} m$^{-20/3}$, C_B^2 in units of 10^{-13} m$^{-2/3}$ μG^2,

l_0 is in pc, L is in kpc and $\Delta\theta$ is in degree. C_B^2 is the normalisation constant of the magnetic field power spectrum, which also have properties similar to that given in Equation 6.2. From the measured value of D_{RM} = 3.7$\times$10^5 rad^2 m^{-4} (Fig. 6.5), at $\Delta\theta$=0.2°, and from Equation 6.5, we compute C_B^2 = 2.1$\times$10^{-13} m$^{-2/3}$ μG^2, which yields the fluctuating component of the magnetic field as $\sim$2 μG at the outer scale length.

6.4.4 Size of the clumps in the scattering medium

Here we consider a specific distribution of scattering material within the screen. Let the electrons be distributed within the scattering screen (thickness L_{pc}) in clumps of size Z_{pc}.

It is well known that for a given column density of electrons, the scattering diameter of a source depends on the clumpiness of the ionised medium, and by integrating Equation6.2, it is possible to estimate the RMS value of the electron density fluctuation. Since almost all the electrons are distributed in clumps, we assume the RMS electron density in the clumps equals the actual electron density (i.e., the product of the mean electron density within the screen with the ratio of the thickness of the screen to the clump size) in the clumps, and as shown below, it is possible to estimate the size of the clumps.

As in Spangler (1991), he has derived the following relationship between the observed angular diameter due to scattering (θ_1) and the characteristics of the turbulence,

$$\theta_1 = \frac{8.0 \times 10^7 (\Delta n_e)^{1.2} Z_{\rm pc}^{0.6}}{l_0^{0.4}} \,\mathrm{mas}, \tag{6.6}$$

where, θ_1 is defined at a fiducial frequency of 1 GHz, Δn_e is the RMS electron density fluctuation in cm^{-3} in the turbulent medium, $Z_{\rm pc}$ is the path length through the turbulent medium in parsecs, and l_0 is the size of the 'outer scale' in cm. If the probability of encountering the clump within the screen is denoted by f, then in the above equation, $Z_{\rm pc}$ can be expressed as $f \times L_{\rm pc}$. As explained above, all the electrons resides within clumps, and we can write $\Delta n_e \approx n_e/f$, where n_e is the *los* averaged electron density

within the central 2 kpc. With the above approximations, we get

$$f = \frac{1.486 \times 10^{13}}{\theta_1^{1.67} \times l_0^{0.67}} \times n_e^2 \times L_{pc},$$

which allows us to estimate f.

In Sect. 6.4.3.1, we have used a typical value of θ_1 $\sim$300 mas at 1 GHz. Using n_e=0.4 cm^{-3}, we get f=0.017, $Z_{\rm pc}$=35 and within the cloud Δn_e $\sim$20 cm^{-3}. This shows that there will be typically $\sim$1 cell (f $\sim$0.02) along the *l*os, which produces the observed RM. One observable consequence of it is that the optical depth of these clouds are $\sim$1 at 74 MHz. Based on VLA 74 MHz observations of the GC, Anantharamaiah et al. (2002) found that central few kpc of the Galaxy is nearly optically thick at 74 MHz, which provides observational evidence to the above estimated parameters of the clouds.

6.4.5 Which component of the ISM produces the RM ?

In this section, we first discuss the possible components of the ISM that contribute to the observed RM and examine if these considerations are valid near the GC. We finally try to distinguish the component of the ISM, whose properties best match with the scattering screen.

It is widely believed that there are four phases of the ISM, referred to as (i) Hot Ionised Medium (HIM), (ii) Warm Ionised Medium (WIM), (iii) Warm Neutral Medium (WNM) and (iv) the Cold Neutral Medium (CNM). Since, the Faraday rotation is produced by ionised gas in the presence of magnetic field, the warm ionised component of the ISM is likely to be responsible for it. However, it is not clear if the WIM consists mainly of the Reynolds WIM (RWIM) (Reynolds 1991) found in HII regions, or there exists another form of the WIM known as the McKee-Ostriker WIM (MOWIM) (McKee & Ostriker 1977), which mostly exists in the MO warm neutral medium (MOWNM). Heiles (2001) has suggested that the pulsar dispersion measure is mainly caused by the MOWIM, whereas, scattering is mainly caused by the RWIM. We note that if MOWIM

causes most of the dispersion measure (as it is linearly dependent on the electron density), Faraday rotation will also be caused by it.

However, Cordes et al. (1985) have suggested a two-component model for the electron density fluctuations consisting of:

(a) A clumped, highly scattering component with a scale height of $\leqslant$100 pc and filling factor $\sim 10^{-4} - 10^{-2}$, indicative of association with extreme Population I material (HII regions, stellar wind bubbles, supernova remnants, etc.), which is responsible for enhanced scattering in the inner part of the Galaxy.

(b) A nearly uniform, moderately-scattering component with a scale height $\geqslant$500 pc and a large filling factor ($>$0.5).

Anantharamaiah & Narayan (1988) has proposed that the high scattering observed towards the inner Galaxy (Rao & Ananthakrishnan 1984; Dennison et al. 1984) is associated with component (a). They argued that this enhanced scattering is caused by the ionised outer envelopes of the HII regions. The number of HII regions in the inner Galaxy are known to be large and their typical sizes are in the range of 1–10 pc with electron densities of $\sim 10^2$ cm^{-3}. The envelopes of these HII regions could have sizes of several tens of parsecs and typical densities $\sim$1–10 cm^{-3}.

In the previous section, we have shown that the clumps in the scattering screen have $n_e \sim 20$ cm^{-3} and size $\sim$30 pc. It is quite remarkable that the properties of these clumps matches with the parameters of the outer envelopes of the HII regions discussed above and it is likely that a significant fraction of the estimated RM is produced by the outer envelopes of HII regions.

6.4.6 Implications for the GC magnetic field

The Faraday RM is a *l*os integration of the product of the line of sight magnetic field and the electron density. Therefore, if the electron density is small where magnetic field is large, it will result in underestimation of the average magnetic field (where the

average electron density is known). We have shown before that a major fraction of the electrons in the inner Galaxy could be in the form of clumpy diffuse outer envelope of the HII regions. Though these HII regions could be anywhere along the *l*os, the scattering diameter of the extragalactic sources increases in the central few degrees of the Galaxy, which indicate the distribution of the HII regions peaks within the central 1–2 kpc of the Galaxy and the estimated magnetic field mostly indicates the field strengths near the HII regions.

It has long been suspected that there is a all pervasive milliGauss strength magnetic field within $\sim 1^{\circ}$ of the GC. We note that though a good fraction of n_e is in the HII regions, MOWIM is believed to be all pervasive (see part (b) of Sect. 6.4.5). Using the Faraday RM produced by this medium, we can constrain the GC magnetic field. The WIM component having a large scale height ($\sim$0.5 kpc) can be identified with the MOWIM, which has electron density $\approx$0.03 cm^{-3}. Near the GC, we can assume that the MOWIM has densities similar to the rest of the Galaxy. There are about 9 sources in our sample seen through the 1.5° of the GC, and we do not find their RM to be significantly higher than other sources in the sample. With the electron densities of the MOWIM given above and by taking a *l*os path through the GC medium of about 300 pc, we provide an upper limit of 60 μG as the *l*os component of the GC magnetic field. This field strength is much lower than the hypothesised milliGauss magnetic field, which suggests that the strong magnetic fields near the NTFs is only a local enhancement of the field strength.

6.5 Summary

In order to study the properties of the Faraday screen near the GC, we have observed 64 background extragalactic sources through the $-6^{\circ} < l < 6^{\circ}$, $-2^{\circ} < b < 2^{\circ}$ region of the Galaxy using the C and X band of the ATCA and VLA. We detect polarised emission

from 45 sources (65 components) and could unambiguously estimate the RM introduced by the Galaxy towards 61 source components. Based on these observations, we conclude the following:

(i) There is a large scale magnetic field (strength $\sim$0.7 μG) in the central $-6^\circ < l < 6^\circ$, $-2^\circ < b < 2^\circ$ region of the Galaxy, aligned along the plane of the Galaxy.

(ii) This large scale magnetic field points towards us in both the positive and negative longitude of the Galaxy. If the primordial magnetic field is concentrated while the Galaxy is formed, it will result in having a total non-zero magnetic field around the centre. Therefore, our result is consistent with a primordial origin of magnetic field in the Galaxy.

(iii) The outer scale of the Faraday screen sampled by these observations is about 30 pc, which is much larger than the scale size of $\sim 10''$ observed near the NTFs in the GC. This indicates that the properties of this Faraday screen of the GC ISM away from the NTFs could be very different from what is found close to the NTFs.

(iv) Though some of the estimated parameters are uncertain by a factor of few, the RM structure function could not be explained with electron density fluctuations alone. A magnetic field fluctuation of $\sim 2\mu$G along with the electron density fluctuation could explain the observed RM structure function.

(v) We estimate the probability of encountering the scattering material in the central 2 kpc of the Galaxy to be $\sim$0.02, which indicates that the plasma is arranged in the form of dense clumps, whose sizes are $\sim$35 pc and electron density $\sim$20 cm^{-3}. These ionised clouds are likely to be the ionised outer envelope of the HII regions. The estimated physical parameters of the clouds match quite well with what was predicted by Anantharamaiah (1986); Anantharamaiah & Narayan (1988) to explain the detection of the Galactic ridge radio recombination line in the inner Galaxy.

(vi) Assuming that the MOWIM has similar properties in the GC as in the rest of the Galaxy, these observations constrain the maximum line of sight magnetic field to 60 μG

in the GC region, which suggests that the milliGauss magnetic field estimated near the NTFs are localised and does not pervade the central 150 pc of the GC.

Chapter 7

Conclusions and future work

In this thesis, we have investigated some of the properties of some of the discrete sources and the Interstellar medium near the Galactic Centre using observations at several radio frequency bands. In this chapter, we briefly describe the outcome of these studies and possible studies in the future in order to better understand the physical processes in the region.

7.1 Results

7.1.1 Observations of the Galactic Centre at 620 MHz

In order to estimate the low frequency spectral indices of the sources in the region and to constrain their relative location, the GC region was observed with the GMRT at 620 and 580 MHz. These observations have provided us several important pieces of information, which we describe below.

(i) For the first time, Sgr A East is shown to display a break in its spectral characteristics. It has a spectral index of about -0.76 at frequencies above 1.4 GHz. However, between 1.4 and 0.33 GHz, its spectral index is about -0.3, indicating that its spectral index changes by $\approx$0.5 at $\approx$1 GHz. Using the standard synchrotron model for spectral break, we estimate the age of Sgr A East to be about 10^4 years.

(ii) Emission from the $7'$ halo also shows a similar break in the spectrum, which

suggests that the Sgr A East and the $7'$ halo are physically associated.

(iii) Sgr A* has been detected at 580 MHz, which is the lowest unambiguous frequency at which it has been detected and the estimated flux density at this frequency is consistent with what is expected from its higher radio frequency spectral index and the flux density. This indicates that there is no low frequency turnover of its emission above 580 MHz.

(iv) The optical depth of the Sgr A West HII region is estimated to be about 2.6 at 620 MHz. Though Sgr A* is located along the same line of sight, its emission shows no absorption by this HII region, which indicates that Sgr A* is located in front of Sgr A West.

7.1.2 GMRT observations of suspected SNRs with filamentary structures near the Galactic Centre

In order to investigate any possible non-thermal filament beyond the central 1° region of the GC, we have carried out low frequency observations of two filamentary structures, which could be either part of SNR or possible NTF in the region. One of these filamentary structure is G357.1–0.2 and the other one was close to the suspected SNR G3.1–0.6. We also observed the peculiar source, the Tornado nebula, for which no previous high resolution studies below 1.4 GHz was made. This has led to the following conclusions.

(i) Confirmation that G3.1$-$0.6 is supernova remnant. This was the largest suspected SNR ($28' \times 49'$) detected during the Molonglo Galactic Centre survey.

(ii) The detection of two curved extended structures in the field of one of these filamentary structure. These extended objects appear to be part of a large shell like structure (size $\approx 52' \times 72'$) centred at G356.8$-$0.0. Its spectral index is estimated to be steeper than -0.34.

(iii) We find that the three previously suspected supernova remnants, G356.6+0.1, G356.3$-$0.3 and G357.1$-$0.2 are located on an extended object, which appears to be

part of the large shell described above. We suggest that G356.6+0.1 and G356.3−0.3 are actually parts of this large shell which were accidentally identified as separate objects in the MOST survey.

(iv) The peculiar morphology and the spectral index of the object G357.1−0.2 suggests that it is a a plerionic type of supernova remnant with a spectral break around 1 GHz and is located at a distance of more than 6 kpc from us.

(v) We have made spectral tomographic maps of the Tornado nebula between 1.4 GHz and 330 MHz. We find that a few of the filamentary structures appears to show spectral index variation, which could either be explained by difference in the conditions of electron acceleration at the site of shocks, or a curved electron energy spectrum. The overall variation of the spectral index of the extended features across the nebula is consistent with what is seen in other SNRs.

(vi) Using HI absorption towards the Tornado nebula, it can be placed in or beyond the central few hundred pc of the Galactic Centre. Comparison of its HI spectrum with what is observed for the suspected extragalactic source G356.9+0.1 indicate that the Tornado nebula is located at the nearer side of the GC, which for the first time puts an upper limit on its distance.

7.1.3 Constraints on distances to Galactic Centre non-thermal filaments from HI absorption

Out of nine known NTFs in the GC region, the line of sight distance of only two of them were previously estimated. We have carried out HI absorption line study of three other NTFs named as Sgr C, G359.79+0.17 and G359.54+0.18, which has led to the following results.

(i) For the first time, the Sgr C NTF and the HII region are shown to be located within a few hundred parsecs of the GC.

(ii) Our study indicates that the Sgr C HII region is either embedded in or located

behind the -65 km s^{-1} molecular cloud, whereas the Sgr C NTF is located at the near side of the cloud, which argues against any possible interaction between the two objects.

(iii) A molecular cloud with a velocity of -100 km s^{-1} appears to be associated with the central part of the Sgr C NTF and on the basis of the presently existing data, it appears that the magnetic pressure in the NTF is higher than the pressure due to the -100 km s^{-1} cloud.

(iv) HI absorption by the '3 kpc arm' is detected against all the three NTFs, which indicates that the NTF G359.54+0.18 and G359.79+0.17 are located at a minimum distance of 5.1 kpc from the Sun.

(v) Weak HI absorption ($4\,\sigma$ level) at -140 km s^{-1} suggests that the NTF G359.54+0.18 is located at a minimum distance of $\approx$ 8.5 kpc from us.

(vi) The maximum distance of the NTF G359.54+0.18 and G359.79+0.17 is estimated to be 10.5 kpc from the Sun.

The present study extends the number of NTFs that have been found to be located near the GC region to five. With most of the known NTFs now being shown to be near the GC, there remains little doubt that phenomena related to the central region of the Galaxy are responsible for the creation and maintenance of the NTFs.

7.1.4 Magnetic field near the Galactic Centre: Rotation Measure observations of Extragalactic sources

In order to study the properties of the Faraday screen near the GC, we have observed 64 candidate extragalactic sources through the $-6^\circ < l < 6^\circ$, $-2^\circ < b < 2^\circ$ region of the Galaxy using the C and X band of the ATCA and VLA. These observations for the first time provide information on the polarisation fractions of the background sources seen through the region. We provide 4.8 GHz maps of all the observed sources and estimate the angular sizes, spectral indices and polarisation fractions of these sources.

Based on the morphology, spectral characteristics and polarisation properties, we

identify 4 Galactic HII regions in the sample. The remaining 61 sources show non-thermal emission. Except the source G359.2-0.8 (Mouse), which is a known Galactic non-thermal source, we compare the properties of the remaining non-thermal sources with the known types of Galactic non-thermal sources like SNRs, radio pulsars, radio stars, transient sources and Galactic microquasar. None of the sources appear to share the characteristic properties of these Galactic non-thermal sources. We find that their number density, angular size vs. flux density and non-thermal spectral indices are consistent with what is known for the extragalactic sources.

We detect polarised emission from 45 sources (65 components) and could unambiguously estimate the RM introduced by the Galaxy towards 61 source components. Based on these observations, we conclude the following:

(i) There is a large scale magnetic field (strength $\sim$0.7 μG) in the central –6° $< l <$6°, – 2° $< b <$2° region of the Galaxy, aligned along the plane of the Galaxy.

(ii) This large scale magnetic field points towards us in both the positive and negative longitude of the Galaxy. If a primordial magnetic field is concentrated and amplified while the Galaxy is formed, it will result in having a total non-zero magnetic field around the centre. Our result is consistent with such a magnetic field in the Galaxy Centre region.

(iii) The outer scale of the Faraday screen sampled by these observations have a value of 30 pc, which is much larger than the scale size of $\sim$10″ observed near the NTFs in the GC. This indicates that the properties of this Faraday screen of the GC ISM away from the NTFs could be very different from what is found close to the NTFs.

(iv) Though some of the estimated parameters are uncertain by a factor of few, the RM structure function could not be explained with electron density fluctuations alone. A magnetic field fluctuation of $\sim 2\mu$G along with the electron density fluctuation could explain the observed RM structure function.

(v) We estimate the probability of encountering the scattering material in the central

2 kpc of the Galaxy to be $\sim$0.02, which indicates that the plasma is arranged in the form of dense clumps, whose sizes are $\sim$35 pc and electron density $\sim$20 cm^{-3}. These ionised clouds are likely to be the ionised outer envelope of the HII regions. The estimated physical parameters of the clouds match quite well with what was predicted by Anantharamaiah (1988) to explain the detection of the Galactic ridge radio recombination line in the inner Galaxy.

(vi) Assuming that the MOWIM has similar properties in the GC as in the rest of the Galaxy, these observations constrain the maximum line of sight magnetic field to 60 μG in the GC region, which suggests that the milliGauss magnetic field estimated near the NTFs are localised and does not pervade the central 150 pc of the GC. The low value of the magnetic field estimated from our data challenges the paradigm of milliGauss magnetic fields based on the rigidity argument of the NTFs (Yusef-Zadeh & Morris 1987a) and supports the cometary plasma tail model of Shore & Larosa (1999) for the origin of the isolated nonthermal filaments at the Galactic center. The cometary model indicates the NTFs to be dynamic configurations, and not static structures. As such, they are local amplifications of an otherwise weak field and not directly connected to any static global field.

7.2 Future Prospects

7.2.1 Low frequency spectral index of Sgr A*

Our observations at 620 and 580 MHz with the GMRT and its earlier VLA observation at 330 MHz indicate that Sgr A* has a low frequency turnover between 580 and 330 MHz. This can be caused by different physical processes. Since the line of sight HII region Sgr A West appears to be located behind it, we believe that the low frequency turnover of Sgr A* is intrinsic. This intrinsic turnover can be caused by thermal free-free absorption, synchrotron self absorption or Razin effect. Since the expected spectral

indices due to these three physical processes are quite different, future high resolution ($\sim$arc-sec) observations between 580 and 330 MHz will be crucial to identify the cause of the turnover of its observed flux density.

7.2.2 Low radio frequency observations of the Galactic Centre region

The detection of spectral break of Sgr A East highlights the importance of multifrequency observations to distinguish between competing physical processes. The low frequency observations (below 1 GHz) in many cases provide important information about the source property (e.g., intrinsic turnover). However, at these frequencies, the free-free optical depth of the line of sight plasma towards the GC becomes significant, and unless its effect is modelled properly, estimation of source properties like the flux density will be incorrect due to absorption by this line of sight gas. At present, observations at frequencies above 330 MHz is available. However, even at a frequency of 330 MHz, the free-free optical depth of the gas is $\lesssim$1 towards the GC. Therefore, observations at frequencies below 330 MHz (e.g., 230 and 150 MHz band of the GMRT) will be crucial to model the absorption due to line of sight plasma.

7.2.3 Magnetic field in the Galactic Centre region

Our observations of the Faraday RM towards 45 polarised extragalactic sources seen through $-6^\circ < l < 6^\circ$, $-2^\circ < b < 2^\circ$ region of the Galaxy have indicated that the line of sight magnetic field strength is only $\sim \mu$G. These observations also indicate the upper limit of the line of sight magnetic field strength in the central 150 pc of the Galaxy $\lesssim$60 μG. This raises questions on the mG field estimated from observations of the NTFs in the region. It is possible that the magnetic field strength near the NTFs are very different than the dense ISM in the region. However, in order to estimate this upper limit, we had to assume that the MOWIM in the region has similar properties as in the rest of the Galaxy. In the following paragraphs, we suggest two different methods to compare the

magnetic field in the central region with the inner few kpc of the Galaxy.

(i) If several polarised extragalactic sources are identified such that part of them are seen along the NTFs and part of them are randomly distributed towards the direction of the GC, then any systematic difference of RM between these two groups of samples will indicate change in the property of the magnetic field or the electron density near the NTFs. If the scattering measure towards these sources is also estimated, then it will be possible to constrain any possible variation of the line of sight magnetic field near the NTFs. However, the probability of finding such sources with flux densities strong enough to have detectable polarised emission is pretty low with the present telescopes. Future observations with long enough integration time will be useful in this regard.

(ii) The RM introduced to polarised signal from extragalactic sources seen near the GC are likely to be caused by magnetic field sampled at places, where any intervening HII regions (due to high electron density in the HII regions) are located. If we assume the HII regions to be randomly located along our line of sight in the inner 4 kpc of the Galaxy, then the probability of finding one such object in the central 150 pc is about 0.04. Therefore, if we can identify and observe more than 25 polarised extragalactic sources through the central 1° of the GC, and if the line of sight magnetic field in the region is much higher than the general ISM of the Galaxy, then it is likely that we will identify very high RM towards one or two background sources. Therefore, future RM observations of the extragalactic sources in the region with high sensitivity will be important for tightly constraining the GC magnetic field.

7.2.4 Magnetic field in the inner Galaxy

As in Sect. 6.1, the magnetic field in the inner few kpc of the Galaxy is not measured systematically. We have carried out observations which covers only about a third of the central few kpc region of the Galaxy. Therefore, future observations of Faraday RM towards the extragalactic sources seen through the inner $\sim$20° of the Galaxy will be

important to constrain the magnetic field in the region.

Bibliography

Anantharamaiah, K. R. 1985, Journal of Astrophysics and Astronomy, 6, 203

—. 1986, Journal of Astrophysics and Astronomy, 7, 131

Anantharamaiah, K. R., Kassim, N. E., Lazio, T. J. W., Goss, W. M., & Falcke, H. 2002, in IAU Symposium 199: The Universe at low Radio Frequencies, 272–+

Anantharamaiah, K. R. & Narayan, R. 1988, in AIP Conf. Proc. 174: Radio Wave Scattering in the Interstellar Medium, 185–189

Anantharamaiah, K. R., Pedlar, A., Ekers, R. D., & Goss, W. M. 1991, MNRAS, 249, 262

Anderson, M. C. & Rudnick, L. 1993, ApJ, 408, 514

Armstrong, J. W., Cordes, J. M., & Rickett, B. J. 1981, Nature, 291, 561

Baars, J. W. M., Genzel, R., Pauliny-Toth, I. I. K., & Witzel, A. 1977, A&A, 61, 99

Balick, B. & Brown, R. L. 1974, ApJ, 194, 265

Bally, J., Stark, A. A., Wilson, R. W., & Henkel, C. 1987, ApJS, 65, 13

—. 1988, ApJ, 324, 223

Bally, J. & Yusef-Zadeh, F. 1989, ApJ, 336, 173

Bania, T. M. 1977, ApJ, 216, 381

Beck, R., Brandenburg, A., Moss, D., Shukurov, A., & Sokoloff, D. 1996, ARA&A, 34, 155

Becker, R. H. & Helfand, D. J. 1985, Nature, 313, 115

Becker, R. H., White, R. L., Helfand, D. J., & Zoonematkermani, S. 1994, ApJS, 91, 347

Bell, A. R. 1978, MNRAS, 182, 147

Benson, J. M. & Johnston, K. J. 1984, ApJ, 277, 181

Bieging, J. H. 1976, A&A, 51, 289

Binney, J., Gerhard, O. E., Stark, A. A., Bally, J., & Uchida, K. I. 1991, MNRAS, 252, 210

Blondin, J. M., Lundqvist, P., & Chevalier, R. A. 1996, ApJ, 472, 257+

Bower, G. C., Backer, D. C., & Sramek, R. A. 2001, ApJ, 558, 127

Bower, G. C., Falcke, H., & Backer, D. C. 1999, ApJL, 523, L29

Braun, R. & Strom, R. G. 1986, A&A, 164, 193

Broadbent, A., Osborne, J. L., & Haslam, C. G. T. 1989, MNRAS, 237, 381

Brogan, C. L., Frail, D. A., Goss, W. M., & Troland, T. H. 2000, ApJ, 537, 875

Brown, R. L. & Liszt, H. S. 1984, ARA&A, 22, 223

Brogan, C., L., Nord, M., Kassim, N., Lazio, J. & Anantharamaiah, K. 2003, Astron. Nachr./AN 324, No. S1, 17

Burton, W. B. & Liszt, H. S. 1992, A&AS, 95, 9

Case, G. L. & Bhattacharya, D. 1998, ApJ, 504, 761+

Caswell, J. L. & Haynes, R. F. 1987, A&A, 171, 261

Caswell, J. L. & Lerche, I. 1979, MNRAS, 187, 201

Chevalier, R. A. 1974, ApJ, 188, 501

Clegg, A. W., Cordes, J. M., Simonetti, J. M., & Kulkarni, S. R. 1992, ApJ, 386, 143

Cohen, R. J. 1975, MNRAS, 171, 659

—. 1977, MNRAS, 178, 547

Cohen, R. J. & Davies, R. D. 1976, MNRAS, 175, 1

—. 1979, MNRAS, 186, 453

Condon, J. J., Cotton, W. D., Greisen, E. W., et al. 1998, AJ, 115, 1693

Cordes, J. M., Weisberg, J. M., & Boriakoff, V. 1985, ApJ, 288, 221

Cordes, J. M. & Lazio, T. J. W. 2002, astro-ph/0207156

Cotton W. D., et al. 1980, ApJL, 238, L123

Dulk, G. A, & Slee, O. B. 1974, Nature, 248, 33

Cummins, S. E., Thaddeus, P., & Linke, R. A. 1986, ApJS, 60, 819

Davidson, J. A. 1996, in ASP Conf. Ser. 97: Polarimetry of the Interstellar Medium, 504–+

Davies, R. D., Walsh, D., & Booth, R. S. 1976, MNRAS, 177, 319

DeLaney, T., Koralesky, B., Rudnick, L., & Dickel, J. R. 2002, ApJ, 580, 914

Dennison, B., Broderick, J. J., Thomas, M., et al. 1984, A&A, 135, 199

Denoyer, L. K. 1974, AJ, 79, 1253+

Dickey, J. M., Kulkarni, S. R., Heiles, C. E., & van Gorkom, J. H. 1983, ApJS, 53, 591

Dickey, J. M., Terzian, Y., & Salpeter, E. E. 1978, ApJS, 36, 77

Douglas, J. N., Bash, F. N., Bozyan, F. A., Torrence, G. W., & Wolfe, C. 1996, VizieR Online Data Catalog, 8042, 0

Downes, D., Wilson, T. L., Bieging, J., & Wink, J. 1980, A&AS, 40, 379

Downes, D., Goss, W. M., Schwarz, U. J., & Wouterloot, J. G. A. 1978, A&AS, 35, 1

Dreher, J. W., Carilli, C. L., & Perley, R. A. 1987, ApJ, 316, 611

Efron, B. 1979, Ann. Statistics, 7, 1

Ekers, R. D., van Gorkom, J. H., Schwarz, U. J., & Goss, W. M. 1983, A&A, 122, 143

Falcke H., 1999, in ASP Conf. Ser. 186: The Central Parsecs of the Galaxy, pp 113

Frail, D. A., Goss, W. M., & Slysh, V. I. 1994, ApJL, 424, 111

Frick, P., Stepanov, R., Shukurov, A., & Sokoloff, D. 2001, MNRAS, 325, 649

Gaensler, B. M., Green, A. J., & Manchester, R. N. 1998, MNRAS, 299, 812

Gaensler, B. M. & Hunstead, R. W. 2000, Publications of the Astronomical Society of Australia, 17, 72

Gardner, F. F. & Whiteoak, J. B. 1966, ARA&A, 4, 245

Genzel, R., Thatte, N., Krabbe, A., Kroker, H., & Tacconi-Garman, L. E. 1996, ApJ, 472, 153

Genzel, R. & Townes, C. H. 1987, ARA&A, 25, 377

Ghez, A. M., Klein, B. L., Morris, M., & Becklin, E. E. 1998, ApJ, 509, 678

Goss, W. M., Schwarz, U. J., Ekers, R. D., & van Gorkom, J. H. 1983, in IAU Symp. 101: Supernova Remnants and their X-ray Emission, 65–69

Gray, A. D. 1994a, MNRAS, 270, 861+

—. 1994b, MNRAS, 270, 861+

—. 1994c, MNRAS, 270, 847+

—. 1994d, MNRAS, 270, 835+

Gray, A. D. 1996, in The Galactic Center, Astronomical Society of the Pacific Conference Series, Volume 102, Manuscripts presented at the 4th international meeting jointly organized by the European Southern Observatory (ESO) and Cerro Tololo Inter-American Observatory (CTIO), held March 10-15, 1996 in La Serena, Chile, San Francisco: Astronomical Society of the Pacific (ASP), |c1996, edited by Roland Gredel, p.443, 443–+

Gray, A. D., Cram, L. E., Ekers, R. D., & Goss, W. M. 1991, Nature, 353, 237

Gray, A. D., Nicholls, J., Ekers, R. D., & Cram, L. E. 1995, ApJ, 448, 164+

Green, D. A. 1994, ApJS, 90, 817

Guesten, R. & Downes, D. 1980, A&AS, 87, 6

Gull, S. F. 1973, MNRAS, 161, 47

Han, J. L., Manchester, R. N., & Qiao, G. J. 1999, MNRAS, 306, 371

Han, J. L. & Qiao, G. J. 1994, A&A, 288, 759

Haslam, C. G. T., Stoffel, H., Salter, C. J., & Wilson, W. E. 1982, A&AS, 47, 1+

Heiles, C. 2001, in ASP Conf. Ser. 231: Tetons 4: Galactic Structure, Stars and the Interstellar Medium, 294–+

Helfand, D. J. & Becker, R. H. 1987, ApJ, 314, 203

Helfand, D. J., Zoonematkermani, S., Becker, R. H., & White, R. L. 1992, ApJS, 80, 211

Huettemeister, S., Wilson, T. L., Bania, T. M., & Martin-Pintado, J. 1993, A&A, 280, 255

Kardashev, N. S. 1962, Soviet Astronomy, 6, 317

Katz-Stone, D. M., Kassim, N. E., Lazio, T. J. W., & O'Donnell, R. 2000, ApJ, 529, 453

Killeen, N. E. B., Lo, K. Y., & Crutcher, R. 1992, ApJ, 385, 585

Koyama, K., Awaki, H., Kunieda, H., Takano, S., & Tawara, Y. 1989, Nature, 339, 603

Kramer, C., Staguhn, J., Ungerechts, H., & Sievers, A. 1998, in IAU Symp. 184: The Central Regions of the Galaxy and Galaxies, Vol. 184, 173+

Krause, F. 1987, in Interstellar Magnetic Fields: Observation and Theory, 8–12

Kronberg, P. P., Conway, R. G., & Gilbert, J. A. 1972, MNRAS, 156, 275

Kundu, M. R., Angerhofer, P. E., Fuerst, E., & Hirth, W. 1980, A&A, 92, 225

Landecker, T. L., Zheng, Y., Zhang, X., & Higgs, L. A. 1997, A&AS, 123, 199

Lang, C. C., Anantharamaiah, K. R., Kassim, N. E., & Lazio, T. J. W. 1999a, ApJL, 521, L41

Lang, C. C., Morris, M., & Echevarria, L. 1999b, ApJ, 526, 727

Langston, G., Minter, A., D'Addario, L., et al. 2000, AJ, 119, 2801

Larosa, T. N. & Kassim, N. E. 1985, ApJL, 299, L13

LaRosa, T. N., Kassim, N. E., Lazio, T. J. W., & Hyman, S. D. 2000, AJ, 119, 207

LaRosa, T. N., Lazio, T. J. W., & Kassim, N. E. 2001, ApJ, 563, 163

Lasenby, J., Lasenby, A. N., & Yusef-Zadeh, F. 1989, ApJ, 343, 177

Lazio, T. J. W., Anantharamaiah, K. R., Goss, W. M., Kassim, N. E., & Cordes, J. M. 1999, ApJ, 515, 196

Lazio, T. J. W. & Cordes, J. M. 1998a, ApJS, 118, 201

—. 1998b, ApJ, 505, 715

Leahy, D. A., Xizhen, Z., Xinji, W., & Jiale, L. 1998, A&A, 339, 601

Ledden, J. E., Broderick, J. J., Brown, R. L., & Condon, J. J. 1980, AJ, 85, 780

Lis, D. C. & Goldsmith, P. F. 1990, ApJ, 356, 195

Liszt, H. S. 1985, ApJL, 293, L65

—. 1992, ApJS, 82, 495

Liszt, H. S. & Burton, W. B. 1978, ApJ, 226, 790

Liszt, H. S. & Spiker, R. W. 1995, ApJS, 98, 259+

Liszt, H. S., van der Hulst, J. M., Burton, W. B., & Ondrechen, M. P. 1983, A&A, 126, 341

Little, A. G. 1974, in IAU Symp. 60: Galactic Radio Astronomy, 491–+

Lo, K. Y., Shen, Z., Zhao, J., & Ho, P. T. P. 1998, ApJL, 508, L61

Manchester, R. N. 1987, A&A, 171, 205

Martí, J., Mirabel, I. F., Rodríguez, L. F., & Smith, I. A. 2002, A&A, 386, 571

McKee, C. F. & Ostriker, J. P. 1977, ApJ, 218, 148

Mehringer, D. M., Goss, W. M., Lis, D. C., Palmer, P., & Menten, K. M. 1998, ApJ, 493, 274

Mehringer, D. M., Yusef-Zadeh, F., Palmer, P., & Goss, W. M. 1992, ApJ, 401, 168

Melia, F. & Falcke, H. 2001, ARA&A, 39, 309

Mereghetti, S., Sidoli, L., & Israel, G. L. 1998, A&A, 331, L77

Mezger, P. G. & Pauls, T. 1979, in IAU Symp. 84: The Large-Scale Characteristics of the Galaxy, 357–365

Mezger, P. G., Zylka, R., Salter, C. J., et al. 1989, A&A, 209, 337

Mezger, P. O. 1978, A&A, 70, 565

Mills, B. Y. & Drinkwater, M. J. 1984, Journal of Astrophysics and Astronomy, 5, 43

Minter, A. H. & Spangler, S. R. 1996, ApJ, 458, 194

Mirabel, I. F. & Rodríguez, L. F. 1999, ARA&A, 37, 409

Miyazaki, A. & Tsuboi, M. 2000, ApJ, 536, 357

Morris, M. & Serabyn, E. 1996, ARA&A, 34, 645

Muno, M. P., Baganoff, F. K., Bautz, M. W., et al. 2003, ApJ, 589, 225

Nissen, D. & Thielheim, K. O. 1974, Ap. Space Sci., 33, 441

Novak, G., Chuss, D. T., Renbarger, T., et al. 2003, ApJL, 583, L83

Nord M. E., Lazio T. J. W., Kassim N. E., Goss W. M., Duric N., 2004, ApJL, 601, L51

O'Dea, C. P. 1998, PASP, 110, 493

Odenwald, S. F. & Fazio, G. G. 1984, ApJ, 283, 601

Oka, T., Hasegawa, T., Sato, F., Tsuboi, M., & Miyazaki, A. 1998, ApJS, 118, 455

Oka, T., Hasegawa, T., Sato, F., et al. 2001, ApJ, 562, 348

Oort, J. H. 1977, ARA&A, 15, 295

Pedlar, A., Anantharamaiah, K. R., Ekers, R. D., et al. 1989, ApJ, 342, 769

Pineault, S., Landecker, T. L., & Routledge, D. 1987, ApJ, 315, 580

Radhakrishnan, V., Goss, W. M., Murray, J. D., & Brooks, J. W. 1972, ApJS, 24, 49

Rand, R. J. & Kulkarni, S. R. 1989, ApJ, 343, 760

Rand, R. J. & Lyne, A. G. 1994, MNRAS, 268, 497

Rao, A. P. & Ananthakrishnan, S. 1984, Nature, 312, 707

Reich, W. 1982, A&A, 106, 314

Reich, W. & Fuerst, E. 1984, A&AS, 57, 165

Reid, M. J. 1993, ARA&A, 31, 345

Reid, M. J., Readhead, A. C. S., Vermeulen, R. C., & Treuhaft, R. N. 1999, ApJ, 524, 816

Reid, M. J., Schneps, M. H., Moran, J. M., et al. 1988, ApJ, 330, 809

Reynolds, R. J. 1991, ApJL, 372, L17

Rickett, B. J. 1977, ARA&A, 15, 479

Rickett, B. J. 1988, in AIP Conf. Proc. 174: Radio Wave Scattering in the Interstellar Medium, 2–16

—. 1990, ARA&A, 28, 561

Roberts, D. A. & Goss, W. M. 1993, ApJS, 86, 133

Roberts, D. A., Yusef-Zadeh, F., & Goss, W. M. 1996, ApJ, 459, 627

Roelfsema, P. R., Goss, W. M., Whiteoak, J. B., Gardner, F. F., & Pankonin, V. 1987, A&A, 175, 219

Rougoor, G. W. 1964, Bull. Astron. Inst. Netherlands, 17, 381

Rougoor, G. W. & Oort, J. H. 1960, Proc.Nat.Acad.Sci, 46, 1

Roy, S. 2003, A&A, 403, 917

Roy, S. & Rao, A. P. 2002, MNRAS, 329, 775

Saikia, D. J. & Salter, C. J. 1988, ARA&A, 26, 93

Sakano, M., Koyama, K., Murakami, H., Maeda, Y., & Yamauchi, S. 2002, ApJS, 138, 19

Schwarz, U. J. & Lasenby, J. 1990, in IAU Symp. 140: Galactic and Intergalactic Magnetic Fields, 383–+

Scoville, N. Z. 1972, ApJL, 175, L127+

Scoville, N. Z., Yun, M. S., Sanders, D. B., Clemens, D. P., & Waller, W. H. 1987, ApJS, 63, 821

Serabyn, E. & Morris, M. 1994, ApJL, 424, L91

Shaver, P. A., Salter, C. J., Patnaik, A. R., van Gorkom, J. H. & Hunt, G. C. 1985, Nature, 313, 113

Shore, S. N. & Larosa, T. N. 1999, ApJ, 521, 587

Sidoli, L., Belloni, T., & Mereghetti, S. 2001, A&A, 368, 835

Simard-Normandin, M. & Kronberg, P. P. 1980, ApJ, 242, 74

Simonetti, J. H. & Cordes, J. M. 1988, in AIP Conf. Proc. 174: Radio Wave Scattering in the Interstellar Medium, 134–138

Sofue, Y., Fujimoto, M., & Wielebinski, R. 1986, ARA&A, 24, 459

Sofue, Y. & Handa, T. 1984, Nature, 310, 568

Spangler, S. R. 1991, ApJ, 376, 540

Spangler, S. R., Mutel, R. L., Benson, J. M., & Cordes, J. M. 1986, ApJ, 301, 312

Staguhn, J., Stutzki, J., Uchida, K. I., & Yusef-Zadeh, F. 1998, A&A, 336, 290

Swarup, G., Ananthakrishnan, S., Kapahi, V. K. and· Rao, A. P., Subrahmanya, C. R., & Kulkarni, V. K. 1991, Current Science, 60, 95+

Taylor, J. H. & Cordes, J. M. 1993, ApJ, 411, 674

Tsuboi, M., Handa, T., & Ukita, N. 1999, ApJS, 120, 1

Tsuboi, M., Kobayashi, H., Ishiguro, M., & Murata, Y. 1991, PASJ, 43, L27

Uchida, K., Morris, M., & Yusef-Zadeh, F. 1992a, AJ, 104, 1533

—. 1992b, AJ, 104, 1533

Uchida, K. I. & Guesten, R. 1995, A&A, 298, 473+

Uchida, K. I., Morris, M., Serabyn, E., & Guesten, R. 1996, ApJ, 462, 768+

Uchida, Y., Sofue, Y., & Shibata, K. 1985, Nature, 317, 699

Vallee, J. P. 1980, A&A, 86, 251

van Langevelde, H. J., Frail, D. A., Cordes, J. M., & Diamond, P. J. 1992, ApJ, 396, 686

Voges, W., Aschenbach, B., Boller, T., et al. 1999, A&A, 349, 389

Wakker, B. P. & Schwarz, U. J. 1988, A&A, 200, 312

Weiler, K. W. & Panagia, N. 1980, A&A, 90, 269

Whiteoak, J. B., Gardner, F. F., & Pankonin, V. 1983, MNRAS, 202, 11P

Yuan F., Markoff S., Falcke H., 2002, A&A, 383, 854

Yuan F., Quataert E., Narayan R., 2003, ApJ, 598, 301

Yusef-Zadeh, F. 1989, in IAU Symp. 136: The Center of the Galaxy, 243–+

Yusef-Zadeh, F. & Bally, J. 1987, Nature, 330, 455

Yusef-Zadeh, F. & Morris, M. 1987a, AJ, 94, 1178

—. 1987b, AJ, 94, 1178

—. 1987c, ApJ, 322, 721

Yusef-Zadeh, F., Morris, M., & Chance, D. 1984, Nature, 310, 557

Yusef-Zadeh, F., Morris, M., Slee, O. B., & Nelson, G. J. 1986, ApJ, 310, 689

Yusef-Zadeh, F., Roberts, D. A., & Biretta, J. 1998, ApJL, 499, L159+

Yusef-Zadeh, F., Roberts, D. A., Goss, W. M., Frail, D. A., & Green, A. J. 1996a, ApJL, 466, L25

—. 1996b, ApJL, 466, L25

—. 1999, ApJ, 512, 230

Yusef-Zadeh, F. & Wardle, M. 1993, ApJ, 405, 584

Yusef-Zadeh, F., Wardle, M., & Parastaran, P. 1997a, ApJL, 475, L119

—. 1997b, ApJL, 475, L119

Zhao, J., Bower, G. C., & Goss, W. M. 2001, ApJL, 547, L29

Zoonematkermani, S., Helfand, D. J., Becker, R. H., White, R. L., & Perley, R. A. 1990, ApJS, 74, 181